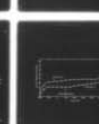
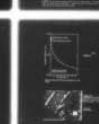
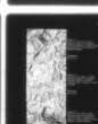
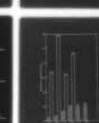
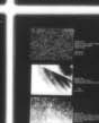


D-A045 331

CARNEGIE-MELLON UNIV PITTSBURGH PA DEPT OF METALLURG--ETC F/G 7/4  
THE ROLE OF TRAPPING ON HYDROGEN TRANSPORT AND EMBRITTLEMENT.(U)  
JUL 77 G M PRESSOUYRE, I M BERNSTEIN N00014-75-C-0265  
TR-7 NL

INCLASSIFIED

1 OF 4  
AD  
A045 331





AD A 045331

The Role of Trapping on  
Hydrogen Transport and  
Embrittlement  
G. M. Pressouyre and  
I. M. Bernstein

*Handwritten:* 1003  
in file

DDC  
1003  
1003

AD A 045331

Technical Report No. 7

to

Office of Naval Research under  
Contract N00014-75-C-0265, NR 036-099 (C-MU) ✓

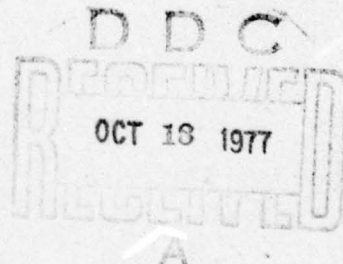
The Role of Trapping on Hydrogen  
Transport and Embrittlement

G. M. Pressouyre

I. M. Bernstein

Department of Metallurgy & Materials Science ✓  
Carnegie-Mellon University  
Pittsburgh, PA. 15213

July 1977



**DISTRIBUTION STATEMENT A**

Approved for public release;  
Distribution Unlimited

Submitted in partial fulfillment of the requirement for the  
degree of Doctor of Philosophy at Carnegie-Mellon University.



## TABLE OF CONTENTS

	<u>Page Number</u>
Acknowledgements.....	i
List of Tables.....	iii
List of Figures.....	v
Abstract.....	ix
 I. INTRODUCTION.....	 1
II. MICROSTRUCTURAL AND MECHANICAL CHARACTERISTICS OF THE ALLOYS, IN THE ABSENCE OF HYDROGEN.....	11
A. The Phase Diagram of the Fe-Ti and Fe-Ti-C Systems.....	11
B. Microstructures of the Alloys.....	14
C. Mechanical Properties of the Hydrogen-Free Alloys.....	24
III. DIFFUSION AND TRAPPING OF HYDROGEN THROUGH IRON AND IRON-TITANIUM MEMBRANES.....	33
A. Past Studies and the Concept of Trapping.....	33
B. Experimental Evidence of Trapping.....	35
C. Experimental Technique.....	41
D. Experimental Results.....	53
E. Analysis of Reversible Trapping.....	62
E.1. Titanium as a Reversible Hydrogen Trap.....	62
E.2. The Possibility of Surface Effect.....	116
E.3. The Possibility of Concentration Effect..	133
E.4. General Conclusions.....	134
F. Analysis of Irreversible Trapping.....	135
F.1. Theoretical Considerations.....	135
F.2. Application of the Theory to Experimental Results.....	140
F.3. Experimental Verification of the Theory....	143
F.4. Discussion.....	146
F.5. Conclusion.....	151
G. General Conclusions.....	152
IV. HYDROGEN-INDUCED CRACKING OF FE-TI ALLOYS (STATIC HYDROGEN EMBRITTLEMENT).....	154
A. Introduction.....	154
B. A Kinetic Model of Hydrogen-Induced Cracking in Fe-Ti Alloys.....	157
B.1. Development of the Model.....	157
B.2. Theoretical Results.....	170
B.3. Experimental Results.....	187
B.4. Discussion of the Hydrogen-Induced Cracking Model.....	198
B.5. Conclusion on the Hydrogen-Induced Cracking Model.....	212

*Letter on file*

BY _____ DATE _____ DISTRIBUTION OR AVAILABILITY CODES	DISC. _____ AVAIL. CODES IF SPECIAL
--	--

Table of Contents (Con't)Page Number

C.	A TEM Study of Some Effects of Hydrogen Charging.....	213
	C.1. Experimental Technique.....	213
	C.2. Experimental Observations.....	214
	C.3. Discussion.....	222
	C.4. Conclusions.....	226
D.	General Conclusions on Static Hydrogen Embrittlement and Proposed Criteria for its Control.....	227
V.	EFFECT OF HYDROGEN ON MECHANICAL PROPERTIES OF FE-TI ALLOYS (DYNAMIC HYDROGEN EMBRITTLEMENT).....	231
	A. Summary of Past Studies on the Effect of Hydrogen on Mechanical Properties of Iron Alloys	231
	B. Experimental Procedure.....	237
	C. Experimental Results.....	239
	C.1. Preliminary Remarks.....	239
	C.2. The Stress-Strain Curves.....	240
	C.3. Hydrogen Embrittlement of Fe-Ti Alloys as Measured by the Loss in Reduction in Area..	241
	C.4. Effect of Strain Rate and Temperature on the RA Loss of Fe-Ti Alloys Due to Hydrogen Embrittlement.....	244
	C.5. Fractography of Hydrogen-Charged Fe-Ti Alloys.....	246
	D. A Qualitative Model of Hydrogen Embrittlement...	256
	D.1. Development of the Model.....	256
	D.2. Application of the Model to Experimental Results.....	259
	E. Criterion for the Design of an Alloy Resisting Dynamic Hydrogen Embrittlement.....	261
	F. Conclusions.....	262
VI.	CONCLUSIONS - SUMMARY.....	263
	SUGGESTIONS FOR FUTURE WORK.....	270
	APPENDIX A - Identification of Titanium Carbide Particles.....	A-1
	APPENDIX B - Computation of Particle Density.....	B-1
	APPENDIX C - Free Energies for Hydride Formation....	C-1
	APPENDIX D - The Electrical Analogy.....	D-1
	APPENDIX E - Computer Programs for the Hydrogen-Induced Cracking Model.....	E-1
	APPENDIX F - Twin Identification.....	F-1
	REFERENCES	



#### ACKNOWLEDGEMENTS

Completion of this thesis would not have been possible without the help and encouragement of numerous people. I would firstly like to thank my Thesis Advisor, Professor I. M. Bernstein, who first stimulated my interest on the consequences of trapping on hydrogen embrittlement, and whose previous work on this subject formed the basis of this work; I am particularly grateful for the encouragement, patience and serious considerations he always gave to the theoretical considerations developed in this research.

Various people in the Metallurgy and Materials Science Department have made valuable contributions to this thesis. I would like to thank Professor C.H.P. Lupis for useful discussions on the thermodynamics contained in this work, Professors J. C. Williams and D. E. Laughlin for great help in the interpretation of electron microscopy pictures, and Professor R. F. Sekerka for some help in the mathematics of the electrical analogy. Mr. R. Garber and other fellow graduate students have contributed lively discussions and lent technical assistance throughout the course of this research. The technical and secretarial staff of the department also deserve considerable credit; particularly Mrs. J. Gibson, who singlehandedly typed the bulk of the thesis, with the aid of Mrs. A. Crelli, and Mr. N. T. Nuhfer for valuable technical assistance.

A great deal of the machining was done by Mr. Ed Fraticelli,

while Mr. R. Miller deserves some special thanks for his patient drafting of the Figures in this thesis.

Professor H. W. Pickering, of Penn State University, is gratefully acknowledged for useful criticism of the diffusion part of the thesis.

Finally, in addition to my thesis advisor, I would like to express my appreciation to my thesis committee, consisting of Professors. W. W. Mullins, A. W. Thompson, J. C. Williams, of Carnegie-Mellon University, and Dr. B. G. Ateya, of Penn State University.



# LIST OF TABLES

<u>TABLE NO.</u>	<u>TITLE</u>	<u>PAGE NO.</u>
I	Chemical Composition of the Alloys Used in this Study	15
II	Oxidation Potentials	44
III	Values of the First Order Interaction Coefficient $e_H^I$ in Liquid Iron	65
IV	Values of the First Order Interaction Coefficient $e_{Ti}^I$ in Liquid Iron	66
V	Variation of $e_{Ti}^N$ with Temperature	66
VI	Values of $\Delta G$ for Hydride Formation	66-67
VII	Value of the Ratio $D$ (with solute)/ $D_0$ for Various Wt% Additions of Solute	87
VIII	Experimental Values and Relationships between Trapping Parameters	101
IX	Calculated Values of the Trapping Parameters for Alloy B	104
X	Calculated Values of the Trapping Parameters for Alloy $D_2$	105
XI	Functional Dependence of Steady State Flux on Input Current Density for Metals of Interest	119
XII	Value of the Ratio of Experimental $J_\infty$ to the Ideal $J_\infty$	126
XIII	Ratio of the Area Where Trapping Occurs to the Area Available for Diffusion	127
XIV	Surface Occupancy of Titanium Traps	128
XV	Values of the Parameters Characterizing Irreversible Trapping	141
XVI	Ratios of the First Polarization Diffusivities for Each Non-Carburized Alloy and its Carburized Counterpart	145

### LIST OF TABLES (Con't)

TABLE NO.	TITLE	PAGE NO.
XVII	Classification of the Traps Present in Fe-Ti and Fe-Ti-C Alloys	153
XVIII	Set of Criteria for a Static Hydrogen Embrittlement Resisting Alloy	229
XIX	Set of Criteria for a Dynamic Hydrogen Embrittlement Resisting Alloy	261



# LIST OF FIGURES

<u>FIGURE</u>	<u>TITLE</u>	<u>PAGE NO.</u>
1	The Fe-Ti Diagram	12
2	Portions of the Fe-Ti-C Diagram	13
3	Optical, Transmission and Scanning Electron Micrographs of All Alloys	19-22
4	Densities of Titanium Carbides	23
5	Ultimate Tensile Strength of Each Alloy	29
6	Fractograph of Alloy B Pulled in Tension, Free of Hydrogen	30
7	Fractographs of Various Hydrogen-Free Alloys, Pulled in Tension in Liquid Nitrogen	30-31
8	Diffusivity of Hydrogen in Ferrite at Various Temperatures	34
9	Variation of Hydrogen Diffusivity with Void Density	37
10	Transmission Electron Micrograph of Tritium Trapped at Dislocations	37
11	Transmission Electron Micrograph of Tritium Trapped at Grain Boundaries	39
12	Transmission Electron Micrograph of Tritium Trapped at Titanium Carbide Particles	39
13	Experimental Set-Up for Permeation	42
14	Variation of $J_{\infty}$ with Output Side Potential	51
15	Normalized Output Flux of Hydrogen for First Polarization Permeation Transients	55
16	Normalized Output Flux of Hydrogen for First Polarization Decay Transients	56
17	Normalized Output Flux of Hydrogen for Second Polarization Permeation Transients	57

# LIST OF FIGURES (Con't)

<u>FIGURE</u>	<u>TITLE</u>	<u>PAGE NO.</u>
18	Normalized Output Flux of Hydrogen for Second Polarization Decay Transients	58
19	Evidence for Irreversible and Reversible Trapping	59
20	Normal Diffusion Transients	73
21	Diffusion with Trapping, According to the McNabb-Foster Theory and Caskey-Pillinger Study	77
22	Diffusivity of Hydrogen through Ferrite Versus Titanium Content, Order of Polarization and Method Employed	86
23	Diffusivity of Hydrogen through Ferrite for Various Solute Additions	88
24	Experimental Verification of a Linear Relationship between $D_0/D$ and Density of Titanium Atoms	93
25	Variation of the Steady State Concentration of Hydrogen $C_0$ with Titanium Content	93
26	Occupancy, $n$ , of Titanium Traps Versus Steady State Concentration $C_0$	97
27	Fit of Second Polarization Permeation Transients of Alloy B with McNabb-Foster Theory	103
28	Fit of Second Polarization Permeation Transients with Electrical Analogy	103
29	Oriani's Model of a Trapping Site	111
30	Variation of Steady State Flux with Square Root of Current Density	121
31	Evolution of Permeation Transients of Ferrovac E and Alloy B with Increasing Current Density	121
32	Experimental Modelling of Surface Trapping	125
33	Theoretical Modelling of Surface Trapping	125



# LIST OF FIGURES (Con't)

<u>FIGURE</u>	<u>TITLE</u>	<u>PAGE NO.</u>
34	Variation of Steady State Flux with Membrane Thickness (Ferrovac E)	131
35	Variation of Steady State Flux with Membrane Thickness (Alloy B)	131
36	Variation of Steady State Flux with Membrane Thickness and Current Density	132
37	Variation of Trapping Rate Parameters for Irreversible and Reversible Trapping ( $\bar{k}/\bar{p}$ ) with Trapping Densities ( $F_i/F_r$ )	142
38	Diffusivity of Hydrogen through Carburized Alloys, and for Several Polarizations	144
39	Extent and Kinetics of Grain Boundary Cracking for Ferrovac E and Alloy B	158
40	Evolution of the Total Hydrogen Population, and of Hydrogen Populations on Grain Boundaries and TiC Particles with Time	176
41	Relationship between Grain Boundary Hydrogen Population and Grain Boundary Cracking	178
42	Influence of $N\theta$ on Grain Boundary Cracking	180
43	Influence of $K_1$ on Grain Boundary Cracking	182
44	Influence of $a$ on Grain Boundary Cracking	183
45	Scanning Electron Micrograph of Hydrogen Induced Crack	190
46	Optical Micrograph of Hydrogen Induced Cracks	190
47	Grain Boundary Cracking Versus Charging Time and Titanium Content	193
48	Grain Goundary Cracking for Alloys C and CC	195
49	Kinetics of Grain Boundary Cracking Versus Current Density	197

# LIST OF FIGURES (Con't)

<u>FIGURE</u>	<u>TITLE</u>	<u>PAGE NO.</u>
50	Maximum Amount of Grain Boundary Cracking Versus Current Density	199
51	Solubility of Hydrogen in Ferrovac E and Alloy B Versus Current Density	203
52	Permeation Experiment at High Current Density	209
53	Dislocation Formation in Hydrogen Charged Alloy CC	217
54	Twin Formation in Hydrogen Charged Alloy CC	219
55	Possible Crack Nucleation Sites in Hydrogen Charged Alloy CC	224
56	Tensile Test of Tritium Charged Steel and Resulting Tritium Release	233
57	RA Loss Versus Current Density for All Alloys	242
58	Effect of Strain Rate on RA Loss	245
59	Effect of Temperature on RA Loss	245
60	Scanning Electron Fractographs of All Hydrogen Charged Alloys	247
61	Summary of the Research Organization	264



CARNEGIE-MELLON UNIVERSITY

The Role of Trapping on Hydrogen Transport  
and Embrittlement

Abstract

The achieved goal of the present research was to propose sets of criteria that would help in the design of alloys more resistant to hydrogen embrittlement.

The thesis research is based upon the original idea that a fine and homogeneous distribution of particular kinds of traps could achieve the above goal. This starting idea was developed from an investigation of existing hydrogen embrittlement theories, which showed that a common factor of all theories was the presence in the matrix of large deleterious accumulations of hydrogen at specific sites.

Fe-Ti alloys in both the carburized and uncarburized condition were chosen as the model material to simulate internal trapping of hydrogen.

Microstructure characterization revealed that all alloys consisted of a ferrite matrix in which free substitutional titanium atoms and titanium carbide particles were present. Techniques were developed to distinguish between reversible traps (titanium atoms, dislocations, grain boundaries, coherent particles) and irreversible traps (such as titanium carbide particles). This characterization separation was achieved both experimentally (using an electrochemical permeation cell) and theoretically (by proposing two new models of reversible and irreversible trapping, and by comparison with existing theories).

A classification of the traps in terms of strength, density, occupancy and reversible character, was then obtained.

Based upon the results of trap characterization, hydrogen embrittlement of Fe-Ti alloys was then examined. A distinction was made between a static form of hydrogen embrittlement (hydrogen-induced cracking in the absence of an external stress), where hydrogen is available by lattice diffusion, and a dynamic form of embrittlement, where hydrogen diffuses as dislocation atmospheres during a tensile test.

The kinetics and extent of static hydrogen embrittlement was both theoretically modelled and experimentally investigated. Both reversible and irreversible traps delay the kinetics of cracking, but in different ways. For example, irreversible traps can create a plateau behavior in the time dependence of cracking, while reversible traps cannot. On the other hand, only reversible traps seem to influence the maximum extent of damage; increasing the titanium content decreased the extent of damage.

Because hydrogen's availability is different during dynamic hydrogen embrittlement (as in a tensile test), results differed for tensile tested hydrogen charged Fe-Ti alloys. In particular, the best alloys were those with a fine distribution of irreversible TiC particles. A qualitative model was proposed to explain the reasons for this.

Lastly, sets of criteria were proposed for the design of alloys that would resist both static and dynamic hydrogen embrittlement.



## INTRODUCTION

It is common practice to begin a research project reviewing existing literature. Trying to do so when the researcher's subject is hydrogen embrittlement will lead to unexpected surprises; the amount of articles or books written on this subject is enormous, numbering well into the thousands. The confused researcher may then want to adopt the tactics of reading in depth only the recent literature, leaving the older studies aside as only historically interesting. Neglecting the scientific impact of the first contributions to the phenomena of hydrogen embrittlement would, however, be a regrettable mistake. A good example often cited in literature reviews, is one of the earliest publications on the subject, by a W. H. Johnson<sup>(1)</sup> of Manchester, England, in 1875, more than a century ago! In his thorough analysis, W. H. Johnson enunciated all the basic effects of hydrogen on the mechanical properties of iron: for example, he described the reversibility or irreversibility of the damage, the concept of brittle delayed failure, the influence of strength level, or of prior deformation, etc.... One would then think that, with the great number of additional observations performed since 1875, a better understanding and a clearer picture of the phenomena would have emerged. Such is not the case. The multiplicity and sometimes, contradictory nature of the results as well as the variety of proposed theories may well have clouded the issue more than ever. In fact, one can think of hydrogen embrittlement as a "cancer of metals," elusive in its origin, diversified in its manifestations, universal in its attack, and

as difficult to cure as the disease. For example, hydrogen will destroy or degrade the properties of an impressive range of materials, from high strength steels to the softest iron; even materials that were once thought to be immune, such as austenitic stainless steels or aluminum alloys, now seen to be susceptible to its deleterious effects (see, for example, the review paper by Bernstein and Thompson<sup>(2)</sup> for general reference). Furthermore, hydrogen may be introduced in a metal at any time during its preparation (casting, welding, surface treatment, heat treating, etc...), or when used in particular and often critical applications (pipelines, containers, gas wells, nuclear reactors, ships, etc...). Failures once classified as stress corrosion cracking now seem to be just another example of hydrogen embrittlement.<sup>(2)</sup>

What then is the reason for such a diversified role of hydrogen on the physical and mechanical properties of metals? And, since it is not always possible to prevent the introduction of hydrogen, is it possible to design an alloy in such a way that hydrogen's harmful effects can be reduced, or eliminated? These are the questions that the present study will address. Since the potential choice of materials and experimental techniques is quite large, a judicious selection for the present investigation had to be made at the start. The following sections are presented to justify our final choice, without intending to give a detailed review of the literature; this will be done at the start of the individual chapters.

#### The State of Hydrogen in Metals:

Hydrogen is unique for its very particular position as the first element in the periodic table. This privileged position brings two immediate consequences:



- a) the electronic structure (1 s electron) of hydrogen makes it a very chemically active element; for example, hydrogen can as easily combine with elements located on the left of the periodic table (e.g., forming hydrides such as LiH) as with elements located on the right of the periodic table (e.g., HF, HCl, H<sub>2</sub>O ).
- b) the atomic size of hydrogen is very small, thereby allowing relatively fast motion in a crystalline material, and thus making its availability for any physical or chemical reaction large.

There can thus exist three basic and different states of hydrogen in a metal: atomic, molecular and combined with other elements.

In its atomic state, and because of its electronic structure, hydrogen may either: (1) keep its electron, (2) gain another electron to become an anion H<sup>-</sup>, or (3) lose it to the conduction band of the metal. The first possibility has, to the best of my knowledge, never been reported; the second possibility applies to hydrogen when it is present in alkali metals and alkaline earth metals; the third possibility is by far the most commonly found,<sup>(3)</sup> as in transition metals for example. In this last case, the fact that hydrogen is ionized induces a strong perturbation<sup>(4)</sup> of the electrons in the conduction band of the metal, in order to compensate for the introduced positive charge (one speaks of a screened proton in that case). The most important effect, what atomic hydrogen does to the binding energy between neighboring metal atoms, is not known.

Molecular hydrogen can form at internal sites, for example as hydrogen

gas in cracks or voids.

As for hydrogen in the combined state, this can be as a hydride, combined with such elements as carbon or oxygen.

All three states may be present at the same time in the same material, each one giving rise to a particular set of properties. Although no particular state may be qualified as most dangerous (in terms of degradation of properties), hydrogen in its atomic state is probably the most important, first, because the atomic form is a precursor state before forming a gas or combining to another element, and second, hydrogen is most mobile when it exists as a proton. The location of atomic hydrogen in the lattice is varied and one must make a distinction between diffusing and trapped hydrogen. Diffusing hydrogen is thought to occupy octahedral sites<sup>(5)</sup> in such metals as  $\alpha$ -Fe, although some possibility remains that it could also reside in tetrahedral sites.<sup>(6)</sup> The concept that hydrogen may be trapped at some particular sites in the lattice was suggested some time ago by Darken and Smith,<sup>(7)</sup> and has been developed since, as we shall subsequently see. Such trapped hydrogen will not be as mobile as diffusing hydrogen, depending on the strength of the trap (i.e., its reversible character). Generally, hydrogen will be trapped by crystal defects where it is energetically favorable for the interaction to occur; various traps have been identified and their interaction energy with hydrogen measured, such as dislocations, interfaces, stacking faults, grain boundaries, and voids.

#### Proposed theories for hydrogen embrittlement

The term "hydrogen embrittlement" has been used in many ways, and too often in a rather vague and undefined manner. It will be



distinguished in this study by describing two forms of hydrogen embrittlement: a static form and a dynamic form. By "static" is meant the hydrogen-induced cracking of a metal in the absence of an external stress. This effect of hydrogen manifests itself by the formation of blisters on the surface of a material, and cracks in the interior of the materials. On the other hand, the "dynamic" form of hydrogen embrittlement will designate all degradation of mechanical properties when a material containing hydrogen is subjected to an external stress; for example, the degree of embrittlement may be measured by the loss of ductility during a tensile test, as evidenced by a decreased reduction in area. The origin for the distinction between the static and the dynamic form will be fully considered later on.

Several theories have been proposed to explain one or both forms of hydrogen embrittlement, as will now be briefly described:

- a) The Pressure Theory: Originated by Zapffe and Sims,<sup>(8)</sup> this theory proposes that the formation of high gas pressures in internal cavities is responsible for the embrittling effect of hydrogen.<sup>(9,10,11)</sup> While it is probably the reason why cracks expand in the static form of hydrogen embrittlement, it cannot adequately explain why these cracks nucleated in the first place. Furthermore, it is inconsistent with the observations that hydrogen embrittlement may exist even when the internal hydrogen concentration is too low for the formation of high pressure gas.<sup>(12)</sup> In fact, the formation of molecular hydrogen is probably a later step in the already advanced

degradation of properties, such as the formation of cracks and other internal cavities. Because atomic hydrogen exists before molecular hydrogen is able to form in the material, the primary origin of the problem must relate to what atomic hydrogen does first in and to the lattice. This aspect is the concern of the other proposed theories.

- b) The Reduction of Cohesive Energy: In this model, originally proposed by Troiano<sup>(13)</sup> and recently elaborated by Oriani,<sup>(14)</sup> hydrogen is believed to collect in the lattice at points of maximum triaxial stress near the crack tip, where it is then assumed to reduce the binding energy. The energy to propagate this crack would then be lowered. The fact that large concentrations of hydrogen may exist near the crack tip has now been well documented experimentally<sup>(15)</sup> and theoretically.<sup>(16)</sup> However, the hypothesis that the cohesive energy will be reduced remains without strong theoretical basis (see for example, Ref. 13), as so little is still known about binding energies in crystals. Nevertheless, this model is attractive as the most general explanation for the origin of most hydrogen embrittlement cases.
- c) The Reduction of Surface Free Energy: This model has been widely used and applied to many cases.<sup>(17,18,19)</sup> It is however only a particular case of the cohesive energy model. The difference between the two models resides in the location of hydrogen positioned in the matrix near the crack tip, while the surface energy model concerns hydrogen atoms adsorbed on the internal surface of the crack, near the tip.



d). The Reduction in Mobility of Dislocations: Proposed by

Oriani<sup>(20)</sup> the effect of hydrogen would be to restrict cross-slip, thereby allowing the development of large local strain concentrations which would, in turn, lead to crack nucleation and growth. This explanation would be hard to apply to the case of static hydrogen embrittlement; nevertheless, the fact that hydrogen will be dragged along with dislocations has recently received experimental<sup>(21)</sup> and theoretical confirmation,<sup>(22)</sup> so a direct effect on dislocation dynamics is possible.

Various other theories have also been proposed, sometimes contradictory to the major theories that were presented above (e.g., Beachem<sup>(23)</sup>). However, factors common to most of the theories can be identified and used to develop direction for the present research.

Conclusions: Direction of the Research.

As was mentioned earlier, the ultimate aim of the present study is to propose criteria for the design of hydrogen-resisting alloys. After having read the previous sections on "Proposed Theories for Hydrogen Embrittlement," it is clear that most existing models do not offer a universal explanation for all hydrogen embrittlement cases. Rather, each model seems to apply to some particular case, corresponding to the particular state of hydrogen in the lattice. However, it is possible to find a common denominator to all these theories:

in order to obtain hydrogen embrittlement, it is necessary to have at a particular site in the lattice a large accumulation of hydrogen.

Such a particular site can be an internal cavity in the pressure theory,

a crack tip in the cohesive energy theory, an interface or the internal surface at a crack tip for the surface energy theory, dislocations for the reduced mobility of dislocations theory, and so on.

Agreeing to this generality, it is now possible to propose a starting criterion for the control of hydrogen embrittlement:

in order to design a hydrogen-resisting alloy, it will be necessary to prevent the formation of large accumulations of hydrogen anywhere in the material. The present thesis will investigate the possibility that this can be achieved by controlling the microstructure such that hydrogen will be uniformly distributed throughout the lattice.

The question now arises as to what kind of microstructure will provide such homogeneous distribution of hydrogen in the lattice. The answer lies in the trapping effect; if a microstructure presents a uniform distribution of small, strong, hydrogen traps, then accordingly, the distribution of hydrogen will be uniform and fine. There only remains the selection of such a good trap, keeping in mind that it must satisfy three conditions:

- a) the trap must be strong
- b) the trap must be small in size
- c) it must be possible to finely distribute this trap in the lattice

Since a trap is usually a lattice defect, the smallest type of defect is a foreign solute atom. In order to satisfy conditions a) and c), this solute atom must have a strong attraction for hydrogen and exist in solid solution in the material.



In the choice of this solute, we have been helped by the previous work of Bernstein and Rath<sup>(24)</sup> on Fe-Ti alloys. These authors have shown that Fe-Ti alloys were less susceptible to cracking than pure iron when charged with hydrogen. Since titanium as a solute atom appears capable of strongly interacting with hydrogen (titanium hydride is very stable), is small in size, and may exist in solid solution in  $\alpha$ -iron up to 3wt% (see Figure 1, Chapter I), it appears to satisfy the three conditions for a "good" trap that were laid down. Thus, this material, i.e., Fe-Ti binary alloys will be adopted for this study. The Fe-Ti binary also has the additional interesting property that, upon addition of carbon, titanium carbide particles will form (see Chapter I, Figure 2). Since recent works have shown that these particles are strong hydrogen traps,<sup>(25)</sup> and that they may be finely distributed in the iron matrix,<sup>(26)</sup> the addition of carbon to the binary Fe-Ti will provide us with yet another trap that obeys the three conditions for good trapping. Finally, another justification for the choice of Fe-Ti alloys as the material of study is that, due to its simple microstructure, it will be easier to distinguish the importance of each individual parameter, and thus, easier to model and understand the effects of hydrogen.

The first half of the thesis will be devoted to proving that titanium solute atoms and titanium carbide particles do indeed satisfy the three conditions for a "good" hydrogen trap. This will be accomplished in Chapter I by characterizing the microstructure of all alloys (i.e., verification of conditions b) and c)), and in Chapter II by characterizing the trapping efficiency of the assumed traps (i.e., verification of condition a)).

Finally, the results gained in the first half of the thesis will be applied to the problems of static hydrogen embrittlement (Chapter III on hydrogen-induced cracking) and dynamic hydrogen embrittlement (Chapter IV).



## CHAPTER I

MICROSTRUCTURAL AND MECHANICAL CHARACTERISTICS OF THE  
ALLOYS, IN THE ABSENCE OF HYDROGENA. The Phase Diagrams of the Fe-Ti and Fe-Ti-C Systems.-

For reasons developed in the Introduction, the base material of this study will consist of pure  $\alpha$ -iron (ferrite) to which specific quantities of titanium and carbon will be added. Both of these additions will be kept small in order to obtain a simple alloy microstructure. The phase diagrams for both the Fe-Ti and Fe-Ti-C systems are well known, since the use of titanium in steel as an interstitial getter is now common practice.<sup>(27)</sup> The Fe-Ti diagram<sup>(28)</sup> is shown in Figure 1, while relevant portions of the ternary Fe-Ti-C<sup>(29)</sup> are shown in Figure 2.

Considering first the binary, Figure 1 shows that titanium will exist in solid solution as a substitutional element in ferrite up to  $\sim 3$  wt%. Moreover, no significant ordering has been observed,<sup>(30)</sup> at least in the composition ranges of interest in this investigation. We can thus expect generally a homogeneous distribution of titanium atoms on substitutional sites in the ferrite matrix. Upon adding carbon to the Fe-Ti binary, titanium carbide (TiC) will form preferentially to cementite ( $\text{Fe}_3\text{C}$ ), until the dissolved titanium is exhausted.<sup>(29)</sup> This results from the strong affinity of titanium for carbon (see Chapter II and Appendix C). In our alloys, the concentration of carbon will be chosen such that the formation of  $\text{Fe}_3\text{C}$  will not take place. Instead, a two-

BEST AVAILABLE COPY

Fe-Ti Iron-Titanium

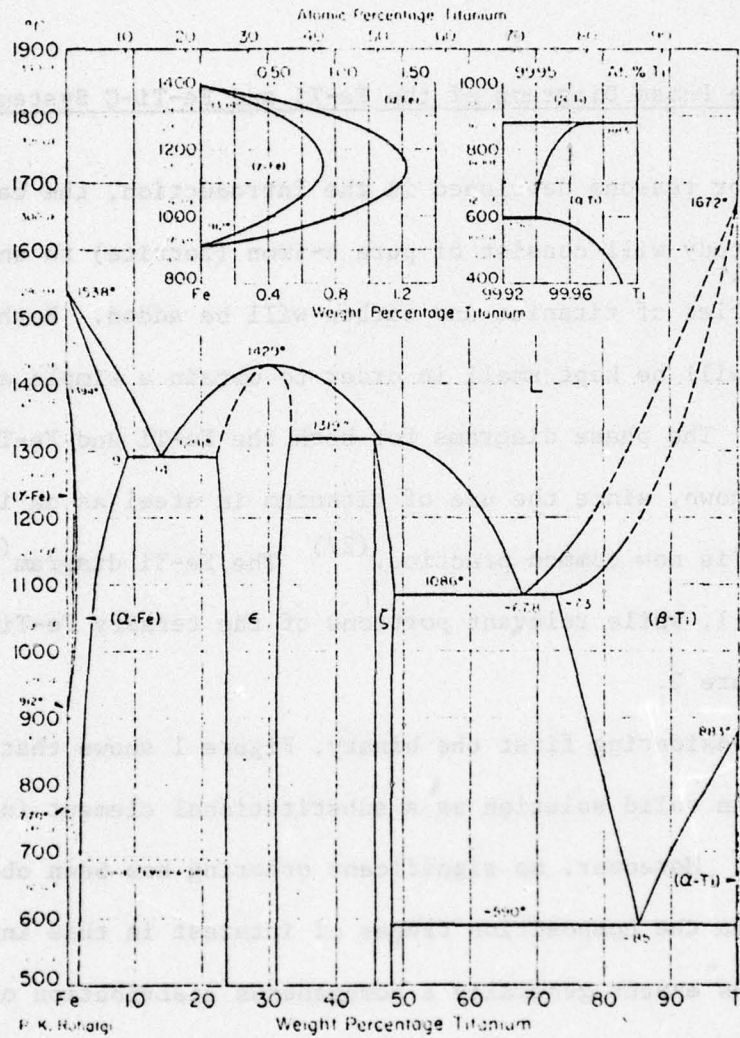
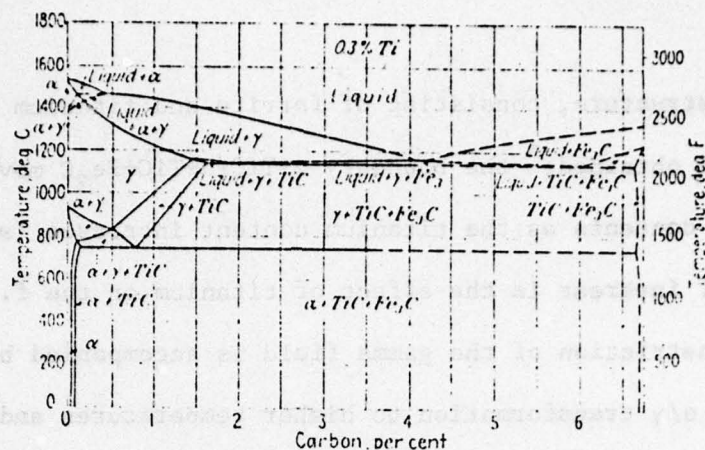
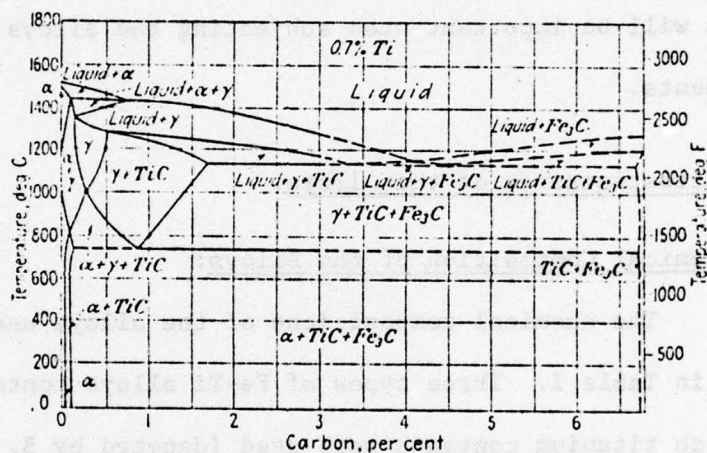


FIGURE 1. The Iron-Titanium Phase Diagram. (28)

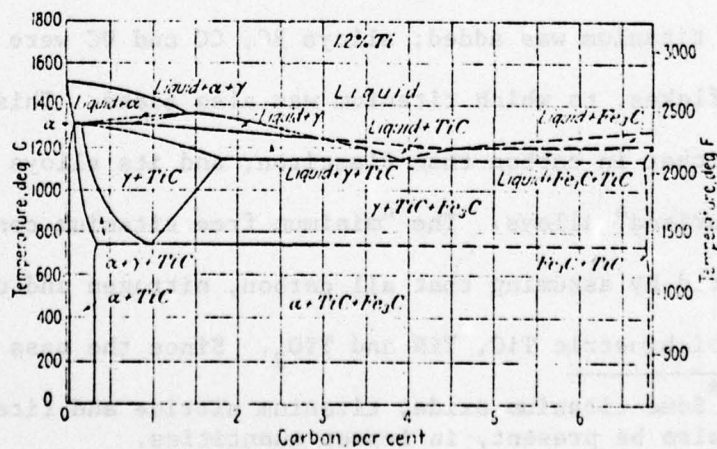




(a)



(b)



(c)

FIGURE 2.  
Portions of the Iron-Titanium-Carbon Ternary<sup>(29)</sup> at Various Titanium Concentrations: a) 0.3%Ti, b) 0.7%Ti, c) 1.2%Ti.

BEST AVAILABLE COPY

phase structure, consisting of ferrite and titanium carbide particles will be obtained;\* the boundary  $\alpha\text{-TiC}/\alpha\text{-TiC}+\text{Fe}_3\text{C}$  moves toward higher carbon contents as the titanium content increases (see Figure 2).

Also of interest is the effect of titanium on the f.c.c. gamma field. The constriction of the gamma field is accompanied by a displacement of the  $\alpha/\gamma$  transformation to higher temperatures and carbon contents. At 1.2%Ti, for example, and for low carbon contents, the alloys may consist of  $\alpha\text{-TiC}$  at all temperatures up to the melting point. These points will be important when subjecting the alloys to various heat treatments.

#### B. Microstructures of the Alloys.

##### Chemical Composition of the Alloys:

The chemical compositions of the alloys used in this study are given in Table I. Three types of Fe-Ti alloys containing low, medium, and high titanium contents were used (denoted by B, C and D respectively), each one with a "carburized" counterpart (i.e., BC, CC and DC). Alloys B, C and D were prepared at U. S. Steel from vacuum-melted Plastiron<sup>+</sup> to which titanium was added; alloys BC, CC and DC were made of Glidden<sup>#</sup> iron flakes, to which titanium was also added. This latter base iron was richer in carbon than Plastiron, and its alloys are denoted as "carburized" alloys. The "minimum free titanium content" (MFTC) was computed by assuming that all carbon, nitrogen and oxygen was tied up as stoichiometric TiC, TiN and TiO<sub>2</sub>. Since the mass ratios of titanium

\* Some titanium oxide, titanium nitride and titanium carbo-nitride will also be present, in lesser quantities.

<sup>+/#</sup> Proprietary brands of commercial purity iron.



TABLE I

Chemical Composition of the Alloys Used in  
This Study; ppm are Weight ppm.

Alloy	Ti (wt%)	Minimum Free titanium (wt%)	C (ppm)	N (ppm)	O (ppm)
Ferrovac E					
A	0	-	56	10	18
B	0.15	0.12	50	22	39
BC	0.09	0	320	-	-
C	0.63	0.57	110	30	55
CC	0.50	0.24	650	-	-
D <sub>1</sub>	1.20	1.10	270	30	27
D <sub>2</sub>	1.50	1.40			
DC	1.38	1.22	390	-	-

to carbon, nitrogen and oxygen are 4, 3.4 and 3 respectively, the MFTC is:

$$\text{MFTC} = (\text{wt\%Ti}) - (4\text{wt\%C} + 3.4\text{wt\%N} + 1.5\text{wt\%O})$$

This is a minimum because the stoichiometric composition is rarely achieved in these compounds, as will be discussed.

#### Previous Studies on Similar Alloys:

The microstructural features of ternary Fe-Ti-C have been the object of much study, particularly by Honeycombe and co-workers.<sup>(31-36)</sup> Using alloys with chemical composition comparable to ours, these authors have demonstrated that:<sup>(34)</sup>

- a) a well-defined banded dispersion of titanium carbides is obtained during the early stages of transformation, particularly when the carbide nucleates at the  $\gamma/\alpha$  boundary.
- b) titanium carbide particles of size less than 6nm are approximately spheroidal in shape; larger particles can be either spheroids or thick plates.
- c) with increasing size, the particles pass through the sequence of coherent ( $\leq 3\text{nm}$ ) to semi-coherent (3-20 nm) to incoherent ( $\geq 20\text{nm}$ ).
- d) the titanium carbide particles and the matrix exhibit the Baker-Nutting relationship, i.e., for planes in the particle versus planes in the adjacent matrix:

$$(001) \text{ Ferrite } // (001) \text{ TiC}$$

$$[100] \text{ Ferrite } // [\bar{1}\bar{1}0] \text{ TiC}$$

where TiC has a face-centered cubic lattice of the NaCl type.



The composition of titanium carbide is highly variable, depending on the respective titanium and carbon contents; the composition range is given as  $x = 0.40$  to  $x = 1.02$  for  $\text{TiC}_x$ .<sup>(37)</sup> Since nitrogen may also be present and form  $\text{TiCN}$ , this can lead to relatively large variations in measured lattice parameters. For example, Reference 45 lists  $a(\text{TiC})$  as  $4.360 \text{ \AA}$ , while Reference 46 gives  $a(\text{TiC}_{x=0.28}) = 4.268 \text{ \AA}$  and  $a(\text{TiC}) = 4.321 \text{ \AA}$ . Upon adding nitrogen, the lattice parameter may be as low as  $4.236 \text{ \AA}$ .<sup>(47)</sup> Also, the lattice parameter of iron is changed by titanium; titanium increases the lattice parameter of  $\alpha$ -iron,<sup>(38)</sup> following the relationship,  $a(\text{Fe}) + 0.0031 (\text{at.\%Ti}) = a(\text{Fe-Ti})$ . Using  $1.5\text{wt\%Ti}$  and a lattice parameter for ferrite of  $2.866 \text{ \AA}$ , the lattice parameter change for Fe-1.5Ti is thus:  $a(\text{Fe-1.5wt\%Ti}) = 2.870 \text{ \AA}$ , i.e., a 0.16% increase.

#### Experimental Procedure

As-cast specimens were hot rolled at  $800^\circ\text{C}$ , followed by cold rolling to various thicknesses (depending on the type of experiment to be performed). Recrystallization was achieved by heat treating under an argon atmosphere at  $800^\circ\text{C}$ , until the desired grain size (generally  $80\mu$ ) was achieved. The microstructures were characterized by optical, scanning electron (JEOL SEM  $35\mu$ ) and transmission electron microscopy (JEM 100B microscope). Specimens for optical examination were mechanically polished and etched with 2% nital to reveal the ferrite grain boundaries.

Thin foils for transmission electron microscopy were made by first chemical polishing in a  $47\% \text{H}_2\text{O}$ - $47\% \text{H}_2\text{O}_2$ - $6\% \text{HF}$  solution to a thickness of about  $2.5 \times 10^{-3} \text{ cm}$ , followed by electropolishing at room temperature in a sodium chromate-acetic acid bath (in the ratio of one to five) at 20 volts. Because the window technique was used and the specimen had to be taken out

of the bath often, oxidation of the foil surface was a problem; this was prevented by continuous washing in acetic acid.

### Results

Typical microstructures are shown in Figure 3. As expected, all alloys exhibited ferrite and titanium carbide particles. The particles were identified as such by selected area diffraction (see Appendix A). Particles densities were computed using standard quantitative metallography techniques. Details are given in Appendix B, and the results plotted on Figure 4. It is seen that the titanium carbide particles may be separated into two classes: large particles (average size  $\geq 1\mu$ ) and small particles (size  $\leq 1\mu$ ). The large particles are present in large quantities in high titanium content alloys (e.g., alloy D and DC), in which they also exhibit their largest size ( $\sim 2\mu$ ). On the other hand, low titanium content and high carbon content alloys exhibited finer and more numerous particles, such as alloys BC and CC. The difference in density and size of titanium carbide particles between alloys BC or CC and D or DC is particularly striking. In fact, alloys BC and CC have  $10^4$  times more particles than alloys D or DC, while the particle size is decreased by more than a factor of ten.

The distribution of particles was generally homogeneous, although there were cases where stringer distributions were observed (see Figure 3). No extensive preferential grain boundary segregation seemed to occur, but some boundaries contained numerous particles due to impingement during grain growth. In some very few instances (particularly alloy C), there appeared to exist some remnants of the original fine banded structure. In most cases, however, a highly textured background (tweed-like structure) was present, as evidenced on Figures 3 and on Figures 48, 49 in Chapter III.



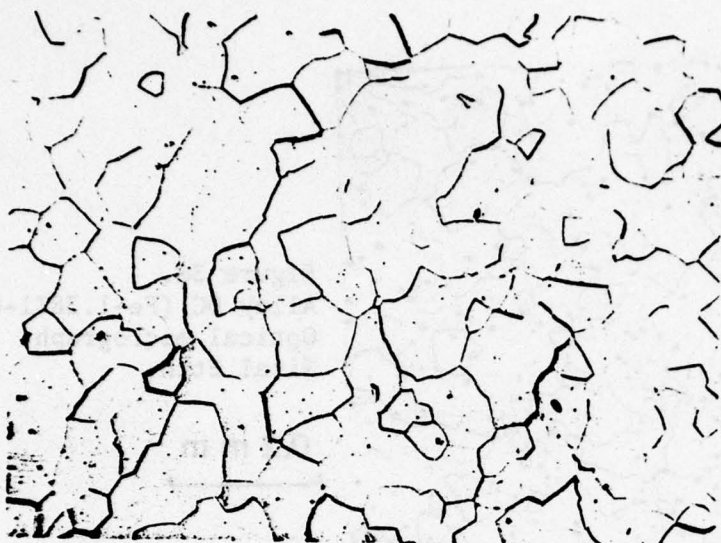


Figure 3a.  
Alloy B (Fe-0.15Ti)  
Optical micrograph.  
Nital Etch.

0.2 mm



Figure 3b.  
Alloy C (Fe-0.63Ti)  
Optical micrograph.  
Nital Etch.

0.2 mm

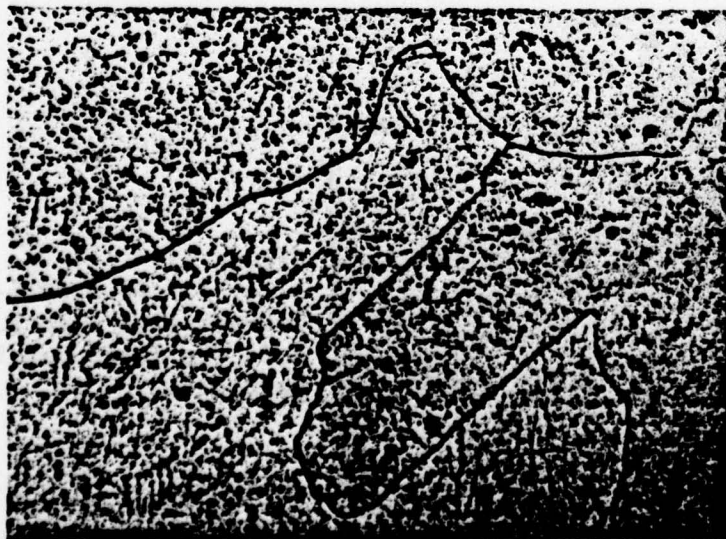


Figure 3c.  
Alloy CC (Fe-0.5Ti-0.065C)  
Optical micrograph.  
Nital Etch.

0.02 mm

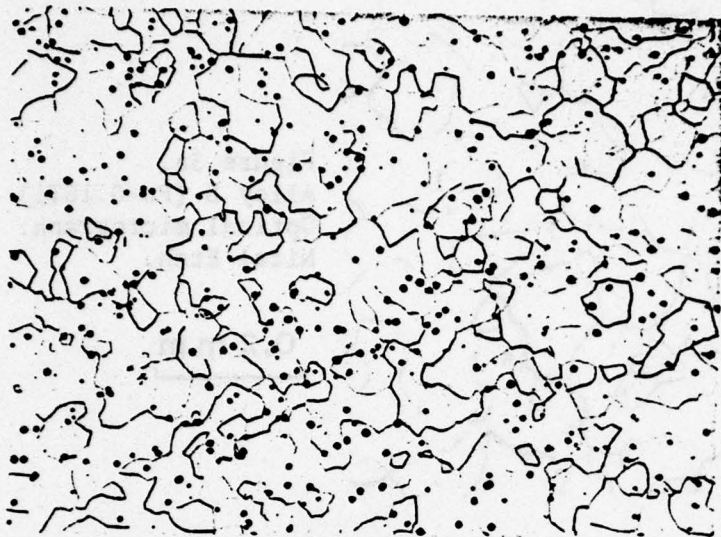


Figure 3d.  
Alloy DC (Fe-1.38Ti-0.039C)  
Optical micrograph.  
Nital Etch.

0.2 mm

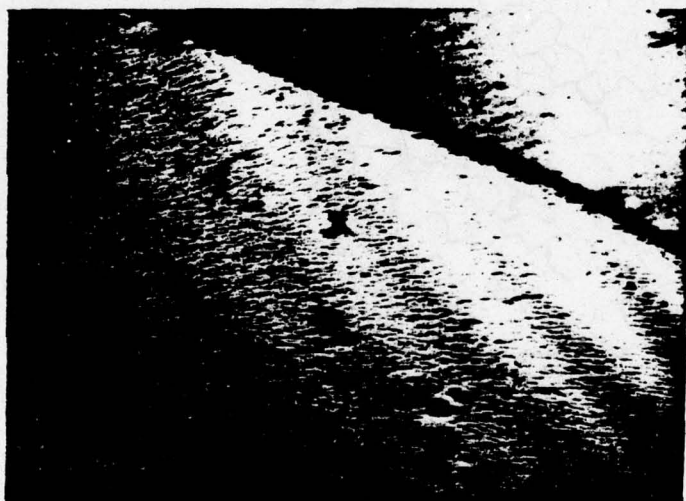


Figure 3e.  
Alloy B (Fe-0.5Ti)  
Transmission electron micrograph.

1  $\mu$

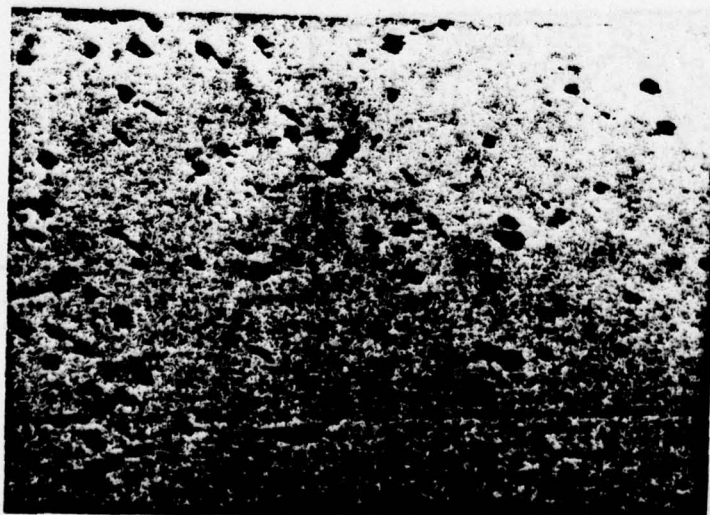


Figure 3f.  
Alloy BC (Fe-0.09Ti-0.032C).  
Transmission electron micrograph.  
Note the large density of small  
particles.

0.6  $\mu$





Figure 3g.  
Alloy C (Fe-0.63Ti)  
Transmission electron micrograph.

2  $\mu$



Figure 3h.  
Alloy CC (Fe-0.5Ti-0.065C)  
Transmission electron micrograph.  
Note the large density of particles.

1  $\mu$

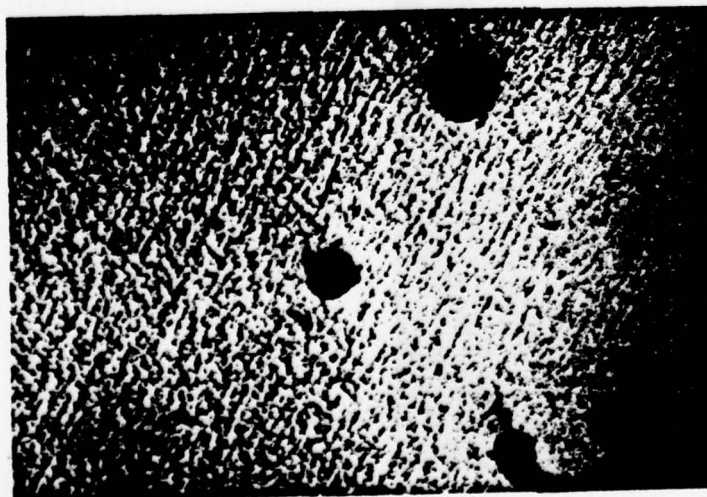


Figure 3i.  
Alloy CC (Fe-0.5Ti-0.065C)  
Transmission electron micrograph.  
One of the regions exhibiting a  
tweed like structure.

0.4  $\mu$



Figure 3j.  
Alloy CC (Fe-0.5Ti-0.065C)  
Transmission electron micrograph.

$1\ \mu$

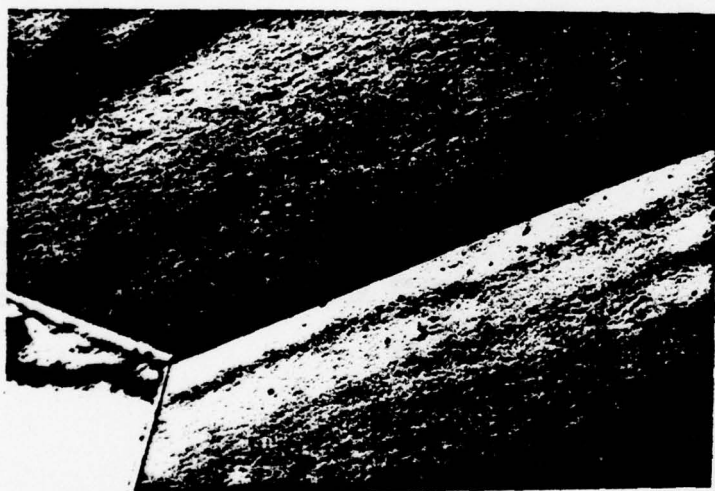


Figure 3k.  
Alloy D<sub>1</sub> (Fe-1.25Ti)  
Transmission electron micrograph.

$0.6\ \mu$

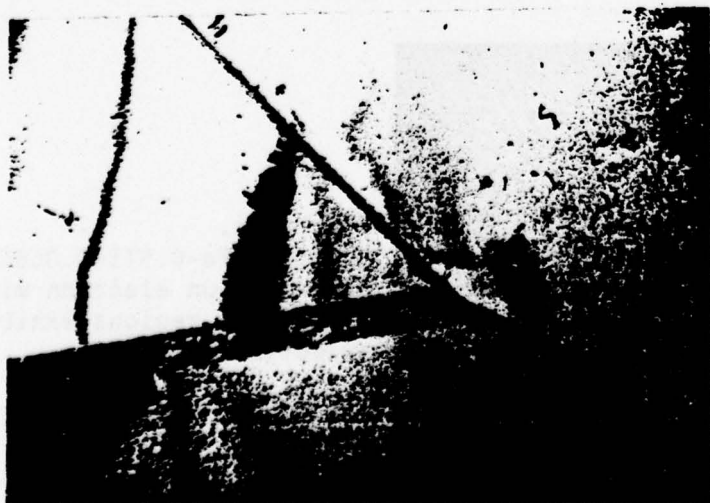


Figure 3l.  
Alloy DC (Fe-1.38Ti-0.039C)  
Transmission electron micrograph.

$1\ \mu$



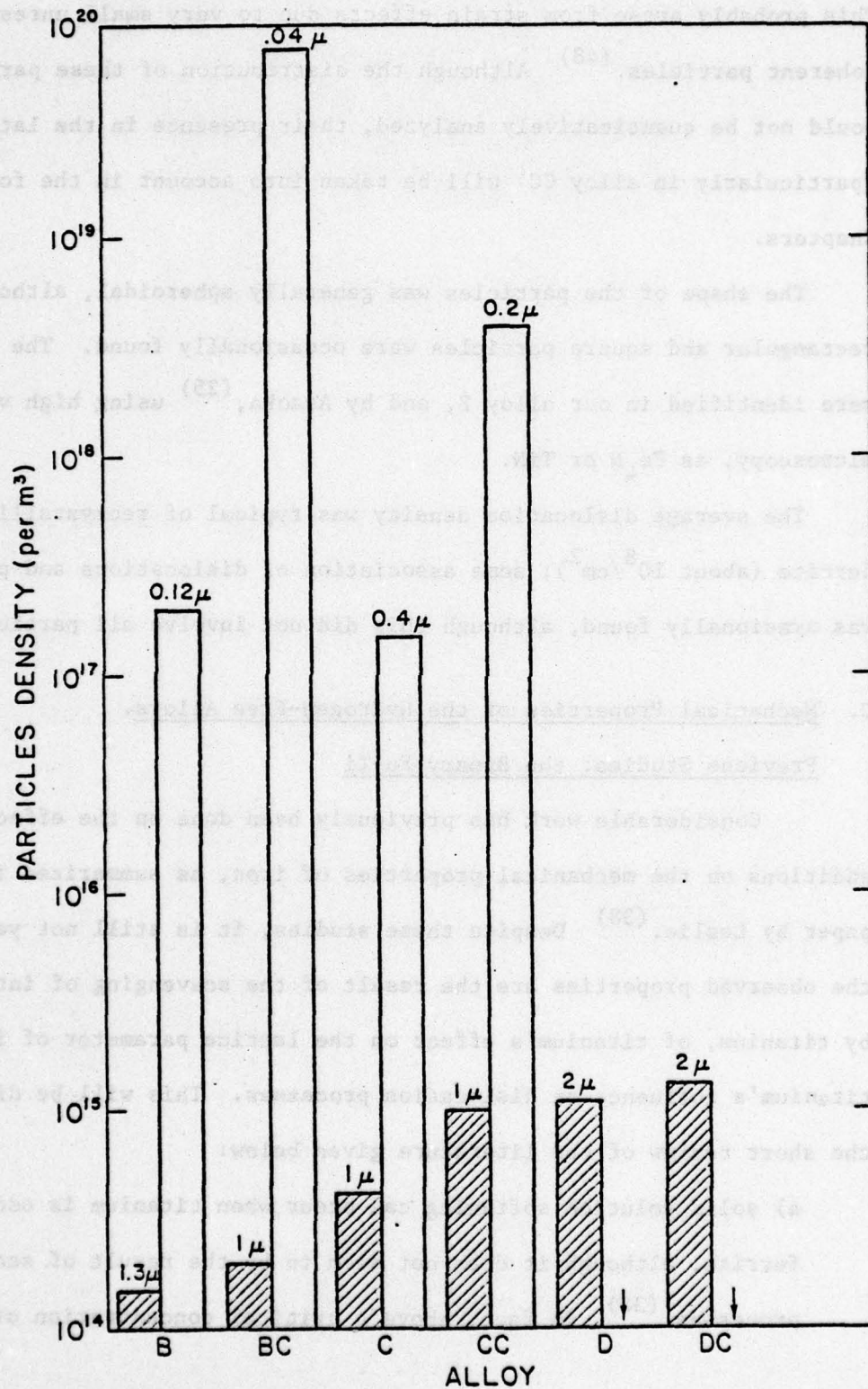


FIGURE 4.  
Density of Titanium Carbide Particles in Each Alloy. The Average Particle Size is Indicated in Microns. Light Bars are for Small Size Particles, Dark Bars for Large Size Particles.

This probably arose from strain effects due to very small unresolvable coherent particles.<sup>(48)</sup> Although the distribution of these particles could not be quantitatively analyzed, their presence in the lattice (particularly in alloy CC) will be taken into account in the following Chapters.

The shape of the particles was generally spheroidal, although some rectangular and square particles were occasionally found. The latter were identified in our alloy B, and by Asaoka,<sup>(25)</sup> using high voltage microscopy, as  $\text{Fe}_4\text{N}$  or  $\text{TiN}$ .

The average dislocation density was typical of recrystallized ferrite (about  $10^8/\text{cm}^2$ ); some association of dislocations and particles was occasionally found, although this did not involve all particles.

#### C. Mechanical Properties of the Hydrogen-Free Alloys.

##### Previous Studies: the Binary Fe-Ti

Considerable work has previously been done on the effect of titanium additions on the mechanical properties of iron, as summarized in a review paper by Leslie.<sup>(38)</sup> Despite these studies, it is still not yet clear if the observed properties are the result of the scavenging of interstitials by titanium, of titanium's effect on the lattice parameter of iron, or of titanium's influence on dislocation processes. This will be discussed in the short review of the literature given below:

- a) solid solution softening can occur when titanium is added to ferrite, although it does not seem to be the result of scavenging processes.<sup>(38)</sup> In fact, above a critical concentration of solute,



at which there is a maximum softening, solid solution strengthening occurs. (The value at which this happens is not given for titanium.<sup>(38)</sup>)

b) Static strain aging was not observed in an alloy similar to alloy B, although due to interaction with other solutes, (e.g., Si, Mn, Ni, Mo, Pt) dynamic strain aging may occur.<sup>(38)</sup>

c) Work hardening of iron is affected in a minor way by titanium.<sup>(38)</sup>

d) In additional studies of interest, including those of Rack,<sup>(39)</sup> Gupta et al,<sup>(40)</sup> McMahon,<sup>(41)</sup> and Bernstein,<sup>(24)</sup> the following observations have been made:

i) At low temperature,<sup>(39)</sup> twinning and concomitant micro-crack formation occurs. Specifically, the few particles of titanium carbides on grain boundaries can be cracked by the impingement of deformation twins, thereby serving as crack nucleation sites. Also of importance at low temperatures is the fact that increasing the amount of titanium reduces the occurrence of intergranular cracking.

ii) McMahon<sup>(41)</sup> found that titanium is initially not very effective in gettering the oxygen which is supposed to reduce grain boundary cohesion. Instead, because titanium will first combine with the carbon, the formation of C-O complexes on grain boundaries will be prevented. Therefore, oxygen will be present on the boundary as a free interstitial and it will promote intergranular cracking. One should then expect grain boundaries to be sites of potential weaknesses in low titanium content

Fe-Ti alloys. However, adding more titanium, at least above the amount of carbon (in atom percent) will increase the probability of scavenging oxygen, and thus reduce intergranular cracking.

(iii) The gettering of carbon and nitrogen by titanium causes the Petch slope to be unaffected by cooling rate from a high temperature anneal, contrary to Ferrovac E.<sup>(24)</sup> The absence of this effect shows that variations in the Petch slope are due to the concentration and distribution of interstitial solutes (C and N), and are not related to secondary effects, such as quenched-in dislocations.<sup>(24)</sup>

iv) Finally, Leslie and Sober<sup>(42)</sup> found that the ductility of an alloy similar to B was not reduced and was even improved by the presence of hard inclusions (such as TiC), provided the particles were not more than 5000Å in both diameter and spacing.

#### Previous work on the Fe-Ti-C ternary system

For the ternary Fe-Ti-C having a fine banded dispersion of TiC particles, Honeycombe and co-workers have examined its mechanical properties in some detail (see References 31 to 35). Such a dispersion can be obtained either by isothermal transformation in the temperature range 600°-850°C, or by quenching and tempering; each heat-treatment leading to different mechanical properties.<sup>(32)</sup> In particular, at the lowest isothermal transformation temperature (600°C), corresponding to the finest carbide dispersion, yield strengths of  $1.04 \times 10^5$  psi ( $7.3 \times 10^7$  kg/m<sup>2</sup>) were obtained



(compared with  $10^4 - 2 \times 10^4$  ( $7 \times 10^6 - 1.4 \times 10^7 \text{ kg/m}^2$ ) psi for a binary Fe-Ti alloy).<sup>(39)</sup> As the transformation temperature increased to  $850^\circ\text{C}$ , the dispersion of carbides increased and the yield strength fell to values as low as  $3.5 \times 10^4$  psi ( $2.4 \times 10^7 \text{ kg/m}^2$ ). At such high transformation temperatures in fact, the banded dispersion did not persist, due to rapid coarsening. On the other hand, the ductility of the steels did not vary much with transformation temperature; (no explanation was given for this insensitivity). For the same alloys,<sup>(32)</sup> the second type of heat treatment, i.e., quenching and tempering within the same temperature range, gave rise to slightly higher strength levels, but the resulting ductility was considerably lower at higher strength levels. Also, it was found that an expanded Orowan relationship<sup>(43)</sup> for the initial yield stress was applicable. In any case, the yield strength resumed its lower values when the sheet spacing was larger than  $70\mu\text{m}$  and the particle size larger than  $20\mu\text{m}$ . These results will be seen to be in agreement with ours.

Finally, it should be mentioned that some work has been done on the effect of titanium carbide and titanium carbonitride on the mechanical properties of maraging steels.<sup>(36,44)</sup> It was generally found that the formation of those particles, particularly on grain boundaries, was detrimental to such properties as toughness, ductility and fatigue strength.

#### Present Work on the Fe-Ti and Fe-Ti-C Systems:

Because of their prior thermal history and subsequent microstructures (i.e., relatively large particles, few fine banded dispersions),

all alloys exhibited an ultimate tensile strength only slightly higher than pure iron (Ferrovac E). This is shown in Figure 5, where increasing the titanium content slightly increased the tensile strength from  $3.6 \times 10^4$  psi ( $2.5 \times 10^7$  kg/m<sup>2</sup>) for pure iron to  $4.7 \times 10^4$  psi ( $3.3 \times 10^7$  kg/m<sup>2</sup>) to alloy DC. This is either the result of solid solution strengthening in the case of high titanium content alloys (if one is above the concentration for solid solution softening), or of strengthening by particles, in the case of medium titanium content alloys. All alloys exhibited large ductility in tension (93-96% R.A.), comparable to Ferrovac E. Fracture surfaces consisted of dimples, with occasional titanium carbide particles found at the bottom of the coalescing voids. An example of this type of rupture is shown in Figure 6 for alloy B.

Stress-strain curves exhibited a marked yield point for Ferrovac E which was absent during room temperature testing for all other alloys. It reappeared, however, when testing at 0°C for Fe-0.15Ti (alloy B), and became very marked at -50°C and liquid N<sub>2</sub> temperature. It never reappeared for higher titanium content alloys (C,D), even at liquid N<sub>2</sub> temperature. These results imply that scavenging of carbon and nitrogen by titanium is most effective at higher titanium content.

The fracture surfaces of specimens tested in liquid nitrogen exhibited features in agreement with previous studies (see References 39,41). As seen in Figure 7, low titanium content alloys fractured intergranularly, while increasing titanium increased the amount of cleavage. Also note the large spacing and size of carbide particles on the grain boundaries of the high titanium content alloy compared to a low or medium titanium content alloy. (Figures 7b and 7e). These observations will be reconsidered in later chapters.



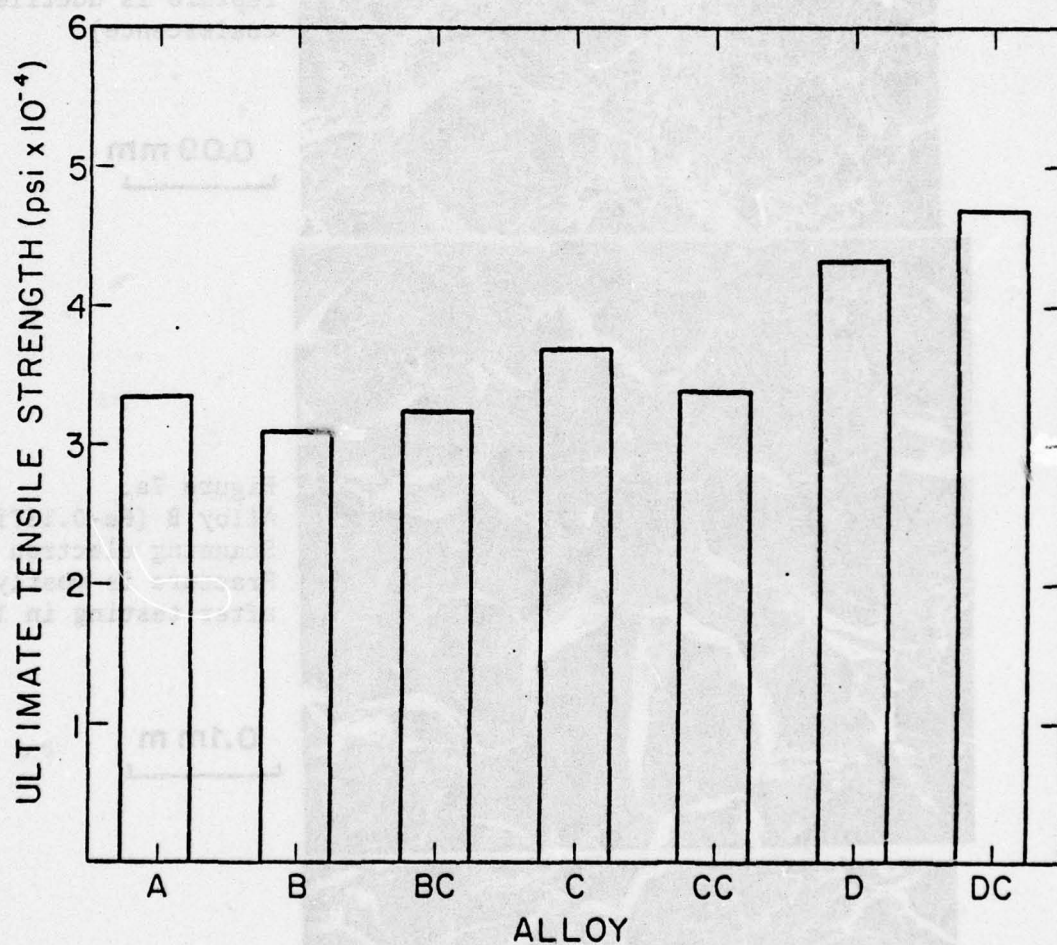


FIGURE 5.  
Ultimate Tensile Strength (psi  $\times 10^{-4}$ ) of Each Alloy.

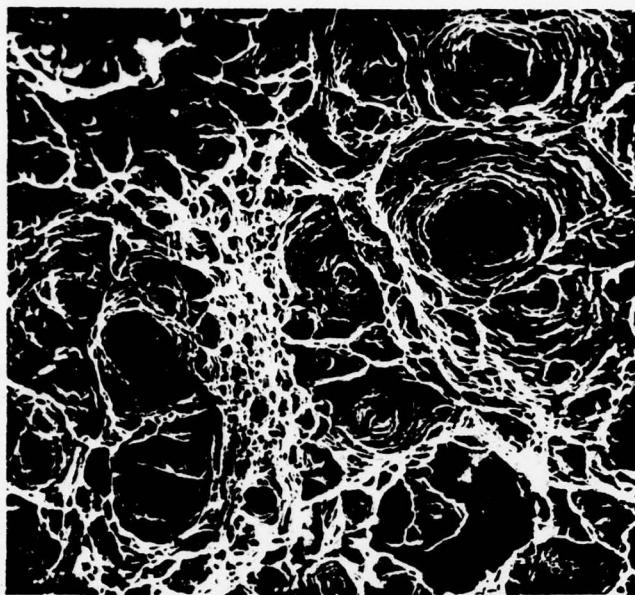


Figure 6.  
Alloy B (Fe-0.15Ti)  
Scanning electron micrograph of  
fracture surface after tensile test  
at room temperature. The specimen  
was not hydrogen charged, and the  
rupture is ductile (microvoid  
coalescence).

0.09 mm



Figure 7a.  
Alloy B (Fe-0.15Ti)  
Scanning electron micrograph.  
Fracture is mostly intergranular  
after testing in liquid nitrogen.

0.1 mm

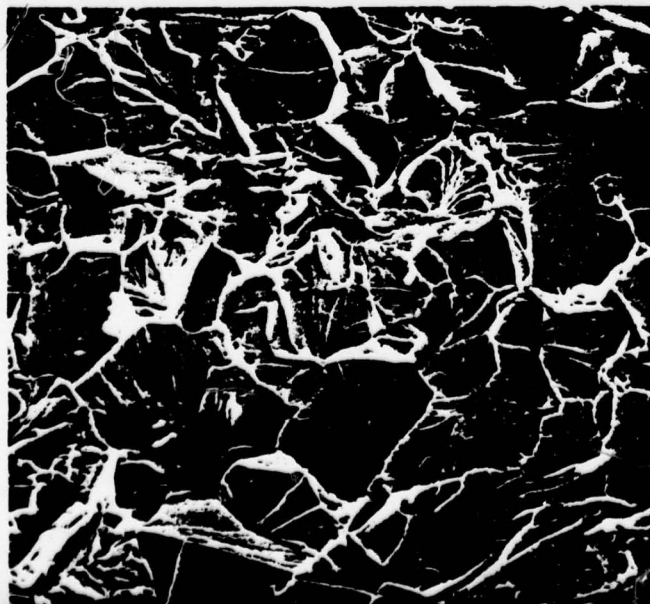
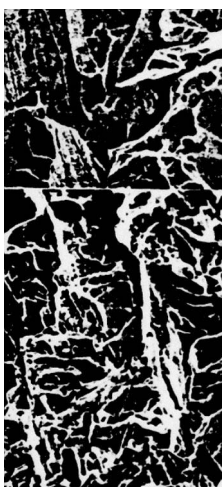


Figure 7b.  
Alloy C (Fe-0.63Ti)  
Scanning electron micrograph.  
Fracture is mixed cleavage-  
intergranular after testing in  
liquid nitrogen.

0.09 mm





The microstructure of the alloys, as well as their hydrogen-free mechanical properties have thus been characterized. The hydrogen trapping parameters of each material will now be analyzed.

Figure 12.  
Alloy DC (Pa-0.751-0.0650)  
Scanning electron micrograph.  
Fracture surface is mostly  
intergranular after casting in  
liquid nitrogen.

0.05 mm

Figure 13.  
Alloy DC (Pa-1.2671 - 0.0390)  
Scanning electron micrograph.  
Fracture surface is mostly  
cleavage after casting in liquid  
nitrogen.

0.05 mm

Figure 14.  
Alloy DC (Pa-1.3671-0.0650)  
Scanning electron micrograph.  
One of the few intergranular  
regions, showing particle distribution  
within a grain boundary.

0.05 mm



## Chapter II

### DIFFUSION AND TRAPPING OF HYDROGEN THROUGH IRON AND IRON-TITANIUM MEMBRANES

#### A. Past Studies and the Concept of Trapping

The literature on the diffusion of hydrogen through  $\alpha$ -iron is enormous. It is thus more realistic to refer primarily to existing literature reviews, if one wants a clear and general view of this problem. Among those are Oriani's,<sup>(3)</sup> Birnbaum and Wert,<sup>(49)</sup> and more recently, Volkl and Alefeld.<sup>(50)</sup> Despite the large number of investigations, the data on the diffusion coefficient of hydrogen through  $\alpha$ -iron shows a tremendous scatter: as shown on Figure 8,<sup>(50)</sup> the value of  $D_{\alpha\text{Fe}}^{\text{H}}$  varies, at room temperature, between  $4 \times 10^{-9} \text{ cm}^2/\text{sec}$  and  $8 \times 10^{-5} \text{ cm}^2/\text{sec}$ , almost five orders of magnitude.

Several possibilities have been proposed to account for this large scatter:<sup>(50)</sup>

(1) Trapping of hydrogen at lattice imperfections, such as dislocations, grain boundaries, precipitates, voids, impurities, etc..., leading to a slower effective diffusion. This concept was first suggested by Darken and Smith<sup>(7)</sup> in 1949, who showed that if one was to calculate the hydrogen diffusivity from the time required for it to appear at the output side of a metal membrane, one would underestimate its value by a factor proportional to the concentration of lattice dissolved hydrogen at the input side of the diaphragm, and inversely proportional to the mean total concentration of hydrogen in the specimen.

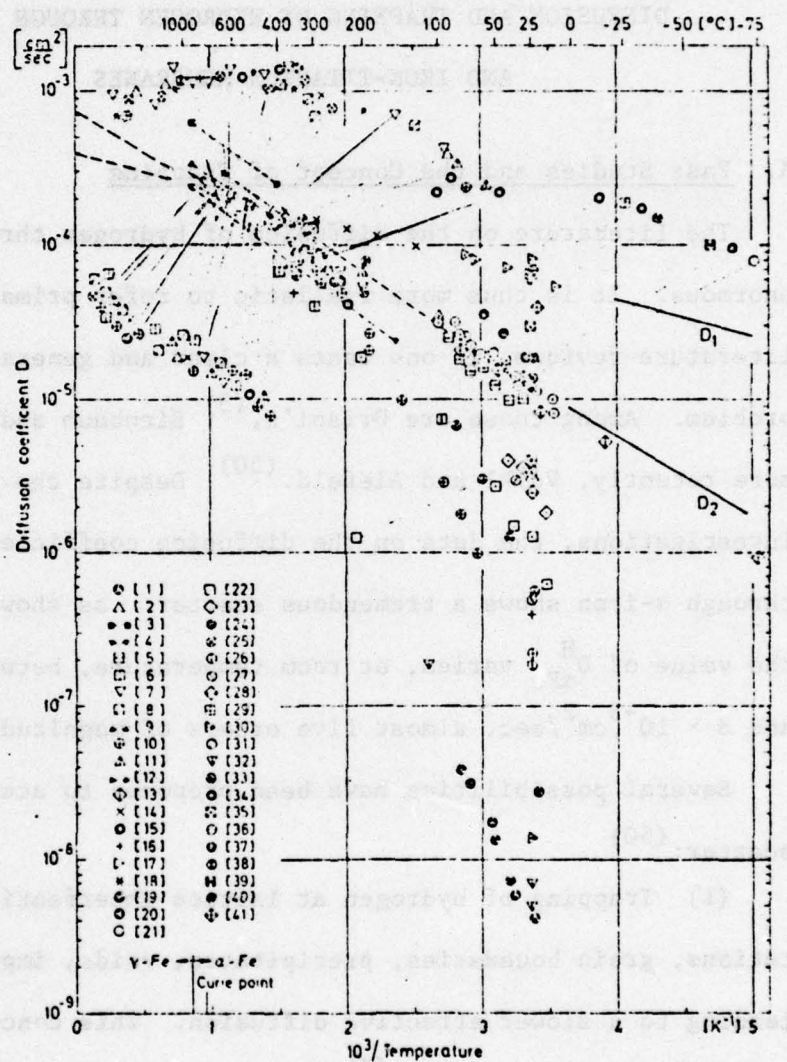


FIGURE 8.  
Variation of the Diffusivity of Hydrogen in Ferrite with Temperature<sup>(50)</sup>;  
Note the Large Scatter at Room Temperature.



Since then, more elaborate theories have been formulated, such as McNabb and Foster's<sup>(51)</sup> or Oriani's,<sup>(52)</sup> which will be considered later in more detail.

(2) Surface dependent diffusion: Again, the diffusivity of hydrogen through ferrite would be underestimated because a particular reaction of hydrogen with the specimen surface may be rate controlling. However, the difference between this possibility and trapping is not always obvious, since trapping may also occur on the surface and be responsible for the surface reaction. Surface effects will be discussed in greater depth in the course of this chapter.

(3) The formation of immobile di-interstitials,<sup>(53)</sup> the reaction rate and extent of which should also decrease the hydrogen lattice diffusivity.

(4) The formation of hydrogen gas in voids or pores, which may decrease or enhance the apparent diffusion process.

Thus, the concept of trapping is certainly the most important of all the above-mentioned possibilities, since possibilities (3) and (4) may also be classified as trapping (self-trapping in case (3) and pore or void trapping in case (4)) and trapping may also play a part in the surface effects mentioned in (2)). Consequently, attention will be devoted to the literature which experimentally suggests or demonstrates the presence of trapping.

#### B. Experimental Evidence of Trapping

The existence and nature of hydrogen trapping sites in materials has been revealed by numerous experimental techniques. Those sites



have been indirectly identified by monitoring the diffusion of hydrogen through materials where suspected traps were present and comparing the results to a pure material. More directly, the exact nature of the sites may be revealed by techniques such as autoradiography, where the trace left on a photographic emulsion by radio-active hydrogen (tritium), helps to identify its position in the lattice. Several trapping sites have so far been identified:

(1) Voids and Microvoids:

Hydrogen can collapse into voids to form hydrogen gas at a pressure related to the surrounding hydrogen lattice concentration. (54,55,56) Figure 9<sup>(56)</sup> shows the decrease in apparent diffusivity hydrogen in a steel due to an increase in the volume of voids. Those voids were formed at the interface between inclusions and the matrix. It is interesting to note that the magnitude of the volume percent of voids was found by the authors to be dependent on the nature of the inclusion; a large void volume was associated with hard and brittle inclusions (alumina, silica), while the reverse occurred with more plastic inclusions (such as MnS). Another example of the effect of voids on hydrogen location in the matrix is the work of Ouchi, Bernstein and co-workers.<sup>(57)</sup> These workers showed that when Kirkendall porosity, due to the differential diffusion of aluminum in iron was present, the extent of hydrogen-induced damage was greatly reduced. Here again, the evidence of hydrogen trapping by voids or pores is quite strong.

(2) Dislocations:

Numerous examples may be found in the literature concerning the

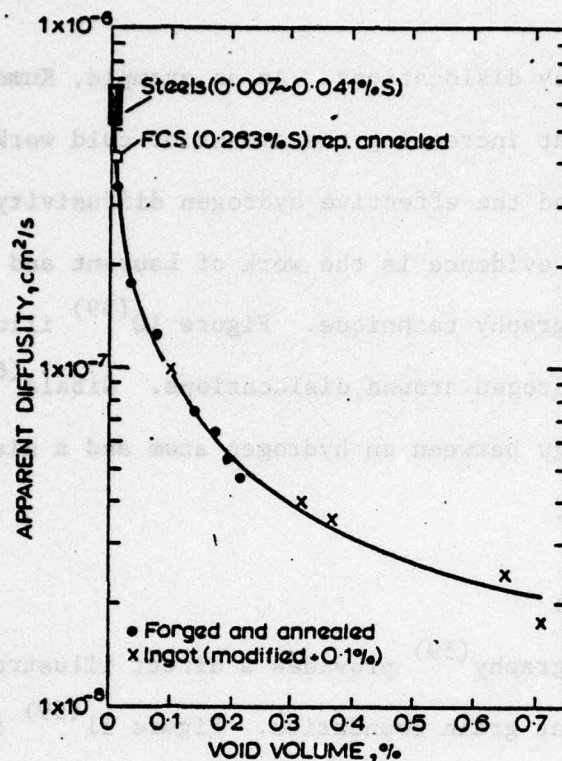


**Figure 9**

(56)

Apparent diffusivity (23°C) plotted against true void volume

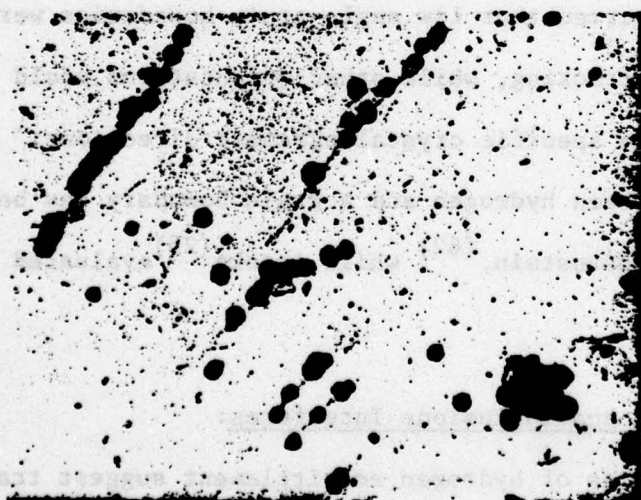


**Figure 10**  
Transmission Electron Micrograph of tritium trapped at dislocations. (Ref. 59)

5.4 μ



trapping of hydrogen by dislocations. As an example, Kumnick and Johnson<sup>(58)</sup> showed that increasing the amount of cold work in an Armco iron specimen decreased the effective hydrogen diffusivity. However, the best experimental evidence is the work of Laurent and co-workers<sup>(59)</sup> who used an autoradiography technique. Figure 10<sup>(59)</sup> illustrates the segregation of hydrogen around dislocations. Gibala<sup>(60)</sup> evaluated the binding energy between an hydrogen atom and a dislocation as approximately  $0.25 \text{ eV}$ .

### (3) Grain Boundaries:

Again, autoradiography<sup>(59)</sup> provides a direct illustration of the trapping of hydrogen at grain boundaries. Figure 11<sup>(59)</sup> clearly demonstrates this fact. A result worthy of notice is that this trapping is selective, i.e., all boundaries do not seem to have the same trapping ability for hydrogen. This was also shown by Bernstein and Rath,<sup>(61)</sup> who observed that low angle grain boundaries were immune to hydrogen-induced cracking, while other orientations would crack or not crack depending on specific crystallographic directions. The interaction energy between hydrogen and a grain boundary has been estimated to be  $0.27 \text{ eV}$  by Bernstein,<sup>(62)</sup> while Asaoka<sup>(25)</sup> evaluated it as  $0.55\text{--}0.61 \text{ eV}$ .

### (4) Precipitates and Inclusions Interfaces:

Several studies of hydrogen embrittlement suggest trapping of hydrogen at the precipitate-matrix interface. For example, Boniszewski proposed hydrogen trapping on manganese sulfide inclusions.<sup>(54)</sup> If we follow the ideas suggested in part (c) above, the larger the incoherency of the interface, the greater its ability to trap hydrogen. More recently, Asaoka,<sup>(25)</sup> using autoradiography on an alloy similar to

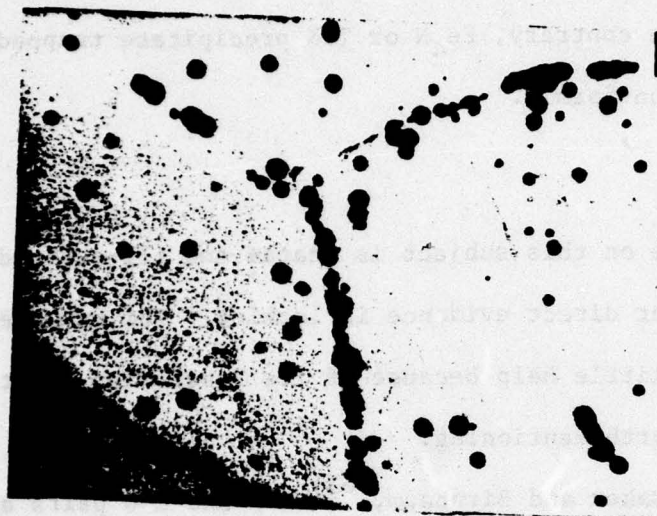


**Figure 11**  
Transmission Electron Micro-  
graph Of Tritium Trapped At  
Grain Boundaries. ( Ref. 59)

4.3 μ

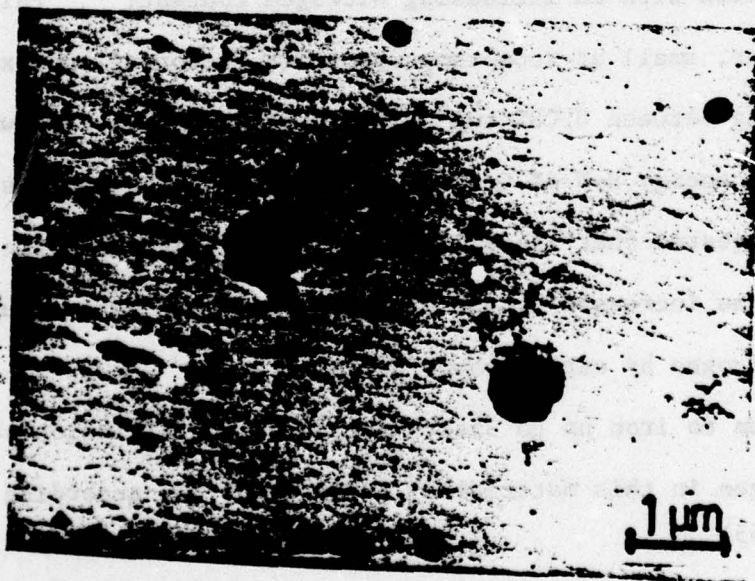


**Figure 12**  
Transmission Electron Micro-  
graph Of Tritium Trapped At  
Titanium Carbides Particles.  
( Ref.25)

1 μm



alloy B, showed that spherical titanium carbide particles were one of the strongest traps in the lattice ( $E = 0.8 \text{ eV}$ ) and that trapping was uniformly distributed on the interface with the matrix as shown in Figure 12). On the contrary,  $\text{Fe}_4\text{N}$  or  $\text{TiN}$  precipitate trapped less strongly and less uniformly.

(5) Solute Atoms:

The literature on this subject is scarce and ill-defined. The main problem is that direct evidence is lacking. For example, autoradiography is of little help because of its resolution limit. However, some results are worth mentioning.

According to Baker and Birnbaum,<sup>(63)</sup> H-N and H-O pairs are formed in niobium. This results in a decrease in the diffusion coefficient of hydrogen in niobium with an increasing nitrogen content;<sup>(50)</sup> this decrease is, however, small at room temperature (a factor of approximately two for N/Nb varying between 0.08% and 0.55%), which is in accord with the low interaction energy H-N of  $0.09 \text{ eV}$  calculated by the authors.<sup>(63)</sup>

Gibala<sup>(64)</sup> suggested that since the magnitude of the anelastic relaxation effect was increased by the presence of carbon as a solute, the trapping of hydrogen by carbon could be important.

Adding chromium to iron up to 35at.% decreases the diffusion coefficient of hydrogen in this material by a factor of 30, according to Bockris et al.<sup>(65)</sup>

Dresler and Froberg<sup>(66)</sup> obtained a decrease of  $D_{\text{Fe}}^{\text{H}}$  from  $4 \times 10^{-6} \text{ cm}^2/\text{sec.}$  to  $8 \times 10^{-7} \text{ cm}^2/\text{sec}$  by adding 5wt% of nickel to iron.

They attributed this decrease to stronger interaction forces between hydrogen and nickel. Other workers,<sup>(67)</sup> using a different technique, found almost no variation up to 15%Ni. Surface effects are a probable cause for the discrepancy in the results. This is one of the reasons why it is intended to examine surface effects in detail.

The formation of H-H pairs has been suggested in various articles<sup>(3,63)</sup> and evidence from anelastic methods<sup>(63)</sup> tends to support this idea. The binding energy of the H-H pair has been evaluated at 0.065 eV,<sup>(63)</sup> which is quite small compared to the value of the binding energy hydrogen-dislocation or hydrogen-grain boundary.

In concluding this section, it is clear that direct evidence exists concerning the trapping of hydrogen at "large" crystal defects, such as voids, precipitates, grain boundaries, dislocations, etc.... However, atomic defects, such as solute atoms, may also act in a similar way, although the estimated binding energies are quite small ( $<0.1$  eV) compared to those for larger defects ( $>0.25$  eV). The fact that trapping at the atomic level may occur is quite important however since it lends support to our introductory premises, thereby encouraging us to look further into the role of titanium as an innocuous trapping center.

### C. Experimental Technique

#### C.1. The Apparatus

All permeation experiments were carried out using an electrochemical cell originally developed by Devanathan and Stachursky.<sup>(68)</sup> Figure 13 shows a schematic of the experimental set-up. The cell itself is composed of two glass compartments clamped to both sides of the



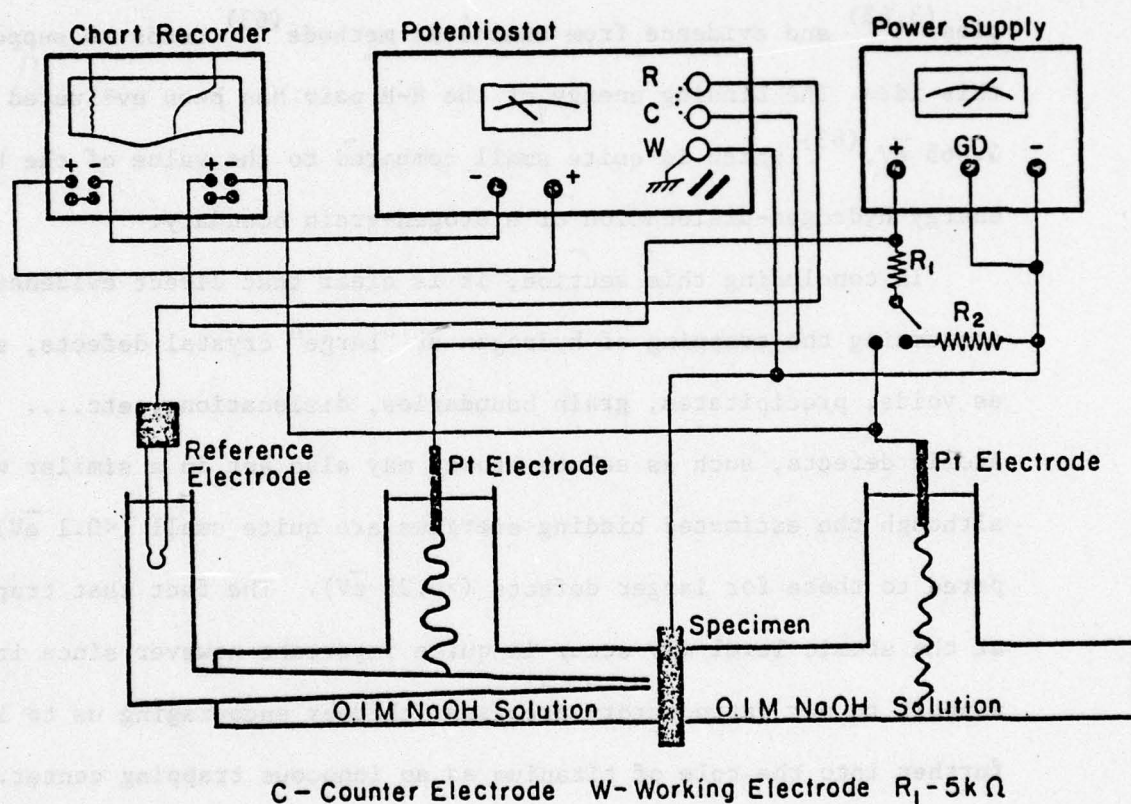
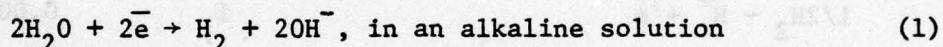


FIGURE 13.  
Experimental Set-up Used for all Permeations.

metal membrane to be studied (specimen on Figure 13). One distinguishes between the "cathodic" side (right compartment on Figure 13), and the "anodic" side (left compartment on Figure 13). The cathodic side is filled with deionized 0.1 N NaOH solution and a potential is maintained between the specimen (=cathode) and a platinum counter electrode (=anode) by the power supply. The cathodic current density is controlled at will using a variable resistance  $R_1$ . A mechanical stirrer was also inserted close to the anode and the whole cell was tilted to allow easy escape of any gas bubbles which may accumulate on the cathode or input side of the specimen. Such an accumulation could reduce the extent of the input side electrochemical reaction, which, in total, can be represented as:



The anodic compartment is also filled with a 0.1N NaOH solution prepared with deionized distilled water. In this compartment, the specimen (or its output side) plays the role of the anode while the platinum counter electrode is the cathode. A saturated calomel (mercury, mercurous chloride, potassium chloride) electrode is added to this compartment as a reference electrode; the potentiostat (a Wenking, model 66TS3) establishes a potential (with respect to this reference electrode) sufficient to oxidize all the hydrogen existing on this (output) side of the membrane. The useful function of the potentiostat is that, after establishing this oxidation potential, it can indefinitely maintain this pre-determined value. The current necessary to maintain this



TABLE II

Reaction	No.	E <sub>ox</sub> (volts)
$2\text{H}_2\text{O} \rightarrow \text{O}_2 + 4\text{H}^+ + 4\text{e}^-$	7	-1.229 v
$\text{Pt} \rightarrow \text{Pt}^{2+} + 2\text{e}^-$	6	-1.2 v
$\text{Pd} \rightarrow \text{Pd}^{2+} + 2\text{e}^-$	5	-0.83 v
$4\text{OH}^- \rightarrow \text{O}_2 + 2\text{H}_2\text{O} + 4\text{e}^-$	4	-0.401 v
Saturated calomel electrode	3	-0.2415 v
$2\text{As} + 3\text{H}_2\text{O} \rightarrow \text{As}_2\text{O}_3 + 6\text{H}^+ + 6\text{e}^-$	2	-0.234 v
$1/2\text{H}_2 \rightarrow \text{H}^+ + \text{e}^-$	1	0.000 v
$\text{Fe} \rightarrow \text{Fe}^{3+} + 3\text{e}^-$	1'	0.036 v
$\text{Fe} \rightarrow \text{Fe}^{2+} + 2\text{e}^-$	2'	0.409 v
$\text{Fe}(\text{OH})_2 + \text{OH}^- \rightarrow \text{Fe}(\text{OH})_3 + \text{e}^-$	3'	0.56 v
$\text{As} + 4\text{OH}^- \rightarrow \text{AsO}_2 + 2\text{H}_2\text{O} + 3\text{e}^-$	4'	0.68 v
$\text{H}_2 + 2\text{OH}^- \rightarrow 2\text{H}_2\text{O} + 2\text{e}^-$	5'	0.8277 v
$\text{Ti} + 2\text{H}_2\text{O} \rightarrow \text{TiO}_2 + 4\text{e}^- + 4\text{H}^+$	6'	0.86 v
$\text{Ti} \rightarrow \text{Ti}^{2+} + 2\text{e}^-$	7'	1.63 v
$\text{Na} \rightarrow \text{Na}^+ + \text{e}^-$	8'	2.7109 v

Table II: Oxidation potentials from Handbook of Chemistry and Physics, 55th Edition, CRC Press. Note: oxidation becomes easier as potential is more positive. For example, if the chosen potential is -200 mV, then all reactions with  $E > -200\text{mV}$  will occur

potential is thus a direct measure of the flux of hydrogen appearing on the output side of the membrane, since the anodic reaction for this oxidation of hydrogen will be:



and since Faraday's law states that:

$$m_{\text{H}} = \frac{n_{\text{H}} M_{\text{H}}}{N_{\text{a}}} = \frac{M_{\text{H}} i t}{n_{\text{e}} F} \Rightarrow \frac{n_{\text{H}}}{t A} = J_{\text{H}} = \frac{N_{\text{a}}}{n_{\text{e}} F} \frac{i}{A} \quad (3)$$

where:

$m_{\text{H}}$  = mass of  $n_{\text{H}}$  hydrogen atoms

$N_{\text{a}}$  = Avogadro's number

$M_{\text{H}}$  = atomic mass of hydrogen

$i$  = anodic current

$t$  = time

$A$  = working area of membrane

$F$  = Faraday's constant

$n_{\text{e}}$  = number of electrons involved in the electrochemical reaction

$J_{\text{H}}$  = flux of hydrogen

In other words, the output flux of hydrogen is proportional to the anodic current as:

$$J_{\text{H}} (n^{\text{r}} \text{ of atoms of H/cm}^2 \cdot \text{sec}) = K i, i \text{ in amperes} \quad (4)$$

where:

$$K = \frac{N_{\text{a}}}{n_{\text{e}} F A} = \frac{6.02 \times 10^{23} \text{ atoms}}{1 (\text{electron}) \times 96500 (\text{amp} \times \text{sec.}) \times A (\text{cm}^2)} \quad (5)$$



or:

$$K = 6.24 \times 10^{18} / A \text{ (atoms/amp. sec. cm}^2\text{)} \quad (6)$$

Finally,

$$J_H \left( \frac{\text{atoms}}{\text{cm}^2 \cdot \text{sec}} \right) = 6.24 \times 10^{18} i_a \text{ with } i_a = \frac{\text{amp.}}{\text{cm}^2} \quad (7)$$

At all times, the coverage of the output side will be zero, or in other words, the output side boundary condition will be:

$$t \geq 0, C_H = 0, \text{ on the anodic side of the membrane} \quad (8)$$

#### Other Accessories:

A chart-recorder was used to record simultaneously both the increase in the anodic current, as the potentiostat retains its imposed potential (i.e., the output flux of hydrogen), and the input current density. This latter measurement allows us to determine precisely when the permeation started.

An integrator was occasionally used for the determination of the diffusion coefficient by the lag time method, discussed in a later section. When in use, the input current was not recorded.

An electrolytic cell consisting of two platinum electrodes for deionizing the sodium-hydroxide solution.

A Beckman electronic pH-meter for the precise preparation of all the solutions (used for charging or plating purposes).

## C.2. Setting Up the Equipment

### (a) Choice of the Anodic Potential

As stated before, this potential had to be chosen to ensure oxidation of all the hydrogen coming out of the specimen. Table II shows that any potential above (more negative than) the reference potential of hydrogen can do this. However, as seen in Table II, this negative potential will also oxidize iron, and will even do this preferentially to oxidizing hydrogen (since  $E_{\text{oxidation}}(\text{Fe}) = + 0.409 \text{ v}$ ). In order to prevent this from happening, the output side of the sample can be coated with a metal that is noble enough (very negative  $E_{\text{ox.}}$ ) to withstand oxidation at the imposed anodic potential. Another constraint on the choice of the coating metal is that it must be quite permeable to hydrogen. Palladium was used as such a protective anodic layer, since its potential is quite high ( $-0.83\text{v}$ . on Table II), its diffusivity for hydrogen is of the order of  $3.2 \times 10^{-7} \text{ cm}^2/\text{sec}$  and its hydrogen solubility is very much higher than iron ( $\sim 10^6$  times higher than iron). The following limits have consequently been put on the anodic potential:

$$0\text{v} > E_{\text{anodic}} (\text{ref.: H}_2\text{electrode}) > -0.83\text{v}$$

Table II also gives other potentials for oxidation reactions which may be of interest here. In particular, one sees that titanium is more subject to oxidation than iron, an additional justification for the coating of the output side with palladium. The need for deionizing the sodium hydroxide solution is emphasized by the possibility of reactions such as 5', 3' and 4 occurring at the same time as the oxidation of hydrogen. These reactions should not be too much of a problem however, since they involve several molecules, and thus have a low probability



of occurrence. Reactions with arsenic are included for later reference. It should be noted that the listed potentials are standard ones, and that their actual value during the experiment will change according to such factors as pH, temperature, etc... The above reasoning should then be taken as a rough comparison between the magnitude of the potentials, which will probably stay, according to Nernst's equation, in the order given in Table II.

(b) Choice of the Cathodic Potential

In order for the reaction (5')  $2\text{H}_2\text{O} + 2\text{e} \rightarrow \text{H}_2 + 2\text{OH}^-$  to occur, the cathodic potential had to be greater than 0.8277 volts (see Table I). Deionizing the solution was a very important step, because all reactions with an oxidation potential less than 0.8277 v could occur as reduction reactions (Ex.:  $\text{Fe}^{2+} + \text{e} \rightarrow \text{Fe}$ ). This would have resulted in deposits on the input surface of the specimen which could have reduced its permeability to hydrogen. Similar deposits have, in fact, been observed during these experiments and the permeation results obtained were discarded. The solution was deionized in the electrolytic cell discussed previously, and electrolyzed for 24 hours at a current of a few milliamperes.

(c) Preparation of the Specimens

All specimens were cold rolled to various thickness between 5 and 40 mils and annealed at  $800^\circ\text{C}$  in argon for 2 to 4 hours to obtain a grain size of approximately  $80\mu$ . The membranes were then mechanically and chemically polished to a mirror-like finish. The chemical solution used was a solution of  $2/3 \text{H}_3\text{PO}_4$  and  $1/3 \text{H}_2\text{O}_2$ . When the desired surface

quality was obtained, the samples were then plated with palladium on one or both sides, depending on the experiment to be performed. This was done electrolytically using a "Sel-Rex Palladex VI\*" electroplating bath, which yields a low porosity, crack-free, smooth palladium deposit. The thickness of the palladium layer was about  $10^{-5}$  cm. Using  $D_{\text{Pd}}^{\text{H}} = 3.2 \times 10^{-7} \text{ cm}^2/\text{sec}$ , the time for a hydrogen atom to cross the palladium layer is approximately:

$$t = x^2/D = (10^{-5})^2/3.2 \times 10^{-7} = 3 \times 10^{-4} \text{ sec}$$

The protective layer was thus by no means a diffusion barrier.

When thinner membranes were to be used, they were thinned down chemically in a 50%  $\text{H}_2\text{O}$ -40%  $\text{HNO}_3$ -10%  $\text{HF}$  solution, then polished by the usual method and plated. The minimum thickness safe enough to withstand deformation from clamping to the permeation cell was about 5 mils.

After final polishing, specimens were sealed to the permeation cell, using gaskets and rubber O-rings.

#### (d) Preparation of the Solution

The 0.1 N NaOH solution used throughout this experiment was obtained by dissolving 4 grams of Baker reagent grade sodium hydroxide (in pellets) in one liter of distilled water. The pH obtained was 12.26.

#### (e) First Trials

It is of importance to verify the effectiveness of the protective palladium layer deposited on the output side of the membrane (anodic compartment). This was done by varying the applied anodic

---

\*Made by the Sel-Rex Company, 75 River Road, Nutley, NJ 07110.



potential and measuring the steady state flux of hydrogen. If the palladium layer is effectively protecting the iron membrane from dissolution, one should see a plateau in the steady state flux ( $J_{\infty}$ ) over a wide range of anodic potentials. This plateau corresponds to the reaction  $H \rightarrow H^+ + e^-$ . Figure 14 illustrates that this condition is satisfied. These results were obtained using a 34 mils thick Ferrovac E membrane, and a 39 mils thick Fe-0.15Ti membrane, both of which were also palladium plated on the input side (for reasons given below). A plateau exists between approximately -100mV and 400mV (oxidation potentials are versus the saturated calomel electrode, see Table II). The plateau disappears at  $E > 500\text{mV}$  where the palladium layer may start to dissolve (it should predictably dissolve at 588.5mV versus saturated calomel electrode, or 830mV versus hydrogen electrode) and at  $E = -200\text{mV}$  where the oxidation potential is not high enough to ionize the existing hydrogen (since we are now close to -241.5mV, the hydrogen potential versus saturated calomel electrode). The anodic potential was thus selected for all experiments as:

$$E_{\text{anodic}} = +100\text{mV (versus saturated calomel electrode)}$$

This potential is far enough from both limits (-241.5mV and 588.5mV) to insure complete ionization of hydrogen and a nondissolving palladium layer.

The cathodic current density used in most experiments was maintained at  $0.8\text{mA/cm}^2$ . This choice was governed by the following reasons:

- i) It was found that for long time experiments, the contamination

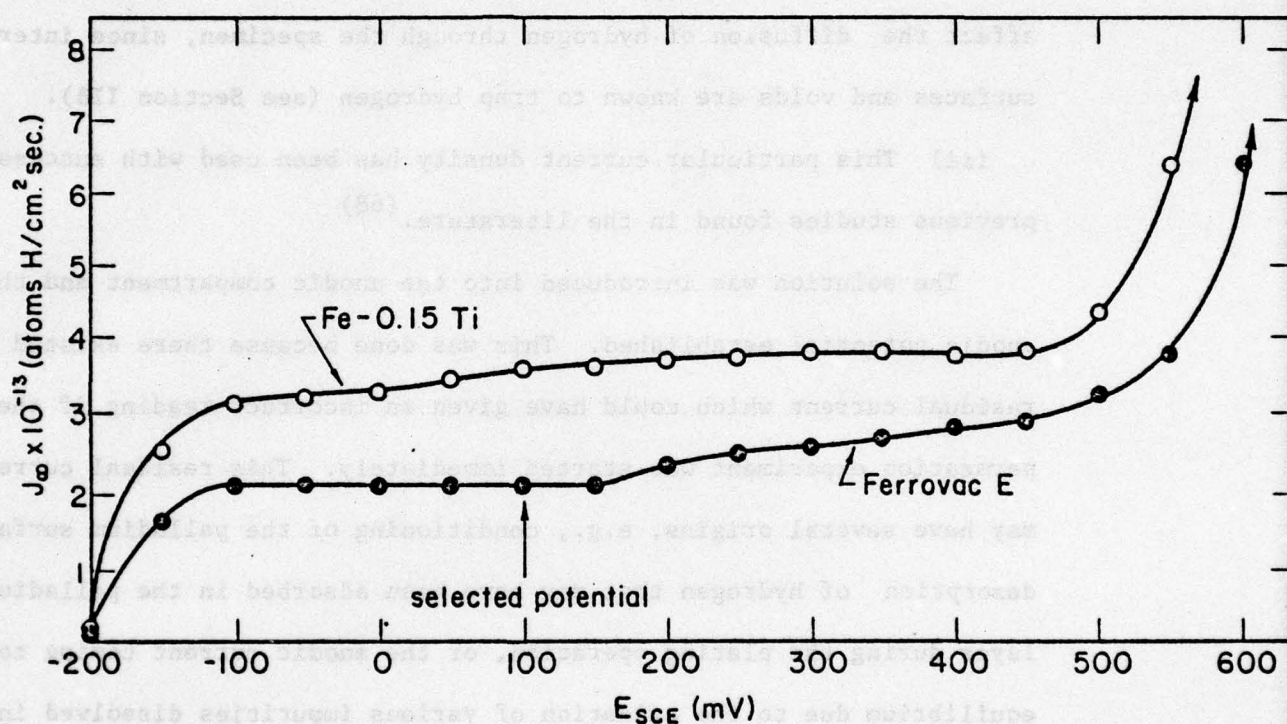



FIGURE 14.  
Variation of the Output Flux of Hydrogen with the Output Side Potential  
(versus saturated calomel electrode).



of the input surface was less at low current densities than at high current densities. We shall see later that such a contamination can quite strongly alter the shape of the permeation transients.

ii) At high current densities, cracking may occur in the lattice or along grain boundaries, as will be seen in Chapter III. The addition of those cracks to the existing lattice defects will profoundly affect the diffusion of hydrogen through the specimen, since internal surfaces and voids are known to trap hydrogen (see Section IIB).

iii) This particular current density has been used with success in previous studies found in the literature. (68)



The solution was introduced into the anodic compartment and the anodic potential established. This was done because there existed a residual current which could have given an incorrect reading if the permeation experiment was started immediately. This residual current may have several origins, e.g., conditioning of the palladium surface, desorption of hydrogen that may have been adsorbed in the palladium layer during the plating operation, or the anodic current coming to equilibrium due to the oxidation of various impurities dissolved in the solution. At steady state, the residual current was stabilized at a very low value, around  $1\mu\text{A}/\text{cm}^2$ . When steady state was reached, the cathodic solution was poured into the cathodic compartment and the polarization immediately started. The sensitivity of this method was quite high and hydrogen fluxes as low as  $5 \times 10^{10}$  atoms  $\text{H}/\text{cm}^2\text{sec}$  could be detected. Various technical problems were present, such as a strong noise background. These were remedied by putting the reference electrode

in a copper Faraday cage, isolating and grounding all wires, and absorbing the remaining noises by capacitances in parallel to the permeation circuit.

#### D. Experimental Results:

##### D.1. The Experiment

In order to keep the analysis of the results simple, the permeation of the noncarburized alloys were performed first, i.e., alloys A, B, C and D<sub>2</sub>. As seen in Chapter I, these alloys have been characterized as consisting of  $\alpha\text{Fe}+\text{TiC}$  + dissolved titanium in various amounts. Since all experimental variables, such as charging solution, membrane thickness, current density, etc..., were kept sensibly constant, variations in diffusion behavior can reasonably be attributed to the different nature of the permeated membrane. Moreover, all entry sides of all specimens have been plated with palladium, as was the output side. Since titanium or titanium carbonitride particles may be present in varying amounts on the surface of the membranes, doing so ensured similar hydrogen discharge and entry conditions for all alloys. Such a precaution has been amply justified, as discussed in Appendix D and Section II, E.2, on surface effects.

The permeation of carburized alloys BC, CC and DC was then performed, following an analysis of the results on their low carbon counterparts. This procedure allowed a more logical verification of the predictions and findings of this analysis.



#### D.2. Permeation Behavior of the Uncarburized Alloys

The results concerning the effect of titanium additions on the diffusion of hydrogen in ferrite are illustrated in Figures 15 through 19, for noncarburized alloys A, B, C and D<sub>2</sub>. Initial polarization rise and decay transients are presented in Figure 15 and 16 respectively. As the titanium content of iron increases, the permeation becomes slower. For example, the time to reach steady state goes from 35 minutes for Ferrovac E to 300 minutes for Fe-0.15Ti and to more than 1000 minutes for Fe-1.5Ti. This strongly suggests the presence of trapping. The decay transients show the same effect.

Figures 17 and 18 illustrate a similar response for the second polarization. Again, the presence of titanium decreases the permeation and evolution rates of hydrogen through ferrite, although the effect is decreased relative to the initial polarization behavior.

The slow kinetics of hydrogen diffusion in  $\alpha$ -Fe when titanium is added is perhaps best illustrated by the variation in break through time with increasing titanium content. The breakthrough time is that time necessary for hydrogen to cross the membrane in sufficient quantity to be detected by the potentiostat on the output side. Since originally all the traps are free, the breakthrough time is directly related to the efficiency of the trap populations. Figures 15 and 17 show an appreciable increase in the breakthrough time with increasing titanium content, decreasing in extent for the second polarization.

These results also permit an evaluation of the reversibility of traps as shown in Figure 19, which compares the permeation transients

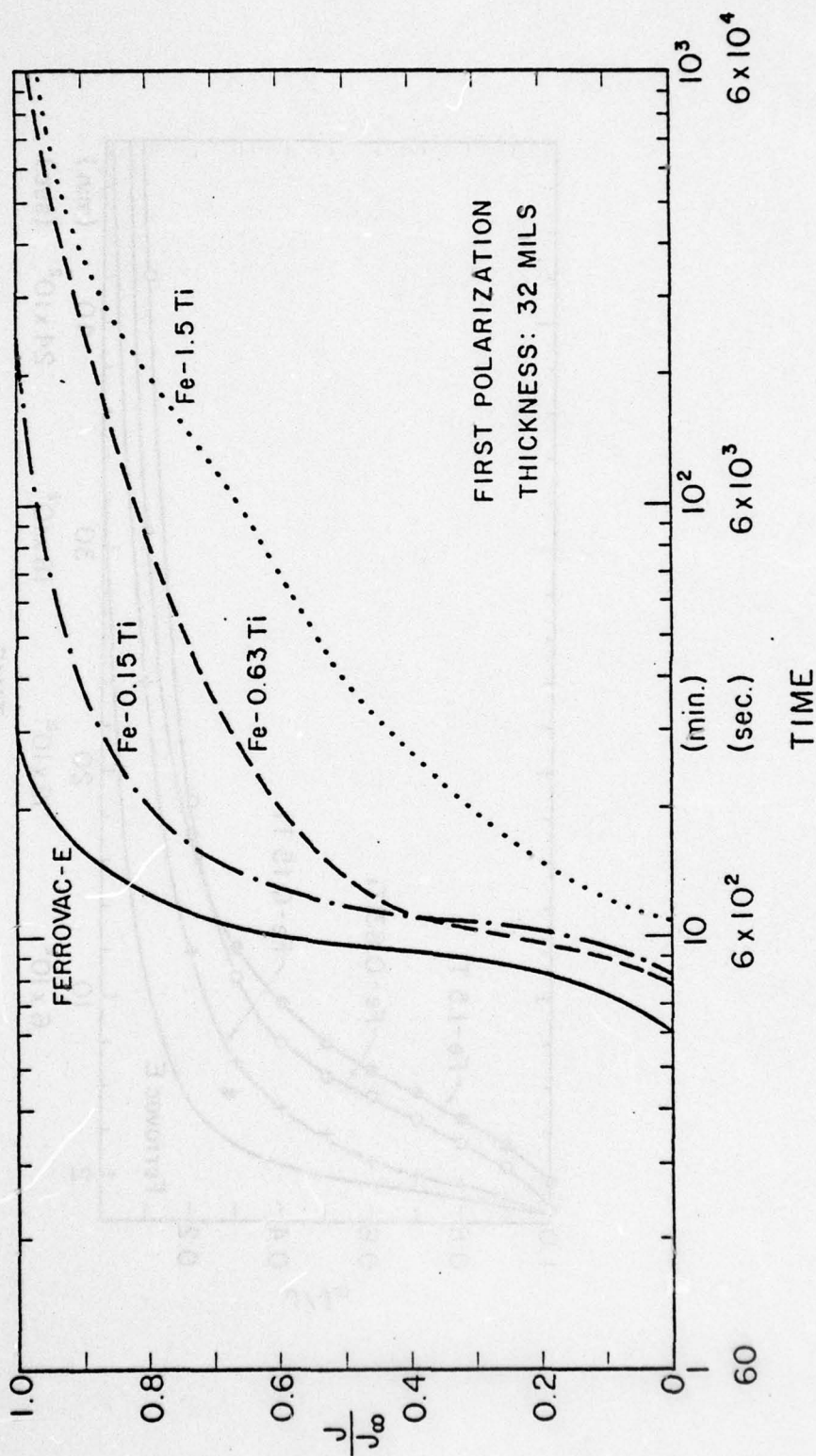


FIGURE 15. Normalized Output Flux of Hydrogen Versus Time (first polarization permeation transients).



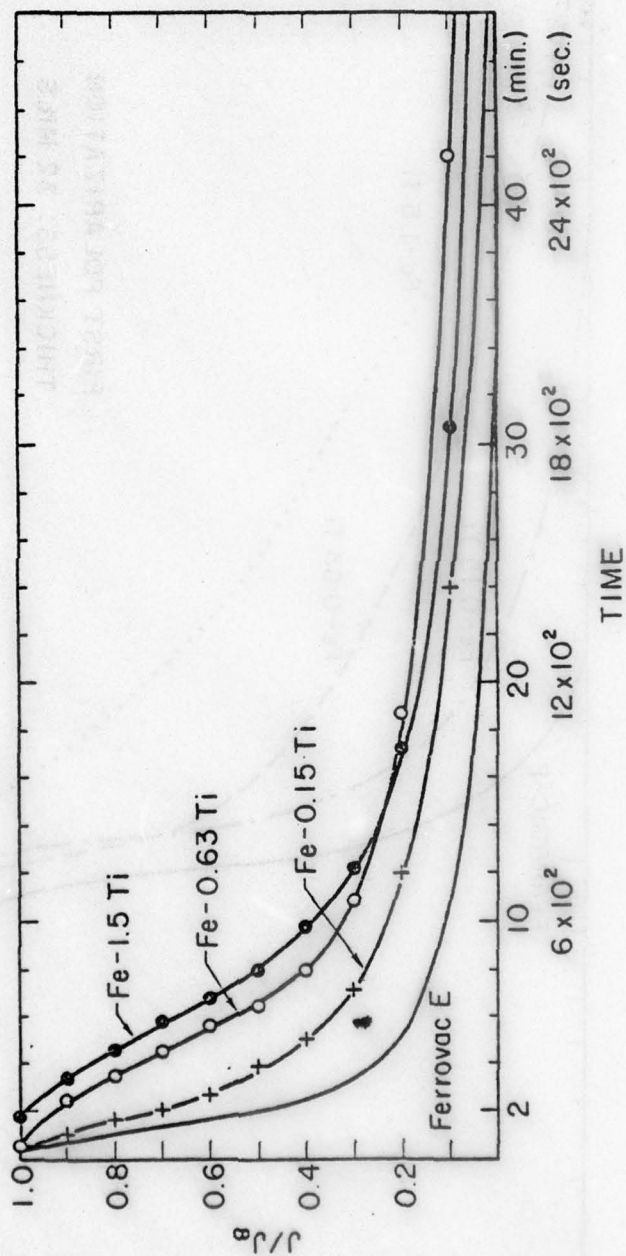


FIGURE 16. Normalized Output Flux of Hydrogen Versus Time (first polarization decay transients).  
(Symbols on the Curves are Used to Distinguish between transients, and are not Experimental Data; The whole Curves were experimentally obtained).

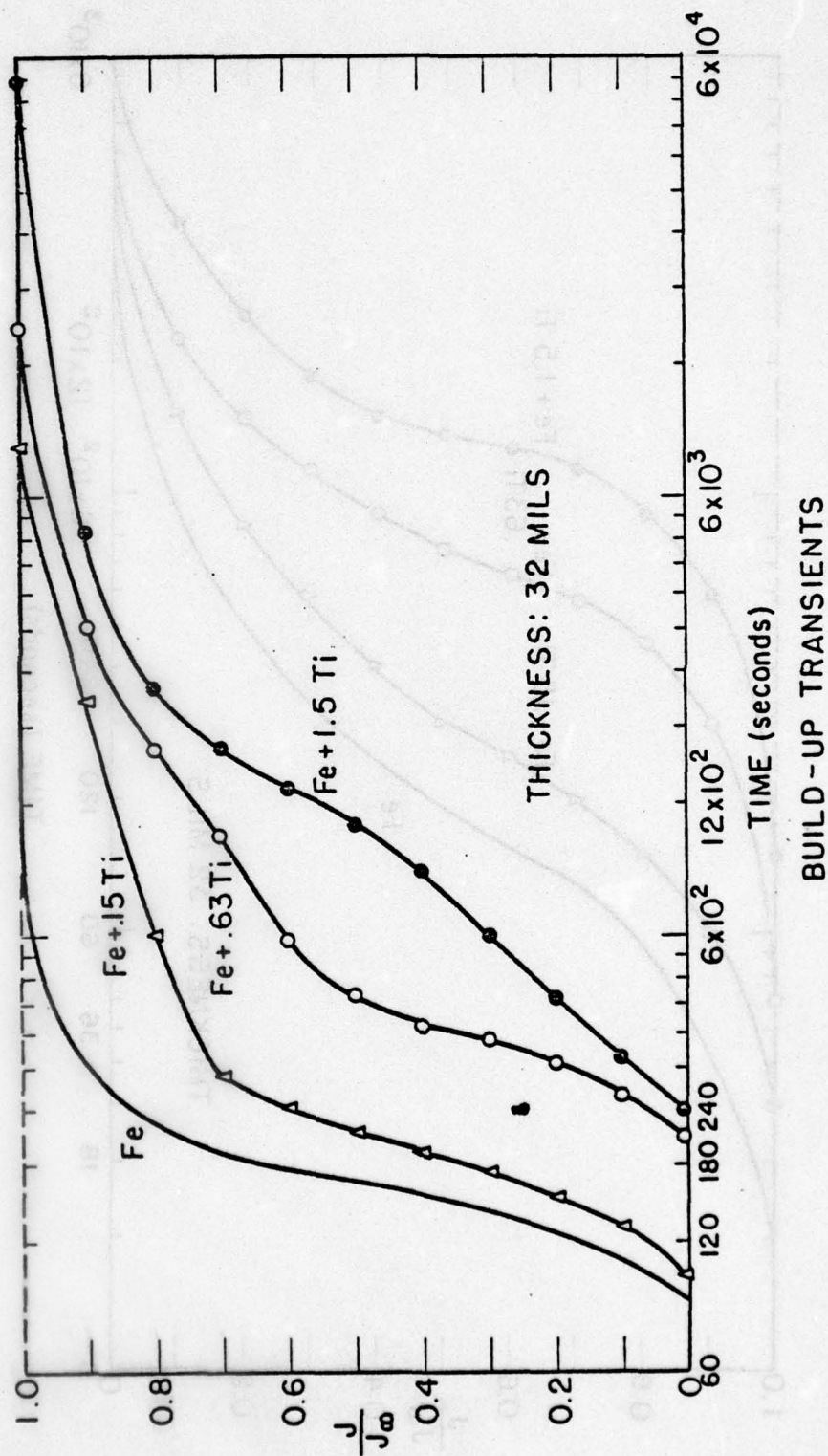


FIGURE 17. Normalized Output Flux of Hydrogen Versus Time (second polarization permeation transients). (Symbols on the Curves are Used to Distinguish between transients, and are not Experimental Data; Instead, The Whole Curves Were Experimentally Obtained ).



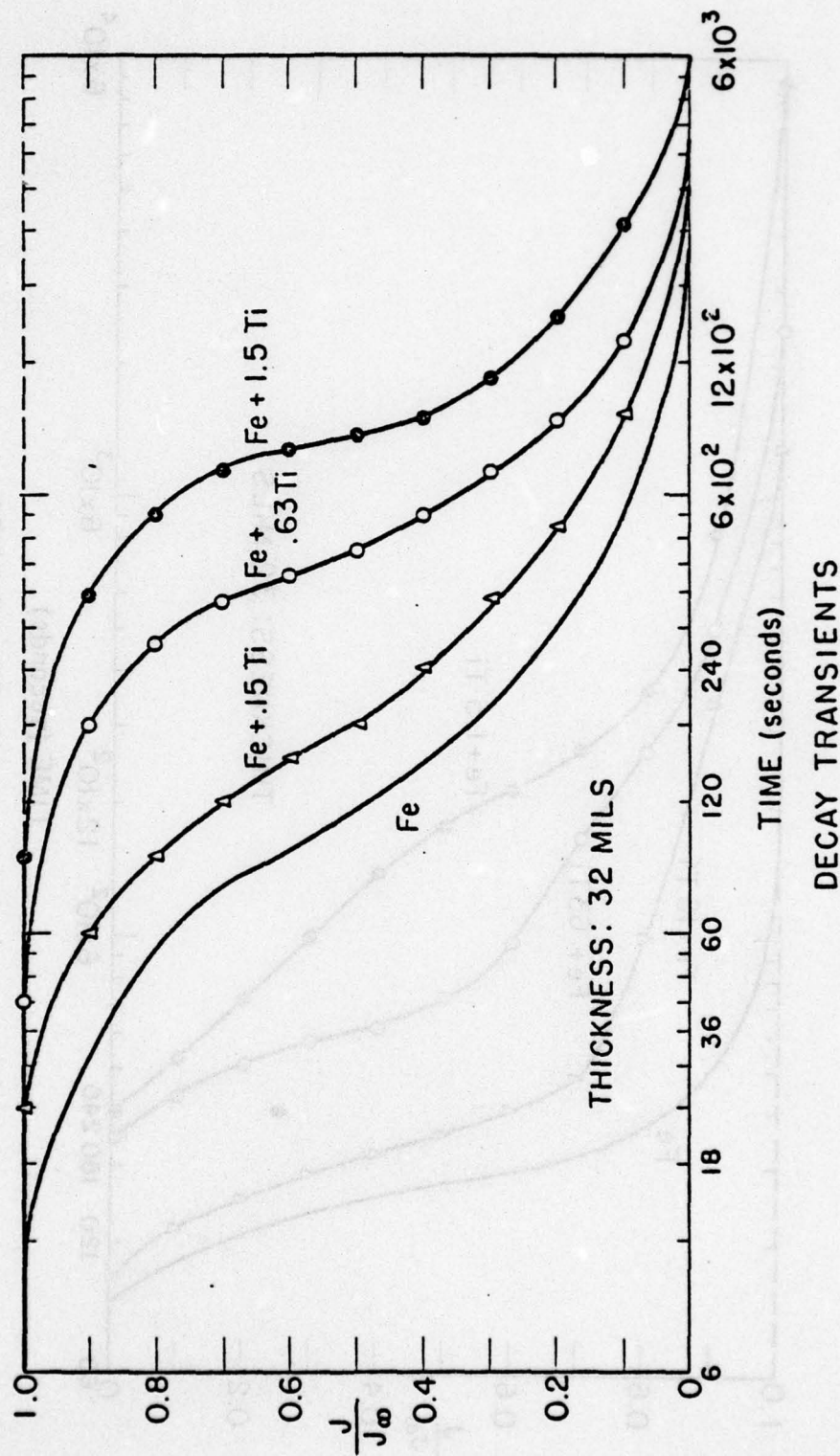


FIGURE 18. Normalized Output Flux of Hydrogen Versus Time (second polarization decay transients). (Symbols on the Curves are Used to Distinguish between transients, and are not Experimental Data; Instead, The Whole Curves Were Experimentally obtained ).

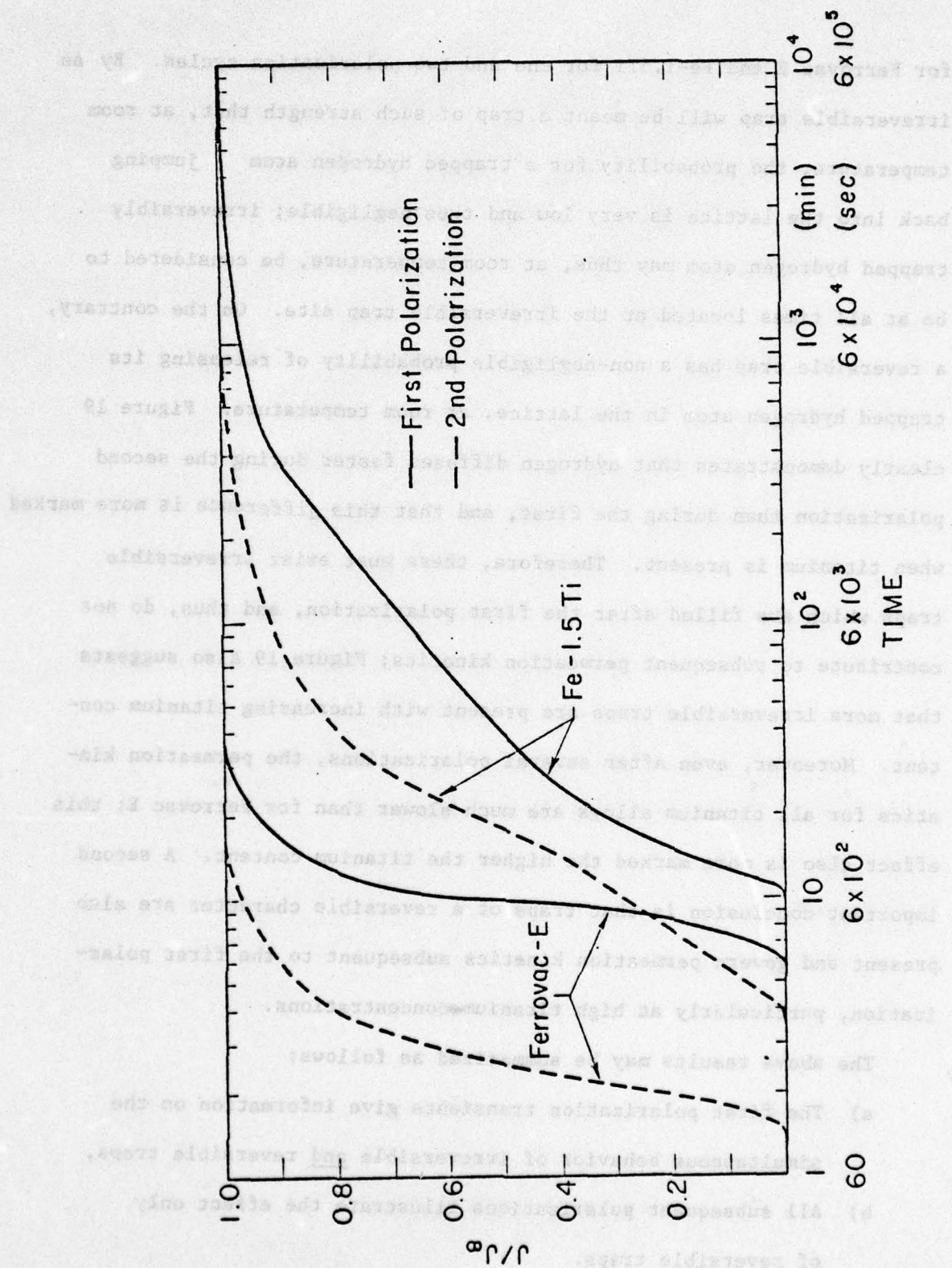


FIGURE 19. Comparison of the First and Second Polarization Permeation Transients for Ferrovac E and Fe-1.5Ti. This Diagram Illustrates the Presence of Both Reversible and Irreversible Trapping.



for Ferrovac E and Fe-1.5Ti for one and two polarization cycles. By an irreversible trap will be meant a trap of such strength that, at room temperature, the probability for a trapped hydrogen atom jumping back into the lattice is very low and thus negligible; irreversibly trapped hydrogen atom may thus, at room temperature, be considered to be at all times located at the irreversible trap site. On the contrary, a reversible trap has a non-negligible probability of releasing its trapped hydrogen atom in the lattice, at room temperature. Figure 19 clearly demonstrates that hydrogen diffuses faster during the second polarization than during the first, and that this difference is more marked when titanium is present. Therefore, there must exist irreversible traps which are filled after the first polarization, and thus, do not contribute to subsequent permeation kinetics; Figure 19 also suggests that more irreversible traps are present with increasing titanium content. Moreover, even after several polarizations, the permeation kinetics for all titanium alloys are much slower than for Ferrovac E; this effect also is more marked the higher the titanium content. A second important conclusion is that traps of a reversible character are also present and govern permeation kinetics subsequent to the first polarization, particularly at high titanium concentrations.

The above results may be summarized as follows:

- a) The first polarization transients give information on the simultaneous behavior of irreversible and reversible traps,
- b) All subsequent polarizations illustrate the effect only of reversible traps.

c) Both trapping effects are stronger the higher the titanium content.

This last conclusion suggests that the nature of irreversible and reversible traps is related in a direct way to the presence of titanium in the iron matrix. The nature of the irreversible traps is easily revealed. Asaoka,<sup>(25)</sup> cathodically charging an alloy similar to alloy B, and then degassing it at various temperatures, found by autoradiography that titanium carbide particles retained hydrogen for times much longer than other traps, such as grain boundaries and dislocations. These particles are thus the most irreversible traps of the lattice, having large interaction energy with hydrogen of about 0.8-1.0 eV.<sup>(25)</sup> A similar behavior is expected for the alloys of this study, with titanium carbide particles being the irreversible traps which are primarily responsible for the delay in the first polarization permeation kinetics. Irreversible trapping will be analyzed in details in a subsequent section; reversible trapping will now be characterized.

It will be initially assumed that titanium substitutional atoms or small clusters provide the primary reversible traps. The following study is meant to demonstrate the validity of this hypothesis. To accomplish this, the second polarization transients will be analyzed in depth. The resulting findings will be used not only to study reversible trapping, but by difference will provide a characterization of the irreversible trapping occurring during the first polarization. Other possible causes to explain the delay in permeation due to the presence of titanium such as surface trapping, or hydrogen concentration changes will also be investigated. These will be shown to be only minor



contributors, leaving trapping by substitutional titanium as the primary agent responsible for the observed diffusion behavior of Fe-Ti alloys.

## E. Analysis of Reversible Trapping

### E.1. Titanium as a Reversible Hydrogen Trap

#### E.1.a. Theoretical Evidence for an Attraction Titanium-Hydrogen

As previously discussed, the driving force governing the trapping of hydrogen by a particular site may have various origins, and a clear identification is not always possible. For example, the force can be of chemical (thermodynamical) origin when hydrogen forms a gas ( $H_2$ ,  $CH_4$ ) or a hydride (e.g.,  $TiH_2$ ), or of mechanical origin when hydrogen is subjected to the stress field of a dislocation. Other forces may arise from the particular electronic state of hydrogen in the lattice. In all cases, obviously, hydrogen will seek to reduce its free energy. In the particular case of titanium, it is possible to show that most of these forces may exist, all tending to attract hydrogen to the titanium site, or to neighboring interstitial sites.

#### (1) The Thermodynamical Force Between Titanium and Hydrogen

There are several ways of demonstrating the existence of a thermodynamic driving force. The simplest way is to look at the sign and amplitude of the first order interaction coefficient between titanium and hydrogen. Other ways include the calculation of

the driving force for the formation of the hydride  $\text{TiH}_2$  in iron.

The First Order Interaction Coefficient  $e_{Ti}^H$

The activity,  $a_i$ , of component  $i$  in solution in iron is given by:

$$a_i = f_i (\%Ti) \quad (9)$$

where  $f_i$  = activity coefficient of  $i$  in iron and  $(\%i)$  is its weight percent. Now,  $f_i$  is related to the other dissolved elements in iron by: (63)

$$\log f_i = \sum_j e_i^j (\%j) + \sum_j r_i^j (\%j)^2 + \sum_j \sum_k r_i^{j,k} (\%j)(\%k) + 0(\%)^3 \quad (10)$$

Here,  $j$  designates every element dissolved in iron (including  $i$ ),

$e_i^j$  = first order interaction coefficient between  $j$  and  $i$ ,  $(\%j)$  = weight percent of  $j$  in Fe,  $r_i^j$  = second order interaction coefficient between  $i$  and two atoms of  $j$ ,  $r_i^{j,k}$  = second order interaction coefficient between  $i$  and  $j$  and  $k$ ,  $0(\%)^3$  = remaining term with third power of  $(\%i, j, k)$  and higher.

Usually,  $r_i^j$  and  $r_i^{j,k}$  are quite small, and to a good approximation, for small  $(\%)$

$$\log f_i = \sum_j e_i^j (\%j) \quad (11)$$

The important point is that  $e_i^j$  directly relates to the affinity that exists between elements  $i$  and  $j$  in iron. (70) Indeed, a negative  $e_i^j$  is indicative of a thermodynamic attraction between  $i$  and  $j$ , while a positive  $e_i^j$  denotes a thermodynamic repulsion between  $i$  and  $j$ . The



more negative  $e_i^j$ , the stronger the attraction, and vice-versa.

Values of  $e_i^j$  are tabulated in the literature, (71,72,73) mainly for elements dissolved in liquid iron (1600°C). Their equivalent value at room temperature may be estimated using the equation: (74)

$$e_i^j(T_1) = e_i^j(T_2) + \frac{h_i^j}{2.3R} \left[ \frac{1}{T_1} - \frac{1}{T_2} \right] \quad (12)$$

where  $h_i^j$  is the excess enthalpy interaction coefficient of the first order between i and j; these are also tabulated. (72) In all cases, a negative interaction coefficient  $e_i^j$  at 1600°C will be more strongly negative at room temperature. Unfortunately, very few values of  $h_i^j$  are known; in particular,  $h_{Ti}^H$  is not known. However, an order of magnitude estimate of the increase in  $e_i^j$  with decreasing temperature may be obtained by comparison with known cases of similar elements. Various tables have been developed to emphasize the importance of  $e_{Ti}^H$  and compare its magnitude and sign to other known values of interest. In particular:

- a) Table III shows that  $e_{Ti}^H$  ranks among the most negative interaction coefficients, meaning that titanium is one of the most attractive elements for hydrogen in iron. Indeed, Reference 71 ranks titanium first and Reference 72 ranks it fifth, after Nd, Ta, La and O.
- b) Table IV shows that hydrogen will compete with oxygen and nitrogen for trapping by titanium. The coefficient  $e_{Ti}^C$  is not known, but should be strongly negative since titanium readily forms titanium carbide in iron. (27) This competition is very important

TABLE III

ATTRACTION $e_i^H < 0$				REPULSION $e_i^H > 0$			
Element i	Ref. 71	Ref. 72	Ref. 73	Element i	Ref. 71	Ref. 72	Ref. 73
Ce	-	-0.60	-	Ag	-	-	0.17
Co	-	-0.14	-	Al	0.34	0.24	0.35
Cr	-0.11	-0.33	-0.11	As	-	-	0.34
Cu	-	-0.24	-	Au	-	-	0.12
La	-	-4.3	-	B	0.53	0.49	0.54
Mn	-0.077	-0.31	-0.077	C	0.72	0.67	0.72
Mo	-	-0.20	-0.12	Ge	-	0.41	0.72
Nb	-0.21	-0.61	-0.21	H	0.00	0.00	-
Nd	-	-6.0	-	N	-	-	0.34
Ni	0	-0.25	-(0.00)	P	0.34	0.21	0.34
O	-	-3.10	-	Pd	-	0.20	-
Ta	-3.60	-4.40	-0.23	Pt	-	-	0.08
Ti	-3.85	-1.10	-	Rh	-	0.37	-
V	-	-0.59	-0.24	S	0.26	0.12	0.26
W	-	-	-0.39	Sb	-	-	0.34
Zr	-	-	-0.13	Si	0.76	0.64	0.76
				Sn	0.62	0.12	0.62
				W	-	0.088	-
				Co	0.11	-	0.11
				Cu	0.031	-	0.032

Table III: Values of the first order interaction coefficient  $e_i^H$  in liquid iron at  $1600^\circ\text{C}_H$ . A circled element means that contradictory information is present ( $e_i^H$  both  $>0$  and  $<0$ ).

Note:

$e_i^H$  is related to  $e_H^i$  by the equation:

$$e_i^H = \frac{M_i}{M_H} e_H^i \quad \text{where } M_i = \text{atomic weight of } i.$$



TABLE IV

Element j	O	C	N	H	Ti
$e_{Ti}^j$	-1.8	-	-1.8	-1.1	0.013

Table IV: Values of the first order interaction coefficient  $e_{Ti}^j$  at 1600°C in liquid iron. (From Ref. 72).

TABLE V

	Variation with temperature	$e_{Ti}^N(1600^\circ\text{C})$	$e_{Ti}^N(25^\circ\text{C})$
$e_{Ti}^N$	$-13900/T + 5.61$	-1.8	-41.0

Table V: Variation of  $e_{Ti}^N$  with temperature T(°K).  
From Ref. 72.

TABLE VIa

Alloy \ (%H)	$5.4 \times 10^{-8}$	$1.18 \times 10^{-5}$	$0.62 \times 10^{-2}$
Fe-0.15Ti	-10.14	-16.57	-23.82
Fe-1.50Ti	-10.85	-17.28	-25.26

Table VIa: Values of  $\Delta G$  (kcal/mole) for the reaction:  
 $Ti(\%) + 2H(\%) = TiH_2(s)$ .

TABLE VIb

Alloy (%)	$1.18 \times 10^{-5}$	$0.62 \times 10^{-2}$
Fe-0.15Ti	9.41	2.08
Fe-1.50Ti	-11.24	-18.58

Table VIb: Values of  $\Delta G$  (kcal/mole) for the reaction:  $\text{TiC(s)} + 2\text{H(\%)} = \text{TiH}_2\text{(s)} + \text{C(\%)}$ .

TABLE VIc

Alloy (%)	$1.18 \times 10^{-5}$	$0.62 \times 10^{-2}$
Fe-0.15Ti	39.35	31.89
Fe-1.50Ti	18.68	11.28

Table VIc: Values of  $\Delta G$  (kcal/mole) for the reaction:  $\text{TiC(s)} + 2\text{H(\%)} = \text{TiH}_2\text{(s)} + \text{N(\%)}$ .



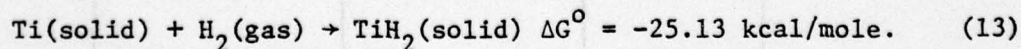
because it then becomes doubtful that a particle  $\text{Ti}(\text{OCN})$  would dissociate so that the released titanium can trap hydrogen or form a hydride  $\text{TiH}_2$ .

c) Table V demonstrates that  $e_{\text{Ti}}^{\text{N}}$  becomes strongly negative at room temperature; since nitrogen and hydrogen behave in the same way with titanium ( $e_{\text{Ti}}^{\text{H}} = -1.1$ ,  $e_{\text{Ti}}^{\text{N}} = -1.8$ ), one could expect the same magnitude of variation with temperature for  $e_{\text{Ti}}^{\text{H}}$ .

In conclusion, the first order interaction coefficient  $e_{\text{Ti}}^{\text{H}}$  demonstrates that titanium is one of the most attractive elements for hydrogen in iron, even at room temperature. However, hydrogen competes with elements such as oxygen, nitrogen and carbon for trapping by titanium. This means that in order to trap hydrogen efficiently, titanium should be present as an unreactive solute, or in other words, that the content of other trappable solutes in iron should be low with respect to the total titanium content.

#### The possibility of hydride formation:

It can be shown that there exists a thermodynamic driving force for elemental titanium and hydrogen to form the hydride  $\text{TiH}_2$ , even at room temperature. This results from the strongly negative value of the room temperature standard free energy change,  $\Delta G^0$ , for the reaction: (75)



However, we really want to examine what happens to this reaction at room temperature when titanium and hydrogen are both dissolved in iron.

For this, one has to consider the reaction:



where  $\underline{\text{Ti}}$  = dissolved titanium atom in iron

$\underline{\text{H}}$  = monoatomic hydrogen in iron

$\text{TiH}_2(\text{s})$  = precipitated hydride.

The calculations are detailed in Appendix C, along with those for the dissociation of  $\text{TiO}_2$ ,  $\text{TiN}$ , and  $\text{TiC}$  by hydrogen. The results are given in Table VI and confirm the predictions obtained from the interaction coefficient, i.e., there is a strong driving force for the formation of an hydride,  $\text{TiH}_2$ , in iron at room temperature (since  $\Delta G$  is negative). However, this chemical driving force disappears if titanium is already associated with oxygen, nitrogen or carbon. It should be noted that the existence of a driving force does not imply that the reaction will actually take place. Other considerations are of equal or greater importance in this regard, such as the kinetics of the reaction, associated strain energy, etc.... The driving force is, however, a necessary condition for the reaction to take place.

## (2) The Electronic Force Between Titanium and Hydrogen

There is now considerable experimental and theoretical evidence that dissolved hydrogen exists in the atomic form in metals and occupies interstitial sites in ferrite.<sup>(3)</sup> Moreover, we know that hydrogen dissolves in transition metals by ionizing, i.e., giving up its electron to the collective electron gas of the metal.<sup>(3)</sup> For the sake of equilibrium, the excess electron thus introduced by the interstitial proton will



locally attract the valence electrons, so as to screen the charge:<sup>(76)</sup>  
 this is why one speaks of dissolved hydrogen as a "screened proton."  
 In transition metals, this screening most probably occurs in the d-band.

An interesting feature of the particular dissolved state of hydrogen is the effect of impurities. Indeed, because hydrogen introduces an excess electron, an impurity which introduces an "electron vacancy" will attract hydrogen so as to achieve local neutrality. As Friedel<sup>(76)</sup> states: "one expects hydrogen to be repelled at short range by impurities on the right of the matrix in the periodic table, and attracted by impurities on the left." An examination of the periodic table shows titanium to be located on the left of iron, which means that one should expect an attraction, titanium-hydrogen. An illustration of the Friedel prediction may be found in the literature for solid solutions NiFe and FeNi,<sup>(77)</sup> although those elements are quite close to one another in the periodic table, and the effect is small. The effect of titanium on hydrogen should be much stronger, because titanium is further away from iron than is nickel, and thus needs more electrons to fill its conduction band.

In concluding this section, we emphasize the fact that there will exist at least two attractive forces between titanium and hydrogen in iron. While their origins are varied, all strongly support the affinity between titanium and hydrogen. Indeed, we could have used the same arguments to explain the decrease in diffusivity of hydrogen through ferrite with chromium additions:<sup>(65)</sup>  $e_H^{Cr}$  is negative, and Cr is on the left of Fe in the periodic table. However, the same characteristics for

the case of titanium are much more striking, e.g.,  $e_{Ti}^H = 3.33 \times e_{Cr}^H$ ; and titanium is further from iron than is chromium in the periodic table. This difference in the magnitude of the necessary characteristics for the attraction titanium-hydrogen, compared to chromium-hydrogen should manifest itself by a larger effect of titanium additions on the diffusivity of hydrogen in ferrite compared to chromium. This will be examined in the next section.

#### E. 1.b. Trapping Theories

The concept of trapping is not recent,<sup>(7)</sup> and several theories have now been proposed to explain the diffusion of hydrogen in iron under trapping conditions. It is useful to briefly examine these theories, in the light of our experimental evidence for trapping.

##### (1) Normal Diffusion: Fick's Laws

When no traps are present in the lattice and if the diffusion medium is isotropic, then Fick's first and second laws state that:

$$J = -D_o \frac{dC}{dx} \text{ and } \bar{V} \frac{dC}{dt} = \frac{d}{dx} \left[ D_o \frac{dC}{dx} \right] \quad (15)$$

where  $J$  = flux of the diffusing species along the concentration gradient  $dC/dx$ , and  $D_o$  = normal diffusivity in the homogeneous lattice. In our permeation experiment, the boundary conditions are:

$$t = 0, C(x=0) = C(x=L) = 0$$

$$t > 0, C(x=0) = C_o, C(x=L) = 0$$

If  $L$  = thickness of the membrane and  $C_o$  = input concentration of hydrogen. Then, at steady state, from Fick's first law:



$$J_{\infty} = -D_0 (C_0 - 0) / (0 - L) = \frac{D_0 C_0}{L} \quad (16)$$

where  $J_{\infty}$  = steady state flux of hydrogen after an infinitely long time of permeation.

For the time-dependent solutions (permeation and decay rates), one uses second Fick's law and solves the differential equation with a Laplace or Fourier transform, keeping  $D_0$  constant. The two equivalent solutions for the rise transient are,

$$\text{Laplace: } \frac{J}{J_{\infty}} = \frac{2}{(\pi\tau)^{1/2}} \sum_{n=0}^{\infty} (-1)^n \exp \left[ \frac{-(2n+1)^2}{4\tau} \right] \quad (17)$$

$$\text{Fourier: } \frac{J}{J_{\infty}} = 1 + 2 \sum_{n=1}^{\infty} (-1)^n \exp \left( -n^2 \pi^2 \tau \right) \quad (18)$$

$$\text{where } \tau = \text{dimensionless time} = \frac{D_0 t}{L^2} \quad (19)$$

For all practical purposes, ten terms are sufficient in each summation to accurately describe the variation of  $J/J_{\infty}$  with time. Figure 20 is such a plot for both the Laplace and Fourier solutions, for  $n = 10$ .

It should be noted that other input boundary conditions may exist in the particular case of permeation experiments. In particular, consider the conditions<sup>(78)</sup>

$$t = 0, J(x=0) = J(x=L) = 0$$

$$t = 0, J(x=0) = J_0, J(x=L) = 0$$

The solution<sup>(78)</sup> for a Laplace transform in this case is:

$$\frac{J}{J_{\infty}} = 1 - \frac{4}{\pi} \sum_{n=0}^{\infty} \left[ \frac{(-1)^n}{(2n+1)} \exp \left( \frac{-\pi^2 (2n+1)^2 \tau}{4} \right) \right] \quad (20)$$

This particular case predicts a slower diffusion rate than the previous equations for a concentration step function as a boundary condition. However, the use of a step flux as a boundary condition suggests a rate limitation at the input surface. Because of this, this solution will not be considered here, but will be mentioned in the chapter on surface effects.

For the steady transients, using the boundary condition:

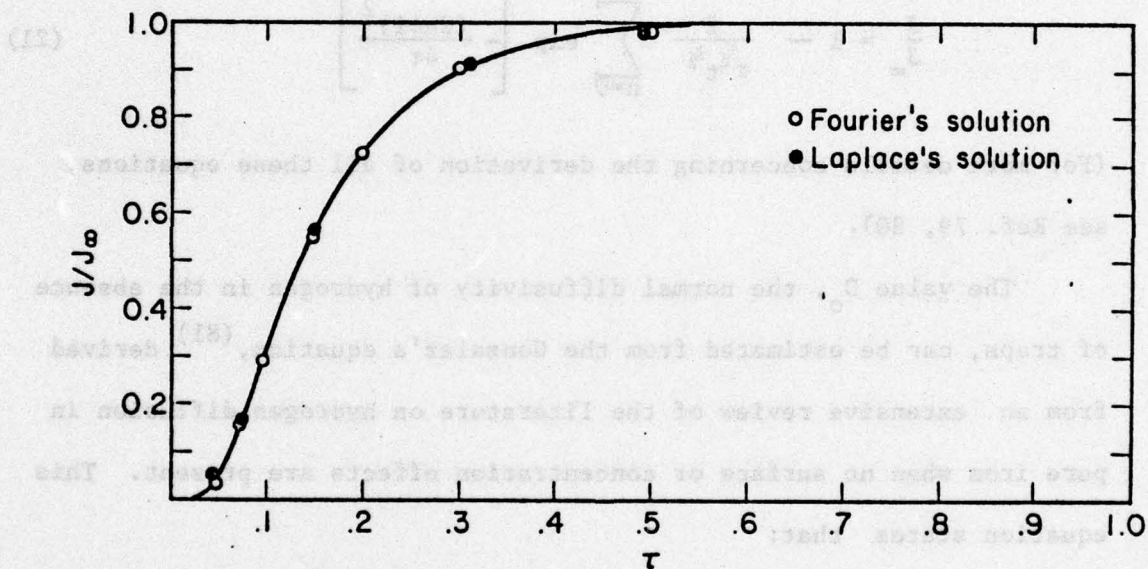
$$x = 0, \frac{\partial C}{\partial x} = 0, \text{ the solution for the Laplace solution:}$$


FIGURE 20.  
Normal Diffusion Transients, Calculated Using Fourier and Laplace Transforms.



This particular case predicts a slower diffusion rate than the previous equations for a concentration step function as a boundary condition. However, the use of a step flux as a boundary condition suggests a rate limitation at the input surface. Because of this, this solution will not be considered here, but will be reexamined in the chapter on surface effects.

For the decay transients, using the boundary condition:

$t > 0, C(x=0, L=0)$ , one obtains for the Laplace solution:

$$\frac{J}{J_{\infty}} = 1 - \frac{2}{\pi^{1/2} t^{1/2}} \sum_{n=0}^{\infty} \exp \left[ -\frac{(2n+1)^2}{4\tau} \right] \quad (21)$$

(For more details concerning the derivation of all these equations, see Ref. 79, 80).

The value  $D_0$ , the normal diffusivity of hydrogen in the absence of traps, can be estimated from the Gonzalez's equation,<sup>(81)</sup> derived from an extensive review of the literature on hydrogen diffusion in pure iron when no surface or concentration effects are present. This equation states that:

$$D_0 = 0.78 \times 10^{-3} \exp (-1900/RT) \text{ in cm}^2/\text{sec} \quad (22)$$

At 25°C (298°K), this gives a value of  $D_0 = 3.2 \times 10^{-5} \text{ cm}^2/\text{sec}$ .

(Note: The notation  $D_0$  used here designates the coefficient of diffusion of hydrogen in pure  $\alpha$ -iron, and should not be confused with the asymptotic value of  $D$  in the expression  $D = D_0 \exp (-Q/RT)$ .)

(2) The McNabb and Foster Theory<sup>(51)</sup>

McNabb and Foster developed a quite general model for hydrogen atoms trapped or delayed at certain fixed sites during diffusion through the lattice. No assumptions are made concerning the nature or origin of these traps except that they be uniformly distributed throughout this metal. The diffusion constant  $D$  is assumed to be isotropic, independent of concentration and of the fraction of occupied traps. Their general equations modify the corresponding Fick's laws which are now written as:

$$\begin{aligned} \frac{du}{d\tau} + \frac{dw}{d\tau} &= \nabla^2 u \\ \frac{dw}{d\tau} &= \lambda u - \mu w - \nu w u \end{aligned} \quad (23)$$

These equations are dimensionless and:

$u = C/C_0$  where  $C$  and  $C_0$  have the same meaning as before.

$w$  = relative trapped concentration =  $nN_T/C_0$  where  $N_T$  is the density of traps (number/volume) and  $n$  the fraction of traps occupied.

$\tau = D_0 t/L^2$  as seen before,

$\lambda$  and  $\nu$  are related to the capture rate constant,  $k$ ,

$$\lambda = N_T k L^2 / D_0 \quad \text{and} \quad \nu = C_0 k L^2 / D_0 \quad (24)$$

and  $\mu$  is related to the release rate constant,  $p$ , as:

$$\mu = p L^2 / D_0 \quad (25)$$

where  $k$  and  $p$  are defined by:

$$\frac{dn}{dt} = kC(1-n) - pn \quad (26)$$



This relation expresses the rate of increase of the number of atoms in the trapped population as the difference between the rates of capture and release.

The resulting time dependent solutions, where they can be obtained, are quite complicated and may be simplified only for certain cases. Specifically, the finite-difference method has been applied to these equations for boundary conditions appropriate to hydrogen permeation in a plane.<sup>(82)</sup> The resulting computer-generated curves illustrate the variation in shape of  $J/J_\infty$  versus time with parameters  $\lambda$ ,  $\mu$  and  $\nu$ , as illustrated in Figure 21. In Figure 21a one can see that at constant capture rate and trap density ( $\lambda, \nu$ ) the permeation rate decreases with decreasing release rate  $\mu$ ; the same result is obtained when the capture rate (or trap density) increases, as depicted in Figure 21b. Finally, although the ratio, capture/release ( $\lambda/\mu$ ), may remain constant, Figure 21c shows that one can obtain quite different shapes of  $J/J_\infty$ . In particular, curve 2 on Figure 21c exhibits an initial fast rise, and a very slow approach to steady state. This particular behavior will be of interest when the experimental data are analyzed. In every case, however, the apparent diffusivity  $D$  is less than the lattice diffusivity  $D_0$  obtained for simple diffusion without traps. In the particular case where the traps are sparingly occupied ( $C_0 k/p \ll 1$ ), few atoms will remain trapped. Nevertheless, diffusion is slowed and:

$$D = \frac{D_0}{1 + \frac{N_T k}{p}} \quad \text{for} \quad \frac{C_0 k}{p} \ll 1 \quad (27)$$

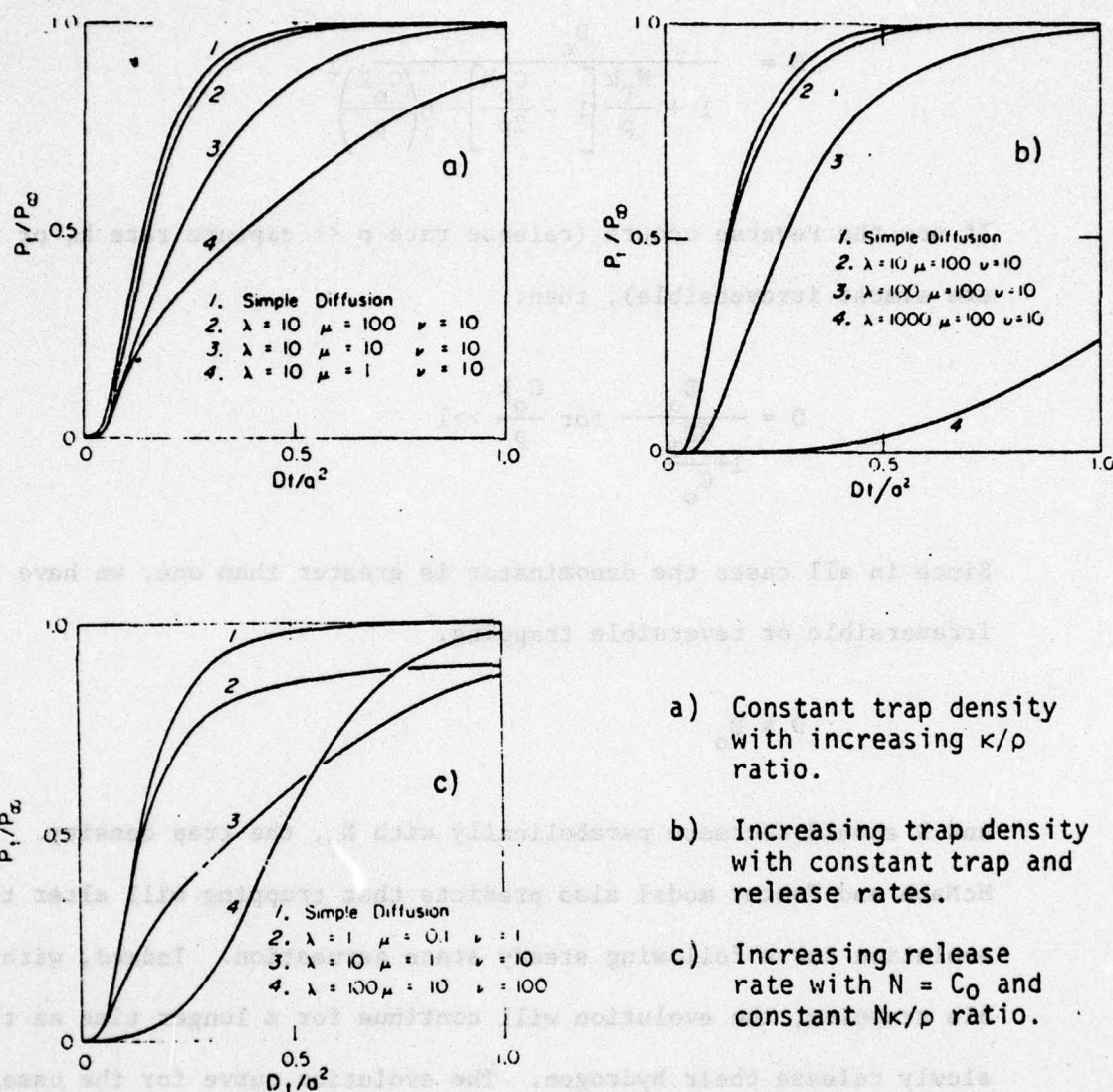


Figure 21 : Diffusion with Trapping, according to the Mc Nabb-Foster Theory (Ref. 51) and to the Caskey Pillinger study (Ref. 82).



The intermediate solution is:

$$D = \frac{D_o}{1 + \frac{N_T k}{p} \left[ 1 - \frac{C_o k}{2p} \right] + 0 \left( \frac{C_o k}{p} \right)^2} \quad (28)$$

If now the reverse occurs (release rate  $p \ll$  capture rate  $k$ , or traps are almost irreversible), then:

$$D = \frac{D_o}{1 + \frac{3N_T}{C_o}} \quad \text{for } \frac{C_o k}{p} \gg 1 \quad (29)$$

Since in all cases the denominator is greater than one, we have for irreversible or reversible trapping.

$$D < D_o$$

and  $D$  should decrease parabolically with  $N_T$ , the trap density. The McNabb and Foster model also predicts that trapping will alter the evolution curve following steady state permeation. Indeed, with reversible trapping, the evolution will continue for a longer time as the traps slowly release their hydrogen. The evolution curve for the case of irreversible trapping will more closely correspond to that for simple diffusion. (82)

### (3) Oriani's Theory (52)

This model reformulates the McNabb and Foster theory using the assumption of local equilibrium between trapped and untrapped populations of dissolved hydrogen. It assumes that there exists a trapping

reaction:

$H_{\text{diffusing}} = H_{\text{trapped}}$  having an equilibrium constant

$$K = \frac{1}{\theta_o} \left( \frac{\theta_T}{1-\theta_T} \right) \quad (30)$$

where  $\theta_o$  = fraction of lattice sites occupied (simple diffusion)

$\theta_T$  = fraction of trapping sites occupied

The apparent diffusivity  $D$  is then given by:

$$D = \frac{D_o}{1 + \frac{C_T}{C_o} (1 - \theta_T)} \quad (31)$$

which strongly resembles the equations derived by McNabb and Foster.

Here,  $C_o$  is the hydrogen concentration for normal lattice sites and  $C_T$  its concentration for trapping sites.

Again, one can see that  $D$  parabolically decreases with the amount of trapped hydrogen  $C_T$ , which itself is proportional to the number of traps per unit volume  $N_T$ , (i.e.,  $C_T = N_T \theta_T$ ). Interestingly, when  $\theta_T = 1$ ,  $D = D_o$ , or the effect of trapping disappears; this certainly is restrictive since all traps may be filled ( $\theta_T = 1$ ), but their effect may still be felt through the lattice. We shall elaborate on the reasons for this in a later section.

#### (4) Koiwa's Theory (83)

While the above models were based on the continuous diffusion approximation, Koiwa's considers the problem on an atomistic scale. In his model, Koiwa considers the case of interstitial atoms diffusing among randomly dispersed substitutional foreign atoms, which



are assumed to act as trapping centers. Assumptions are that the diffusing interstitials occupy only octahedral interstices, or only tetrahedral ones, and that only the neighboring interstices of the foreign substitutionals may act as trapping sites.

If the change in saddle point energy,  $\Delta E$ , near traps, is zero (which means that the interstitials can visit all interstices with an equal probability), then the apparent diffusivity  $D$  is given by:

$$D = \frac{D_0}{1 - 2C' + 2C'(\nu_0/\nu_1)\exp(E_B/k_B T)} \quad \text{if } \Delta E = 0 \quad (32)$$

where  $C'$  = atomic fraction of trapping centers,

$\nu_0$  = frequency factor in normal diffusion,

$\nu_1$  = frequency factor associated with release from trap,

$E_B$  = binding energy

$k_B$  = Boltzmann constant,  $T$  = temperature.

For the more general case ( $\Delta E \neq 0$ ),  $D$  is given by:

$$D = \frac{D_0}{1 - F(C') + F_1(C')/\alpha + F_2(C')/\alpha\beta + F_3(C')/\beta} \quad (33)$$

Where  $F(C')$ ,  $F_1(C')$ ,  $F_2(C')$  and  $F_3(C')$  are functions of the concentration,  $C'$ , of trapping centers, of the kind of occupancy considered and of the mean separation of trapping centers. As a matter of fact, they all increase with increasing  $C'$ . Finally,  $\alpha$  and  $\beta$  are factors which depend on  $\nu$  (frequency of diffusion,  $\nu_0$ , for capture,  $\nu_2$ , and for release,  $\nu_1$ ) and which vary exponentially with  $E_B$ ,  $\Delta E$  and  $T^{-1}$ .

As a major result, the apparent diffusivity may be shown to decrease with increasing  $E_B$ , increasing  $C'$  and decreasing  $\Delta E$

as was the case for previous models.

#### (5) The Electrical Analogy (84)

We have developed an analogy between the ability of an electrical capacitance to store electrons and that of a trapping site to store hydrogen atoms. This model is described in Appendix D in greater detail. Briefly, we assume the specimen crystal to consist of layers of atom planes, of one atom diameter thickness, and as a first approximation to be devoid of surface effects. The ability of each atom plane to trap hydrogen is represented in the analog circuit by a capacitor  $C$ ; the corresponding diffusional capacitance  $\bar{C}$  is made up of two additive terms:  $\bar{C} = \bar{C}_O + \bar{C}_T$ , where  $\bar{C}_O^*$  is the total capacitance of a plane due to ordinary trapping sites, always present in the lattice (dislocation, voids, grain boundaries, etc.), and  $\bar{C}_T$  is due to extraordinary trapping sites, such as titanium, and which provides, in our system, the major contribution to  $\bar{C}$ .

A major advantage of this analog approach is the simplicity with which one can solve for the transient output current in the electrical circuit, and its respective flux counterparts. By analogy with the electrical current in the last branch of the circuit, the permeation flux is given by:

$$\frac{J}{J_\infty} = 1 + (-1)^N e^{-t/T_N} + 2 \sum_{n=1}^{N-1} (-1)^n \exp \left[ \frac{-2DtN^2(1 - \cos \frac{n\pi}{N})}{L^2} \right] \quad (34)$$

and

$$T_N = \frac{DN^2}{4L^2}$$

---

Note :  $\bar{C}_O$  also includes lattice sites, which may be considered as very weak trapping sites.



which is valid for a step concentration boundary condition. Here,  $N$  is the total number of atomic planes and  $L$  is the thickness of the specimen. Note that the sum is not infinite as for solutions in simple diffusion, but that the number of terms is directly related to the specimen thickness. Under a step flux boundary condition, the above solution becomes:

$$\frac{J}{J_{\infty}} = 1 + \frac{1}{N} \sum (-1)^n \cot\left(\frac{2n-1}{2N} \times \frac{\pi}{2}\right) \exp\left[-\frac{2N^2Dt \left[1 - \cos\left(\frac{2n-1}{N} \times \frac{\pi}{2}\right)\right]}{L^2}\right] \quad (35)$$

The expression for the apparent diffusivity (analogous to  $1/RC$  as shown in Appendix D) is:

$$D = \frac{D_o}{1 + \frac{N_T n_T^H C_o^H}{N_o n_o^H C_T^H}} \quad (36)$$

We thus obtain a parabolic law, which agrees with the above proposed expressions for  $D$ . Here,  $N_T$  is the number of extraordinary trapping sites per volume,  $n_T^H$  = number of hydrogen atoms that may be trapped at one extraordinary site, and  $N_o$  and  $n_o^H$  are the corresponding parameters for ordinary sites;  $C_o^H$ ,  $C_T^H$  are hydrogen concentrations around lattice and trapping site, respectively. A quick check shows that if  $N_T$  or  $n_T^H$  are large compared to  $N_o$  and  $n_o^H$ , the  $nD = D_o$ , which is expected. On the other hand, if  $N_T n_T^H < N_o n_o^H$  then  $D = D_o$ . One can also see that the product  $N_T n_T^H$  is an important parameter. A larger number of traps  $N_T$  may not be sufficient to significantly decrease  $D$ ; one may also need a high trapping capacity  $n_T^H$ . On the other hand, a small number of traps  $N_T$  may be

D-A045 331

CARNEGIE-MELLON UNIV PITTSBURGH PA DEPT OF METALLURG--ETC F/G 7/4  
THE ROLE OF TRAPPING ON HYDROGEN TRANSPORT AND EMBRITTLEMENT.(U)  
JUL 77 G M PRESSOUYRE, I M BERNSTEIN

N00014-75-C-0265

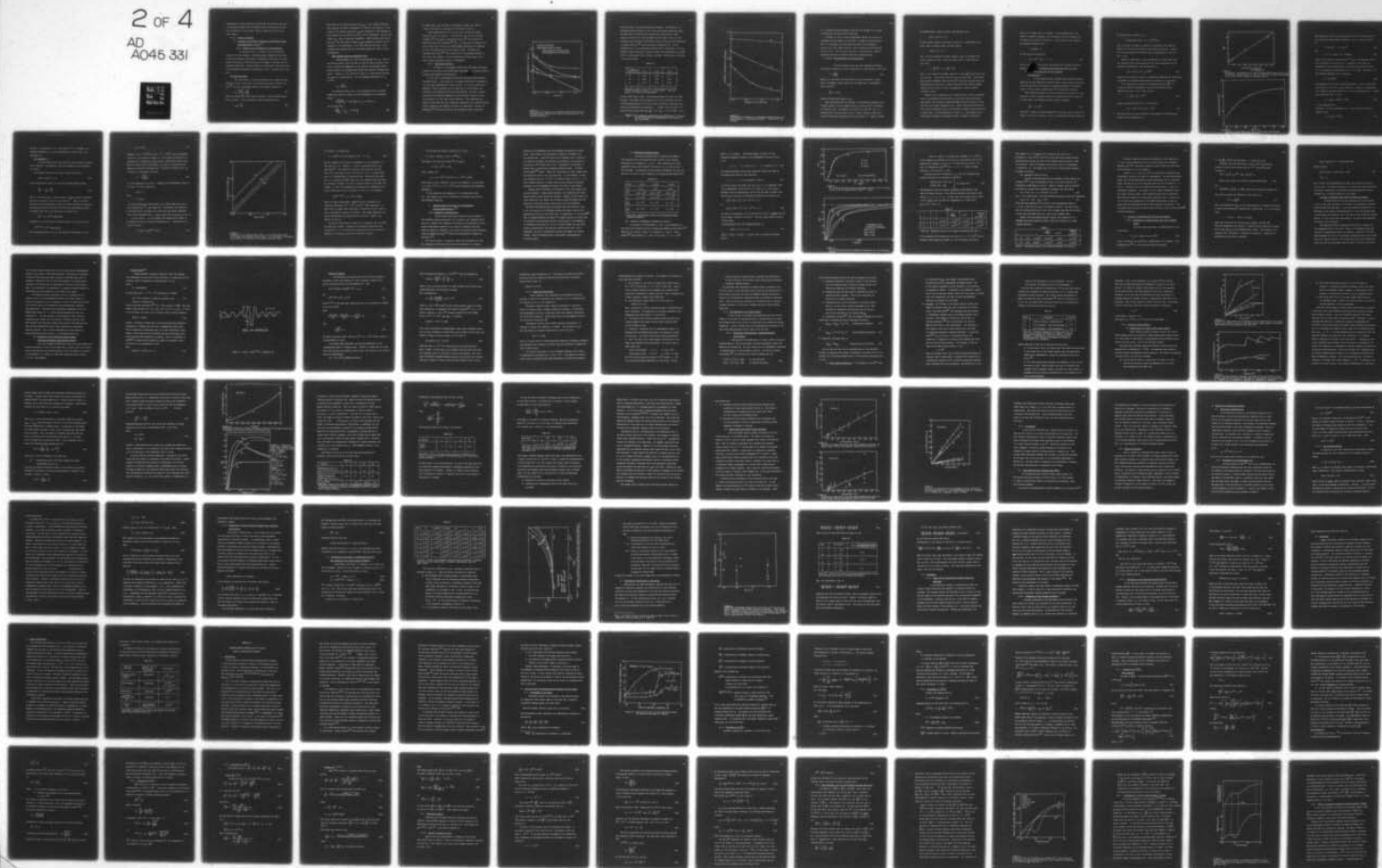
UNCLASSIFIED

TR-7

NL

2 OF 4

AD  
A045 331





compensated by a high trapping efficiency  $n_T^H$ . One may also note that our expression agrees well with McNabb-Foster's and Oriani's, except for the addition of this product feature (instead of  $N/C_0$  for the other cases).

#### E.1.c. Tests for Trapping

##### (1) Analysis of the Effect of Trapping on Diffusivity Using the McNabb-Foster's Model<sup>(51)</sup>

###### (1)(i) Methods for the Evaluation of the Diffusivity

As discussed above, a necessary, but not sufficient condition for the presence of trapping during a permeation experiment, is that the diffusion coefficient of hydrogen in the material studied must be less than  $D_0$  (the diffusivity of hydrogen in the same, but now trap-free materials). Several methods are available for the calculation of this apparent diffusivity from permeation data. The most widely used are:

##### The time lag method:

The total amount of diffusing hydrogen which passes through a membrane in time  $t$  may easily be calculated from simple diffusion theory;<sup>(85)</sup> as time  $t$  approaches infinity, this amount reduces to:

$$Q_t = \frac{DC_0}{a} \left[ t - \frac{L^2}{6D} \right] \quad (37)$$

where all symbols have their previous meaning. This expression shows that  $Q_t$  versus  $t$  has an intercept on the time axis given by:

$$t_{\text{lag}} = \frac{L^2}{6D} \quad (38)$$

This intercept is called the time lag ( $t_{lag}$ ). By a similar reasoning this time lag is found to correspond to a value of  $J/J_{\infty}$  equal to a 0.63. A plot of  $J/J_{\infty}$  versus time gives  $t_{lag}$  and, knowing "L", the thickness of the specimen, one can obtain D from the above relationship. One can also obtain  $t_{lag}$  using an electrical integrator, which directly plots  $Q_L$  versus time. One then easily obtains  $t_{lag}$  by taking the intercept of the asymptote to the obtained  $Q_L = f(t)$  curve with the time axis. Good agreement was obtained with the two methods during the course of this investigation.

#### Other Methods Using the Permeation Curve:

Another method is to use the breakthrough time,  $t_b$ . This is the fastest method, since one does not need the whole transient. Moreover, it should be independent of any internal concentration effect, since initially the hydrogen atoms should have crossed a hydrogen-free matrix. However, it may reflect the effect of a slow surface reaction and thus be an underestimate. The corresponding expression for  $t_b$  is: (68)

$$t_b = \frac{L^2}{15.3 D} \quad (39)$$

The inflection point (p.i) of the permeation curve is another method that does not require the entire permeation to be completed.

Since:

$$\left(\frac{d(J/J_{\infty})}{dt}\right)_{pi} = 5.922 \frac{D}{L^2} \text{ and } J_{p.i} = 0.2442 J_{\infty}$$

one can show that:

$$\left(\frac{dJ}{dt}\right)_{pi} \times \frac{1}{J_{p.i.}} = 24.25 \frac{D}{L^2} \quad (40)$$



In other words, once the point of inflexion is found, the value of  $J$  and of the slope at this point are sufficient to give  $D$ .

Other methods make use of the fact that  $D$  should be constant along the curve  $J/J_{\infty}$  versus  $t$ . In particular, one can use the decay transient,<sup>(68)</sup> the time to reach steady state,<sup>(85)</sup> the variation of permeation rate with thickness,<sup>(68)</sup> etc... In the case of trapping, however, because the curves do not follow simple diffusion,  $D$  is expected to vary with position on the  $J/J_{\infty}$  versus  $t$  curve. As Caskey and Pillinger have shown,<sup>(82)</sup> this variation of  $D$  with position should, in fact, give some insight as to the reversibility of the traps, and is thus a useful independent source of information.

#### (1)(ii) Experimental Results

In Figure 22, the apparent diffusivity  $D$  has been calculated, using both the time-lag and breakthrough time method for various titanium contents and successive polarizations.

In all cases, the diffusion coefficient decreases with increasing titanium content. If one takes for the normal diffusivity of hydrogen in iron the value experimentally found at wt%Ti = 0, it can be seen that  $D$  exhibits a tenfold decrease with the addition of 1.5% titanium, calculated by both methods and for both polarizations. In order to better illustrate the impressive magnitude of this decrease, Figure 23 shows the variation of  $D$  with other solute additions. This comparison can safely be made since the other permeation experiments were conducted using similar techniques and chemical solutions for permeation. Dresler and Frohberg's<sup>(66)</sup> results on Fe-Ni are not presented in this comparison,

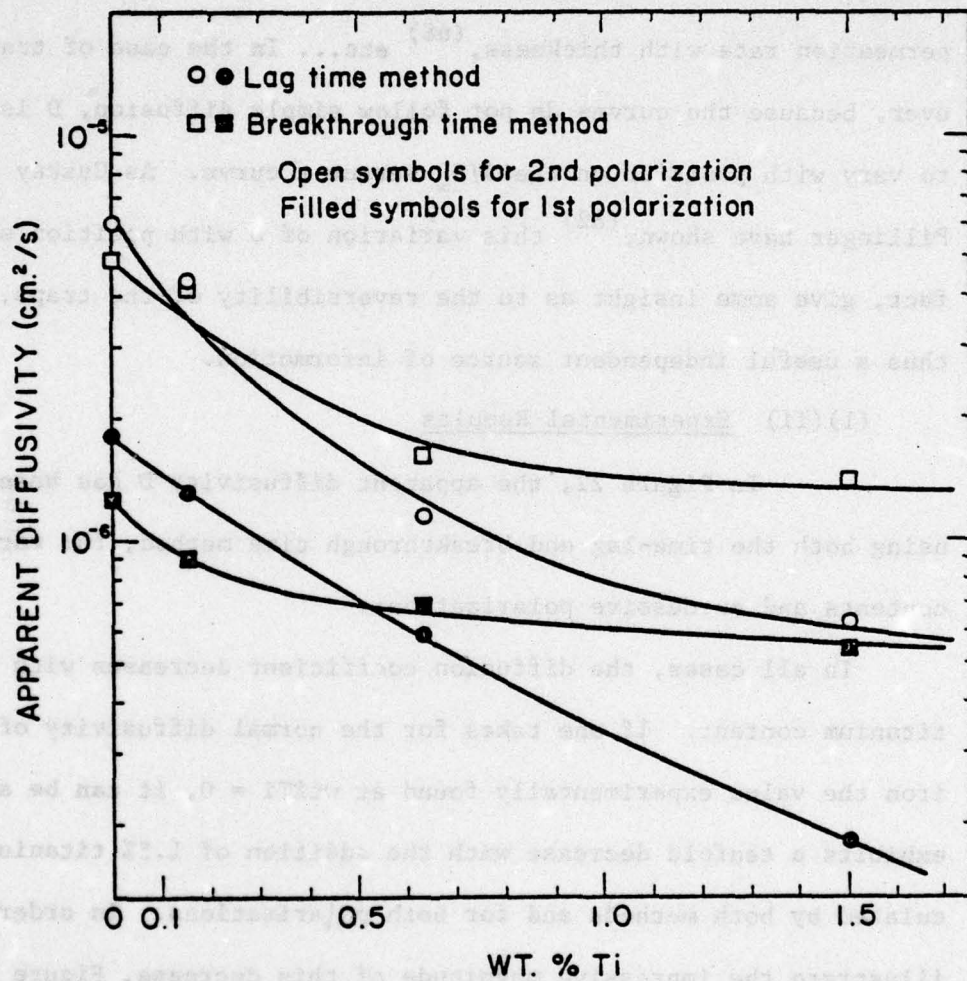


FIGURE 22.  
Variation of the Diffusivity of Hydrogen through Ferrite with Titanium Content (wt%Ti), with Order of Polarization and with the Method Employed.



since they used a gas phase permeation technique. The diffusion coefficients shown in Figure 23 for Cr and Ni have been calculated using the same time to reach half the steady state, which gives a value similar to that for the time lag method we have used. Also, our calculations used the second polarization since the first is often subjected to surface effects,<sup>(86)</sup> and irreversible trapping by TiC. If one considers each of the experimental diffusivity for wt% solute = 0 as the standard normal diffusivity, Figure 23 shows that titanium has a stronger effect in decreasing  $D^*$  than chromium or nickel. This is also illustrated in the table below:

TABLE VII

wt% solute solute	0.15	0.50	1.50
Ni	0.96	0.89	0.77
Cr	0.80	0.50	0.18
Ti	0.72	0.19	0.10

Table VII: Value of the ratio  $D$  (with solute)/ $D_0$  for various wt% additions of solute.  $D_0$  is the value for wt% solute = 0, found in each experiment.

As this table shows, 0.5wt% of titanium decreases  $D$  as much as 1.5wt% chromium. The effect of each solute on  $D$  is very consistent with the corresponding magnitude of its first order interaction coefficient (see previous thermodynamic considerations). Indeed, the more recent reference given in Table III lists  $e_{Ni}^H = -0.25$ ,  $e_{Cr}^H = -0.33$  and  $e_{Ti}^H = -1.10$ ,

\*Note : All subsequent considerations on diffusivity  $D$  will make use of the diffusivity experimentally found using the time lag method .

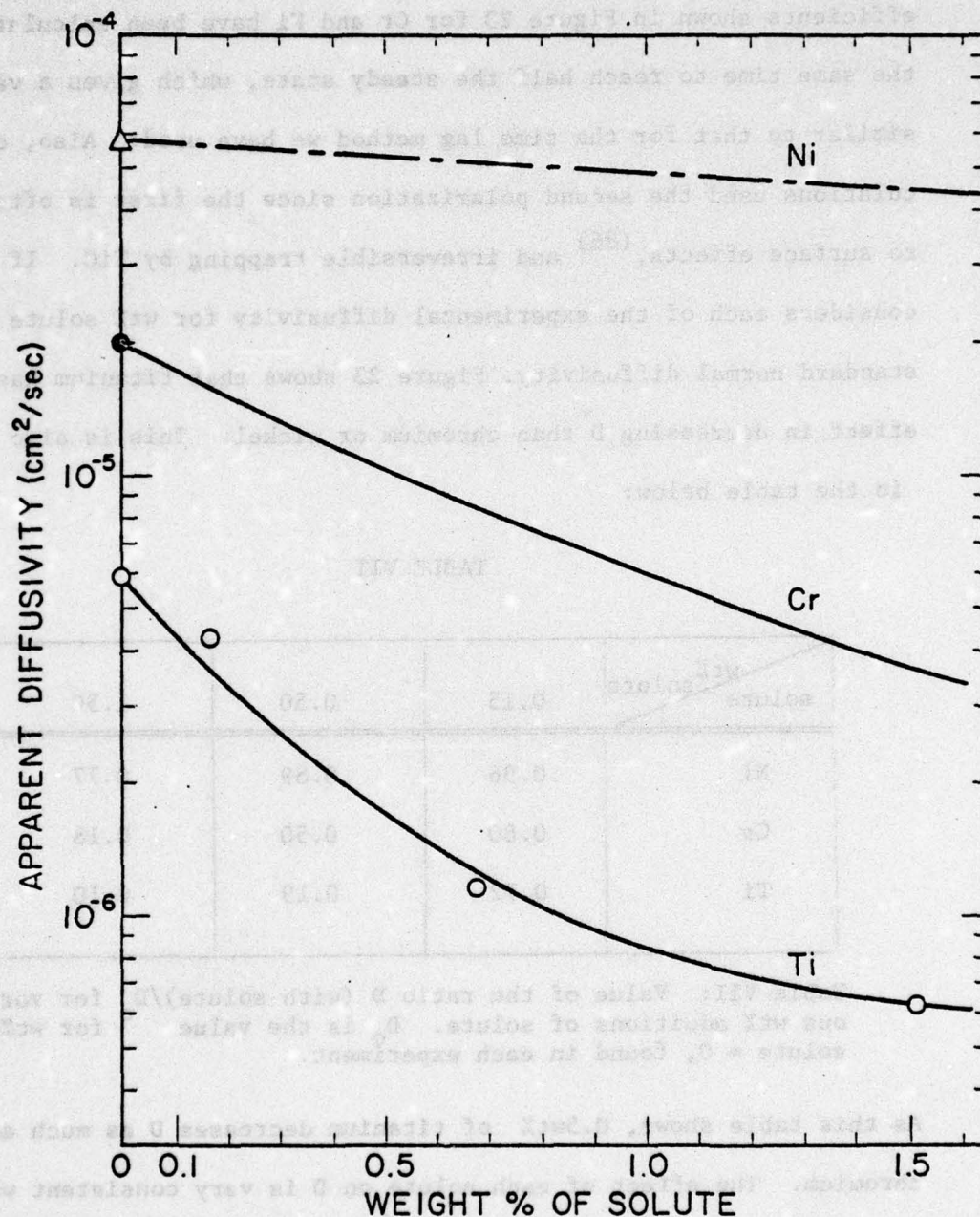


FIGURE 23.  
Variation of the Diffusivity of Hydrogen through Ferrite with  
Solute Content, in the Case of Nickel<sup>(67)</sup>, Chromium<sup>(65)</sup> and  
Titanium.



i.e., titanium has the strongest attraction for hydrogen or, in terms of diffusivity,  $D(\text{Fe-Ti}) < D(\text{Fe-Cr}) < D(\text{Fe-Ni})$ .

In Figure 22, there is some disagreement between the values of  $D$  calculated by each method, in particular, at higher titanium contents. This is in agreement with the prediction that if the permeation curves do not obey simple diffusion, then  $D$  should vary with position (on  $J/J_\infty$  vs  $t$ ). The fact that this effect is greater with 1.5wt% Ti reinforces the idea of titanium being the trapping species.

(1)(iii) The Definition of a Titanium Trap:

We have previously seen that when trapping was present, the apparent diffusivity could be expressed by a relationship of the form:

$$D = \frac{D_o}{1 + KN_T} \quad (41)$$

where  $D_o$  is the normal lattice diffusivity,  $N_T$  the density of traps, and  $K$ , a parameter, which varies with the model used. Consequently, a plot of  $D_o/D$  as:

$$\frac{D_o}{D} = 1 + KN_T \quad (42)$$

should be linear with respect to  $N_T$ .

Since the diffusivity was observed to experimentally decrease with titanium content, we will assume that  $N_T$  is related to  $N^{\text{Ti}}$ , the density of titanium traps. The simplest way would be to take  $N^{\text{Ti}} = N_T$ , i.e., consider each Ti atom as being a trap. However, doing so would imply certain restrictions concerning the trap occupancy,  $n$ . Indeed, consider

the McNabb-Foster trapping reaction (see Equation (26)):

$$dn/dt = kC(1-n) - pn$$

If the release constant  $p$  was equal to zero (i.e., irreversible trapping), then, at steady state, one would obtain:

$$dn/dt = 0 \Rightarrow n = 1$$

Thus, for this idealized trapping situation, only one hydrogen atom may be trapped per site. If  $N_T$  was taken as  $N^{Ti}$ , a 100% occupancy would mean:

$$n = n_H^{Ti} / N^{Ti} = 1 \Rightarrow n_H^{Ti} = N^{Ti}$$

that is, the density of hydrogen atoms on Ti sites ( $n_H^{Ti}$ ) would equal that of the sites. This clearly does not have to be the case. Since hydrogen occupies octahedral sites in ferrite<sup>(3)</sup> and since titanium atoms are substitutionals, there are at least 6 potential first nearest neighbor trapping sites around a Ti atom (corresponding to the six nearest octahedral sites).

However, once a hydrogen atom is trapped at one of these octahedral sites, the remaining five sites may not trap with similar efficiency. More likely, the reversibly trapped hydrogen atom will partially occupy more than one nearest octahedral site, thereby reducing the probability for a second diffusing H atom to be reversibly trapped by this particular titanium atom. If this probability is high, i.e., the trapped H atom equivalently occupies all octahedral sites, a single Ti atom may be



said to be a single trap for hydrogen. If the probability is low, however, continued trapping is still effective, and the occupancy of a single Ti atom may be as high as 6. In any case, we will consider the maximum occupancy to be:

$$1 \leq n(\text{max}) < 6$$

so that  $N_T$  may be defined as:

$$N_T = z N^{\text{Ti}} \quad \text{with } 1 < z < 6 \quad (43)$$

We can then define a trap due to the presence of titanium in ferrite as one of nearest octahedral sites associated with a Ti atom.

(c) Values obtained from this analysis:

The Ratio  $k/p$ :

If the assumption that individual solid solution titanium atoms are the most important reversible trap is valid, then as discussed, a plot of  $D_o/D$  versus the density of titanium atoms per  $\text{cm}^3$  should be linear, since  $N_T$  varies linearly with  $N^{\text{Ti}}$  (see Equation 43 above).

This evidently assumes that the distribution of titanium in solid solution in ferrite remains uniform as discussed previously (Chapter I). In other words, the following relation should be obeyed:

$$\frac{D_o}{D} = a + b N^{\text{Ti}} \quad (44)$$

where  $N^{\text{Ti}}$  = number of titanium atoms/ $\text{cm}^3$  in the alloy, and "a" should be close to 1 if the fit is good. For  $D_o$ , the experimental value found for

D in Ferrovac E, was used, i.e.,

$$D_o \text{ (from this work)} = 6.1 \times 10^{-6} \text{ cm}^2/\text{sec}$$

$D_o/D$  is plotted in Figure 24, using D's calculated by the time lag method for the second polarization (see Figures 22 and 23). Values of N are the densities of titanium atoms corresponding to 0.15, 0.63 and 1.5 wt%.

Figure 24 shows that a linear relationship is obeyed supporting the assumption that titanium atoms are the traps responsible for the decrease in diffusivity. The relationship is:

$$D_o/D = 0.89 + 6.26 \times 10^{-21} N_{Ti} \quad (45)$$

Because of the obtained linearity, information concerning the distribution of hydrogen in the matrix when titanium is present can be obtained.

If we assume that the traps are sparingly occupied ( $\frac{C_o k}{p} \ll 1$ , as will be verified subsequently) then the McNabb-Foster model Equation (42) give K as  $K = k/p$ , so that

$$b = z \frac{k}{p} = 6.26 \times 10^{-21} \quad (46)$$

Using inequality(43) above for z, one obtains:

$$1.04 \times 10^{-21} < k/p \leq 6.26 \times 10^{-21} \quad (47)$$

The ratio of  $k/p$  is thus a function of the number of traps considered (since it is a function of z).



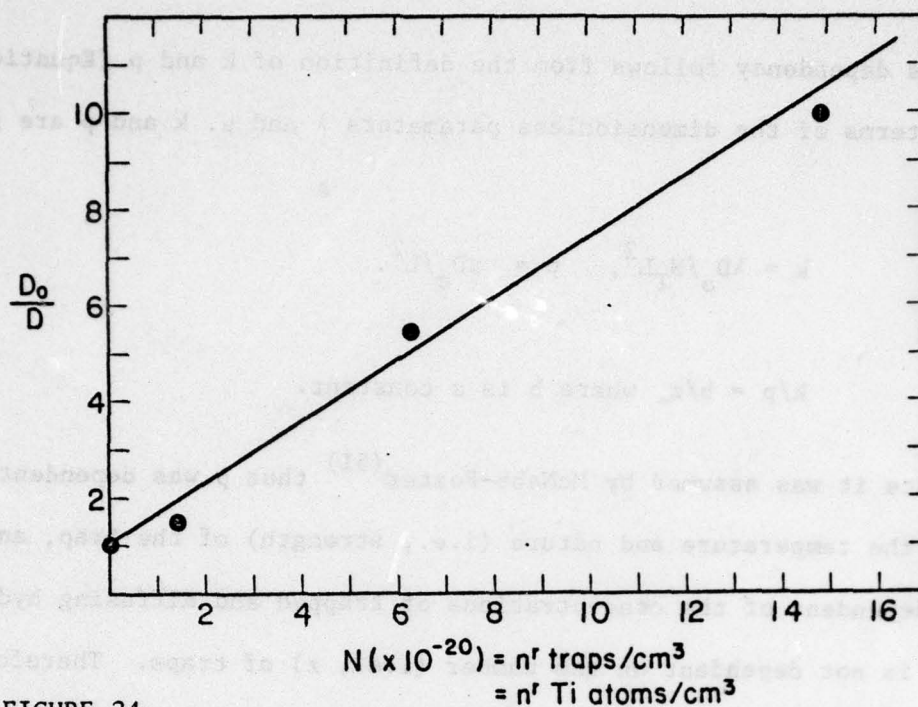


FIGURE 24.

Experimental Verification of a Linear Relationship Existing between  $D_0/D$  (diffusivity through Ferrovac E over the diffusivity through a particular Fe-Ti alloy) and the Density of Titanium Atoms  $N$ .

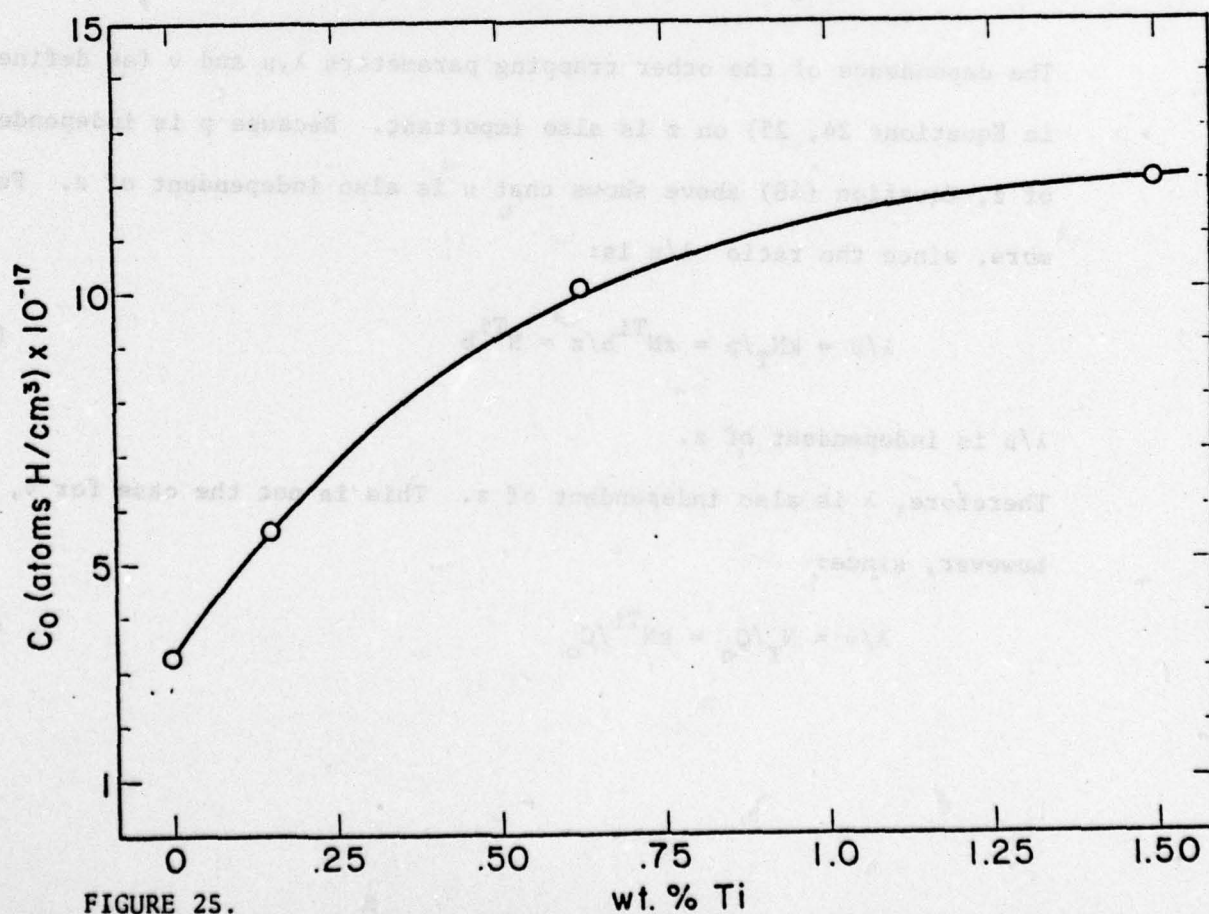


FIGURE 25.

wt. % Ti  
Variation of the Steady State Value of the Input Side Hydrogen Concentration ( $C_0$ ) with Titanium Content.

This dependency follows from the definition of  $k$  and  $p$  (Equation 26). In terms of the dimensionless parameters  $\lambda$  and  $\mu$ ,  $k$  and  $p$  are given by,

$$k = \lambda D_o / N_T L^2, \quad p = \mu D_o / L^2. \quad (48)$$

and

$$k/p = b/z \quad \text{where } b \text{ is a constant.} \quad (49)$$

Since it was assumed by McNabb-Foster<sup>(51)</sup> that  $p$  was dependent solely on the temperature and nature (i.e., strength) of the trap, and independent of the concentrations of trapped and diffusing hydrogen, it is not dependent on the number (i.e.,  $z$ ) of traps. Therefore,  $k$  is the parameter dependent on  $z$ , varying as:

$$k = \lambda D_o / z N^{Ti} L^2. \quad (50)$$

The dependence of the other trapping parameters  $\lambda, \mu$  and  $\nu$  (as defined in Equations 24, 25) on  $z$  is also important. Because  $p$  is independent of  $z$ , Equation (48) above shows that  $\mu$  is also independent of  $z$ . Furthermore, since the ratio  $\lambda/\mu$  is:

$$\lambda/\mu = k N_T / p = z N^{Ti} b / z = N^{Ti} b \quad (51)$$

$\lambda/\mu$  is independent of  $z$ .

Therefore,  $\lambda$  is also independent of  $z$ . This is not the case for  $\nu$ , however, since:

$$\lambda/\nu = N_T / C_o = z N^{Ti} / C_o \quad (52)$$



Because  $\lambda$  is independent of  $z$ ,  $v$  will depend on  $z$ . In summary, the trapping parameters  $p$ ,  $\lambda$ ,  $\mu$  are independent of  $z$ , while  $k$  and  $v$  are dependent on  $z$ .

The occupancy  $n$ :

From the limits set on the ratio  $k/p$ , other values of interest may be computed. In particular, the trap occupancy may be calculated as follows:

The trapping reaction at the input surface is given by:

$$dn/dt = kC_o(1-n) - pn \quad (53)$$

At the steady state  $dn/dt = 0$ , and the following relation holds:

$$\frac{C_o k}{p} = \frac{n}{1-n} = \frac{bC_o}{z} \quad (54)$$

where  $n$ , as we have seen, is the fraction of traps occupied by hydrogen and  $k/p$  is the slope of the plot  $D_o/D$  versus  $N_{Ti}$ . Thus, in order to evaluate  $n$ , the concentration  $C_o$  has to be known; this may be achieved by using Equation (16) and the fact that from these experimental results, the steady state flux  $J_\infty$  for Ferrovac E was found to be:

$$J_\infty^{Fe} = 2.3 \times 10^{13} \text{ atoms/cm}^2 \text{ sec}$$

Furthermore,  $J_\infty$  increased with titanium content, up to (for Fe-1.5Ti)

$$J_\infty^{Fe-1.5Ti} = 10^{14} \text{ atoms/cm}^2 \text{ sec}$$

The corresponding value of  $C_o$  is then obtained from Equation (16) as:

$$C_o = J_{\infty} L / D_o \quad (55)$$

Taking  $D_o = 6.1 \times 10^{-6} \text{ cm}^2/\text{sec}$  and  $L = 7.6 \times 10^{-2} \text{ cm}$ , the corresponding values of  $C_o$  are plotted on Figure 25. The hydrogen concentration  $C_o$  increases with increasing titanium content (about twice as much hydrogen in Fe-1.5Ti, than in Fe-0.15Ti). This was to be expected from a negative interaction coefficient  $e_H^{\text{Ti}}$ . According to Equation (54), the occupancy  $n$  is expressed as follows:

$$n = \frac{bC_o/z}{1+bC_o/z} \quad (56)$$

$n$  is thus dependent on  $C_o$  and  $z$ . Judging by the experimental values of  $b$ ,  $C$  and  $z$ , it may be seen that:

$$bC_o/z \ll 1.$$

Then:

$$n = bC_o/z$$

$n$  is then approximately proportional to  $C_o$ , which means that  $n$  will also increase with  $N^{\text{Ti}}$  (see Figure 25). Furthermore, the occupancy  $n$ , as defined here by the number of H atoms ( $n_H$ ) per nearest octahedral site, varies inversely with  $z$ . These results are illustrated in Fig. 26.

On the contrary, if the occupancy was defined as the number of H atoms per Ti atom, it would be independent of  $z$ . Indeed, with the first definition:

$$n = n_H / N_T = n_H / z N^{\text{Ti}} = bC_o/z \quad (57)$$



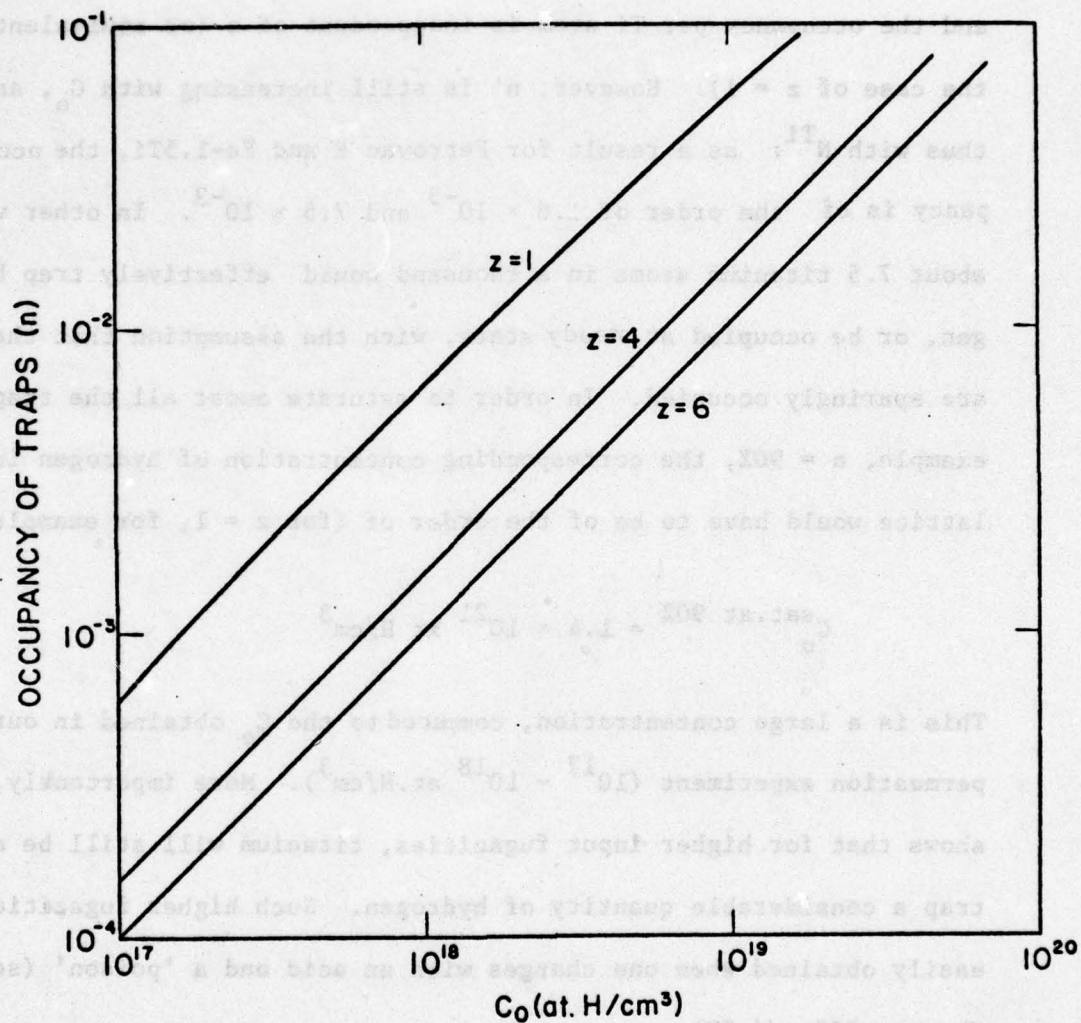


FIGURE 26.  
Occupancy ( $n$ ) of Titanium Traps Versus  $C_0$ , the Steady State Value of the Input Side Hydrogen Concentration.  $z$  is the Number of Octahedral Sites around a Ti Atom that are Considered Potential Traps.

If, however,  $n$  is defined as:

$$n' = n_H / N^{Ti}, \text{ then with Equation (57): } n' \approx b C_O. \quad (58)$$

and the occupancy per Ti atom is independent of  $z$  (or equivalent to the case of  $z = 1$ ). However,  $n'$  is still increasing with  $C_O$ , and thus with  $N^{Ti}$ : as a result for Ferrovac E and Fe-1.5Ti, the occupancy is of the order of  $1.8 \times 10^{-3}$  and  $7.5 \times 10^{-3}$ . In other words about 7.5 titanium atoms in a thousand would effectively trap hydrogen, or be occupied at steady state, with the assumption that the traps are sparingly occupied. In order to saturate almost all the traps, for example,  $n = 90\%$ , the corresponding concentration of hydrogen in the lattice would have to be of the order of (for  $z = 1$ , for example):

$$C_O^{\text{sat.at 90\%}} = 1.4 \times 10^{21} \text{ at H/cm}^3$$

This is a large concentration, compared to the  $C_O$  obtained in our permeation experiment ( $10^{17} - 10^{18} \text{ at.H/cm}^3$ ). More importantly, it shows that for higher input fugacities, titanium will still be able to trap a considerable quantity of hydrogen. Such higher fugacities are easily obtained when one charges with an acid and a 'poison' (see Chapter III and IV).

The above calculations are based on the assumption that the traps are sparingly occupied. Although the calculations agree with this hypothesis of  $n \ll 1$ , one should also demonstrate that the reverse assumption  $n \approx 1$  does not also lead to realistic results.



If the traps are heavily occupied ( $n \approx 1$ ) then:

$$D = D_0 / (1 + 3N_T / C_0) = D_0 / (1 + 3zN^{T1} / C_0) \quad (59)$$

The slope of the plot  $D_0/D$  versus  $N^{T1}$  now gives:

$$b = 6.26 \times 10^{-21} = 3z/C_0 \quad (60)$$

and  $C_0$  ranges from:

$$C_0 = 4.8 \times 10^{20} \text{ at.H/cm}^3 \text{ to } 2.8 \times 10^{21} \text{ at.H/cm}^3$$

This clearly is not a realistic value if one compares it to the values  $C_0 = 3.28 \times 10^{17}$  or  $C_0 = 1.2 \times 10^{18} \text{ at.H/cm}^3$  obtained in the permeation experiment.

It thus seems that the assumption of  $n \ll 1$  holds better than  $n \approx 1$ . This supports the use of titanium as an innocuous trap even for high hydrogen fugacities.

## 2. Analysis Based on the Shape of the Transients,

Following McNabb-Foster: <sup>(51)</sup>

### (2)(i) Qualitative considerations:

We have briefly mentioned previously that the shape of the transients yields information as to whether or not trapping occurs, and if so, whether such trapping is reversible or irreversible in nature. Typical experimental permeation and evolution transients have been shown in Figures 15 through 19, and we shall now analyze these transients using the McNabb and Foster <sup>(51)</sup> model and the approach of Caskey and Pillinger. <sup>(82)</sup>

The latter authors, as expected, showed that increasing the ratio  $k/p$  (trapping rate/release rate) and the trap density,  $N_T$  caused a

decrease in the permeation rate and prolonged the approach to steady state. These effects are illustrated in Figures 15 through 19 for all polarizations. Since the nature of the supposed trap, titanium is not expected to change, this decrease is equivalent to an increase in trap density ( $N^{\text{Ti}}$ ) rather than in  $k/p$ . Furthermore, the approach to steady state is slower with increasing titanium content. As Caskey and Pillinger<sup>(82)</sup> state: "where the trap density is large, steady state is reached only after a very long time and....is very gradual, so that the permeation rate at  $\tau = Dt/L^2 = 5$  is nearly equal to that at  $\tau = 10$ ." Such a gradual approach to steady state has been observed constantly throughout all our experiments, no matter the state of the surfaces.

Trapping should also affect the evolution curves, once steady state has been achieved. Unlike simple diffusion, the permeation and transposed evolution curves should not coincide. Figures 16 and 18 show that these predictions are obeyed; the evolution curves are faster than the permeation curves and approach steady state only very gradually.

Additional information from the evolution curves is difficult since we are now seeing only the hydrogen leaving the output side and thus, ignoring any flux out of the input side. In particular, it can be shown<sup>(87)</sup> that for simple diffusion the amount of hydrogen leaving the output side is one-third the total amount stored at steady state in the membrane; the remaining two-thirds are, in fact, leaving through the input side. However, qualitatively, the evolution curves do show that, as for permeation, the rate of desorption is slower the higher the titanium content. This is consistent with a trap density increasing with titanium content.



(2) Quantitative Considerations:

As we have discussed before, analyzing the shape of the transients with the Caskey-Pillinger computer study requires knowledge of the parameters  $\lambda$ ,  $\mu$  and  $\nu$ . Some restrictions on these parameters exist, mainly because the values of  $C_o$ ,  $N_T$  and the ratio  $k/p$  are known. In particular, with the help of Equations (51) and (52) the ratio  $\lambda/\mu$  and  $\lambda/\nu$  may be computed, as tabulated below (Table VIII):

TABLE VIII

Alloy	0.15Ti	0.63Ti	1.50Ti
$\lambda/\mu$	0.93	3.83	9.30
$N_T$	$1.48 \times 10^{20}$	$6.22 \times 10^{20}$	$1.48 \times 10^{21}$
$C_o$	$5.6 \times 10^{17}$	$1.0 \times 10^{18}$	$1.2 \times 10^{18}$
$\lambda/\nu$ ( $z=1$ )	$2.6 \times 10^2$	$6.2 \times 10^2$	$1.2 \times 10^3$
$\lambda/\nu$ ( $z=6$ )	$1.6 \times 10^3$	$3.7 \times 10^3$	$7.2 \times 10^3$

Table VIII: Experimental values and relationships between trapping parameters.

## (a). Analysis of Permeation transients of Alloy B:

An estimate of the parameters  $\lambda$ ,  $\mu$  and  $\nu$  and consequently of the capture and release rates may be made using Caskey and Pillinger's<sup>(82)</sup> tables of  $J/J_\infty$  versus  $\tau$ , where  $\tau$  is defined as  $\tau = D_o t/L^2$ . These authors<sup>(82)</sup> used values of  $\lambda$ ,  $\mu$  and  $\nu$  of the form:  $\lambda$ ,  $\mu$  or  $\nu = 10^{+n}$

where  $n$  is an integer. From their tables, the ratio of their analytical parameters closest to our experimental values are found to be

$$\lambda/\mu = 1; \quad \lambda/v = 100 \text{ if } z = 1; \quad \lambda/v = 1000 \text{ if } z = 6 \quad (61)$$

The computer-generated curve whose parameters matched the same relationships was found for the conditions

$$\lambda_1 = \mu_1 = 1, \quad v_1 = 0.01 \text{ as shown in Figure 27} \quad (62)$$

It will be noticed that while the ratio  $\lambda_1/\mu_1 = 1$  is reasonably close to the experimental value of 0.93, the ratio  $\lambda_1/v_1 = 100$  is quite different from the experimental value of 260 and 1600, see Table VIII. The fit can be improved by adjusting  $v_1^*$ , which will vary with  $z$  as:

$$\lambda_1/v_1^* = 260 \Rightarrow v_1^* = 3.8 \times 10^{-3} \text{ if } z = 1$$

or

$$\lambda_1/v_1^* = 1600 \Rightarrow v_1^* = 6.2 \times 10^{-4} \text{ if } z = 6 \quad (63)$$

The effect of decreasing  $v$  on the theoretical curve is a slight lowering of the latter portion of the curve. This is a small effect as demonstrated below:

In dimensionless form, the trapping equation is:

$$dw/d\tau = \lambda u - \mu w - v u w \quad (64)$$

where  $u = C/C_0$ ,  $w = N_T/C_0$ ,  $\tau = D_0 t/a^2$ , with all symbols as defined before.



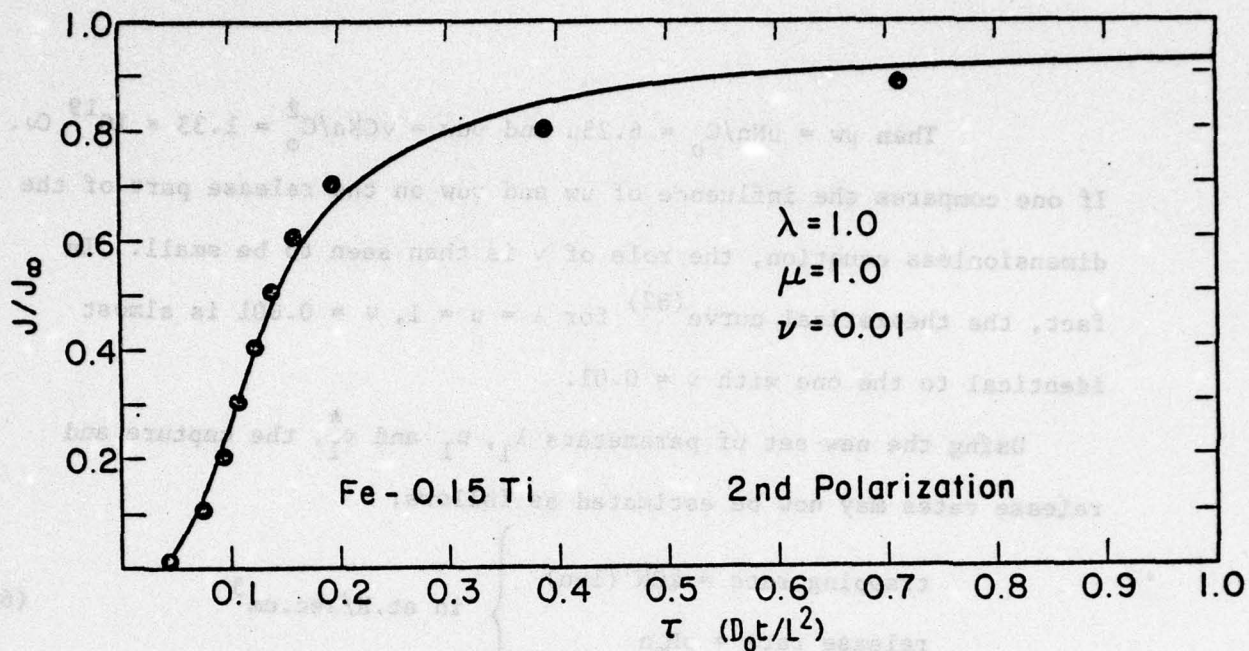


FIGURE 27.

Fit of the Second Polarization Permeation Transient of Alloy B (black circles) with the McNabb-Foster Theory<sup>(51)</sup> (line).

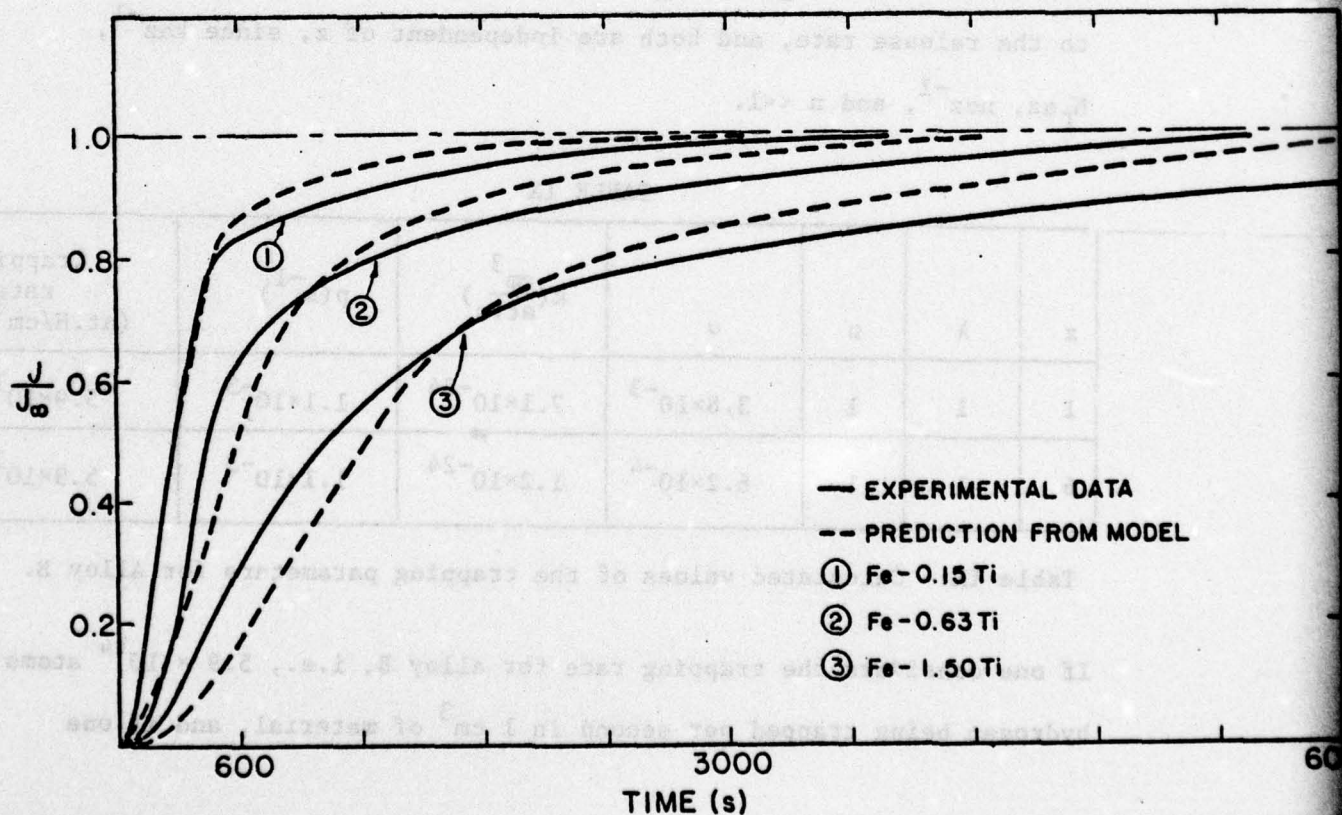


FIGURE 28.

Fit of Second Polarization Permeation Transients with the Electrical Analogy.

$$\text{Then } \mu w = \mu N n / C_0 = 6.25 \mu \text{ and } v u w = v C N n / C_0^2 = 1.33 \times 10^{19} C v.$$

If one compares the influence of  $\mu w$  and  $v u w$  on the release part of the dimensionless equation, the role of  $v$  is then seen to be small. In fact, the theoretical curve<sup>(82)</sup> for  $\lambda = \mu = 1$ ,  $v = 0.001$  is almost identical to the one with  $v = 0.01$ .

Using the new set of parameters  $\lambda_1$ ,  $\mu_1$  and  $v_1^*$ , the capture and release rates may now be estimated as follows:

$$\left. \begin{array}{l} \text{trapping rate} = k C N (1-n) \\ \text{release rate} = p N_T n \end{array} \right\} \text{ in at.H/sec.cm}^3 \quad (65)$$

The parameters  $k$  and  $p$  are readily calculated, using Equation (48)

Table IX presents results of calculations performed using steady state values, i.e.,  $C = C_0$ ,  $n = n_s$ . In this case, the trapping rate is equal to the release rate, and both are independent of  $z$ , since  $k a z^{-1}$ ,  $N_T a z$ ,  $n a z^{-1}$ , and  $n \ll 1$ .

TABLE IX

$z$	$\lambda$	$\mu$	$v$	$k(\frac{\text{cm}^3}{\text{at.s}})$	$p(\text{s}^{-1})$	Trapping rate (at.H/cm <sup>3</sup> .s)
1	1	1	$3.8 \times 10^{-3}$	$7.1 \times 10^{-24}$	$1.1 \times 10^{-3}$	$5.9 \times 10^{14}$
6	1	1	$6.2 \times 10^{-4}$	$1.2 \times 10^{-24}$	$1.1 \times 10^{-3}$	$5.9 \times 10^{14}$

Table IX: Calculated values of the trapping parameters for Alloy B.

If one considers the trapping rate for alloy B, i.e.,  $5.9 \times 10^{14}$  atoms of hydrogen being trapped per second in  $1 \text{ cm}^3$  of material, and if one



one compares it to the density of Ti atoms in this alloy, i.e.,  
 $N(\text{alloy B}) = 1.48 \times 10^{20} \text{ at.Ti/cm}^3$ , we find that few Ti atoms actively participate at any unit of time in the trapping reaction (about 4 atoms in a million). This is consistent with the fact that Ti is supposedly a reversible, i.e., low energy trap, and that its steady state occupancy is going to be small.

(b) Analysis of alloy C and  $D_2$

Because of the particular set of parameters used by Caskey and Pillinger,<sup>(82)</sup> it was not possible to find a curve that would fit the transients corresponding to alloy C. However, results could be obtained for alloy  $D_2$ , because the experimental parameters have the ratios:

$$\lambda/\mu = 9.30, \lambda/\nu = 1.2 \times 10^3 \text{ and } 7.2 \times 10^{-3} \quad (66)$$

for  $z = 1, 6$ , respectively, and the following analytical ratios were compatible:

$$\lambda_1/\mu_1 = 10 \text{ and } \lambda_1/\nu_1 = 10^{-3}. \quad (67)$$

Using the same technique as for alloy B, the corresponding values of  $\lambda$ ,  $\mu$  and  $\nu$ , and thus of  $k$  and  $p$  are listed in Table X. One will notice that the trapping efficiency of Fe-1.5Ti is higher than that of Fe-0.15Ti, as seen from the higher values of  $\lambda$  and of the trapping rates.

Indeed, with increasing titanium content, the probability of a hydrogen atom being trapped increases, while its probability of being released decreases.

TABLE X

$z$	$\lambda$	$\mu$	$\nu$	$k(\frac{\text{cm}^3}{\text{at.s}})$	$p(\text{s}^{-1})$	Trapping rate (at.H/cm <sup>3</sup> )
1	8.7	0.93	$6.2 \times 10^{-4}$	$6.6 \times 10^{-24}$	$1 \times 10^{-3}$	$1.2 \times 10^{16}$
6	8.7	0.93	$10 \times 10^{-4}$	$1.1 \times 10^{-24}$	$1 \times 10^{-3}$	$1.2 \times 10^{16}$

Table X: Calculated values of the trapping parameters for alloy  $D_2$ .

The major reason one should have confidence in this analysis of  $\lambda$ ,  $\mu$  and  $\nu$  and the quality of the fit is that since  $D_0/D$  is linearly dependent upon  $N^{Ti}$ , this makes titanium the most likely trap and allows the calculation of  $\lambda/\mu$ ,  $\lambda/\nu$ ,  $N_T$  and  $C_0$ .

Because  $\lambda$ ,  $\mu$ ,  $\nu$ ,  $N_T$  and  $C_0$  have to obey specific relations, this considerably restricts the scope of investigation. In other experimental cases, such as when dislocations or grain boundaries are the considered traps, the value of  $N_T$  is not precisely known nor are the value of  $\lambda$ ,  $\mu$ , and  $\lambda/\nu$ . One must try to fit analytical relations with  $\lambda$ ,  $\mu$  and  $\nu$  as adjustable parameters. As a matter of fact, several theoretical curves may exhibit the same shape, while having different sets of parameters. This could not happen in our particular restrictive case. Further, one of the underlying assumptions of the McNabb-Foster model is that the traps should be homogeneously distributed throughout the lattice. This is clearly more the case for solute atoms such as Ti, than for dislocations<sup>(88)</sup> or grain boundaries.

### (3) Analysis of Permeation Data Using Other Theories

#### (3)(i) Equivalence of theories other than that of McNabb-Foster

As we have seen previously, all expressions of  $D$  are of the form:

$$D = D_0 / (1 + KN_T) = D_0 / (1 + bN^{Ti}) \quad (68)$$

$K$  has a different, but equivalent, significance in all theories. With McNabb-Foster:<sup>(51)</sup>  $K = k/p$ ; with the electrical analogy:



$$K = n_T^H C_O^H / N_O n_O^H C_T^H; \text{ and with Oriani: } K = \theta_T / (1 - \theta_T) \theta_O N_O.$$

Comparing first the Nabb-Foster's theory with the electrical analogy, we notice that one may take  $N_T = N^{Ti}$ , since  $n_T^H$  already contains  $z$ :

$$\text{Since } N_O n_O^H \approx C_O, N^{Ti} \approx N_T / z \text{ and } n_T^H \approx nz$$

$$N_T k/p = N_T C_O k/C_O p = N_T n/C_O (1-n) \text{ using McNabb-Foster,} \quad (69)$$

and

$$n_T^H C_O^H N^{Ti} / N_O n_O^H C_T^H = N_T n C_O^H / C_O C_T^H \text{ with the electrical analogy} \quad (70)$$

Thus, the two models are identical in this result if:

$$1/1-n \approx C_O^H / C_T^H \quad (71)$$

where (see Appendix D)  $C_{H,T}^O$  are the concentrations of hydrogen surrounding a normal and extraordinary trapping site, respectively. In a low occupancy case:

$$1/1-n \approx 1 \quad \text{since } n \text{ is small.}$$

then, this would mean for the electrical analogy, that  $C_H^O = C_T^H$ .

With this assumption, the values of  $n$  deduced from the electrical analogy will be the same as for the McNabb-Foster's model. The validity of the assumption  $C_H^O = C_T^H$  however, is difficult to ascertain. Comparing the McNabb-Foster with Oriani's approach:

$$N_T k/p = N_T n/C_o (1-n) \quad \text{as previously seen}$$

and with Oriani:

$$N_T \theta / (1 - \theta_T) \theta_o N = N_T n / (1 - n) C_o \quad \text{since} \quad (72)$$

$$\theta_o N_o = C_o$$

Thus, Oriani's and the McNabb-Foster models are rigorously identical in this case. The electrical analogy is the only model which introduces the further consideration of different diffusing populations around a trapping site, a valuable addition to the theory.

#### Analysis of Permeation Data with the Electrical Analogy

Because Oriani does not give equations for the variations of  $J/J_\infty$  versus time, analysis of the shape of the permeation transients cannot be made from this model. As for the effective diffusivity, its expression is the same as the McNabb-Foster, so that the results based on its analysis are identical, as is the case for the electrical analogy. However, in this latter model some comments can now be made regarding the shape of the transients.

The equations derived in Appendix D were used to computer fit the experimental data, as follows: taking  $N = 50$  (higher values were found not to significantly alter the results), a value of  $D$  ( $\cong 1/RC$ ) was determined that best fit the build-up transients curve for Fe-0.15Ti. Since the titanium contents of Fe-0.63Ti and Fe-1.5Ti are respectively about four and ten times higher than Fe-0.15Ti, the value of  $RC$  found



for 0.15Ti was simply multiplied by four and ten, and the corresponding values of  $J/J_\infty$  versus  $t$  were then calculated. The results are depicted in Figure 28 and show that while a precise fit between theory and experiment is lacking for the 0.63 and 1.5Ti samples, the relative positionings of the theoretical and experimental curves are in good agreement. More importantly, the agreement is obtained by simply varying the capacitance in direct proportion to the number of Ti atoms.

The disparity between theoretical and real transients is considered a result of the oversimplifications of the model, where all traps are considered to act as capacitors. Also, the particular electrical circuitry used is not necessarily the most physically realistic (see Appendix D). Instead of three independent parameters as for the McNabb-Foster model ( $\lambda$ ,  $\mu$ ,  $\nu$ ) this analogy possesses only one; the capacitance  $C$ . The real strength of this analogy is that it gives a reasonably good estimate for the effective diffusivity and the trapping strength (see interaction energy calculations), much more directly than with the McNabb-Foster model, which requires more complicated computer programs. Also, we shall subsequently use this analogy to study complicated surface effects in a reasonably simple way.

#### (4) Evaluation of the Interaction Energy between Titanium and Hydrogen using Different Models

Since the strongest binding force that could exist between titanium and hydrogen is that of the hydride  $TiH_2$ , an upper limit to the interaction energy  $E(Ti-H)$  may readily be given as the free energy of formation of this hydride, i.e.,  $E(Ti-H) < 0.73\bar{e}V$  (see additional details section E.1.a.(1), this chapter).

Oriani's Model <sup>(52)</sup>

Oriani proposed, as shown on Figure 29, that the trapping site represents an energy level lower than that of a normal site by the term  $\Delta E_x$ , which is bounded by an energy barrier  $E' + E_a$ .

Thus:

$$K = \exp(-\Delta E_x/RT), \quad (73)$$

We have shown that:  $K = 1.6 \times 10^3$ , which gives, at  $298^\circ\text{K}$ :

$$\Delta E_x = 4407 \text{ cal/mole} = 0.19\text{eV per octahedral site} \quad (74)$$

close to a titanium atom

Since  $E_a$  has been evaluated as <sup>(81)</sup>  $E_a = 1900 \text{ cal/mole} = 0.08\text{eV}$ . The trap depth is thus  $E(\text{Ti-H}) = E' + E_a + \Delta E_x = 0.9 + 0.08 + E' = 0.27 + E' (\text{eV})$ .  $E'$  is not known, but since it is a positive term in Oriani's analysis

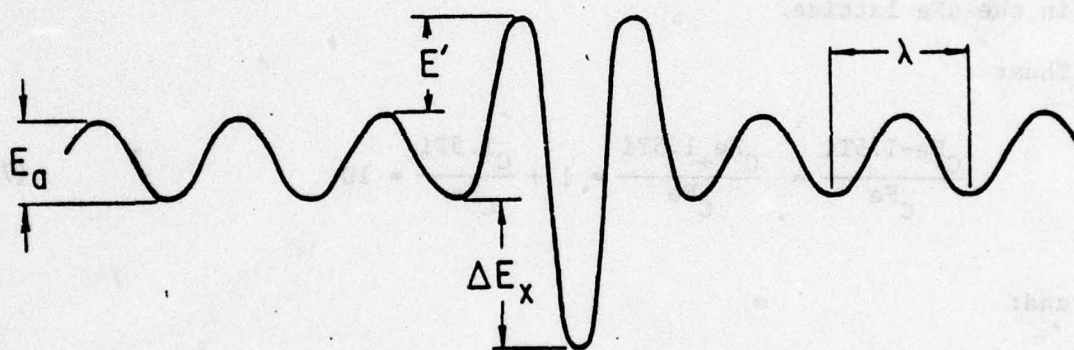
$$E(\text{Ti-H}) > 0.27\text{eV} \quad (75)$$

However, a positive  $E'$  means that a H atom would have more difficulty jumping into a trapping site than into a neighboring lattice site. This is particularly surprising since, as we have seen before, there exists a short range attraction between titanium and hydrogen, which should increase the probability of trapping. Thus, as considered by Koiwa, <sup>(83)</sup> it would be more realistic to take  $E'$  as negative, and of the order of a few hundredths of an eV.

Thus:

$$E(\text{Ti-H}) \approx 0.27\text{eV, if } E' < 0 \quad (76)$$





MODEL FOR TRAPPING SITE.

FIGURE 29. Oriani's Model<sup>(52)</sup> of a Trapping Site.

### Electrical Analogy:

The diffusivity calculated using the electrical analogy is equivalent to  $1/RC$  (see Appendix D), and by assuming a similar  $R$  for both Fe and Fe-Ti alloys (see also Appendix D): then:

$$D^{\text{Fe-1.5Ti}}/D^{\text{Fe}} = C^{\text{Fe}}/C^{\text{Fe-1.5Ti}} = 0.10 \quad (77)$$

But:

$$C^{\text{Fe-1.5Ti}} = C^{\text{Fe}} + C^{1.5\text{Ti}} \quad (78)$$

where  $C^{1.5\text{Ti}}$  is the additional capacitance due to the presence of 1.5wt%Ti in the  $\alpha\text{Fe}$  lattice.

Thus:

$$\frac{C^{\text{Fe-1.5Ti}}}{C^{\text{Fe}}} = \frac{C^{\text{Fe}} + C^{1.5\text{Ti}}}{C^{\text{Fe}}} = 1 + \frac{C^{1.5\text{Ti}}}{C^{\text{Fe}}} = 10 \quad (79)$$

and:

$$\frac{C^{1.5\text{Ti}}}{C^{\text{Fe}}} = 9 \quad (80)$$

The above calculation used a value for  $D^{\text{Fe}} = 6.1 \times 10^{-6} \text{ cm}^2/\text{sec}$ , which is our experimental  $D_0$  value.

We consider each capacitance as directly proportional to its corresponding number of trapping sites. Further, we assume that all sites other than titanium are ordinary lattice sites, and, since in a bcc lattice, there are approximately

$$N_0 = 2.6 \times 10^{23} \text{ octahedral sites/cm}^3$$



with an interaction energy  $E_a = 0.08 \text{ eV}$ <sup>(81)</sup> then (see Appendix D):

$$E(\text{Ti-H}) = \frac{C_{\text{Fe}}^{1.5\text{Ti}}}{C_{\text{Fe}}} \times \frac{\theta_o}{\theta_T} \times \frac{N_o}{N_T} \times E_a \quad (81)$$

where  $\theta_o$  and  $\theta_T$  are the fraction of sites (ordinary and titanium sites respectively) that are effectively occupied.

But, by definition:

$$\theta_o = \frac{C_o}{N_o} = \frac{2.8 \times 10^{17}}{2.6 \times 10^{23}} = 1.08 \times 10^{-6} \quad (82)$$

where  $C_o = 2.8 \times 10^{17} \text{ at.H/cm}^3$  is the value previously found for steady state permeation, in agreement with Oriani's estimate<sup>(52)</sup> of  $\theta_o = 10^{-6}$

Finally, since  $N_T = 1.48 \times 10^{21} \text{ titanium atoms/cm}^3$  for Fe-1.5wt%Ti, and  $\theta_T = 10^{-3} \rightarrow 5 \times 10^{-3}$  (see page ) we obtain:

$$E_1(\text{Ti-H}) = 0.027 \rightarrow 0.14 \text{ eV} \quad (83)$$

This value is obviously an underestimate, since other "ordinary" sites, such as grain boundaries or dislocations exist besides lattice sites, and exhibit a higher interaction energy, of the order of:

$$E'_a(\text{disloc., G.B.}) = 0.25 \text{ eV} \quad (84)$$

Using the same  $\theta_o = 10^{-6}$ , but replacing  $E_a$  by  $E'_a$  gives  $E_2(\text{Ti-H}) = 0.08 \rightarrow 0.44 \text{ eV}$ . In this case,  $N_o$  is probably less than the value taken for octahedral sites, so that this is now an overestimate. The actual value of  $E(\text{Ti-H})$  is probably between  $E_1(\text{Ti-H})$  and  $E_2(\text{Ti-H})$  since ordinary sites are a mixture of lattice sites and more powerful sites, such as

dislocations, grain boundaries, etc. In any case, the limits calculated using the electrical analogy include the value previously calculated using Oriani's model, of:

$$E(\text{Ti-H}) \leq 0.27 \text{ eV}$$

#### E.1.d. Summary and Conclusions

Strong evidence, both experimental and theoretical has been provided to support the hypothesis that titanium acts as a trapping center for hydrogen in iron at room temperature.

Theoretical evidence points toward the existence of attractive forces of various origins between titanium and hydrogen. In particular, the thermodynamic force has a magnitude larger than normally encountered for other solute additions. This follows from the large negative value of the interaction coefficient  $e_{\text{H}}^{\text{Ti}}$ .

Experimental results show a tenfold decrease in diffusivity of hydrogen in ferrite with addition of 1.5wt%Ti. The variation of  $D_0/D$  with the density of titanium atoms follows a law of the type:

$$D_0/D = a + bN_{\text{Ti}}$$

This is in accord with all reviewed existing theories on trapping, and supports the hypothesis that titanium is the most important reversible trapping species in these alloys.

The value of the slope,  $b$ , has a different meaning in each theory; its magnitude was evaluated as  $b = 6.26 \times 10^{-21}$ . This important parameter can be used in conjunction with other quantities to develop the parameter



characterizing the trapping of titanium. For example, the following results have been obtained:

a) The occupancy of the traps at steady state varies between  $3.5 \times 10^{-3}$  for Fe-0.15Ti to  $7.5 \times 10^{-3}$  for Fe-1.5Ti. This is a low occupancy situation which suggests that titanium atoms still have a significant trapping capacity. This is important for further trapping at higher input fugacities.

b) The interaction energy  $E(\text{Ti-H})$  is of the order of:

$$E(\text{Ti-H}) \approx 0.27 \text{ eV}$$

Thus, titanium has a similar trapping strength as dislocations or grain boundaries. Its importance is its high concentration and homogeneous fine distribution, in the lattice.

c) The shape of the build-up transients after several polarizations suggest that single titanium atoms constitute most of the reversible traps.

d) A good fit, consistent with all experimental results, is obtained with the McNabb-Foster model, as developed by Caskey and Pillinger. The values found for the trapping parameters  $\lambda$ ,  $\mu$  and  $\nu$  for each alloy, again suggest reversibility of the traps, and similarity with dislocations. For alloy B and  $D_2$  those values are:

$$\text{Alloy B (Fe-0.15Ti): } \lambda = \mu = 1, \quad \nu = 3.8 \times 10^{-3}$$

$$\text{Alloy } D_2 \text{ (Fe-1.5Ti): } \lambda = 8.71, \quad \mu = 0.93, \quad \nu = 0.007.$$

The fact that  $D_0/D$  was proportional to  $N^{\text{Ti}}$  allowed  $\lambda$ ,  $\mu$  and  $\nu$  to be calculated without ambiguity, in this study. Fitting

with the electrical analogy model, although less satisfactory, is also consistent with titanium solute atoms being the dominant reversible trapping species.

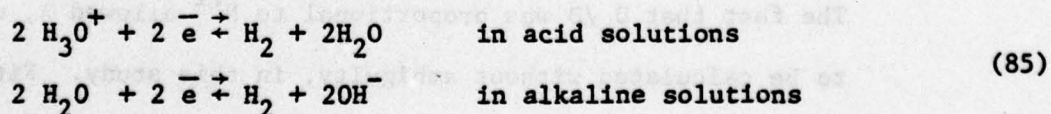
In concluding this discussion on titanium being a reversible trap in Fe-Ti alloys, it has been shown that not only do the experimental results support this idea, but that all trapping theories consistently describe the characteristic trapping features of titanium, as presented above. One can then picture titanium as a reversible trap of average trapping strength, but with great trapping capacity at high hydrogen fugacities.

#### E.2. The Possibility of a Surface Effect

In this section we consider the possibility that the previous results on the effect of titanium addition on the diffusivity of hydrogen through ferrite could be due to a particular rate controlling surface phenomenon. It will be shown that for the experimental conditions of the input side being palladium plated, this is not the case.

##### E.2.a. Theoretical Considerations: Hydrogen Discharge and Evolution

The kinetics of hydrogen entry in  $\alpha$ -iron, either by electrochemical means or from the gas phase, has been extensively studied (see Reference 89 through 98). Our main concern for our experimental conditions is hydrogen entry by electrochemical reaction. According to McBreen and Genshaw,<sup>(89)</sup> the reactions that produce hydrogen gas are:





The resulting hydrogen molecule may then discharge and be either:

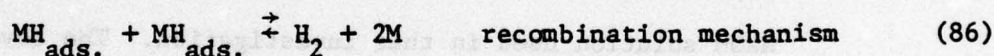
a) physically adsorbed on the metal surface; if the molecule does not dissociate and no electron transfer occurs, this step is not important for internal diffusion.

b) chemisorbed when the bond length is extended and there is partial electron transfer. This is also relatively unimportant for internal diffusion.

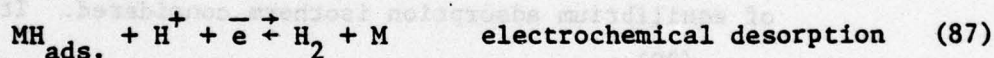
c) dissociated with each atom adsorbed on the metal surface. This is a crucial step, since now hydrogen is in a form suitable for absorption and diffusion into the lattice.

This step is described by the formalism  $MH_{ads}$ .

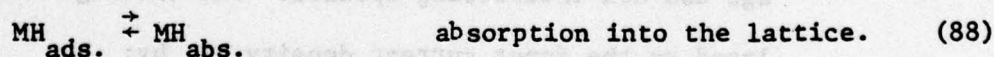
It is generally accepted<sup>(89)</sup> that the adsorbed hydrogen has two possible ways of escaping the surface (hydrogen evolution):



or



In completion, the entry step is:



One can thus see that the two characteristics of the adsorption process, coverage and free energy of adsorption, are going to be of importance in controlling hydrogen entry in the materials. Considering each in turn:

a) Free energy of adsorption: It is possible to show<sup>(89)</sup> that

by lowering the  $MH_{ads}$  bond energy, the permeation rate increases. This may be accomplished by adding specific ions to the solution (generally called "poisons"), or by treating the specimen's surface. In particular, the presence of impurities on the surface may strongly affect the free energy of adsorption, and consequently, the ease of entry and subsequent diffusion of hydrogen into the metal.

- b) Coverage: The coverage of the surface directly affects the number of hydrogen atoms that will be absorbed and diffuse, since it has been shown<sup>(90)</sup> that hydrogen must pass through an intermediate adsorbed state on the metal substrate prior to entry. This condition is valid for acid as well as alkaline solutions,<sup>(90)</sup> and in particular, for the 0.1N NaOH solution used in this investigation. The coverage,  $\theta$ , will depend on the input current density and on the kind of equilibrium adsorption isotherm considered. It has been shown<sup>(80)</sup> that for iron in a 0.1N NaOH solution, the adsorption is Langmuirean in nature, which implies low coverage and non-interacting species. The coverage is then related to the input current density,  $i$ , by:

$$\theta = Ki^{1/2}$$

When the coverage is not low, or when interactions between the adsorbed atoms is appreciable, or whenever the surface offers heterogeneous adsorption sites (different adsorption energies), other isotherms have to be considered. The difficulty in such



cases is the determination of such isotherms. We will only consider the simplest case in this development.

From the above simplified considerations, one can see that internal diffusion will dominate the adsorption process, if it is slower than all possible surface reactions. The various surface mechanisms in a number of metals have been investigated;<sup>(89)</sup> those of interest to us, Fe, Ti, Pd, are listed below, along with functional relationships describing the absorption-permeation process:

TABLE XI

Metal	Mechanisms	$J_{\infty}=f(i)$
Fe	Coupled discharge - Recombination*	$i^{1/2}$
Ti	Fast discharge - Slow electrochemical	$i^{2/3}$
Pd	Fast discharge - Slow recombination	$i-i^{1/2}$

Table XI: Functional dependence of steady state flux on input current density for metals of interest. \*Coupled discharge - recombination, means that the rates of the reverse reactions (reverse of discharge and reverse of recombination) are negligible.

Several important factors can be implied from this table:

- a) In the case of iron, the steady state flux should be proportional to the square root of the current density; this has been widely demonstrated experimentally, using both alkaline and acid solutions.<sup>(89)</sup>
- b) For both titanium and palladium, the discharge is fast and the evolution is slow. This is usually the case for elements which strongly attract hydrogen, thereby retaining it on the surface, in agreement with our previous considerations on the strength of the bond titanium-hydrogen.

Therefore, a test of the dependence of  $J_{\infty}$  versus  $i^{1/2}$  would indicate what type of adsorption-absorption mechanism is present on the input surface. It would not, however, sufficiently rule out the dominance of the surface effect over bulk diffusion as the rate controlling mechanism. To be sure that bulk diffusion controls the kinetics of hydrogen permeation through a material, supplementary tests have to be performed. Most of those tests are based on the fact that, if diffusion is rate controlling, then Fick's laws are obeyed; in particular:

$$J_{\infty} \propto L^{-1} \quad (89)$$

as was shown in Equation (16).

Both tests ( $J_{\infty} \propto i^{1/2}$  and  $J_{\infty} \propto L^{-1}$ ) will now be performed.

#### E.2.b. Tests for Surface Effects:

##### (1) Steady state flux versus input current density

Since internal trapping is known to occur, all surface effect studies have to be carried out under steady state conditions where all active traps are saturated or in equilibrium with the diffusing population, and do not play a role in the diffusion process.

Such tests were performed using both Ferrovac E iron and Fe-0.15Ti samples both of thickness  $8.5 \times 10^{-2}$  cm. The membranes were studied in both the uncoated and palladium coated condition. The results are depicted in Figures 30-31, and show the following:

- (a) The transients exhibit a humped shape for alloy B (0.15Ti), but not for Ferrovac E, when the membranes are not coated with palladium on the input side.



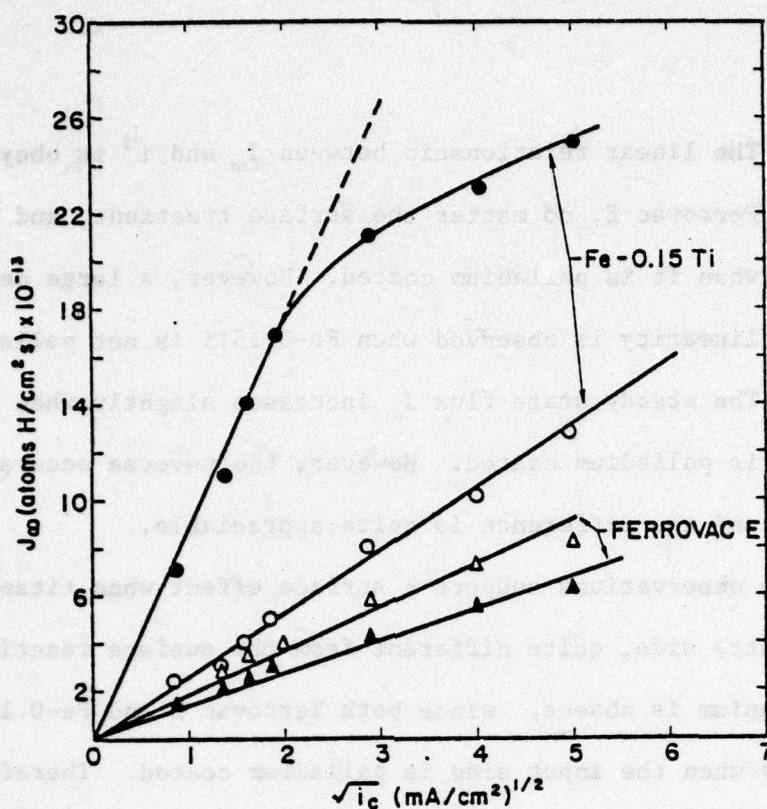


FIGURE 30.  
Variation of Steady State Flux of Hydrogen with the Square Root of the Current Density, for Ferrovac E and Fe-0.15Ti Both Coated (light symbols) or Uncoated (dark symbols) with Palladium on the Input Side.

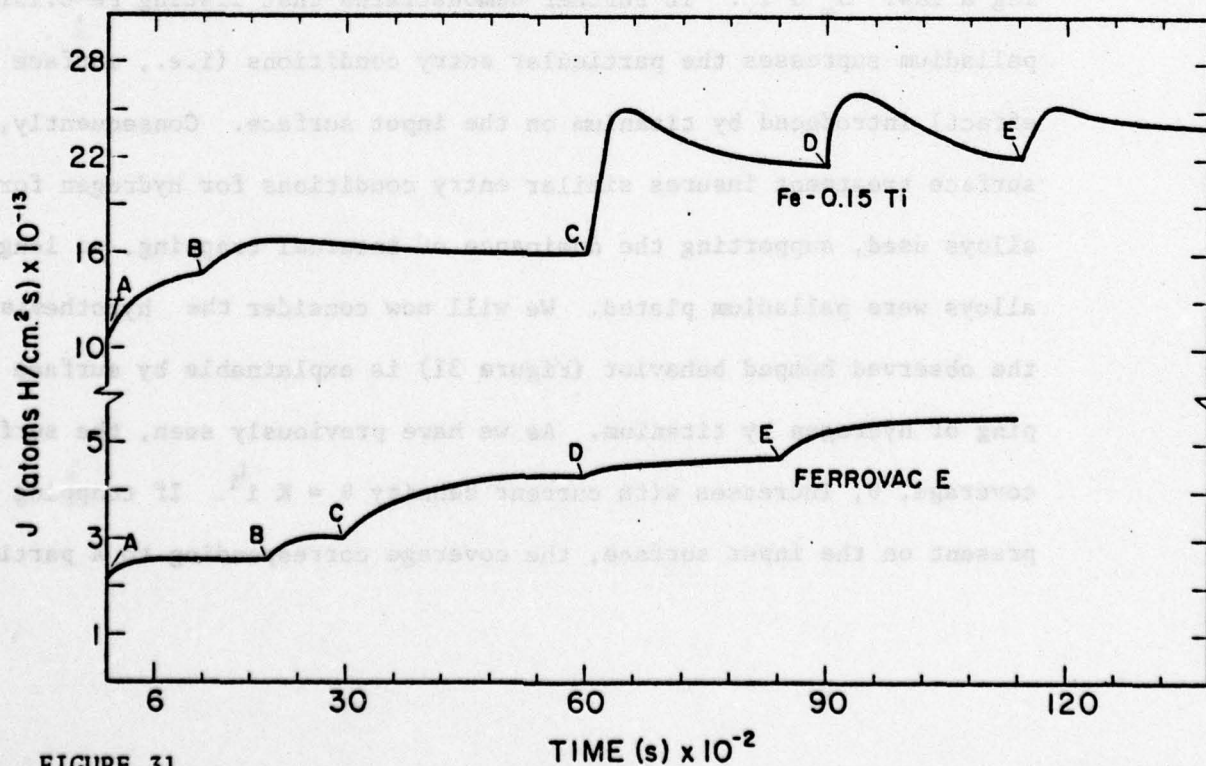


FIGURE 31.  
Evolution of the Permeation Transients with Time and with Increasing Current Density, for Ferrovac E and Fe-0.15Ti when Both are Uncoated on the Input Side.  
A: 2.4mA/cm<sup>2</sup>; B: 3.2mA/cm<sup>2</sup>; C: 8mA/cm<sup>2</sup>; D: 16mA/cm<sup>2</sup>; E: 24mA/cm<sup>2</sup>.

- (b) The linear relationship between  $J_{\infty}$  and  $i^{1/2}$  is obeyed for Ferrovac E, no matter the surface treatment, and for Fe-0.15Ti when it is palladium coated. However, a large departure from linearity is observed when Fe-0.15Ti is not palladium coated.
- (c) The steady state flux  $J_{\infty}$  increases slightly when Ferrovac E is palladium coated. However, the reverse occurs for Fe-0.15Ti, and the difference is quite appreciable.

Both observations support a surface effect when titanium is present on the entry side, quite different from the surface reactions occurring when titanium is absent, since both Ferrovac E and Fe-0.15Ti behave similarly when the input side is palladium coated. Therefore, it can be concluded that Ferrovac E (coated and uncoated with palladium) and Fe-0.15Ti (in the coated case) have similar entry conditions for hydrogen. This is in agreement with Table XI which showed iron and palladium obeying a law:  $J_{\infty} \propto i^{1/2}$ . It further demonstrates that plating Fe-0.15Ti with palladium suppresses the particular entry conditions (i.e., surface effect) introduced by titanium on the input surface. Consequently, this surface treatment insures similar entry conditions for hydrogen for all alloys used, supporting the dominance of internal trapping, so long as all alloys were palladium plated. We will now consider the hypothesis that the observed humped behavior (Figure 31) is explainable by surface trapping of hydrogen by titanium. As we have previously seen, the surface coverage,  $\theta$ , increases with current density  $\theta = K i^{1/2}$ . If trapping is now present on the input surface, the coverage corresponding to a particular



current density will be higher since hydrogen evolution reactions will be slower. In other words, more H atoms will stay on the surface; for example, trapped at titanium atoms sites. A direct result of this is a decrease in the total input area available for diffusion. Specifically, consider the total area, A, as the sum of two areas:

$$A = \text{constant} = A_d(t) + A_t(t) \quad (90)$$

where  $A_d(t)$  is the area available for diffusion (where the reaction  $H_{\text{ads.}} \rightarrow H_{\text{abs.}}$  will take place), and  $A_t(t)$  is the area covered by hydrogen atoms immobilized at trapping sites. As time goes on, the number of atoms trapped increases, so that,  $A_t(t)$  increases with time, while  $A_d(t)$  decreases. Thus, the number of hydrogen atoms that enter the lattice and diffuse will also decrease with time (i.e., the input flux of hydrogen will decrease with time). We may represent this by using the following general exponential term:

$$J_1(t) = \frac{J_\infty^0}{K_1 + K_2} \left[ K_1 + K_2 e^{-kt} \right] \quad (91)$$

where  $J_1(t)$  = flux of hydrogen at the input side

$J_\infty^0$  = steady state flux at the input surface that would be obtained if  $A_t(t) = 0$

$K_1$  and  $K_2$  are positive constants related to the ratios of the surface available for diffusion to the surface impermeable to diffusion, respectively. When  $t \rightarrow \infty$ , then

$$J_1(\infty) = \frac{K_1}{K_1 + K_2} \cdot J_\infty^0 \quad (92)$$

and the input steady state flux will be less than  $J_{\infty}^0$  the input steady state flux for  $A_t(t) = 0$ . Physically,  $K_1$  and  $K_2$  are related to the steady state values of  $A_d(t)$  and  $A_t(t)$ ; indeed, the flux  $J_1(\infty)$  corresponds to an input surface  $A = A_d(\infty) + A_t(\infty)$ , while the flux  $J_{\infty}^0$  corresponds to  $A = A_d(\infty)$ . Thus, the ratio of  $J_1(\infty)$  to  $J_{\infty}^0$  is also given by:

$$\frac{J_1(\infty)}{J_{\infty}^0} = \frac{A_d(\infty)}{A} \quad (93)$$

Comparing Equations (92) and (93), we may thus identify  $A$  as  $K_1 + K_2$  and  $A_d(\infty)$  as  $K_1$  (so that, with Equation (90):  $A_t(\infty) = K_2$ ).

Thus:

$$\begin{aligned} K_1 &= A_d(\infty) \\ K_2 &= A_t(\infty) \end{aligned} \quad (94)$$

Finally,  $k$  describes the rate at which  $A_t(t)$  reaches its steady state value. Equivalently,  $k$  is a measure of the rate of the trapping reactions, or of the deposition of the impermeable layer, or both.

As may be seen from the above equations, a decrease in the initial input flux will result in a decrease in the output flux as well. Experimentally, we modelled this situation by covering part of the input surface of a Ferrovac E membrane with an impermeable layer of lacquer. As shown in Figure 32, the resulting steady state output flux decreases with increasing area covered with lacquer (or with decreasing area available for diffusion, i.e., not covered with lacquer). Theoretically, it



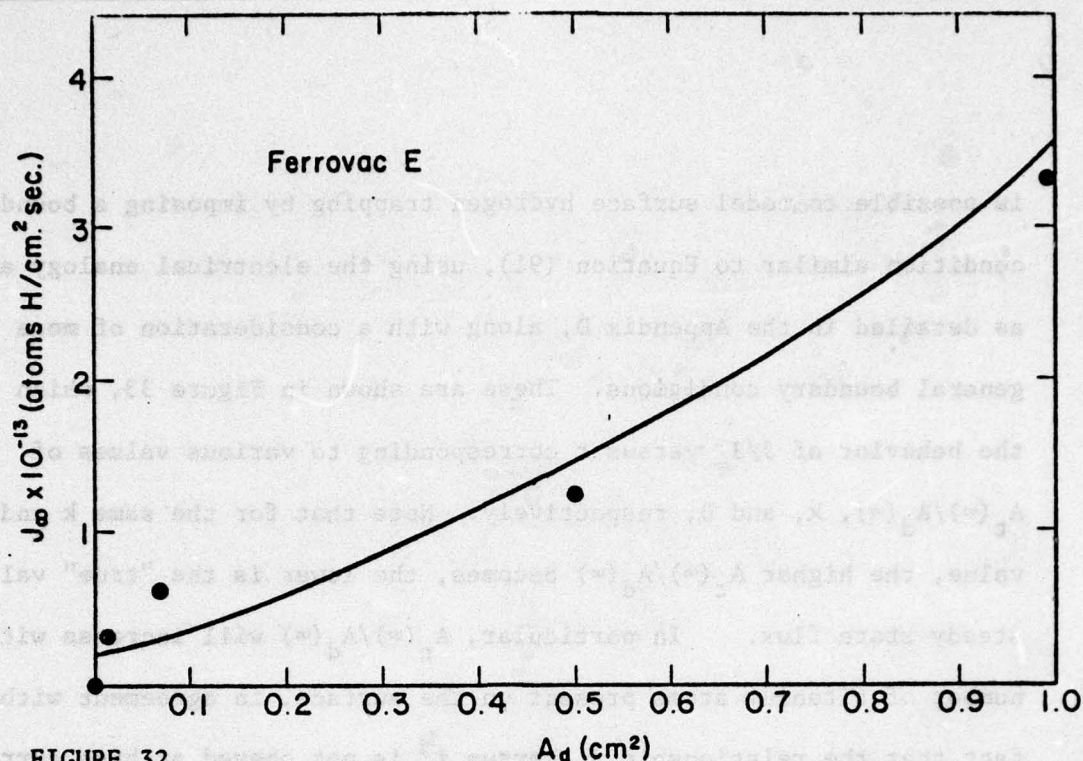


FIGURE 32. Experimental Modelling of Surface Trapping: Evolution of the Steady State Flux of Hydrogen with the Area Available for Diffusion ( $A_d$ ).

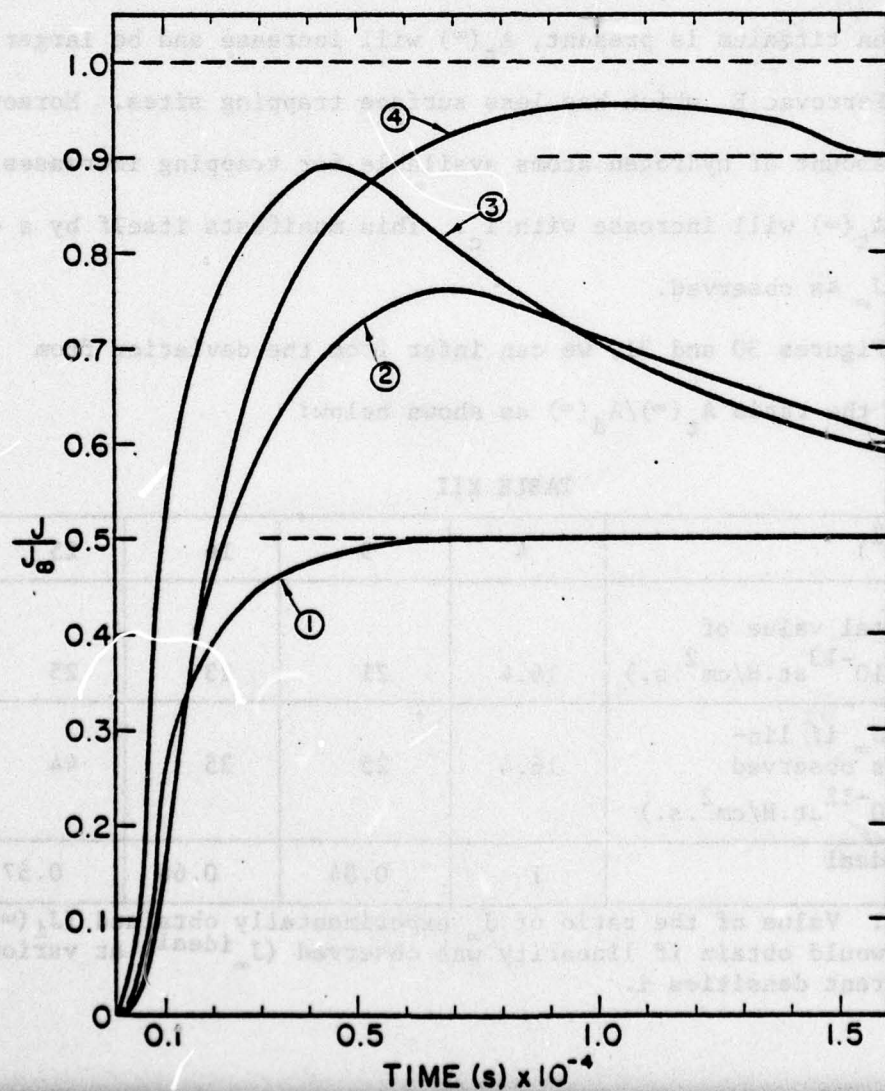


FIGURE 33. Theoretical Modelling of Surface Trapping, Using the Electrical Analogy. Curve 1:

$$A_t(\infty)/A_d(\infty) = 1;$$

$$k = 10^{-2} \text{ s}^{-1};$$

$$D = 2 \times 10^{-6} \text{ cm}^2/\text{s}.$$

Curve 2:

$$A_t(\infty)/A_d(\infty) = 1;$$

$$k = 10^{-4} \text{ s}^{-1};$$

$$D = 10^{-6} \text{ cm}^2/\text{s}.$$

Curve 3:

$$A_t(\infty)/A_d(\infty) = 1;$$

$$k = 10^{-4} \text{ s}^{-1};$$

$$D = 2 \times 10^{-6} \text{ cm}^2/\text{s}.$$

Curve 4:

$$A_t(\infty)/A_d(\infty) = 0.1;$$

$$k = 10^{-4} \text{ s}^{-1};$$

$$D = 10^{-6} \text{ cm}^2/\text{s}.$$

is possible to model surface hydrogen trapping by imposing a boundary condition similar to Equation (91), using the electrical analogy approach as detailed in the Appendix D, along with a consideration of more general boundary conditions. These are shown in Figure 33, which depicts the behavior of  $J/J_\infty$  versus  $t$  corresponding to various values of  $A_t(\infty)/A_d(\infty)$ ,  $k$ , and  $D$ , respectively. Note that for the same  $k$  and  $D$  value, the higher  $A_t(\infty)/A_d(\infty)$  becomes, the lower is the "true" value of the steady state flux. In particular,  $A_t(\infty)/A_d(\infty)$  will increase with the number of titanium atoms present on the surface, in agreement with the fact that the relationship  $J_\infty$  versus  $i^{1/2}$  is not obeyed at high current densities for uncoated Fe-0.15Ti, as compared to uncoated Ferrovac E. Indeed, when titanium is present,  $A_t(\infty)$  will increase and be larger than  $A_d(\infty)$  for Ferrovac E, which has less surface trapping sites. Moreover, since the amount of hydrogen atoms available for trapping increases with  $i$  ( $\propto i^{1/2}$ ),  $A_t(\infty)$  will increase with  $i_c$ . This manifests itself by a decrease in  $J_\infty$  as observed.

From Figures 30 and 31, we can infer from the deviation from linearity, the ratio  $A_t(\infty)/A_d(\infty)$  as shown below:

TABLE XII

$i$ (mA/cm <sup>2</sup> )	4	9	16	25
Experimental value of $J_i(\infty)$ ( $\times 10^{-13}$ at.H/cm <sup>2</sup> .s.)	16.4	21	23	25
Value of $J_\infty$ if linearity was observed $J_\infty^{\text{ideal}}$ ( $\times 10^{-12}$ at.H/cm <sup>2</sup> .s.)	16.4	25	35	44
$J_i(\infty)/J_\infty^{\text{ideal}}$	1	0.84	0.66	0.57

Table XII: Value of the ratio of  $J_\infty$  experimentally obtained ( $J_i(\infty)$ ) to  $J_\infty$  which would obtain if linearity was observed ( $J_\infty^{\text{ideal}}$ ) at various input current densities  $i$ .



Furthermore, with Equations (92) and (94), one has

$$\frac{J(\infty)}{J_0^0} = \frac{A_d(\infty)}{A_t(\infty) + A_d(\infty)} = \frac{1}{1 + A_t(\infty)/A_d(\infty)} = \frac{J(\infty)}{J_{\text{ideal}}} \quad (95)$$

Then:

$$\frac{A_t(\infty)}{A_d(\infty)} = \frac{1 - \frac{J_1(\infty)}{J_0^0}}{\frac{J_1(\infty)}{J_0^0}} \quad (96)$$

The following values of  $A_t(\infty)/A_d(\infty)$  are obtained

TABLE XIII

$i$ (mA/cm <sup>2</sup> )	4	9	16	25
$\frac{A_t(\infty)}{A_d(\infty)}$	0	0.19	0.51	0.75

Table XIII: Ratio of the area where trapping is assumed to occur ( $A_t(\infty)$ ) to the area available for diffusion ( $A_d(\infty)$ ) at various input current densities.

In other words, at low current density, the area of the input side that is covered with immobilized hydrogen is negligible compared with the area available for diffusion. However, at higher current densities,  $A_t(\infty)$  increases; for example, at 16 mA/cm<sup>2</sup>, one third of the surface is impermeable to hydrogen.

We can then infer the number of hydrogen atoms that are immobilized on the surface around a titanium atom, as follows: since 0.15wt%Ti is equivalent to 0.17% atoms Ti/at.Fe,

$$\frac{A_t(\infty)}{A_d(\infty)} = \frac{n N_{Ti}^A}{N_{Fe}^A} = 0.175 \times 10^{-2} n \quad (97)$$

where  $N_{Ti}^A$  is the number of titanium atoms/area,  $N_{Fe}^A$  the corresponding number of iron atoms, and  $n$  the number of hydrogen atoms immobilized per titanium atom. Values of  $n$  are tabulated below:

TABLE XIV

$A_t(\infty)/A_d(\infty)$	0	0.19	0.51	0.75
$n$	0	$1 \times 10^2$	$2.9 \times 10^2$	$4.3 \times 10^2$

Table XIV: Values of the surface occupancy of titanium atoms ( $n$ ), versus the relative amounts of hydrogen impermeable and permeable areas.

Thus, about a hundred hydrogen atoms would have to be immobilized around a single titanium atom at  $9 \text{ mA/cm}^2$  in order to account for the observed decrease in steady state flux. This appears quite large, since intuitively, and considering the interstitial sites near a Ti atom in a bcc structure, only about six hydrogen atoms should strongly interact with a titanium atom. Can this large value be accounted for by other contributions? Possibilities would include:

- a) Formation of cracks at high input current density
- b) Deposition of an impermeable layer on the input side (e.g., an oxide).



Taking Case a), we shall show later that Fe-Ti alloys are less susceptible to cracking than Ferrovac E, and since non-coated Ferrovac E obeyed the relationship  $J_{\infty} \propto i^{1/2}$ , cracking would not be expected for either material. It is of note that a cracking hypothesis has been widely proposed in the literature<sup>(65,89,99)</sup> to explain the "humped" shape of the transients, although cracks could not be detected. This study and Figures 30 through 33 show that surface effects may be a more plausible explanation for this effect at low current densities and for alkaline solutions and, in general, whenever cracks are not detected.

Considering case (b), the deposition of an impermeable layer on the input surface would have to be related to the presence of titanium atoms, since uncoated Ferrovac E obeyed the law  $J_{\infty} \propto i^{1/2}$ . A possibility is then the formation of an oxide  $TiO_2$ , for example, which would also act as a permeation barrier. However, if an oxide barrier was solely responsible for the observed surface effect when Fe-0.15Ti is not coated with palladium, it would then become difficult to explain why the value of  $J_{\infty}$  for uncoated Fe-0.15Ti is higher than  $J_{\infty}$  for uncoated Ferrovac E. On the contrary, explaining the observed effects by reversible surface trapping of hydrogen of titanium sites (with subsequent clustering), could also explain the high value of  $J_{\infty}$  for Fe-0.15Ti: because the trapping is reversible and results in large clusters of hydrogen on the surface, more hydrogen atoms are allowed to enter the lattice than in the case of Ferrovac E, although less hydrogen atoms will do so than if the trapping was more reversible.

The present test of steady state flow versus current density has

thus showed that:

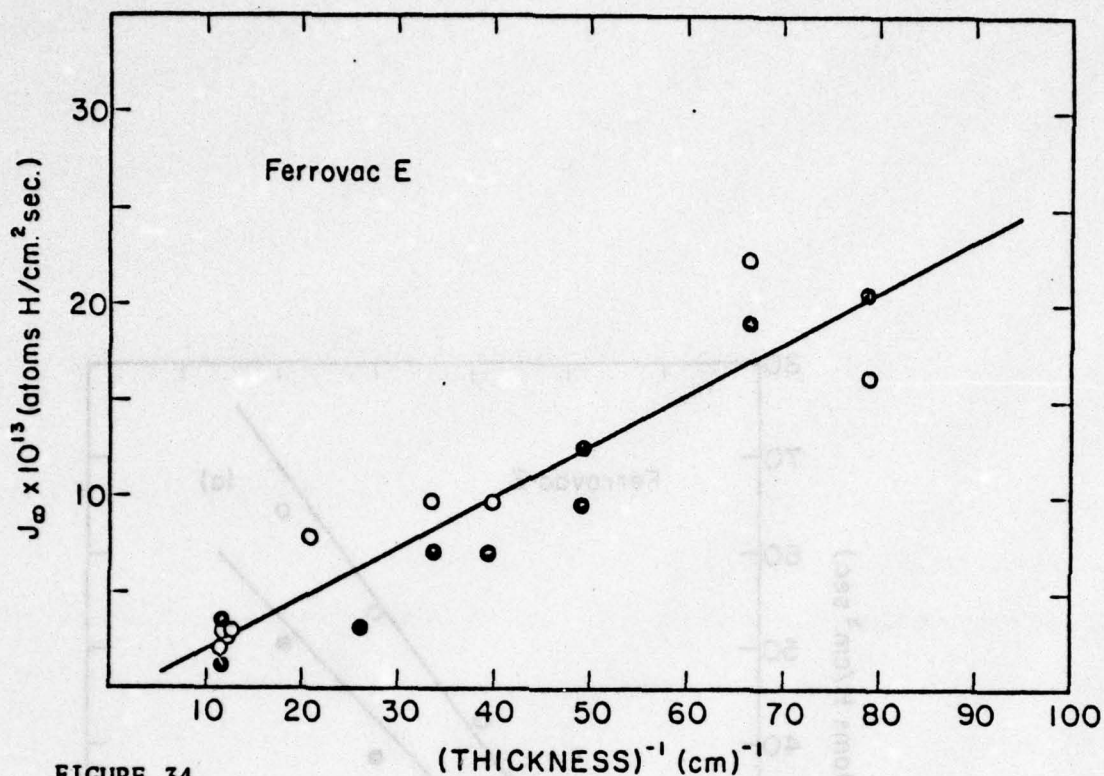
- a) Palladium coated Fe-0.15Ti exhibits similar hydrogen entry conditions as coated and uncoated Ferrovac E. The previous considerations on trapping were thus safely made, since all Fe-Ti alloys were palladium coated.
- b) Uncoated Fe-0.15Ti exhibits different entry conditions that are best explained in terms of significant reversible surface trapping of hydrogen by titanium.

(2) Steady state flux versus inverse thickness

This test should indicate whether diffusion is the rate controlling step, as discussed before. The results are plotted in Figures 34 and 35, and are in good agreement with those of the previous test. That is; Ferrovac E specimens, both uncoated and palladium coated, follow a law  $J_{\infty} \propto L^{-1}$ , and the same law is obeyed for palladium coated Fe-0.15Ti; however, a large scatter is obtained for uncoated Fe-0.15Ti, in particular at small thicknesses ( $L^{-1} = 80.\text{cm}^{-1}$ ). Again, those results point toward a surface effect of a different nature when titanium is present on the input surface. Moreover, the large value of  $J_{\infty}$  obtained at small thicknesses is in accord with a larger surface coverage due to surface trapping. Thus, this test confirms the findings of the  $J_{\infty}$  versus  $i^{1/2}$  results, while showing that, in the case of Ferrovac E and coated Fe-0.15Ti, diffusion is rate controlling.

A final proof that diffusion is the controlling step in the case of coated and uncoated Ferrovac E is offered in Figure 36. In this Figure, the proportionality  $J_{\infty} \propto i^{1/2}$  is seen to hold even at small thicknesses, no matter the input surface treatment of the specimen. Since





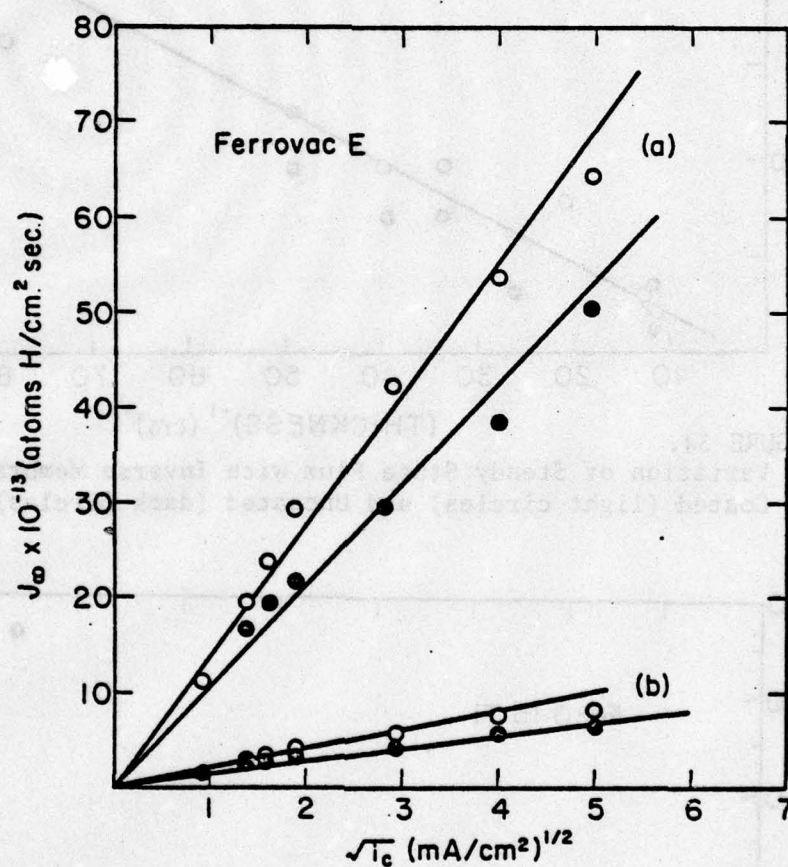


FIGURE 36.

Variation of Steady State Flux of Hydrogen with the Square Root of the Current Density ( $i_c$ ) and Membrane Thickness; a): thickness =  $1.27 \times 10^{-2}$  cms; b): thickness =  $8.64 \times 10^{-2}$  cms.



thickness only influences internal diffusion of hydrogen (which manifests itself by a larger  $J_{\infty}$ ), it is clear that no surface effect is present here. This result and similar proofs have been given in the literature (see Reference 86). Since palladium-coated alloy B behaves in the same way, diffusion is also the rate-controlling step in this case.

#### E.2.c. Conclusions:

It can thus be concluded that a surface effect is present only when an Fe-Ti alloy is not coated with palladium on the input side. The most realistic explanation is that of important reversible surface trapping of hydrogen by titanium, which manifests itself by the breakdown of a linear relation between  $J_{\infty}$  and  $i^{1/2}$ . Theoretical modeling of this effect suggests a relatively strong trapping on the surface, with formation of large clusters of hydrogen around a titanium atom. This surface effect disappears whenever the specimen is coated with palladium on the input side, as was the case for all permeation experiments in Section E.1., and thus cannot be proposed as an alternative to trapping. The previous considerations on trapping are still valid.

#### E.3. The Possibility of a Concentration Effect

In the same way that a surface effect cannot account for the observed diffusion behavior of Fe-Ti alloys, it is also possible to reject a concentration effect as an alternative explanation, using the following argument:

As proposed and experimentally verified elsewhere in the literature,<sup>(80)</sup>

the diffusivity of hydrogen in ferrite increases with increasing concentration of hydrogen. This may be visualized by an increase in hydrogen concentration reducing the probability of occurrence of a backward jump, thus promoting forward diffusion. In the particular case of Fe-Ti alloys, it has been shown (see for example, Figure 25) that the hydrogen concentration increases with increasing titanium content. Thus, one would also expect an increase in diffusivity, which is not the observed case. Explanation of the diffusion behavior of hydrogen in FeTi alloys in terms of a concentration effect has to be discarded. As a matter of fact, the slight increase in diffusivity due to an increased hydrogen concentration with titanium additions would result in an underestimation of titanium trapping capacity.

#### E.4. General Conclusions:

Since a surface or a concentration effect cannot be held responsible for the delay in the diffusion of hydrogen through Fe-Ti alloys when titanium is present as a substitutional solid solution element, the only remaining plausible explanation is hydrogen trapping by titanium atoms, which we have verified both experimentally and by theoretical modelling. The results of these analyses are all consistent with titanium being a reversible trap of average strength (comparable to grain boundary or dislocations), but having a large trapping capacity, thus being capable of continued trapping at higher fugacity. This result of trapping by titanium on mechanical and environmental behavior of Fe-Ti alloys will be fully explored in the following chapters.



## F. Analysis of Irreversible Trapping

### F.1. Theoretical Considerations:

As was discussed on page 60, irreversible trapping will not have any effect on the second polarization transients since, by definition, the irreversible traps will be full and, thus, will not contribute to the diffusion kinetics. The analysis of irreversible trapping must then be performed on the first polarization transients. This is a complicated situation, since reversible trapping is also occurring at the same time. To undertake this, we chose as a variable a combination of both reversible and irreversible trapping. A reversible trap has previously been defined as one of the six octahedral sites nearest to a titanium atom, thereby giving a total reversible trap population,

$N_r$  of:

$$N_r = zN^{Ti} \text{ with } 1 \leq z \leq 6$$

One now has to define what is meant as an irreversible trap.

#### F.1.a. Definition of an irreversible trap

Following Asaoka's study<sup>(25)</sup> and our own considerations concerning irreversible trapping during the first polarization (page 60), the dominant irreversible traps are considered to be the sites located at the interface between a titanium carbide particle and the ferrite matrix. The number of irreversible traps in a particular alloy will thus depend upon the size, shape, and number of these titanium carbide particles. The same shape of the particles will be assumed spherical in all alloys (a good assumption as seen in Chapter I). The size and number of particles have been computed and were presented in Figure 4.

The total number of irreversible traps  $N_i$  can then be expressed as:

$$N_i = y(d)N^{TiC} \quad (98)$$

where  $y$  is a function of the size  $d$  of the particle and  $N^{TiC}$  is the density of titanium carbide particles in ferrite. In fact,  $y$  expresses the number of hydrogen atoms trapped per particle of diameter  $d$ . Let  $u$  be the number of interstitial sites per face of the unit cell;  $u$  will, of course, depend on which atomic plane constitutes the interface (e.g.,  $u$  would be equal to 4 for a (100) type plane). Then:

$$y(d) \approx u \pi d^2 / a^2 \quad (99)$$

#### F.1.b. The trapping reaction

To express the fact that reversible and irreversible trapping are present during the first polarization, the following variable is chosen:

$$\theta = (n_r + n_i) / (N_r + N_i) \quad (100)$$

where  $n_{r,i}$  = density of hydrogen atoms trapped on reversible, irreversible traps, respectively. The complete trapping reaction is then:

$$d\theta/dt = \bar{k} C(1-\theta) - \bar{p}\theta \quad (101)$$

where  $\bar{k}$  and  $\bar{p}$  are total capture and release rates constants, respectively, and  $C$ , is the total hydrogen concentration. Contrary to  $k$  and  $p$  which represented reversible trapping during the second polarization,  $\bar{k}$  and  $\bar{p}$  now represent both irreversible and reversible trapping during the



first polarization.

At steady state,  $d\theta/dt = 0$  and thus  $\bar{k} C(1-\theta_s)$  where  $\theta_s$  is the saturation value of  $\theta$ . Let  $n_{rs}$  and  $n_{is}$  be the saturation values of  $n_r$  and  $n_i$ , respectively. As was demonstrated when analyzing reversible trapping,  $n_{rs}$  is much less than  $N_r$  (small occupancy or incomplete saturation). In this case, it will be assumed that, because titanium carbide particles are strong, irreversible traps, they will completely saturate. This may be rationalized with the following argument: consider a reversible trap with release constant  $p$ ;  $p$  is the probability that a H atom jumps back in the lattice. If more hydrogen is present in the lattice around the trap, this probability  $p$  decreases. In other words, for a reversible trap, trapping and detrapping is a function of its surroundings. On the contrary, an irreversible trap, by definition, does not release its hydrogen, i.e.,  $p = 0$ ; thus there is no "influence" of the surroundings other than the hydrogen that approaches an unsaturated trap will then be captured. In the same way, a H atom in the lattice will feel the influence of a H atom on a nearby reversible trap, because this trapped atom can statistically jump back into the matrix. However, a diffusing H atom will not notice an irreversibly trapped H atom, since the latter does not have a finite probability of backward jumps. Thus, an irreversibly trapped H atom will be replaced in the lattice as if it had 'disappeared.' The only real dependence that an irreversible trap has on the surrounding hydrogen concentration is that an irreversible trap needs diffusing hydrogen to trap. Thus:

$$n_{is} = N_i \quad \text{and:}$$

$$\theta_s = (n_{rs} + N_i)/(N_r + N_i). \quad (102)$$

Because  $n_{rs}/N_r \ll 1$ , let  $x$  be this fraction:  $x = n_{rs}/N_r$ . Then

$$\theta_s = (xN_r + N_i)/(N_r + N_i) \quad (103)$$

Now, replace  $\theta_s$  by its value above in the expression obtained at saturation, and let  $N$  be the total density of traps ( $N = N_r + N_i$ ).

Then:

$$\bar{k}C(1-x)N_r/N = \bar{p} \left[ xN_r/N + N_i/N \right] \quad (104)$$

Let  $F_i = N_i/N$  and  $F_r = N_r/N$  as these fractions of the total trap population which are irreversible and reversible, respectively. The ratio  $\bar{k}/\bar{p}$  of the total capture and release rates constants is thus given by:

$$\frac{\bar{k}}{\bar{p}} = \frac{xN_r + N_i}{C(1-x)N_r} = \frac{1}{C} \left[ \frac{1}{(1-x)F_r} - 1 \right] = \frac{1}{C(1-F_i)} \left[ F_i + \frac{x}{1-x} \right] \quad (105)$$

The last two expressions were obtained by using the fact that  $F_i + F_r = 1$ ; they give the variation of  $\bar{k}/\bar{p}$  with  $F_r$  or  $F_i$ , respectively. Since  $x$  and  $C$  are also a function of  $F_r$  (see page 93), i.e.,  $x$  and  $C$  increase with increasing  $F_r$  (or decreasing  $F_i$ ),  $\bar{k}/\bar{p}$  is thus a complex function of  $F_r$  or  $F_i$ . Considering the last expression where  $\bar{k}/\bar{p}$  is a function of  $F_i$ , and assuming a large  $F_i$  compared to  $F_r$ ,  $\bar{k}/\bar{p}$  may be seen to increase with increasing  $F_i$ , since  $x/(1-x)$  is small and since  $1-F_i$  and  $C$  will decrease with increasing  $F_i$ . This was expected since increasing the number of



irreversible traps should increase the rate at which hydrogen is irreversibly trapped.

F.1.c. Comparison of trapping kinetics between first and second polarization:

In the above considerations, it was assumed that an irreversible trap always saturated, no matter the value of the surrounding concentration of dissolved hydrogen. In thermodynamic terms, it means that the irreversibly trapped hydrogen has no influence on the chemical potential of diffusing and reversibly trapped hydrogen. Experimentally, this was verified by the fact that the concentration  $C_0$  of hydrogen below the input surface (as measured from the steady state flux  $J_\infty$ , see Figure 25) did not vary much with the order of polarization. In turn, this implies that the occupancy of reversible traps (which varies with  $C$ ) will not vary much between first and second polarization. Taking  $x$  (first polarization)  $\approx x$  (second polarization), and since we have seen (Equation (54)) that:

$$x(\text{2nd polarization}) = kC/(p+kC),$$

we can replace  $x$  of Equation (54) in Equation (105) giving

$$\frac{\bar{k}}{p} = \frac{k}{p} \left[ \frac{F_r + F_1}{F_r} \right] + \frac{1}{C} \cdot \frac{F_1}{F_r} = \frac{1}{F_r} \cdot \frac{k}{p} + \frac{1}{C} \cdot \frac{F_1}{F_r} \quad (106)$$

One can easily show that if  $F_1 = 0$ , then  $F_r = 1$  and  $\bar{k}/p = k/p$ , as expected from our previous analysis, since no irreversible trapping must mean that the capture and release rates constants are similar to those for the second polarization.

From the above expression, it is also seen that increasing  $F_1$

will increase the ratio  $\bar{k}/\bar{p}$ , which should result in a decreased diffusivity. Further, since  $1/F_r$  is always greater than one, and since  $F_i/CF_r$  is always positive:

$$\bar{k}/\bar{p} > k/p, \quad (107)$$

consistent with the fact that

$$D(\text{first polarization}) < D(\text{2nd polarization})$$

Finally, since the ratio  $k/p$ ,  $C$ ,  $F_i$  and  $F_r$  are experimentally known or inferred, it is possible to calculate  $\bar{k}/\bar{p}$ . This will now be done.

## F.2. Application of the Theory to Experimental Results

### The variation of $k/p$ with trapping parameters.

Using Table I and Figure 4 of Chapter I, the ratio  $F_i/F_r$  may be computed. Indeed, all that is needed to calculate  $F_i$  and  $F_r$  is the value of  $N_i$  and  $N_r$ . As was seen before, we have:

$$N_r = 6 N^{Ti} \quad (\text{taking } Z = 6) \quad (108)$$

$$N_i = 4\pi d^2 N^{TiC}/a^2 \quad (\text{taking } u = 4). \quad (109)$$

$N^{Ti}$  is given in Table VIII, d and  $N^{TiC}$  in Figure 4 and  $a = 4.36\text{\AA}^{(45)}$  for f.c.c. TiC. Since it was previously described as the sum of two populations of TiC particles (small and large particles),  $N_i$  is in fact:

$$N_i = N_i(\text{small}) + N_i(\text{large}).$$

Values of  $F_i$ ,  $F_r$  and  $F_i/F_r$  are given below:



TABLE XV

Alloy	$N_r$	$N_i$ (small)	$N_i$ (large)	$N_i$	$F_i$	$F_r$	$F_i/F_r$
B	$8.9 \times 10^{20}$	$1.9 \times 10^{17}$	$1.6 \times 10^{16}$	$2 \times 10^{17}$	$2.2 \times 10^{-4}$	$\sim 1$	$2.2 \times 10^{-4}$
BC	$5.3 \times 10^{20}$	$7.4 \times 10^{18}$	$1.3 \times 10^{16}$	$7.4 \times 10^{18}$	$1.4 \times 10^{-2}$	0.98	$1.4 \times 10^{-2}$
C	$3.7 \times 10^{21}$	$1.6 \times 10^{18}$	$2.7 \times 10^{16}$	$1.6 \times 10^{18}$	$4.3 \times 10^{-4}$	1	$4.3 \times 10^{-4}$
CC	$2.9 \times 10^{21}$	$1.0 \times 10^{19}$	$6.6 \times 10^{16}$	$1.0 \times 10^{19}$	$3.4 \times 10^{-3}$	0.99	$3.4 \times 10^{-3}$
D <sub>2</sub>	$8.9 \times 10^{21}$	-	$2.9 \times 10^{17}$	$2.9 \times 10^{17}$	$3.2 \times 10^{-5}$	1	$3.2 \times 10^{-5}$
DC	$2.1 \times 10^{21}$	-	$3.5 \times 10^{17}$	$3.5 \times 10^{17}$	$4.3 \times 10^{-5}$	1	$4.3 \times 10^{-5}$

Table XV: Values of the parameters characterizing irreversible trapping: irreversible traps density ( $N_i$ ), reversible traps density ( $N_r$ ) and their ratios.

The variation of  $\bar{k}/\bar{p}$  versus  $F_i/F_r$ , according to Equation (106) is presented in Figure 37. Some interesting conclusions are apparent:

- a)  $\bar{k}/\bar{p}$  increases with increasing number of irreversible traps ( $F_i/F_r$  increases) and with decreasing hydrogen concentration. In other words, as expected, irreversible trapping is felt more when either the number of irreversible traps is large, or the concentration of hydrogen is low, or both. As seen from the Figure, all curves asymptotically converge toward  $k/p$  (i.e., the value of  $\bar{k}/\bar{p}$  for reversible trapping only) when  $F_i/F_r < 10^{-4}$ , for the concentrations of hydrogen corresponding to the permeation experiments of Chapter II.
- b) It is possible to predict a  $\bar{k}/\bar{p}$  value for all alloys, since

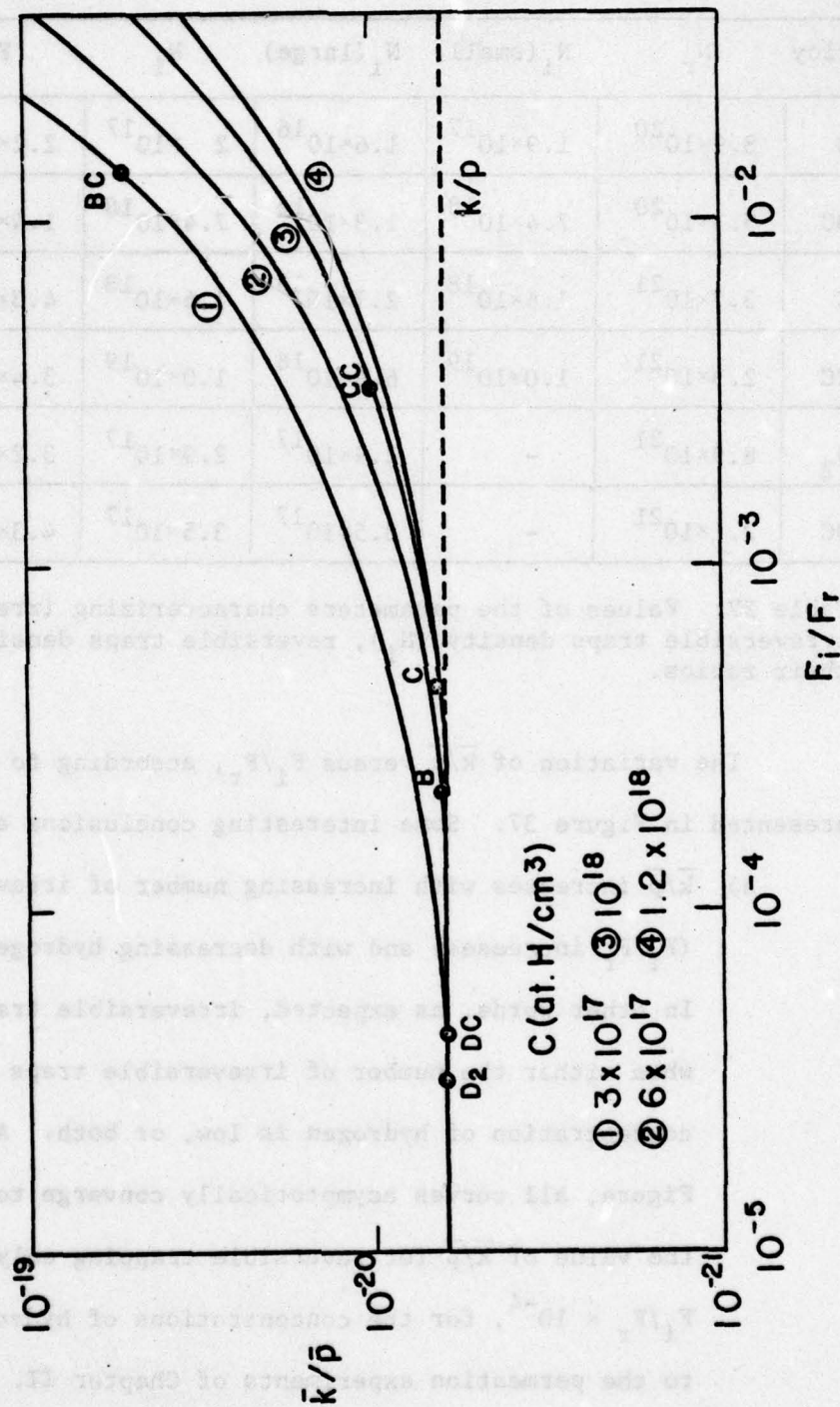


Figure 37 : Variation of Trapping Rate Parameters for first Polarization Permeation ( $\bar{k}/\bar{p}$ ) with Ratio of Irreversible and Reversible Trapping Densities ( $F_i/F_r$ )



$F_i/F_r$  and  $C$  are known\* for all of them. Since an increasing value of  $\bar{k}/\bar{p}$  means a decreased value of the diffusivity  $D$  for the first polarization, the theory predicts using Figure 37 that:

- i)  $D$ (first polarization) for alloys  $D_2$ , DC, and B  $\approx$   $D$ (second polarization) for the same alloys
- ii) the decrease in  $D$  for the first polarization will follow the sequence BC, then CC, then C.
- iii) finally, the analysis predicts that if one compares the first polarization diffusivities  $D(1)$  of a carburized alloys to its non-carburized counterpart, alloys  $D_2$  and DC should have similar first polarization diffusivities, while  $D(1)$  for alloys BC and CC is going to be less than  $D(1)$  for alloys B and C, the effect being strongest for alloys B-BC.

We shall now examine if the above predictions are experimentally verified.

### F.3. Experimental Verification of the Theory:

Using exactly the same experimental technique as before for the analysis of reversible trapping, the diffusivities for the carburized alloys BC, CC and DC were measured for the first and second polarization. The results are plotted on Figure 38, along with the previous results from Chapter II. For the noncarburized alloys (B, C,  $D_2$ ), comparing the first polarization diffusivity  $D(1)$  of a carburized alloy to  $D(1)$  of the non-carburized alloy, the analysis predicts:

---

\*Note: the value of  $C$  for alloy BC was taken as equal to the  $C$  value of Ferrovac E, since its NFTC is  $\approx 0$ . (page 15)

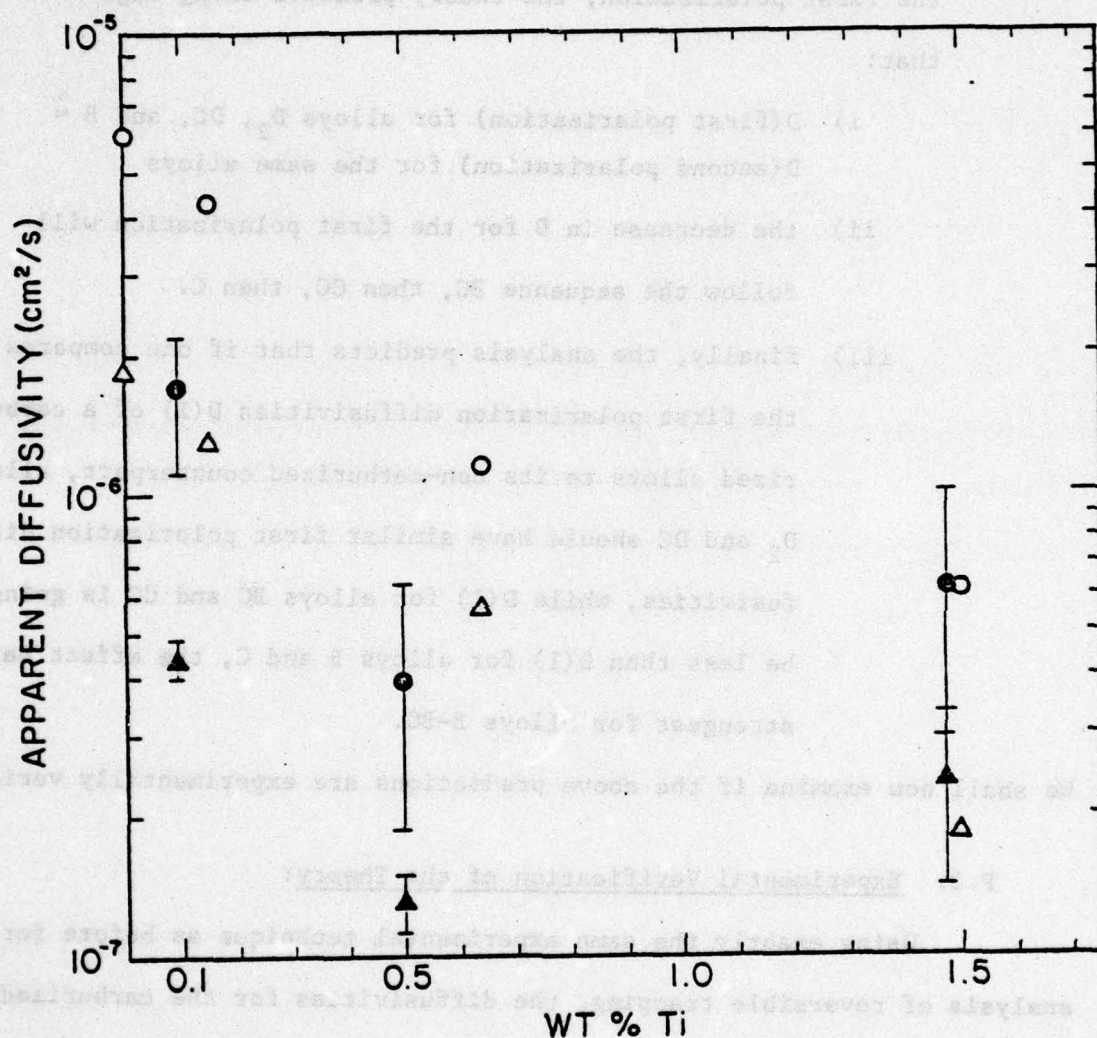


**FIGURE 38.**  
Diffusivity of Hydrogen through Fe-Ti Alloys for First (circles) and Second (triangles) Polarization Permeation Transients. Light Symbols are for Uncarburized Alloys (see Fig.22) and Dark Symbols for Carburized Alloys. Data for the Uncarburized Alloys is Plotted According to the Total Titanium Content of Each Alloy (Table I).



$$\frac{D(1) \text{ for DC}}{D(1) \text{ for D}_2} \approx 1 > \frac{D(1) \text{ for CC}}{D(1) \text{ for C}} > \frac{D(1) \text{ for BC}}{D(1) \text{ for B}} \quad (110)$$

These ratios are tabulated below from Figure 31 as:

TABLE XVI

Alloy	$D(1) (\text{cm}^2/5)$	Ratio $\frac{D(1)(\text{carburized alloy})}{D(1)(\text{non-carb. alloy})}$
B	$1.3 \cdot 10^{-6}$	0.33
BC	$4.3 \cdot 10^{-7}$	
C	$5.6 \cdot 10^{-7}$	0.23
CC	$1.3 \cdot 10^{-7}$	
D <sub>2</sub>	$1.8 \cdot 10^{-7}$	1.3
DC	$2.4 \cdot 10^{-7}$	

Table XVI: Ratios of the first polarization diffusivities for each non-carburized alloy and its carburized counterpart.

Thus, the experimental order is:

$$\frac{D(1) \text{ for DC}}{D(1) \text{ for D}_2} \approx 1 > \frac{D(1) \text{ for BC}}{D(1) \text{ for B}} \approx \frac{D(1) \text{ for CC}}{D(1) \text{ for C}} \quad (111)$$

Comparing this with the predicted order, there is agreement between theory and experiment for alloys D<sub>2</sub> and DC. However, the theory ranked the ratio for CC-C higher than the ratio for BC-B, while experimentally they are similar (within experimental error). The reason for this discrepancy will be considered subsequently.

For the same alloy, the theory predicted that:

$$\frac{D(1) \text{ for BC}}{D(2) \text{ for BC}} < \frac{D(1) \text{ for CC}}{D(2) \text{ for CC}} < \frac{D(1) \text{ for C}}{D(2) \text{ for C}}, \text{ as measured} \quad (112)$$

by the difference between  $\bar{k}/\bar{p}$  and  $k/p$ .

Experimentally, from Figure 31, this order is conserved since,

$$\frac{D(1)}{D(2)} = 0.26 \text{ for BC} < \frac{D(1)}{D(2)} = 0.33 \text{ for CC} < \frac{D(1)}{D(2)} = 0.52 \text{ for C} \quad (113)$$

Where the theory shows some discrepancy is for alloys of small TiC content, such as alloys D<sub>2</sub>, DC and B. Here the theory predicts a similar value of D(1) and D(2), while experimentally the ratio D(1)/D(2) varies from 0.4 (alloys DC) to 0.3 (alloys B and D<sub>2</sub>). The values and limitations of the theory will now be discussed.

#### F.4. Discussion

##### F.4.a. Origin of the discrepancies between theory and experiment

As was implicitly assumed in developing the model, all titanium carbide particles were assumed to be equally efficient in trapping. The trapping capacity was described as only a function of the size and shape of the individual particle, with all particles considered to be irreversible. Actually, this may not be the case; for example, hydrogen atoms could be trapped reversibly around a particle when all sites have been occupied at the interface (i.e., one should consider more than particle surface interactions). Perhaps more importantly, the



observation of a tweed-like structure in some alloys (see Chapter I) implies that small coherent particles are also present. Following a similar argument as was made for grain boundaries (see Bernstein, Ref. 24), a coherent interface will not trap as strongly as an incoherent one, i.e., coherent particles may act as reversible traps. The above arguments could explain why the ratio  $(D(1) \text{ for BC})/(D(1) \text{ for B})$  is not as small as anticipated; alloy BC contains numerous small particles which may not be as irreversible a trap as assumed. In the same way, the fact that the ratios  $D(1)/D(2)$  for alloys  $D_2$ , DC and B are less than one, in contradiction with the model, may be rationalized by assuming that the large TiC particles which are now present in these alloys trap more effectively than expected by only considering the capacity of their interfaces. Such a large coverage of the interface between a large titanium carbide and ferrite has been experimentally observed by autoradiography (see Chapter II, and Asaoka, <sup>(25)</sup>). The reason for this enhancement is not known.

Generally, however, the model helps to consistently explain irreversible trapping. It will be seen now if some quantitative information concerning the irreversible trapping parameters can be obtained.

#### F.4.b. Estimation of the trapping parameters:

A precise calculation of the individual value of  $\bar{k}$  and  $\bar{p}$ , the total capture and release rate constants for the first polarization, is difficult since  $D$  and  $N_1$  values are not as accurately known as the same values for the second polarization. An estimation of  $\bar{k}$  may be given however, by assuming that  $\bar{p} = p$  ( $p$  = release rate constant for reversible

trapping); this is based on the fact that only reversible trapping is responsible for  $\bar{p}$  and assumes that the release constant  $p$  is not changed when irreversible trapping is present (i.e., the probability of a backward jump from a reversible trap is the same when irreversible trapping is present at the same time). Since we have seen (page that  $p = 10^{-3} \text{ s}^{-1}$ , then:

$$\bar{k}(\text{for BC}) = 5.3 \times 10^{-23} \text{ cm}^3/\text{at.s.}, \bar{k}(\text{CC}) = 10^{-23}, \bar{k}(\text{C}) = 6.6 \times 10^{-24}$$

(114)

and

$$\bar{k}(\text{B}, \text{D}_2, \text{DC}) = k(\text{B}, \text{D}_2, \text{DC}).$$

The value of  $k$  for alloy B was found to be around  $7 \times 10^{-24}$  (see page 104), so that  $\bar{k}(\text{BC})/k(\text{B}) = 7.5$ . In other words, adding TiC particles to an alloy similar to B, in the quantity found in alloy BC, will increase by 7.5 the trapping kinetics.

#### F.4.c. Estimation of the interaction energy $E(\text{TiC-H})$

In the same way as  $E(\text{Ti-H})$  was computed using the electrical analogy approach,  $E(\text{TiC-H})$  may be evaluated. Consider alloy CC and the results of Figure 38; the value of  $D(1)$  is inversely proportional to the capacitance  $C(1)$  for the first polarization, and so is  $D(2)$  with  $C(2)$ . However,  $C(1)$  is proportional to the capacitance for irreversible + reversible traps, i.e.,  $C(1) \propto C(N_i) + C(N_r)$ . On the other hand,  $C(2)$  is only proportional to  $C(N_r)$ , so that:

$$\frac{D(2)}{D(1)} = \frac{C(N_r) + C(N_i)}{C(N_r)} = \frac{C(N_i)}{C(N_r)} + 1 \quad (115)$$



From Figure 31, alloy CC:

$$\frac{D(2)}{D(1)} = 3.1 \text{ and thus } \frac{C(N_1)}{C(N_r)} = 2.1 \quad (116)$$

As was demonstrated before:

$$E(N_1) = \frac{C(N_1) \theta(N_r) N_r}{C(N_r) \theta(N_1) N_1} \times E(N_r) \quad (117)$$

$E(N_1)$  is the energy  $E(\text{TiC-H})$  and will thus be an average (i.e., energy  $\text{TiC-H}$  for an average sized particle of density  $N_1$ );  $E(N_r) = E(\text{TiH}) \approx 0.27 \text{ eV}$  (see page 111);  $N_r$  and  $N_1$  are listed as  $2.9 \times 10^{21}$  and  $1.0 \times 10^{13}$  in Table XV, respectively;  $\theta(N_1)$  was assumed to be equal to one (see page 137) and  $\theta(N_r) = \theta(\text{Ti}) = 6 \times 10^{-3}$  (see page 97).

Evaluation of Equation(117) yields

$$E(\text{TiC-H}) \text{ for alloy CC} \approx 0.98 \text{ eV}. \quad (118)$$

Using the other alloys would give either low values (0.16 eV in BC) or unreasonably high ones, but then, these alloys did not obey very well theoretical predictions. The low value would mean that small TiC particles do not trap as effectively as large ones (e.g., in BC), while the high value may result from the fact that large particles trap more than assumed (i.e., there are more sites than just at the interface) as was found when discussing discrepancies between theory and experiment. For the sake of comparison, Asaoka gave a value of  $E(\text{TiC-H})$  as:

$$0.8 \text{ eV} < E(\text{TiC-H}) < 0.98 \text{ eV} \quad (119)$$

which compares with the value for alloy CC.

#### F.5 Conclusion:

A simple theoretical analysis of irreversible trapping by TiC particles during the first polarization transients has been proposed. The variable of interest was defined as being the occupancy per total (reversible + irreversible) number of traps, and was used in the classical trapping equation. The resulting equations allowed us to calculate the ratio  $\bar{k}/\bar{p}$  of the total capture rate constant over the release rate constant. A plot of  $\bar{k}/\bar{p}$  versus the relative magnitudes of irreversible and reversible trapping was obtained, demonstrating that the kinetics of trapping during the first polarization increase with increasing density of irreversible traps and with decreasing hydrogen concentration. Experimental results on the diffusivity of hydrogen through the carburized alloys BC, CC and DC were examined using the theory. Most theoretical predictions were in general verified and allowed us to estimate  $\bar{k}$  and the interaction energy  $E(\text{Ti-C-H})$ . ( $E(\text{TiC-H}) \approx 0.98 \text{ eV}$ ). In particular, the presence of TiC in alloy BC increases by a factor of 7.5 the trapping kinetics, compared to the uncarburized alloy B. Some discrepancies between theory and experiment seem to arise from the fact that small coherent particles have been neglected as possible reversible trapping sites, and from the fact that large TiC may trap more hydrogen than would be present as a monolayer at the interface.



### G. General Conclusions

The trapping characteristics of all the alloys in this study have been analyzed from electrochemical data. The variation in reversible trapping from one alloy to the other has been identified as due to titanium substitutional atoms. A careful theoretical and experimental examination allowed us to conclude that titanium substitutional atoms trap hydrogen with an interaction energy of about  $0.27 \text{ eV}$ , and with an occupancy which increases from  $3 \times 10^{-3}$  to  $7.5 \times 10^{-3}$  at.H/Ti atom when adding from 0.15Ti to 1.5Ti into iron for the fugacity used in the experiment. Since, the fugacity of hydrogen that will be used in subsequent tests will be higher, reversible trapping is expected to still occur, as additional trapping capacity remains. The interaction energy  $E(\text{Ti-H})$  thus places Ti on an equal basis with other potential reversible traps such as grain boundaries and dislocations. Other possible experimental factors such as surface or concentration effects were eliminated as competitors to trapping by titanium, after detailed theoretical and experimental analysis.

Irreversible trapping was attributed to titanium carbide particles, in agreement with literature findings. A simple theoretical analysis allowed us to predict the diffusion behavior of hydrogen for a varying density of irreversible traps. The interaction energy  $E(\text{TiC-H})$  was estimated as being equal on the average to  $0.98 \text{ eV}$ . An important restriction of the analysis was discussed in terms of a different trapping efficiency with different particle size or degree of coherency. In

particular, a small particle seems to be trapping less strongly than a large one.

All results of Chapter II concerning the trapping characteristics of the alloys in use in this study have been summarized in Table XVII. These results contribute basic information for subsequent chapters.

TABLE XVII

Nature of the trap	Character of the trap at room temperature	$E(\text{trap-H}) (\text{eV})$
Titanium carbide particle (TiC)	Irreversible	0.98 0.8 - 0.98 <sup>(25)</sup>
Grain Boundary	Reversible	0.27 <sup>(62)</sup> 0.55 - 0.61 <sup>(25)</sup>
Dislocation	Reversible	0.25 <sup>(60)</sup>
Titanium substitutional atom	Reversible	0.27
Lattice site	Very reversible diffusion site	0.08. <sup>(81)</sup>

Table XVII: Classification of the traps present in Fe-Ti and Fe-Ti-C alloys used in this study.



### CHAPTER III

## HYDROGEN-INDUCED CRACKING OF FE-TI ALLOYS

### (STATIC HYDROGEN EMBRITTLEMENT)

#### A. Introduction

In this chapter we will describe hydrogen-induced cracking as the nucleation and growth of cracks in iron-titanium alloys as a result of cathodic charging with hydrogen, in the absence of an external stress. Several significant contributions in this area have previously been made, <sup>(11,14,25,100-104)</sup> particularly by Bernstein. <sup>(24,61,105,106)</sup>

One of the major findings of these latter studies was that the crack path in iron could be systematically varied from transgranular to intergranular and vice-versa by heat treatment. This led to the hypothesis that the partitioning of interstitial solutes and/or particles at grain boundaries was a determining factor in crack nucleation. As was discussed in Chapter I, this result is compatible with low temperature fracture studies performed on iron (without hydrogen charging). Carbon was shown to be of primary importance in controlling the crack path, although whether carbon protects the grain boundary from the embrittling effect of oxygen, <sup>(107)</sup> or strengthens it by forming carbide complexes, is not clear. In any case, it was observed <sup>(107)</sup> that when samples were quenched from high temperature (little carbon at the grain boundaries) low temperature intergranular brittle fracture occurred. Further, by lowering the temperature before quenching, so

that carbon can partition between the lattice and grain boundary, fracture is transgranular and ductility can be quite large. In Fe-Ti alloys, the situation is somewhat different, since carbon is mostly present as a carbide. <sup>(41)</sup> However, even in this case it has been shown <sup>(25)</sup> that residual or redissolved carbon and carbides can still partition to the grain boundaries, by varying the heat treatment. In particular, using carbon 14 audioradiography technique, Asaoka <sup>(25)</sup> demonstrated that furnace cooled and annealed samples exhibited more carbon and carbide partitioning than quenched specimens. Whenever carbon and/or carbides were not present on the grain boundaries, low temperature fracture tests showed a predominantly brittle intergranular fracture, <sup>(25)</sup>, <sup>(107)</sup> in the absence of hydrogen.

In attempting to relate these results to hydrogen-induced cracking of iron, Bernstein <sup>(105)</sup> has concluded that "the crack path transition could not be directly correlated with the solubility of carbon nor its partitioning between grain boundaries and grain interiors, although these factors are undoubtedly important." The same author found that intergranular cracking in iron was favored by a high annealing temperature, moderately rapid cooling rates, a high oxygen-to-carbon ratio and the absence of mobile interstitial solutes (i.e., mainly carbon). These last two conclusions agree quite well with the fact that Fe-Ti alloys invariably exhibit intergranular cracking when hydrogen charged. <sup>(105)</sup>

As to what exactly serves as a crack nucleus is still a subject of controversy. Several authors <sup>(24)</sup> have proposed that carbide



particles or complexes present on the grain boundaries are the nuclei. For instance, Bernstein<sup>(24)</sup> explains the high crack frequency of furnace-cooled decarburized iron by the existence of grain boundary Fe-O-C complexes, allowing a large concentration of dissociated hydrogen; on the contrary, water quenched specimens do not exhibit such complexes, so that hydrogen may attach to the existing Fe-O pairs, thereby reducing the amount of dissociated hydrogen on grain boundaries. These findings are, however, not valid in Fe-Ti alloys where Asaoka<sup>(25)</sup> showed that grain boundaries, where a large carbide concentration existed, crack less than boundaries with a low carbide population. Asaoka suggests other non-carbon containing particles, or even in some cases, isolated TiC particles can originate the cracking. His basic conclusion is thus that, even though titanium carbide particles may nucleate cracks, if they are present in large amounts on a boundary, they can reinforce its strength so that the crack does not propagate. On the contrary, isolated particles are potentially more dangerous, because the adjacent boundary is weaker. In any event, be it a carbide or not, it is a general consensus in the literature that particles are potential crack nuclei. (104), (106)

In contrast with the above studies, the kinetics of crack nucleation and growth in the presence of hydrogen have been the subject of much less study. Generally, it has been found that the number of cracks in hydrogen charged iron increases continuously with charging time and reaches a maximum value (e.g., Ref. (103), (61)). When titanium is added to iron, however, a striking change occurs as shown by Bernstein and Rath,<sup>(61)</sup>

who found two basic differences in behavior between hydrogen charged Ferrovac-E and Fe-0.15Ti, Figure 39:

- a) for a same grain size and same charging current density Fe-0.15Ti exhibited less damage than Ferrovac E
- b) the kinetics of hydrogen-induced cracking revealed a plateau behavior for Fe-0.15Ti, absent in Ferrovac E.

Clearly, these differences, if explained, could shed light on the phenomena of hydrogen-induced damage in iron alloys, as well as the role of traps. We will analyze such behavior, relating the observations to the nature and strength of traps in the iron-titanium alloys. Specifically, the nucleation process and the nature of cracking nuclei will be discussed.

#### B. A Kinetic Model of Hydrogen-Induced Cracking in Fe-Ti Alloys.

##### B. 1. Development of the model:

This model relies on the findings of the previous chapter on trapping in Fe-Ti alloys, where it was found that in terms of decreasing trapping energy, (see Table XVII):

$$E(\text{TiC-H}) \gg E(\text{GB-H}), E(\text{Ti-H}), E(\text{disl.-H}) \gg E(\text{lattice-H}) \quad (120)$$

We then consider as main variables, four populations of hydrogen in the matrix:

$$N_H^T = N_H^d + N_H^{\text{Ti}} + N_H^{\text{GB}} + N_H^{\text{TiC}} \quad (121)$$

where\*  $N_H^T$  = total concentration of hydrogen

---

\* Note: all populations are expressed in atoms H/cm<sup>3</sup>



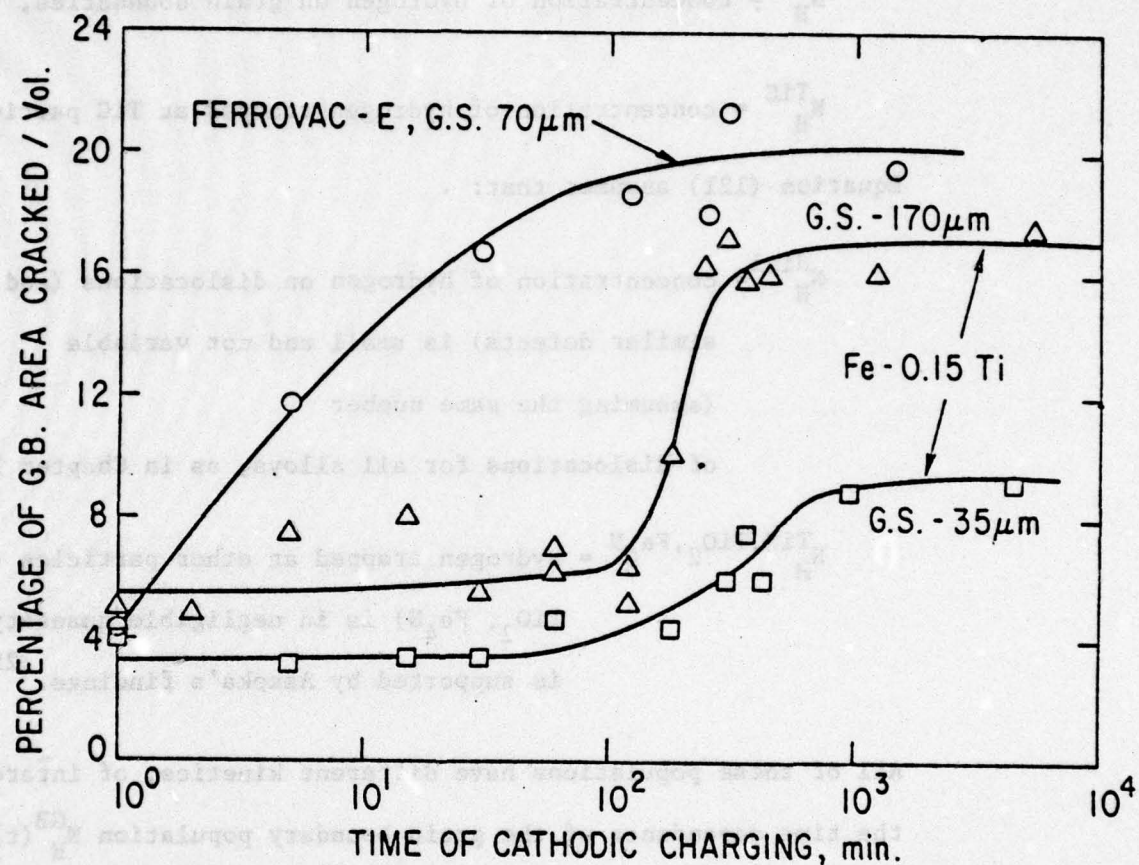


Figure 39 : Extent and Kinetics of Grain Boundary Cracking for Ferrovac E and Alloy B. (Ref.24 ).

$N_H^d$  = concentration of diffusing (lattice) hydrogen,

$N_H^{Ti}$  = concentration of hydrogen trapped at titanium sites,

$N_H^{GB}$  = concentration of hydrogen on grain boundaries,

$N_H^{TiC}$  = concentration of hydrogen trapped at TiC particles

Equation (121) assumes that:

$N_H^{disl.}$  = concentration of hydrogen on dislocations (and other similar defects) is small and not variable (assuming the same number of dislocations for all alloys, as in Chapter I)

$N_H^{TiN, TiO_2, Fe_4N}$  = hydrogen trapped at other particles (TiN,  $TiO_2$ ,  $Fe_4N$ ) is in negligible quantity. This is supported by Asaoka's findings. (25)

All of these populations have different kinetics; of interest here is the time dependence of the grain boundary population  $N_H^{GB}(t)$ , for reasons invoked later on. The kinetics for this population will be found by difference between  $N_H^T$  and the other populations, using Equation (121). To accomplish this, the kinetic behavior of these other populations are calculated below:

#### B.1.a. Calculation of $N_H^T(t)$ :

Consider a membrane of thickness  $L$  of the Fe-Ti alloy



originally free of hydrogen, which is being charged on both sides with hydrogen at a constant concentration  $C_0$ . The initial boundary conditions are:

$$x = 0, L : C = C_0 \text{ at } t > 0$$

$$0 < x < L : C = 0 \text{ at } t = 0$$

Using Fick's second law, and the method of separation of variables, the formal solution at a distance  $x$  in the membrane is:

$$C = C_0 \left[ 1 - 4 \sum_{k=1}^{\infty} \frac{1}{(2k-1)\pi} \sin \frac{(2k-1)\pi x}{L} \exp \left( \frac{-(2k-1)^2 \pi^2 D t}{L^2} \right) \right] \quad (122)$$

where  $k$  is here a dummy variable.

For long times:

$$C \approx C_0 \left[ 1 - \frac{4}{\pi} \sin \frac{\pi x}{L} \exp \left( - \frac{\pi^2 D t}{L^2} \right) \right] \quad (123)$$

For the sake of simplicity,  $N_H^T$  is assumed to vary monotonically in time, and to follow an exponential law of the type:

$$N_H^T(t) = N_H^T = N_{HS}^T (1 - e^{-at}) \quad (124)$$

where

$$N_{HS}^T = \text{saturation value of } N_H^T, \text{ for } t = \infty$$

$a$  = constant, denoting the kinetics of absorption of hydrogen in the lattice, which is usually taken as:

$$a \propto D/L^2 \quad (125)$$

where:

$D$  = diffusion coefficient of hydrogen in the alloy considered

$L$  = thickness of the specimen

To be more rigorous,  $N_H^T(t)$  should also have included a dependence on  $x$ , as:  $N_H^T(x,t) = N_{HS}^T (1-F(x)e^{-at})$ . It will be considered here that one observes the variation in hydrogen populations at a fixed location in the lattice, i.e.,  $F(x) = \text{constant}$ . For the sake of simplicity, this constant was taken as one, ( $F(x) = 1$ ).  $N_H^T(t)$  should then be visualized as the quantity of hydrogen entering the region of the lattice considered, at time  $t$ .

#### B.1.b Calculation of $N_H^{TiC}(t)$

Consider the trapping reaction:



Assuming kinetics of the first order, the trapping rate is:

$$d \theta^{TiC} / dt = k' N_H^T (n_{HS}^{TiC} - \theta^{TiC}) \quad (127)$$

where:

$k'$  = irreversible trapping rate constant,

$$\theta^{TiC} = N_H^{TiC} / N^{TiC}, \text{ with} \quad (128)$$

$N^{TiC}$  = density of titanium carbide particles and

$n_{HS}^{TiC}$  = average number of H atoms trapped at saturation per particle



Thus, at saturation,  $d \theta^{\text{TiC}}/dt = 0$ , or  $\theta_S^{\text{TiC}} = n_{\text{HS}}^{\text{TiC}} = N_{\text{HS}}^{\text{TiC}}/N^{\text{TiC}}$

Equation (126) assumes irreversible trapping by TiC particles

( $p' = 0$ ); this has strong experimental support as previously discussed

(see Asaoka<sup>(25)</sup> and Chapter II). The solution to Equation (127), with

$\theta^{\text{TiC}} = 0$  at  $t = 0$  is:

$$\frac{N_{\text{H}}^{\text{TiC}}(t)}{N^{\text{TiC}}} = \theta^{\text{TiC}}(t) = n_{\text{HS}}^{\text{TiC}} \left[ 1 - \exp \left[ -k' N_{\text{HS}}^{\text{T}} \left( t - \frac{1}{a} + \frac{e^{-at}}{a} \right) \right] \right] \quad (129)$$

A major feature of Equation (129) is that  $\theta^{\text{TiC}}$  may saturate independently

of  $N_{\text{H}}^{\text{T}}$  (i.e., independently of "a"). The fact that the kinetics of

$N_{\text{H}}^{\text{TiC}}(t)$  depend little on "a" is due to "a" being very small compared

to  $t$  ("a"  $\approx 10^{-4} \text{ s}^{-1}$ ; see page 72), so that:

$$e^{-at}/a \approx 1/a \quad (\text{for } t < 10^4 \text{ s}).$$

and for times up to  $t < 1/a$  one has:

$$\theta^{\text{TiC}}(t) \approx n_{\text{HS}}^{\text{TiC}} \left[ 1 - \exp(-k' N_{\text{HS}}^{\text{T}} t) \right] \quad (130)$$

Another important feature of irreversible trapping resides in the

steady state value of its population; indeed, as shown in Equation (129)

or in Equation (130) by taking  $t = \infty$ , an irreversible trap such as

TiC will trap the same quantity of hydrogen, independent of its trap-

ping parameter, or of what is happening elsewhere in the lattice. The

saturation value of  $N_{\text{H}}^{\text{TiC}}$  is solely dependent upon the number of

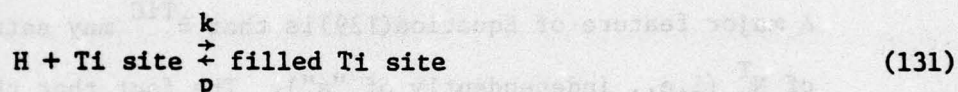
titanium carbide particles  $N^{\text{TiC}}$ , and the total trapping capacity of

these particles  $n_{HS}^{TiC}$ . It would then, for example, be difficult to talk of a dynamic equilibrium between H trapped on TiC and diffusing hydrogen. These considerations are of fundamental importance when applying the model to hydrogen-induced cracking.

### B.1.c. Calculation of $N_H^{Ti}(t)$

#### First approach:

The case of  $N_H^{Ti}(t)$  could be treated similarly to  $N_H^{TiC}(t)$ , by considering:



and for kinetics of the first order, this would lead to a trapping rate:

$$\frac{d\theta^{Ti}}{dt} = kN_H^T(1-\theta^{Ti}) - p\theta^{Ti} \quad (132)$$

where:

$\theta^{Ti} = N_H^{Ti}/N^{Ti}Z$ , with  $N^{Ti}$  = concentration of Ti atoms in the alloy considered and  $1 < Z < 6$  (see Chapter II).

The parameter  $k$  and  $p$  are capture and release constants, respectively, as described before in the McNabb-Foster model. (51)

Replacing  $N_H^T$  by its value (Equation (124)) in Equation (132) and solving for  $\theta^{Ti}(t)$  gives as a general solution:

$$y = \exp \left[ - \int_0^t (kN_{HS}^T(1-e^{-at_1}) + p) dt_1 \right] \left[ \int_0^t \exp \left( \int_0^{t_1} (kN_{HS}^T(1-e^{-at_2}) + p) dt_2 \right) dt_1 \right] \quad (133)$$

where  $y = \theta^{Ti}$



The first integral may be evaluated as:

$$\exp \left[ - \int_0^t (kN_{HS}^T (1-e^{-at_1}) + p) dt_1 \right] = \exp \left[ \frac{kN_{HS}^T}{a} (1-e^{-at}) - (kN_{HS}^T + p)t \right] \quad (134)$$

But, the integral of the form  $\exp At + Be^{-at} dt$  in Equation (131) is, to the best of my knowledge, not solvable in closed form. However, as will be seen subsequently for this particular case, as was true for permeation, a low occupancy exists so that:

$$\theta^{Ti} \ll 1$$

The differential equation thus reduces to:

$$\frac{d\theta^{Ti}}{dt} = kN_{HS}^T (1-e^{-at}) - p\theta^{Ti} \quad (135)$$

which may be solved as:

$$\theta^{Ti} = y = \exp \left[ - \int_0^t p dt_1 \right] \left\{ \int_0^t \exp \left( \int_0^{t_1} p dt_2 \right) kN_{HS}^T (1-e^{-at_1}) dt_1 \right\} \quad (136)$$

Finally:

$$\frac{N^{Ti}(t)}{N^{Ti}} = \theta^{Ti}(t) = \frac{kN_{HS}^T}{p(p-a)} \left[ p(1-e^{-at}) - a(1-e^{-pt}) \right] \quad (137)$$

At steady state:

$$\theta_S^{Ti}(t = \infty) = \frac{N_{HS}^{Ti}}{N^{Ti}} = \frac{kN_{HS}^T}{p} \quad (138)$$

Several features of interest are inferrable from Equation (137)

a) The saturation value  $N_{HS}^{Ti}$  of  $N_H^{Ti}$  is proportional to the trapping constant  $k$ , to the saturation value  $N_{HS}^T$  of the total hydrogen concentration, to the density of the titanium atoms  $N^{Ti}$ , and inversely proportional to the release parameter  $p$ . The proportionality to  $N_{HS}^T$  and the dependence on  $k$  and  $p$  are consistent with a dynamic equilibrium existing between titanium reversible traps and the remaining hydrogen in the matrix. As was shown in the preceding Chapter, Oriani<sup>(52)</sup> also assumed the possibility of dynamic equilibrium, but in his case, between diffusing and trapped hydrogen.

b) A useful feature of Equation (137) is that it reaches steady state at the same time as  $N_H^T$ , because of the term in  $e^{-at}$ . As we shall see later, this means that a reversible trap such as titanium cannot be responsible for the presence of a plateau in the kinetics of hydrogen-induced cracking.

c) Finally, Equation (137) shows that  $N_H^{Ti}$  varies continuously with time, without presenting any maxima or minima. But, as we shall see later on, the existence of the equilibrium  $N_H^{Ti} \rightleftharpoons N_H^d$ , and the fact that  $N_H^d$  does present maxima and minima (see experimental results on Figures 39, 47-49) is in contradiction with  $N_H^{Ti}(t)$  being such a continuously increasing function of time. Because of this anticipation of results, another approach is necessary to calculate  $N_H^{Ti}$ .

#### Second approach:

As considered by Oriani<sup>(52)</sup> and because of the above findings, we assume the following equilibrium:





As shown by Darken, (109) and used by Oriani, (52) for the case of an interstitial, the activity  $a_H^i$  of hydrogen on site  $i$  may be expressed as:

$$a_H^i = K \frac{\theta^i}{1-\theta^i} \quad (140)$$

where:  $\theta^i$  = fractional occupancy of H on site  $i$

$K$  = constant, most commonly, but not necessarily equal to unity. (109)

The validity of Equation (140) is based upon the fact that the sites constitute a finite population, and on the assumption that there is no interaction between occupied sites (quasi-ideal solution (109)).

We may then consider  $K_1$  as being:

$$K_1 = \frac{\theta^{Ti}(1-\theta^d)}{\theta^d(1-\theta^{Ti})} \quad (141)$$

Furthermore, as seen previously, and as will be further verified,

$$\theta^{Ti}, \theta^d \ll 1$$

so that  $K_1$  may also be expressed as: 
$$K_1 = \frac{N_H^{Ti} N^L}{N_H^d N^{Ti}} \quad (142)$$

where  $N^L$  = number of lattice sites/cm<sup>3</sup> and  $N_H^{Ti}$ ,  $N_H^{Ti}$ ,  $N_H^d$  are as before.

From Equation (142)  $N_H^{Ti}$  may be expressed in terms of  $N_H^d$ . As will be verified in the numerical study, and as said, since  $N_H^d$  does not increase monotonously with time,  $N_H^{Ti}$  will now vary in a different way than as predicted by Equation (137). Since this behavior is probably closer to reality, the second approach will be adopted.

B.1.d. Calculation of  $N_H^d(t)$ :

$N_H^d(t)$  will not be calculated, but will instead be eliminated by expressing it in terms of  $N_H^{GB}$ . Since grain boundaries are reversible traps (Asaoka<sup>(25)</sup>) of trapping energy close to Ti (see Table XVII), it is possible to consider a dynamic equilibrium between:



where, as before:

$$K_2 = \frac{a_H^d}{a_H^{GB}} = \frac{\theta^d (1 - \theta^{GB})}{\theta^{GB} (1 - \theta^d)} \quad (144)$$

Furthermore, since  $\theta^d \ll 1$ , 2 cases arise: if

$$\theta^{GB} \ll 1: K_2 = \frac{\theta^d}{\theta^{GB}} = \frac{N_H^d N_H^{GB}}{N_H^{GB} N_H^L} \quad (145)$$

if

$$\theta^{GB} \approx 1: K_2 = \frac{\theta^d (1 - \theta^{GB})}{\theta^{GB}} = \frac{N_H^d (N_H^{GB} - N_H^L)}{N_H^{GB} N_H^L} \quad (146)$$

$N_H^{GB}$  = number of sites on grain boundaries/cm<sup>3</sup>. All information is now available to evaluate  $N_H^{GB}$ .



B.l.e. Calculation of  $N_H^{GB}(t)$ :

$$\text{From Equation (121): } N_H^{GB} = N_H^T - N_H^{Ti} - N_H^{TiC} - N_H^d \quad (147)$$

First case:  $\theta^{GB} \ll 1$

Considering first the case where  $\theta^{GB} \ll 1$ , one has

$$N_H^{GB} = N_H^T - N_H^{TiC} - \frac{N_H^{Ti} K_1 N_H^d}{N^L} - \frac{K_2 N_H^{GB} N^L}{N^{GB}}, \quad (148)$$

or, using Equation (145)

$$N_H^{GB} = N_H^T - N_H^{TiC} - \frac{K_2 K_1 N_H^{Ti} N_H^{GB}}{N^{GB}} - \frac{K_2 N^L N_H^{GB}}{N^{GB}} \quad (149)$$

From which:

$$N_H^{GB}(t) = \frac{N_H^T(t) - N_H^{TiC}(t)}{(K_1 K_2 \frac{N_H^{Ti}}{N^{GB}} + K_2 \frac{N^L}{N^{GB}} + 1)} \quad (150)$$

One may verify by inspection that the boundary conditions are obeyed  
i.e.,

$$N_H^{GB}(t = 0) = 0 \text{ since } N_H^T(t = 0) = N_H^{TiC}(t = 0) = 0 \text{ and}$$

$$N_H^{GB}(t) = 0 \text{ if } N^{GB} = 0$$

Thus at steady state:

$$N_H^{GB}(\infty) = \frac{N_{HS}^T - N_{HS}^{TiC}}{K_1 K_2 \frac{N_H^{Ti}}{N^{GB}} + K_2 \frac{N^L}{N^{GB}} + 1} \quad (151)$$

Second case:  $\theta^{GB} \approx 1$

When  $\theta^{GB}$  is close to 1, Equation (146) has to be used giving:

$$N_H^{GB} = N_H^T - N_H^{TiC} - \frac{(1+K_1 \frac{N^{Ti}}{N^L}) K_2 N_H^{GB} N^L}{N_H^{GB} - N_H^{GB}} \quad (152)$$

This is a second order equation whose solutions are:

$$N_H^{GB} = \frac{N_H^{GB} + y + m \pm \sqrt{(N_H^{GB} + y + m)^2 - 4N_H^{GB}y}}{2} \quad (153)$$

where:

$$y = N_H^T - N_H^{TiC} \quad \text{and} \quad (154)$$

$$m = (1 + K_1 N^{Ti}/N^L) K_2 N^L \quad (155)$$

The correct solution is chosen as the negative one, since this will verify the boundary conditions  $N_H^{GB}(t=0) = 0$  and  $N_H^{GB} = 0$ , when  $N_H^{GB} = 0$

The steady state value is thus:

$$N_H^{GB}(t=\infty) = \frac{N_H^{GB} + y(\infty) + m - \sqrt{(N_H^{GB} + y(\infty) + m)^2 - 4N_H^{GB}y(\infty)}}{2} \quad (156)$$

where:

$$y(\infty) = N_{HS}^T - N_{HS}^{TiC} \quad \text{and } m \text{ is defined as before.}$$



Note:

The unknown populations,  $N_H^{Ti}(t)$  and  $N_H^d(t)$  will vary with  $N_H^{GB}(t)$  according to Equation (142) and (145,146) so that:

$$N_H^d(t) = K_2 \frac{N_H^L}{N_H^{GB}} N_H^{GB}(t) \quad \text{if } \theta^{GB} \ll 1 \quad (157)$$

$$N_H^d(t) = K_2 N_H^L \cdot \frac{N_H^{GR}(t)}{(N_H^{GB} - N_H^{GB}(t))} \quad \text{if } \theta^{GB} \approx 1 \quad (158)$$

and

$$N_H^{Ti}(t) = K_1 \frac{N_H^{Ti}}{N_H^L} \cdot N_H^d(t) \quad (159)$$

All populations  $N_H^{Ti}(t)$ ,  $N_H^d(t)$  and  $N_H^{GB}(t)$  have thus been evaluated in function of  $N_H^T(t)$  and  $N_H^{TiC}(t)$  whose kinetics are known.

B.2. Theoretical Results

Equations (150) through (159) were evaluated by an IBM 360 computer, using ALGOLWX language and numerical values relevant to the experimental conditions used later on (Section B.3). The programs for both  $\theta^{GB} \approx 1$  and  $\theta^{GB} \ll 1$  are shown in Appendix E.

B.2.a. Choice of numerical values

$N_{HS}^T$  is the total concentration of hydrogen in the lattice when steady state is achieved. Under the experimental conditions described in Section B.3, this chapter, and using a Leco hydrogen analyzer, this was found to be:

$$N_{HS}^T = 1.88 \times 10^{20} \text{ at.H/cm}^3. \quad (160)$$

with an experimental error of about  $5 \times 10^{18} \text{ at.H/cm}^3$

(More information concerning this solubility value may be found in Section B.4).

The term "a" is proportional to  $D/L^2$ : as an example for Fe-0.15Ti with the evaluated diffusivity and for a specimen thickness of 30 mils ( $7.6 \times 10^{-2} \text{ cm}$ ):

$$a = 1.7 \times 10^{-4} \text{ s}^{-1} \quad (161)$$

The product  $N_{HS}^{TiC} n_{HS}^{TiC}$ , which is the saturation value of  $N_H^{TiC}$ , and which is denoted by  $N_{\theta}$  in the program, will be:

$$N_{\theta} = N_{HS}^{TiC} n_{HS}^{TiC} \gg 10^{15} \quad (162)$$

This value arises from the fact that  $N^{TiC}$  is at least equal to  $10^{15}$  (see Figure 4, Chapter I) and  $n_{HS}^{TiC}$  is much larger than one (see Chapter II).

The term  $k'$  is the capture rate of irreversible TiC traps: it was shown in Chapter II that this rate for a reversible Ti trap was about  $7 \times 10^{-24}$ . We are sure this will be higher for an irreversible trap, obtaining the following inequality (as discussed in Chapter III, Section F).

$$k' > 7 \times 10^{-24} \quad (163)$$



The term  $K_1$  expresses the equilibrium between diffusing hydrogen and hydrogen trapped at Ti sites which is also valid at steady state, so that:

$$K_1 = \frac{N_{HS}^{Ti} N^L}{N_{HS}^d N^{Ti}} \quad (164)$$

From permeation experiments performed at the fugacities necessary to obtain hydrogen-induced cracking (see Section B.3., this chapter), it was found that:

$$N_{HS}^d = 5.6 \times 10^{18} \text{ at.H/cm}^3 \text{ for alloy B.} \quad (165)$$

Then, with Equation (164), replacing  $N^L$  and  $N^{Ti}$  by their values,

$$K_1 = 4.6 \times 10^4 \theta_S^{Ti} \text{ where } \theta_S^{Ti} = N_{HS}^{Ti} / N^{Ti}. \quad (166)$$

Moreover, the low fugacity experiments in Chapter II showed that  $\theta_S^{Ti} = 10^{-3}$ . At higher fugacity,  $\theta_S^{Ti} > 10^{-3}$ , but  $< 1$  so that:

$$4.6 \times 10^4 > K_1 > 460 \quad (167)$$

The term  $K_2$  expresses the equilibrium between diffusing hydrogen and hydrogen on grain boundaries. Two cases will arise, depending on  $\theta_{GB}$ :

If  $\theta_{GB} \ll 1$ , at steady state:

$$K_2 = \frac{N_{HS}^d N^{GB}}{N_{HS}^{GB} N^L} \quad (168)$$

In the same way as for  $K_1$ , one has:

$$K_2 = 2.1 \times 10^{-5} (\theta_S^{GB})^{-1} \quad (169)$$

No value may be given to  $K_2$ , however, since  $K_1$  and  $K_2$  are not independent.

In fact,  $K_1/K_2 = \theta_S^{Ti}/\theta_S^{GB}$ , from which we can obtain by algebraic manipulation:

$$K_2 = N_{HS}^d N^{GB} / (3.6 \times 10^{43} - 8.3 \times 10^{38} K_1), \text{ for alloy B} \quad (170)$$

This above relationship was used in the computer programs to find  $K_2$  when  $K_1$  was assigned a particular value.

The second case is  $\theta_S^{GB} \approx 1$ , which leads to:

$$K_2 = 2.1 \times 10^{-5} \left[ (\theta_S^{GB})^{-1} - 1 \right] \quad (171)$$

$K_2$  can be expressed directly in terms of  $K_1$ . Without detailing the fairly detailed algebra necessary, the following relationship is obtained:

$$K_2 = 10^{-5} \left[ 8.4 N^{GB} - 8.6y + 1.76 \times 10^{-4} K_3 N^L \right] / (4y - 8.4 \times 10^{-5} K_3 N^L) \quad (172)$$

where:

$$K_3 = 1 + K_1 N^{Ti}/N^L \text{ and } y = N_{HS}^T - N\theta \quad (173)$$

This relationship was a part of the computer program.

The term  $N^{GB}$  represents the number of grain boundary sites per unit volume capable of accepting hydrogen. Considering a grain size of  $80\mu$ , and an operative site every  $\alpha$ -Fe unit cell length, the total number of sites per grain is about  $2.4 \times 10^{11}$ , and the number of grains per  $\text{cm}^3$  is of the order of  $3.7 \times 10^6$  grains/ $\text{cm}^3$  (assuming spherical grains). Since a grain boundary is more than one atom wide and since it contains defects (e.g., particles, voids, dislocations) that may trap more than one hydrogen atom, we estimate that:



$$N_{H}^{GB} > 10^{18} \text{ sites/cm}^3 \quad (174)$$

We have now evaluated all the analytical terms necessary for the computer study of the grain boundary cracking model.

#### B.2.b Time dependence of the grain boundary hydrogen population:

The kinetics of  $N_{H}^{GB}(t)$ ,  $N_{H}^{Ti}(t)$  and  $N_{H}^d(t)$ ...since they will reach steady state together, will be the same. This originates from the fact that they have been considered to be in mutual equilibrium. As an example consider the effect of, say,  $N_{H}^{Ti}(t)$  on the kinetics of  $N_{H}^{GB}(t)$ . The presence of Ti atoms will slow the rise to steady state of  $N_{H}^T(t)$  (by lowering "a"), and thus slow down  $N_{H}^{GB}(t)$ . On the other hand, from Equation (150) for  $\theta^{GB} \ll 1$  and Equation (153) for  $\theta^{GB} \approx 1$ , it can be seen that the kinetics of  $N_{H}^{GB}(t)$  are solely dependent upon the difference in the kinetics of  $N_{H}^T(t)$  and  $N_{H}^{TiC}(t)$ ; i.e.,

$$N_{H}^{GB}(t) = f \left[ N_{H}^T(t) - N_{H}^{TiC}(t) \right] \quad (175)$$

Equation (175) also predicts that the steady state value of  $N_{H}^{GB}(t)$  will be solely dependent on the steady state values of  $N_{H}^{Ti}(t)$  and  $N_{H}^d(t)$ ; i.e., the saturation values of the hydrogen population in equilibrium with it. Theoretically, this comes about by the fact that  $N_{H}^T(t)$  contains  $N_{H}^{TiC}(t)$ , so that:

$$N_{HS}^{GB} = f' \left[ N_{HS}^{Ti} + N_{HS}^d \right] \quad (176)$$

Physically, one may understand this by the fact that because the TiC particles are irreversible traps (not in equilibrium with other populations) they will saturate at a value which is independent of the surrounding concentration (see a discussion of this point in Chapter II, page 137). In the same way, the saturation value of say  $N_H^d(t)$  will not depend on  $N_{HS}^{TiC}$ . Because of the equilibriums,  $N_H^d(t)$  with  $N_H^{Ti}(t)$  and  $N_H^{GB}(t)$ , these latter populations will saturate independently of whatever hydrogen is irreversibly trapped. These important results will now be illustrated as follows:

Figure 40 shows the variation of  $N_H^T$ ,  $N_H^{TiC}$  and  $N_H^{GB}$  with time:

$N_H^{TiC}(t)$  is seen to saturate long before the total population does (at  $t = 3 \times 10^3$  s, compared to  $t \approx 10^5$  s for  $N_H^T(t)$ ). This is due to the irreversible trapping rate  $k'$  (here  $k' = 8 \times 10^{-23}$ ) being higher than the reversible trapping rates; both terms are included in  $N_H^T(t)$ , as demonstrated in Chapter III. Such differences in trapping rates has an interesting consequence on  $N_H^{GB}(t)$ : as more and more hydrogen atoms become irreversibly trapped, the rate at which hydrogen enters the lattice (related to "a") will not be sufficient to supply the necessary quantity of hydrogen going to TiC particles. Since most of the particles are located in the lattice (see Chapter II), the resulting depletion in diffusing hydrogen (i.e.,  $N_H^d$ ) will have to be compensated by hydrogen atoms leaving both the grain boundaries as well as the substitutional Ti sites, in amounts controlled by the equilibrium constants  $K_2$  and  $K_1$ , respectively. As illustrated in



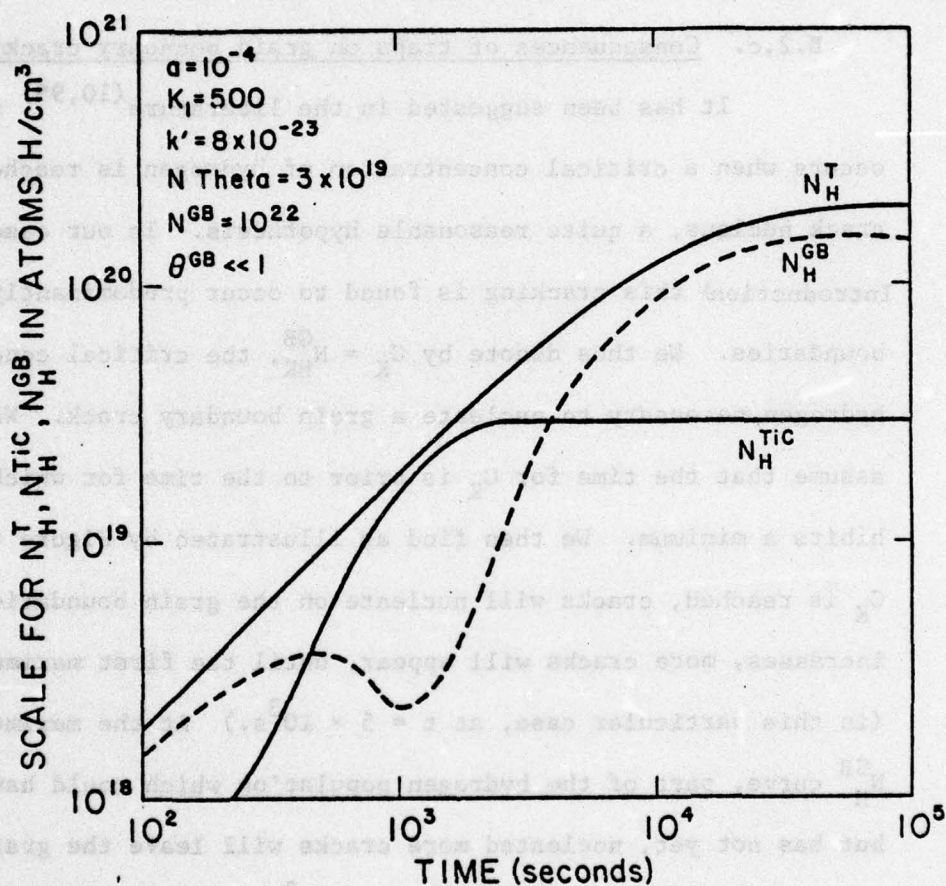


FIGURE 40.  
Evolution of the Total Population of Hydrogen  $N^T_H$ , of the Population of Hydrogen on Grain Boundaries  $N^{GB}_H$  and of the Population of Hydrogen on TiC Particles  $N^{TiC}_H$  with Time.

Figure 40, this depletion of  $N_H^{GB}(t)$  manifests itself as a minimum in the kinetics occurring at  $t = 10^3$  s., that is, when the value of  $N_H^{TiC}(t)$  is closest to  $N_H^T(t)$ . In the same way,  $N_H^d(t)$  and  $N_H^{Ti}(t)$  will also exhibit a minimum at that same time. The consequence of this behavior of the reversible trap population on hydrogen-induced cracking will now be considered.

#### B.2.c. Consequences of traps on grain boundary cracking:

It has been suggested in the literature<sup>(10,99)</sup> that cracking occurs when a critical concentration of hydrogen is reached at a potential crack nucleus, a quite reasonable hypothesis. In our case (see this chapter, Introduction) this cracking is found to occur predominantly on grain boundaries. We thus denote by  $C_K = N_{HK}^{GB}$ , the critical concentration of hydrogen necessary to nucleate a grain boundary crack. We further assume that the time for  $C_K$  is prior to the time for which  $N_H^{GB}(t)$  exhibits a minimum. We then find as illustrated by Figure 41 that when  $C_K$  is reached, cracks will nucleate on the grain boundaries; as  $N_H^{GB}(t)$  increases, more cracks will appear, until the first maximum is reached (in this particular case, at  $t = 5 \times 10^3$  s.) At the maximum in the  $N_H^{GB}$  curve, part of the hydrogen population which could have subsequently, but has not yet, nucleated more cracks will leave the grain boundary until the minimum is reached at  $t \approx 10^3$  s. Because cracking is an irreversible phenomena, the corresponding measure of damage, the extent of grain boundary cracking, will exhibit a plateau from the time at the maximum to the time at which the hydrogen concentration on grain boundaries regains this maximum value. After that, both the damage



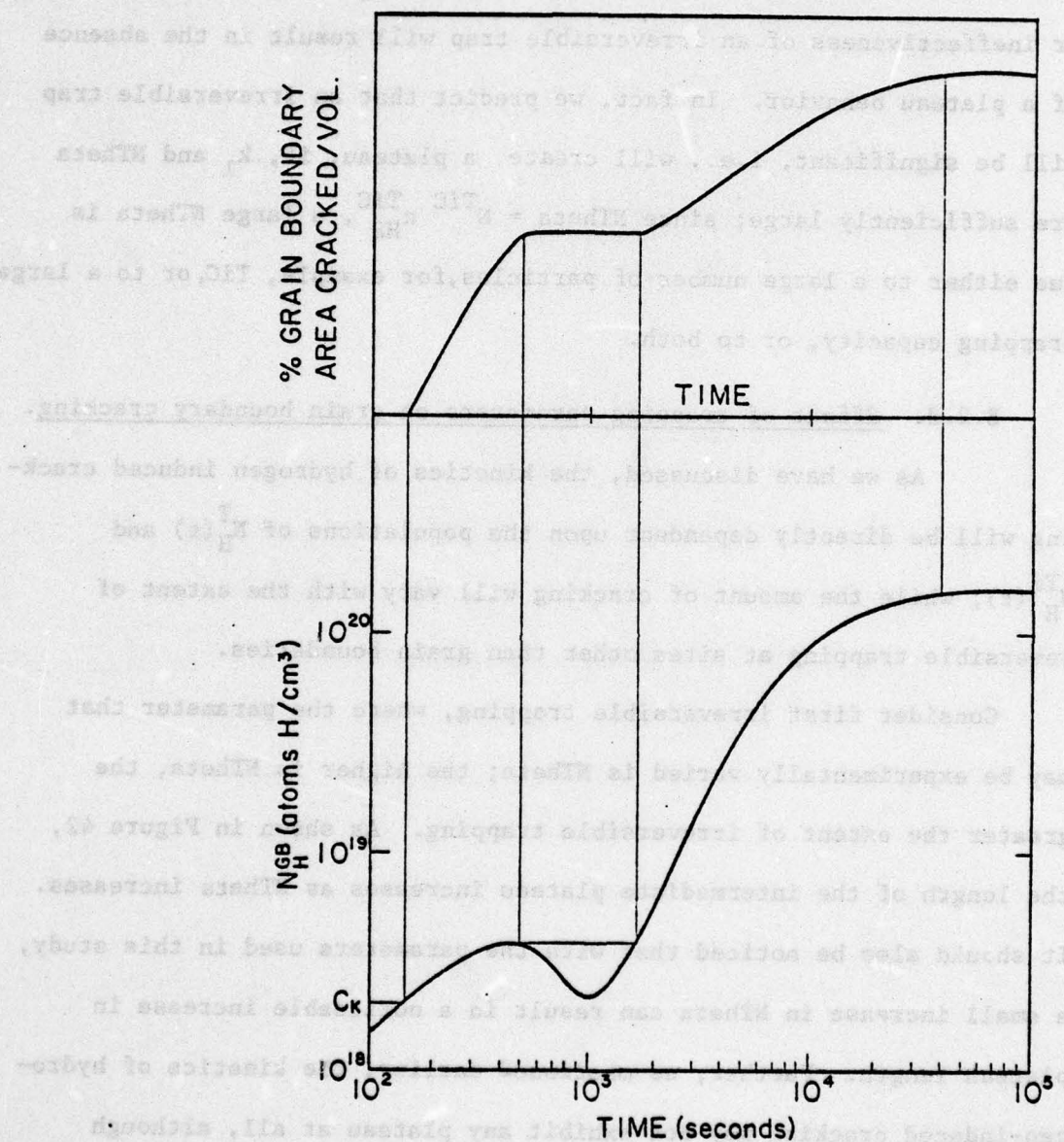


FIGURE 41.  
Relationship Existing between the Hydrogen Population on Grain Boundaries  $N_{GB}$  and of the Population of Hydrogen on TiC Particles  $N_{TiC}$  with Time.

and  $N_H^{GB}(t)$  will proceed towards a second maximum value. Because the appearance of such a plateau is solely due to  $N_H^{TiC}(t)$ , the absence or ineffectiveness of an irreversible trap will result in the absence of a plateau behavior. In fact, we predict that an irreversible trap will be significant, i.e., will create a plateau, if,  $k_1$  and  $N_{\theta}$  are sufficiently large; since  $N_{\theta} = N^{TiC} n_{HS}^{TiC}$ , a large  $N_{\theta}$  is due either to a large number of particles, for example,  $TiC$ , or to a large trapping capacity, or to both.

#### B.2.d. Effect of trapping parameters on grain boundary cracking.

As we have discussed, the kinetics of hydrogen induced cracking will be directly dependent upon the populations of  $N_H^T(t)$  and  $N_H^{Tj}(t)$ , while the amount of cracking will vary with the extent of reversible trapping at sites other than grain boundaries.

Consider first irreversible trapping, where the parameter that may be experimentally varied is  $N_{\theta}$ ; the higher is  $N_{\theta}$ , the greater the extent of irreversible trapping. As shown in Figure 42, the length of the intermediate plateau increases as  $N_{\theta}$  increases. It should also be noticed that with the parameters used in this study, a small increase in  $N_{\theta}$  can result in a noticeable increase in plateau length. Further, as mentioned earlier, the kinetics of hydrogen-induced cracking may not exhibit any plateau at all, although (weak) irreversible trapping may be present; this is the case for curve (1) on Figure 42, where  $N_{\theta} = 10^{19}$ . Thus, the fact that the damage does not present any plateau-like behavior cannot be taken as proof that irreversible trapping is absent. It simply means that



D-A045 331

CARNEGIE-MELLON UNIV PITTSBURGH PA DEPT OF METALLURG--ETC F/G 7/4  
THE ROLE OF TRAPPING ON HYDROGEN TRANSPORT AND EMBRITTLEMENT.(U)  
JUL 77 G M PRESSOUYRE, I M BERNSTEIN

N00014-75-C-0265

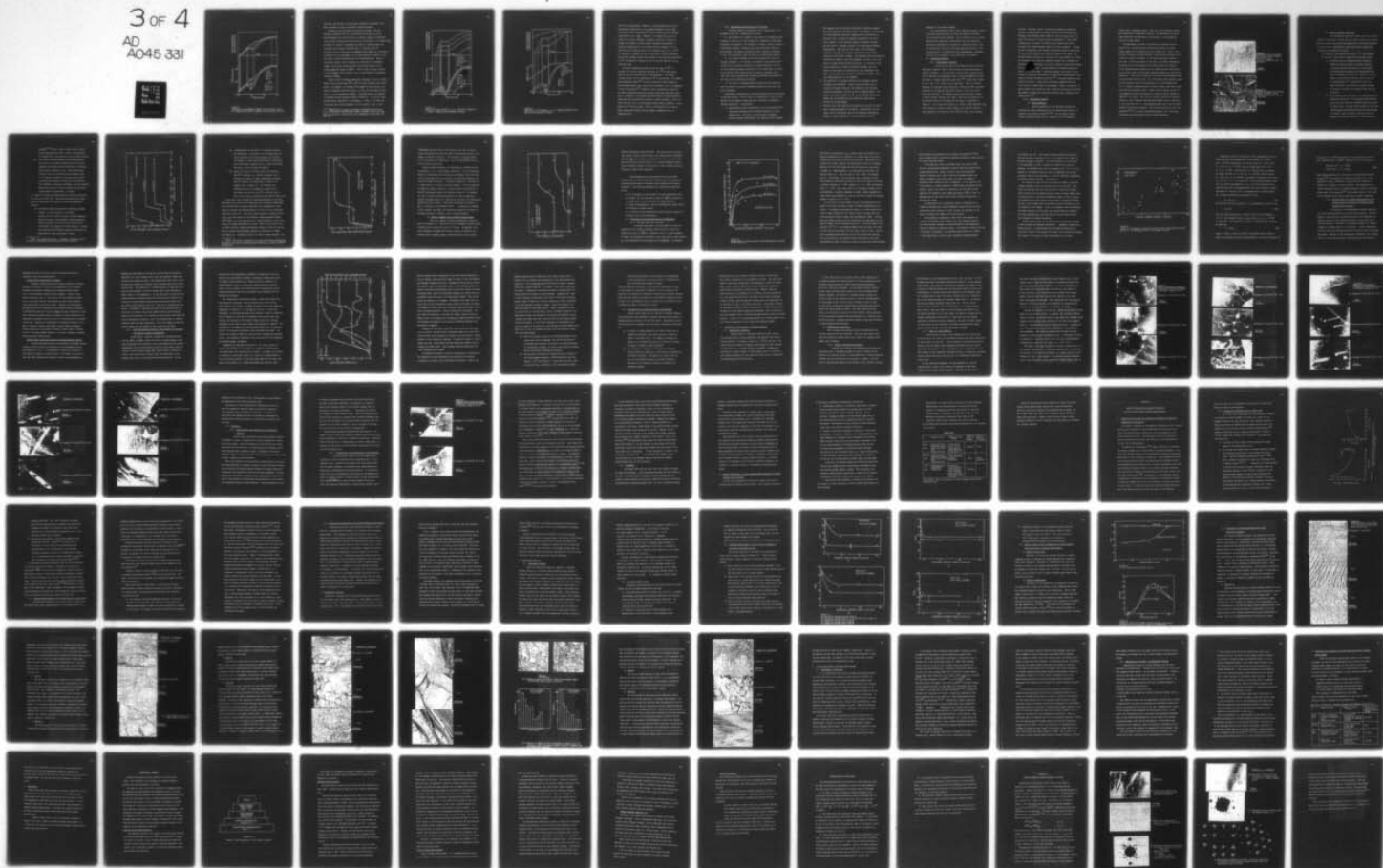
INCLASSIFIED

TR-7

NL

3 OF 4

AD  
A045 331



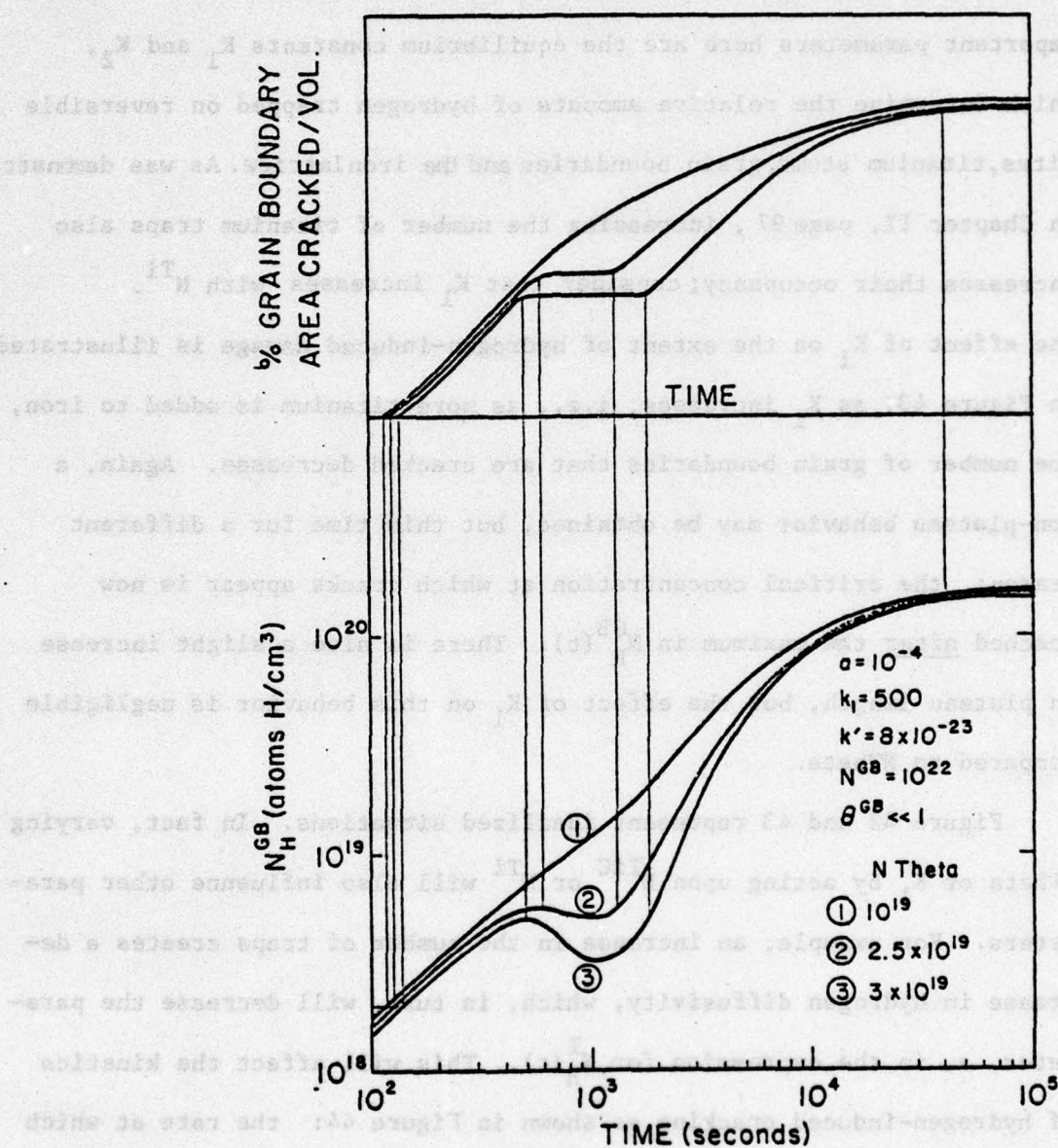


FIGURE 42.  
Influence of the Parameter N Theta (i.e. particles density and trapping efficiency) on  $N_H^{GB}$  and Grain Boundary Cracking.



the extent and kinetics of irreversible trapping are negligible, and thus are masked by other (reversible) trapping phenomena.

Consider now the influence of reversible trapping. The most important parameters here are the equilibrium constants  $K_1$  and  $K_2$ , which determine the relative amounts of hydrogen trapped on reversible sites, titanium atoms, grain boundaries and the iron lattice. As was demonstrated in Chapter II, page 97, increasing the number of titanium traps also increases their occupancy; consider that  $K_1$  increases with  $N^{Ti}$ . The effect of  $K_1$  on the extent of hydrogen-induced damage is illustrated in Figure 43; as  $K_1$  increases, i.e., as more titanium is added to iron, the number of grain boundaries that are cracked decreases. Again, a non-plateau behavior may be obtained, but this time for a different reason: the critical concentration at which cracks appear is now reached after the maximum in  $N_H^{GB}(t)$ . There is also a slight increase in plateau length, but the effect of  $K_1$  on this behavior is negligible compared to  $N_{Theta}$ .

Figure 42 and 43 represent idealized situations. In fact, varying  $N_{Theta}$  or  $K_1$  by acting upon  $N^{TiC}$  or  $N^{Ti}$  will also influence other parameters. For example, an increase in the number of traps creates a decrease in hydrogen diffusivity, which, in turn, will decrease the parameter,  $a$ , in the expression for  $N_H^T(t)$ . This will affect the kinetics of hydrogen-induced cracking as shown in Figure 44: the rate at which cracks nucleate decreases with decreasing,  $a$ . When,  $a$ , is high, the plateau may even totally disappear; on the contrary, a low,  $a$ , will

---

\*Note: A better example is probably a decrease in grain size (i.e. an increase in grain boundary traps), because in that case,  $N_{HS}^d$  does not increase at the same time (see experimental verification on page 158).

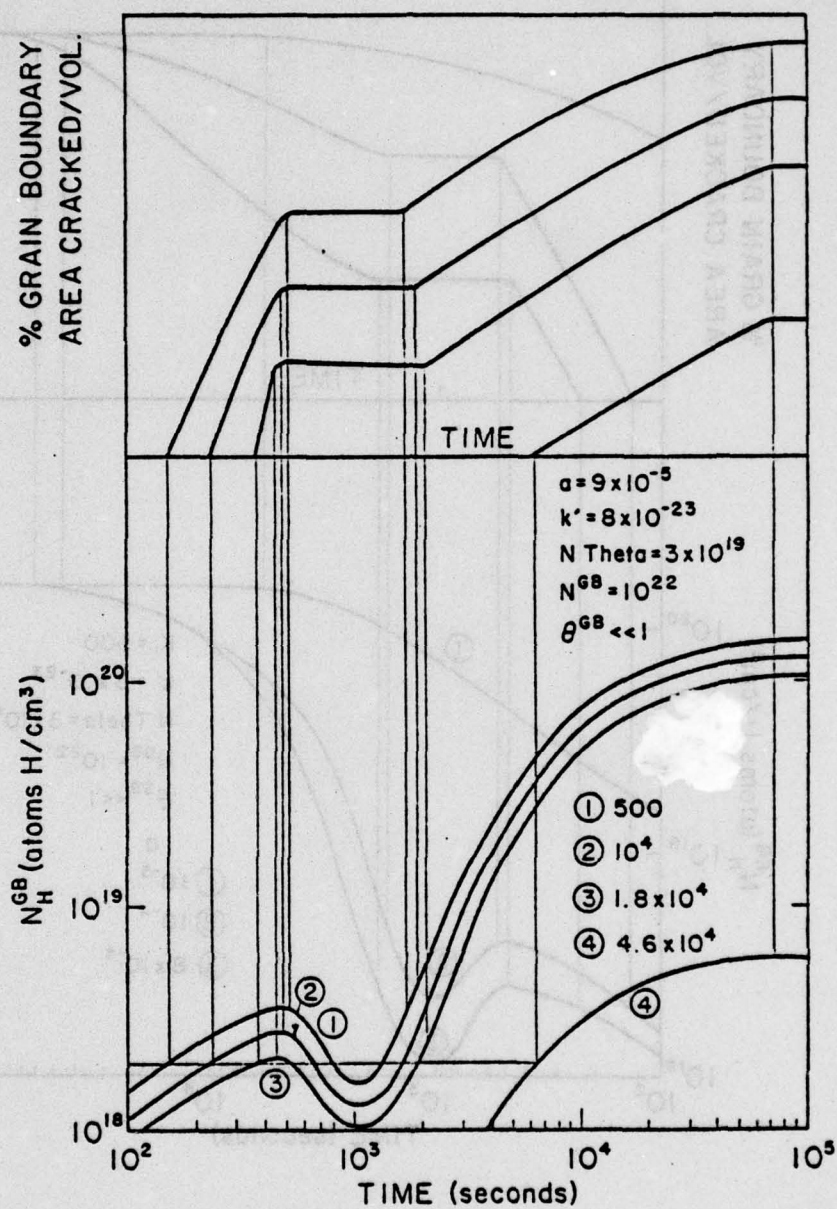


FIGURE 43.

Influence of the Parameter  $K_1$  (i.e. reversible trapping by Ti atoms) on  $N_H^{GB}$  and Grain Boundary Cracking.



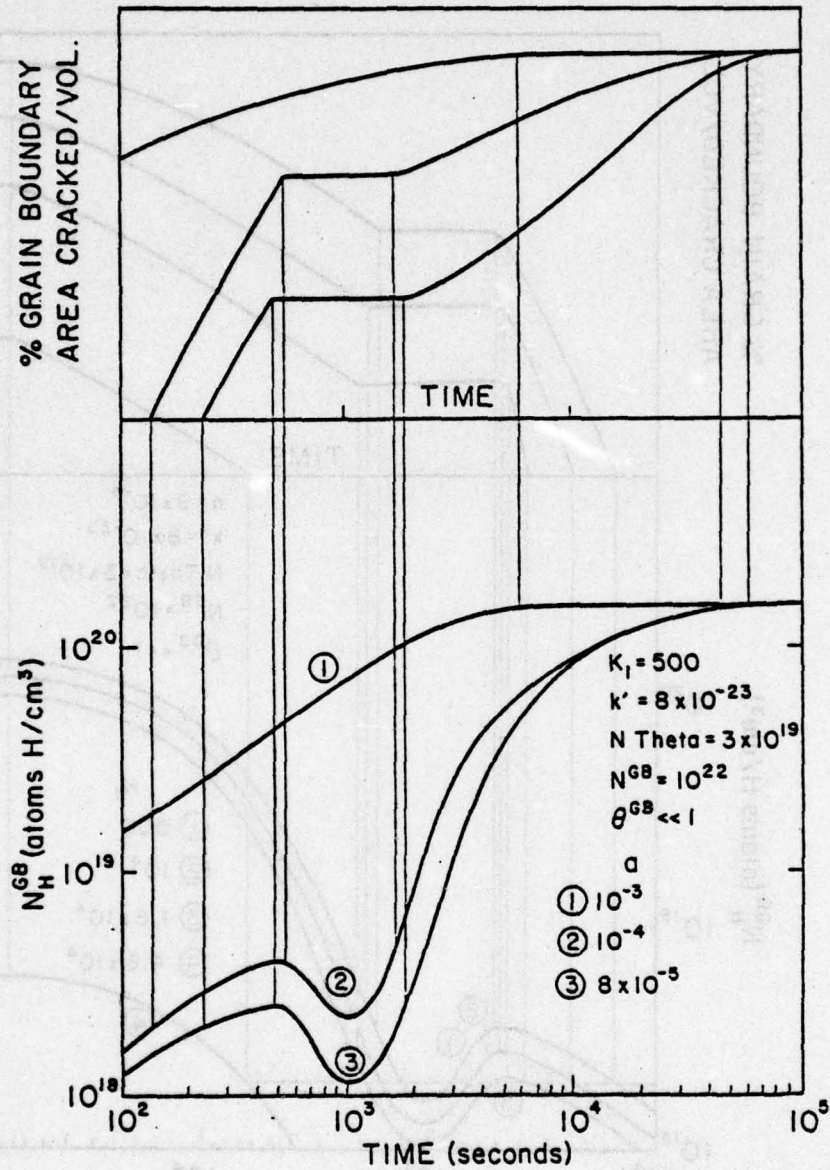


FIGURE 44.  
Influence of the Parameter,  $a$ , (i.e. hydrogen diffusivity) on  $N_H^{GB}$  and Grain Boundary Cracking.

result in a long plateau. Besides, a, other parameters may also be influenced by variations in the trapping parameters, such as  $N_{HS}^T$ . As was seen before, increasing  $N^{Ti}$  also increases the total hydrogen concentration (i.e.,  $N_{HS}^T$ ). Therefore, an increase in  $K_1$  will not result in as large a decrease in damage as predicted on Figure 43, because the decrease in grain boundary hydrogen concentration is partially compensated for by an added influx of hydrogen. On the other hand, the predicted effect of an increase in  $K_1$  (i.e., in  $N^{Ti}$ ) on the amount of damage will not be cancelled out by the corresponding increase in  $N_{HS}^T$ , because this increase is not directly proportional to  $N^{Ti}$  (see Figure 25, Chapter II), as is also the case for  $n$  and  $C_o$  (Equation (56)).

The above considerations were all for the case of  $\theta^{GB} \ll 1$ . Programs run with the equations applicable for  $\theta^{GB} = 1$  gave similar results, with the same influence of the parameters. In reality, choosing between the two conditions on  $\theta^{GB}$  is not obvious. For example, autoradiography studies<sup>(25)</sup> on Alloy B showed that some boundaries were strongly marked, while others were not marked at all. As suggested by Rath and Bernstein,<sup>(61)</sup> trapping on grain boundaries is selective; low angle boundaries being less efficient traps than high angle boundaries. Therefore, low occupancy may characterize low angle boundaries, while high angle boundaries may exhibit a larger occupancy. Since the model does not allow us to distinguish between grain boundaries, a clear choice of  $\theta^{GB}$  cannot be made. This is one limitation of the theory. Other limitations arising from the original assumptions will be discussed below.



### B.2.3 Applications and limitations of the model

The main results of the theory, and its application to experimental data, can be summarized as follows:

- a) the presence of a plateau in the kinetics of hydrogen-induced cracking is solely due to, and evidence for, significant irreversible trapping in the material. The absence of a plateau, without ruling out irreversible trapping, indicates either that reversible trapping is more dominant, that general diffusion is fast, compared to trapping, or that the irreversible traps are weak or of insufficient quantity.
- b) the length and height of the crack plateau will vary with trapping parameters. For instance, the length of the plateau should increase with increasing irreversible trapping efficiency, and less so with decreasing hydrogen diffusivity; on the other hand, the height of the plateau, which characterizes the amount of damage at such a time, will mainly decrease with increasing reversible trap efficiency, and less so with decreasing diffusivity.
- c) the extent of hydrogen-induced cracking will decrease whenever the extent of reversible trapping increases on sites other than grain boundaries.

Experimental verification of the above prediction will be presented in the next section. Prior to this, it is important to point out that because of the original assumptions made, the model is subjected to several limitations. In particular:

- a) newly created cracks are expected to act as strong additional traps where hydrogen would be present primarily as a high pressure gas. The effect on the kinetics of hydrogen-induced cracking would depend on the character of the trapping.

The trapping could be partially reversible in character depending on the nature of the crack nucleus. For example, if the nucleus is a particlematrix interface, trapping may be irreversible at the start (e.g., H atoms are chemically adsorbed at the interface); however, as the interface begins to separate, hydrogen gas will form at a pressure related to the surrounding hydrogen concentration. The crack may then adopt a more reversible character, although to all extent and purpose, the molecular hydrogen is irreversibly trapped. The adjoining lattice hydrogen concentration will depend on the local pressure. In such a case, the effect on damage kinetics would be two-fold: an increase in the plateau length due to added irreversible trapping and a reduction in the extent of cracking due to more reversible trapping. In any case, this situation is difficult to model, and is thus being neglected, but not ignored.

- b) the diffusivity of hydrogen should not be considered constant throughout the experiment. Indeed, since new cracks act as traps and diffusion obstacles, the diffusivity will decrease during the experiment, and will do so in a complex manner. Because of the known influence of,  $a$ , on the cracking curves (see Figure 49), the formation of new cracks will delay the apparition of further damage.
- c) finally, other trap types can be generated by the entry of hydrogen in large quantities in the lattice. Dislocations, for example, will be introduced, with all the expected consequences. However, we have estimated its role and believe it can be



neglected in the formal treatment.

The proposed model is thus a quite idealized situation, where the nature and distribution of traps are assumed to be known and be constant during charging. Such an approach if not strictly quantitatively applicable, nevertheless does give reasonable information regarding the influence of a particular kind of trap on the kinetics and extent of hydrogen-induced cracking in iron-titanium alloys. To demonstrate this experimentally, determined results will be compared to the predictions of the theory.

### B.3. Experimental Results:

#### B.3.a. Experimental procedure:

All the alloys used in this study were heat treated as described in Chapter I and II, and thus have the microstructures described in Chapter I. Care was taken to ensure that a uniform grain size of about  $80\mu$  was maintained, since it has been demonstrated that the amount of damage varies with grain size.<sup>(24)</sup> Square sheet samples of  $1\text{cm} \times 1\text{cm} \times 7.6 \times 10^{-2}\text{cm}$  in size, were used. Prior to cathodic charging, all specimens were mechanically polished and then chemically polished in a 47%  $\text{H}_2\text{O}$ -47%  $\text{H}_2\text{O}_2$ -6%  $\text{HF}$  solution, until a mirrorlike finish was obtained. The charging solution was invariably  $\text{IN-H}_2\text{SO}_4$  to which cathodic 'poisons' were added. The effect of poisons is to facilitate the entry of hydrogen into the metal, as discussed in Chapter II. As in previous studies, (e.g., Ref.61) carbon disulfide ( $\text{CS}_2$ ) and a solution of arsenic trioxide ( $\text{As}_2\text{O}_3$ ) were used and added in a fixed quantity of 10 drops each ( $0.6\text{ cm}^3$ ) per liter to the charging

solution. The  $\text{As}_2\text{O}_3$  'poison' solution was prepared by dissolving 20 mg/cc of  $\text{As}_2\text{O}_3$  powder in IN-NaOH, followed by neutralizing with IN- $\text{H}_2\text{SO}_4$ ; the resulting concentration was 10 mg of  $\text{As}_2\text{O}_3$  per  $\text{cm}^3$  of water (the quantity of  $\text{Na}_2\text{SO}_4$  formed was negligible). The cathodic charging cell was simply a cylindrical glass beaker with spiral platinum wire cathode arranged around its inside perimeter. Because of this configuration, the specimen (anode) was located in the center of the cell and therefore was uniformly charged on all sides. The specimen holder consisted of a thin iron wire, spot welded to a corner of the sheet; this holder was completely covered with a hydrogen impermeable lacquer (microstop) in order to prevent it also being charged with hydrogen, the result of which would be the holder breaking off after long charging times. Following charging, the extent of intergranular cracking was determined by a quantitative metallographic technique on polished transverse sections.<sup>(111)</sup> The grain boundaries were etched in 2% Nital. Using optical microscopy (magnification 100) and a series of random lines on the specimen surface, the percent of grain boundary area cracked per unit volume was calculated by counting the number of cracked and uncracked boundaries which intersected the random lines.<sup>(111)</sup>

### B.3.b. Experimental Results

#### (1) Crack appearance:

Optical examination of the specimens revealed that cracking was always intergranular for the non-carburized alloys, in agreement with previous studies.<sup>(24,61)</sup> Low and medium titanium content carburized alloys (BC, CC) exhibited a few transgranular



cracks, but in negligible amount. Alloy DC, on the contrary, showed more significant transgranular cracking. The implications of these observations will be discussed in the section on crack nucleation, later on in this chapter.

The appearance of cracks is illustrated in Figures 45 and 46. Figure 45 is a scanning electron microscope picture of a blister (upper right) and an intergranular crack (lower left). Once a crack has been nucleated, the high pressure of hydrogen gas developed in the crack will cause it to expand. If the containing grains happen to lie close to the free surface of the sheet, the plastic deformation resulting from the high pressure will appear either as a blister, if the separated grain boundary did not communicate with the surface, or as an open crack if the boundary separation ended up on the surface, (Figure 45). Note also in Figure 45, the plastic strain markings linking the blister and the crack. Also, the blister itself opened up under the high pressure, which is characteristic of a long charging time (i.e., a higher hydrogen pressure); surface blisters after short charging times were generally closed. Figure 46 is an optical picture of a polished and etched cross section of a sheet of alloy B charged at  $20\text{mA}/\text{cm}^2$  for 24 hours. Note that the internal cracks run on several adjoining grain boundaries and that there appears to be a selectivity of the crack path (i.e., a crack meeting another grain does not always separate into several branches). This has been explained by Rath and Bernstein<sup>(24,61)</sup> in terms of grain misorientation (i.e., high angle boundaries crack more easily than low angle boundaries).

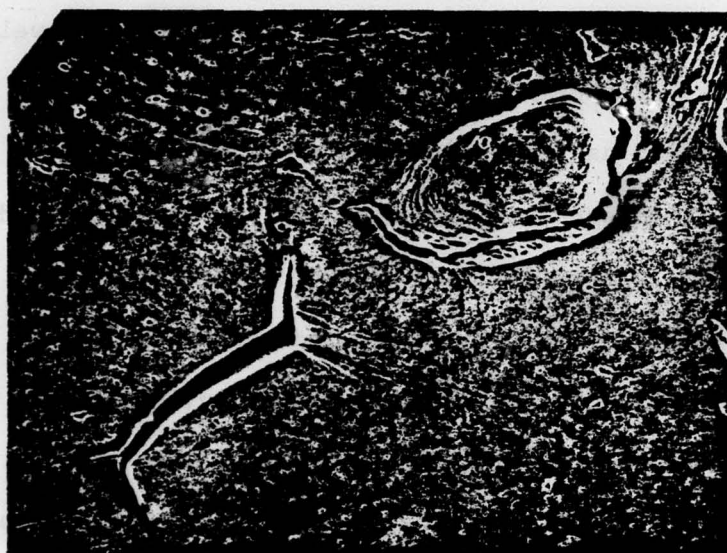


**Figure 45**  
Scanning electron micrograph  
of hydrogen induced surface  
crack and blister  
( Alloy B<sub>2</sub>, charged 24 hrs. at  
30 mA/cm<sup>2</sup> )

46 μ



**Figure 46**  
Optical micrograph of hydrogen  
induced internal cracks  
( Alloy B<sub>2</sub>, charged 24 hrs. at  
30 mA/cm<sup>2</sup> )

0.18 mm



(2) Extent of damage versus time:

The experimental parameters present such as Ti, and TiC content of the alloys, charging time and current density, were systematically varied so as to test the predictions of the theory developed in Section IA-IB. Experimental results were found to agree with theoretical predictions, as follows:

a) Figure 39, from Bernstein and Rath,<sup>(24,61)</sup> when examined in the light of the theory raises several important points:

- i) the kinetic rate of hydrogen-induced cracking in Ferrovac E, does not exhibit a plateau, contrary to the case for Fe-0.15Ti (alloy B). This agrees with the theory's prediction that irreversible trapping is negligible in Ferrovac E, compared to alloy B. Indeed, as was shown in Chapters I and II, and also by autoradiography,<sup>(25)</sup> irreversible traps (e.g.,  $\text{Fe}_4\text{N}$ ) in Ferrovac E are both few in number and weak in strength, compared to the numerous TiCN particles of alloy B.
- ii) for a similar grain size, alloy B is less susceptible to damage than Ferrovac E. The developed theory explains this by the fact that more reversible traps are present in alloy B (e.g., Ti atoms) than in pure iron, and these compete equally with grain boundaries to trap hydrogen. For example, Figure 39 shows a saturation value of damage of about 20% for Ferrovac E. while Bernstein

and Rath<sup>(24,61)</sup> give a value of about 10% for alloy B at the same grain size (70 $\mu$ ): this is a 50% decrease in cracking due to the presence of only 0.15wt% titanium.

- iii) the extent of damage decreases with decreasing grain size; this is but another demonstration of the above arguments concerning relative distribution of hydrogen among various reversible traps. Indeed, decreasing the grain size will increase the grain boundary area, i.e., increase the number of trapping sites on grain boundaries and therefore hydrogen will be distributed more uniformly on the grain boundaries. We have extended Bernstein's results to further reinforce the agreement between theory and experiment, as follows.

b) Figure 47\* illustrates damage kinetics on the non-carburized Fe-Ti alloys of this study. The main points which were raised above are again seen to be valid here, with some additional features:

- i) the plateau length increases with increasing titanium content. As was considered in our theory this may be due to several factors, the more important being an increase in irreversible trapping efficiency (N $\theta$  increases) with increasing titanium content (see Chapter I and Chapter II on this subject). Another cause involves the decrease in hydrogen diffusivity, as monitored by  $\alpha$ , with increasing Ti content.

---

\* Note: all experimental points represent an average value of at least two experiments performed under similar conditions.



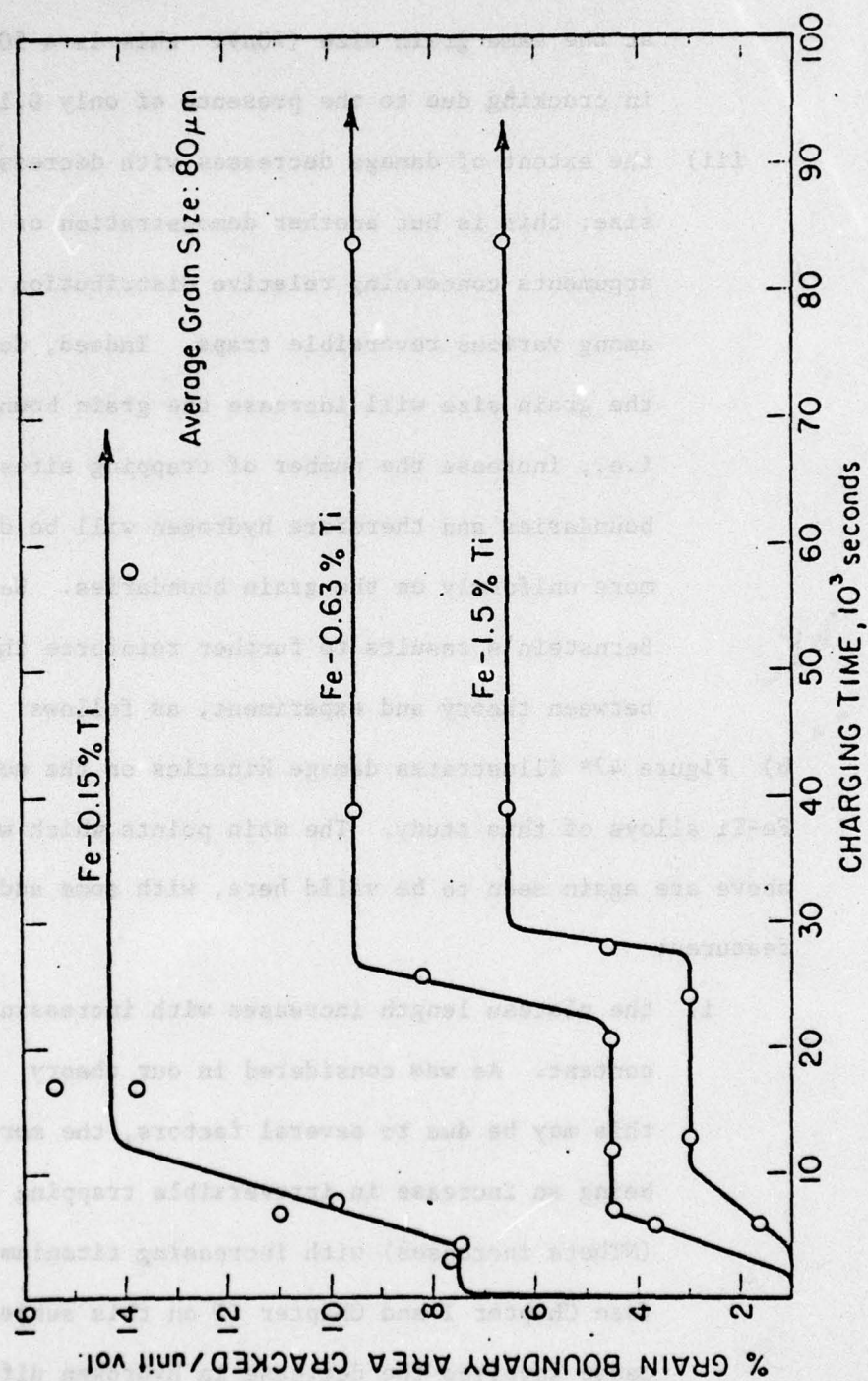


FIGURE 47. Grain Boundary Cracking Versus Charging Time and Titanium Content.

- ii) a demonstration of the effect of a decrease in hydrogen diffusivity is provided by the increased delay in crack initiation as the alloy contains more titanium. For example, it takes almost 300 seconds to observe the first cracks when charging alloy D<sub>2</sub>, versus 120 seconds for alloy C, and 30 seconds for alloy B.
- iii) Again, the extent of cracking varies, as predicted, when  $N^{Ti}$  increases, i.e., when  $K_1$  increases, and, a, decreases the amount of damage considerably decreases (see for example, the predictions of Figure 43 and compare these to Figure 47). For instance, the saturation value of the damage at a grain size of 80 $\mu$  varies from 14% for alloy B\* to 9.5% for alloy C and 6.5% for alloy D<sub>2</sub> (versus more than 20% for pure iron).

Since many of the trapping and diffusing parameters in the above experiments were varied at the same time, more restrictive experiments were performed where important parameters were independently varied. Figure 48 compares the cracking behavior of alloy C to its carburized counterpart (alloy CC). Since the titanium content is similar in both alloys, one would expect the irreversible trapping parameter  $N_{\theta}$  ( $=N^{TiC}_{HS}$ ) to be most important here. Because  $N_{\theta}$  for alloy CC is going to be higher than  $N_{\theta}$  for alloy C (more TiC particles in CC), the theory predicts a longer intermediate plateau for alloy CC than for alloy C, without any appreciable reduction in the extent of damage (see Figure 42). According to Figure 48, this is indeed verified: the

---

\*Note: The results of Figure 47 for alloy B have been duplicated by the author, and are not from Bernstein's Figure 39; the slight difference between the two results probably arises from slightly different charging solution.



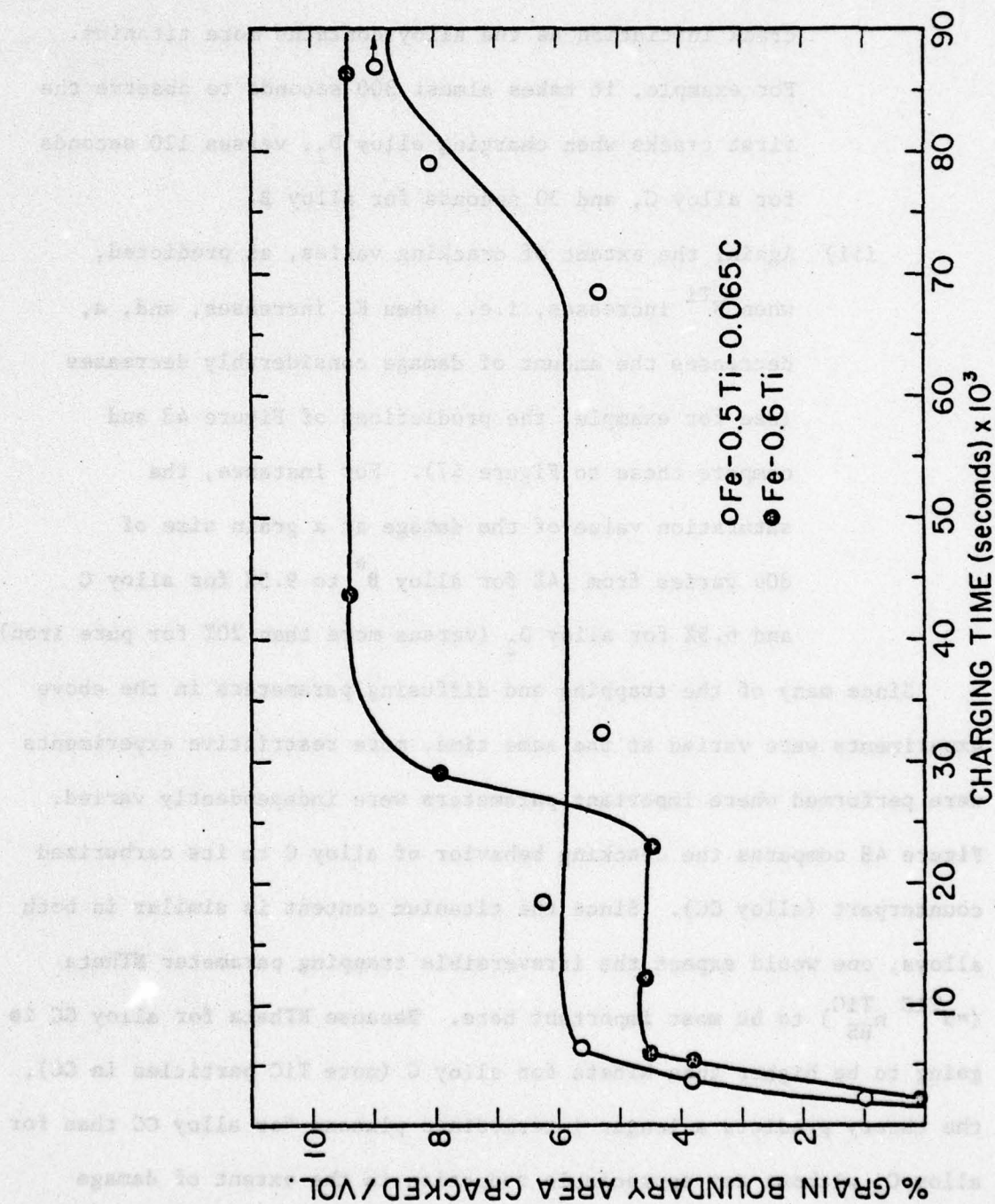


FIGURE 48. Grain Boundary Cracking Versus Charging Time and TiC Content (alloys C and CC).

intermediate plateau lasts for 380 minutes in the case of alloy C versus 1160 minutes for alloy CC, while the saturation values of the damage are similar (around 9%). The difference in height between the two plateaus is not significant, since the experimental data on alloy CC shows some scatter.

Figure 49 shows the effect of concentration to demonstrate the influence of,  $a$ , i.e., the hydrogen diffusivity. As was discussed in Chapter II, decreasing the concentration of hydrogen (which was done here by decreasing the current density) will decrease hydrogen's diffusivity through the lattice. According to Figure 44, a decrease in,  $a$ , should result in a delay of cracking kinetics. This is documented in Figure 49, where a reduction in current density from  $30\text{mA/cm}^2$  to  $5\text{mA/cm}^2$  considerably retards the cracking of alloy B. For example, the time to reach saturation decreases by an order of magnitude. Another noticeable effect is a reduction in the extent of cracking with decreasing current density. This simply illustrates the effect of  $N_{\text{HS}}^{\text{T}}$  on cracking, as was discussed before ; lowering the charging current density lowers  $N_{\text{HS}}^{\text{T}}$ , and consequently decreases the amount of hydrogen available to nucleate cracks on grain boundaries.

### (3) Extent of damage versus charging current density.

This last comment is further illustrated in Figure 50, where the maximum (i.e., saturation) amount of damage is plotted versus charging current density for alloys B, C and  $D_1$ . As expected, this value decreases the higher the titanium content; in addition, the maximum amount of damage reaches a saturation value as the current



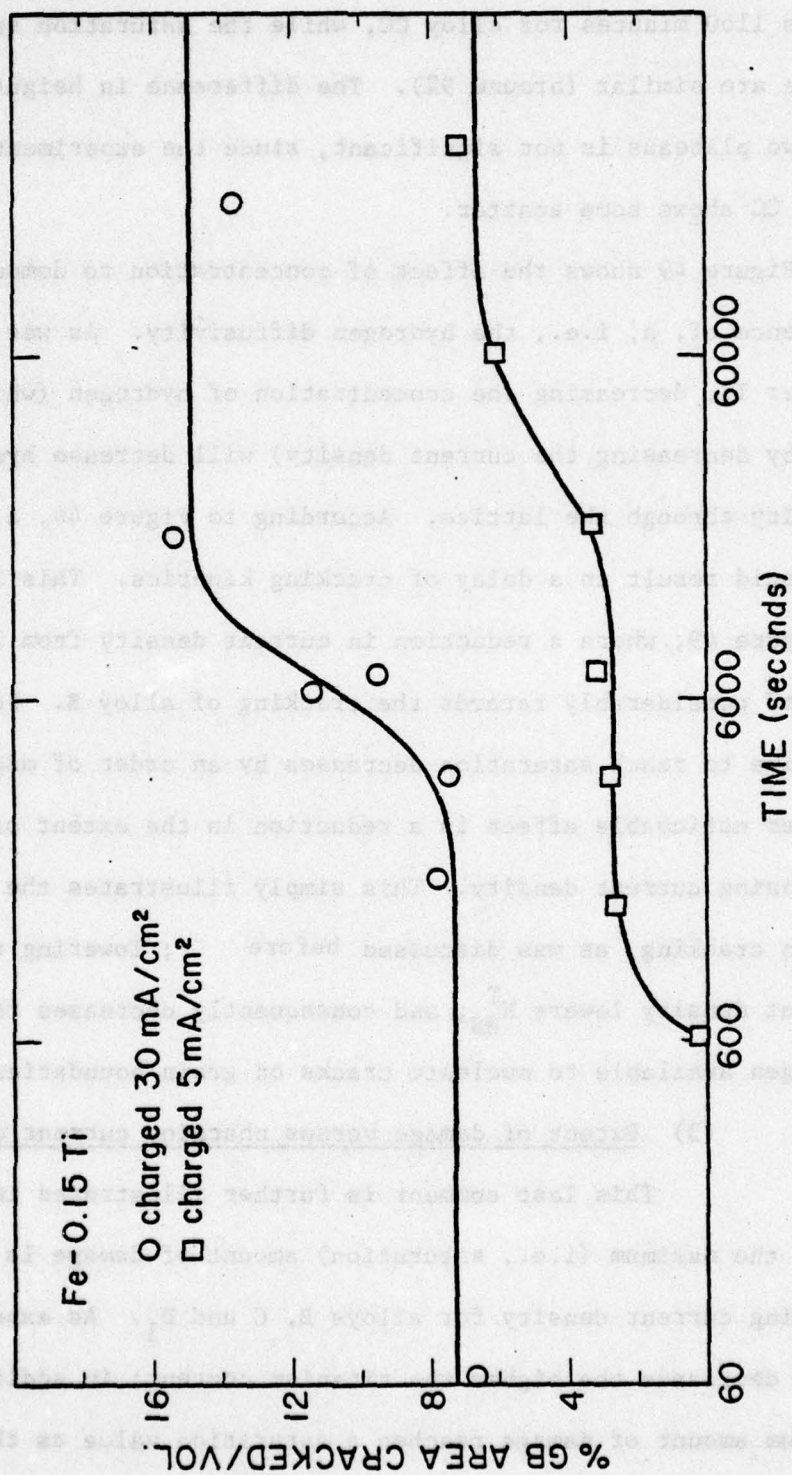


FIGURE 49. Grain Boundary Cracking Versus Charging Time and Current Density (i.e. versus hydrogen diffusivity).

density increases (at around  $50\text{mA}/\text{cm}^2$ ). This may be due to the fact that beyond a certain current density the concentration of dissolved hydrogen ( $N_{\text{HS}}^{\text{d}}$ ) also attains its maximum limit, (i.e., no more hydrogen can be forced into the lattice.), or to electrochemical effects (such as maximum coverage of the surface or other reduction reactions occurring at high current densities).

The preceding section has demonstrated that the model developed may be qualitatively used to predict both the evolution of the kinetics and extent of hydrogen-induced cracking with trapping parameters. The following discussion will address some additional points.

- a) Is it possible to use the model in a more quantitative way? For example, can the theoretical curves for  $N_{\text{H}}^{\text{GB}}(t)$  be matched to the experimental curves describing the damage kinetics?
- b) Could the experimental results be explained by another effect, for instance, a surface effect?
- c) Is there any other experimental evidence for the validity of the model, such as with permeation?

#### B.4. Discussion of the hydrogen-induced cracking model.

##### B.4.a. Matching theory and experiment.

As we have seen before, only the limits or orders of magnitude of the trapping parameters could be given to obtain the theoretical curves for  $N_{\text{H}}^{\text{GB}}(t)$ . Therefore, even if an exact matching of theory and experiment was possible, there would still be some problem as to the uniqueness of the obtained set of parameters. Furthermore,



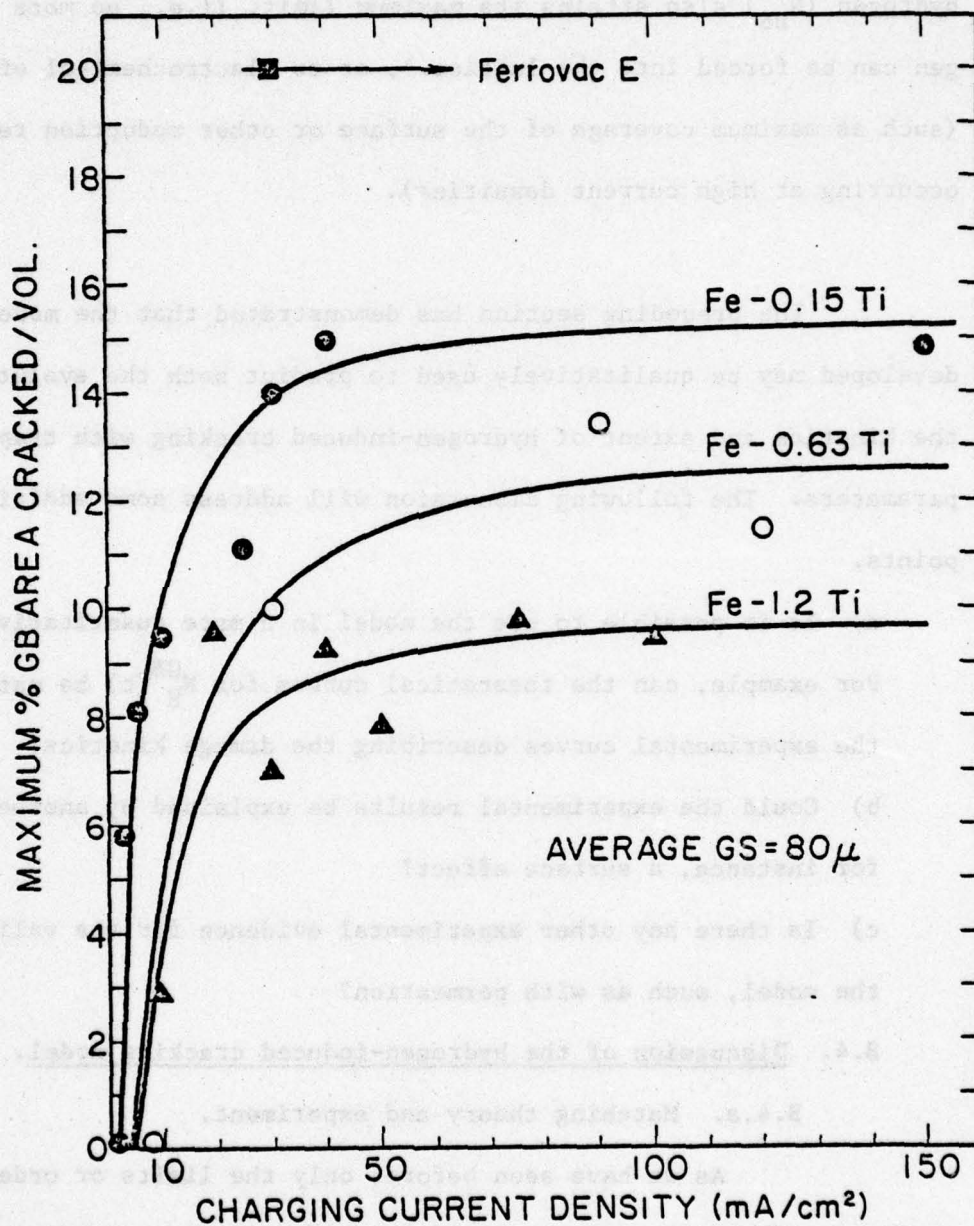


FIGURE 50.

Maximum Amount of Grain Boundary Cracking Obtained at Various Current Densities.

the critical concentration,  $C_K$ , at which cracks will nucleate is a matter of speculation; for instance, it is likely that this concentration will vary with the nature of the nucleus. Nevertheless, an attempt can be made; consider the experimental curves of the damage kinetics for Fe-0.15Ti (Figure 39) and the theoretical curve given in Figure 41. Experimentally, it is seen that for Fe-0.15Ti, the plateau starts at  $t < 60$ s, and ends at  $t \approx 6 \times 10^3$ s, thus lasting about  $6 \times 10^3$  seconds. The theoretical curve of Figure 41, which uses parameters specifically relevant to the case of alloy B, predicts a plateau starting at  $5 \times 10^2$ s, ending at  $t = 1.7 \times 10^3$ s, and lasting about  $1.2 \times 10^3$ s. Thus, while there is a discrepancy between theory and experiment, reasonable agreement is found. Better agreement between theory and experiment is found for the time at which the maximum damage is reached ( $t \approx 4 \times 10^4$ s.).

If one tries to further improve the fit by adjusting the parameters to increase the plateau length, further inconsistencies will result. For example, decreasing the value of,  $a$ , would increase the plateau length (Figure 44), but then the time for steady state and crack nucleation would be longer than experimentally found. Increasing  $K_1$ , or  $N\theta$  (Figures 42 and 43) would have the same effect on the plateau length, but the resulting value of  $K_1$  would be too high to be realistic ( $\theta^{Ti} \approx 1$ ), and increasing  $N\theta$  would not affect the time at which the plateau starts, only the time at which it ends. Finally, if all parameters were varied at once to try to match the starting time of the plateau, the predicted ending time would be less than experimentally found. To be able to match the theory with the experiment



would require the introduction of a variable trap density  $N^{\text{crack}}(t)$  and a variable " $a(t)$ ", with all the resulting mathematical complications, as we have discussed before.

In the same way, trying to precisely match the values of  $N_H^{\text{GB}}$ , with the corresponding experimental values of %GB area cracked/volume creates difficulties. Indeed, it may be seen from experimental results of Figures 39, 47, and 48, that the difference between the amount of damage at the plateau versus the amount of damage at saturation never exceeds an order of magnitude. On the contrary, the theory predicts a larger difference in  $N_H^{\text{GB}}$  between the maximum and the plateau. Again, this could be explained by the fact that we have neglected the possibility that a large percentage of  $N_H^{\text{GB}}$  is 'lost' as hydrogen gas into the newly formed cracks, instead of being used to nucleate new cracks.

The possibility that a significant amount of hydrogen will be present as hydrogen gas in grain boundaries cracks will now be demonstrated and used to explain, at least in part, the inability of the model to estimate the length of the first plateau.

The solubility of hydrogen in alloy B and A was measured as a function of charging current density with a Leco hydrogen analyzer. In this technique, hydrogen is vacuum extracted at high temperature while the specimen is induction heated. A sensitivity of about 0.5wt ppm of hydrogen is obtainable. All specimens were heated to  $T = 1000^\circ\text{C}$ , a value high enough to extract even irreversibly trapped hydrogen

(see Asaoka, Ref. 25). The cathodic charging technique was exactly the same as before (see page 41), i.e., all samples were charged in poisoned  $\text{IN-H}_2\text{SO}_4$  at  $30\text{mA/cm}^2$ . The only difference was in the size of the specimens; in order to measure the solubility in the Leco analyzer, the specimens were cubes of dimensions  $0.5 \times 0.5 \times 0.5$  (cm). Compared to the sheets previously used, the thickness  $L$  is now much increased, which in turn decreases,  $a$ , with all predicted consequences on hydrogen-induced cracking, see Figure 44.

The results for alloy B and A are plotted on Figure 51 and show a higher hydrogen content for Ferrovac E than for Fe-0.15Ti. This remark and the fact that the concentration of 'dissolved' hydrogen should increase with increasing titanium content strongly suggest that an important part of extracted hydrogen was present as gas in cracks; this argument would also explain why the amount of extracted hydrogen (40 ppm) is much higher than the solubility limit of hydrogen in iron (see Appendix C for example). This is in agreement with the previously discussed limitation of the theory that cracks should be considered as strong trapping sites, and with the fact that the model locates most hydrogen on the grain boundaries.

Another important part of the total amount of extracted hydrogen is most probably the hydrogen irreversibly trapped at titanium carbides particles. A rough estimate of the pressure present in the cracks may be made if one assumes that nearly all the extracted hydrogen was present in the cracks as ideal hydrogen gas in the cracks.



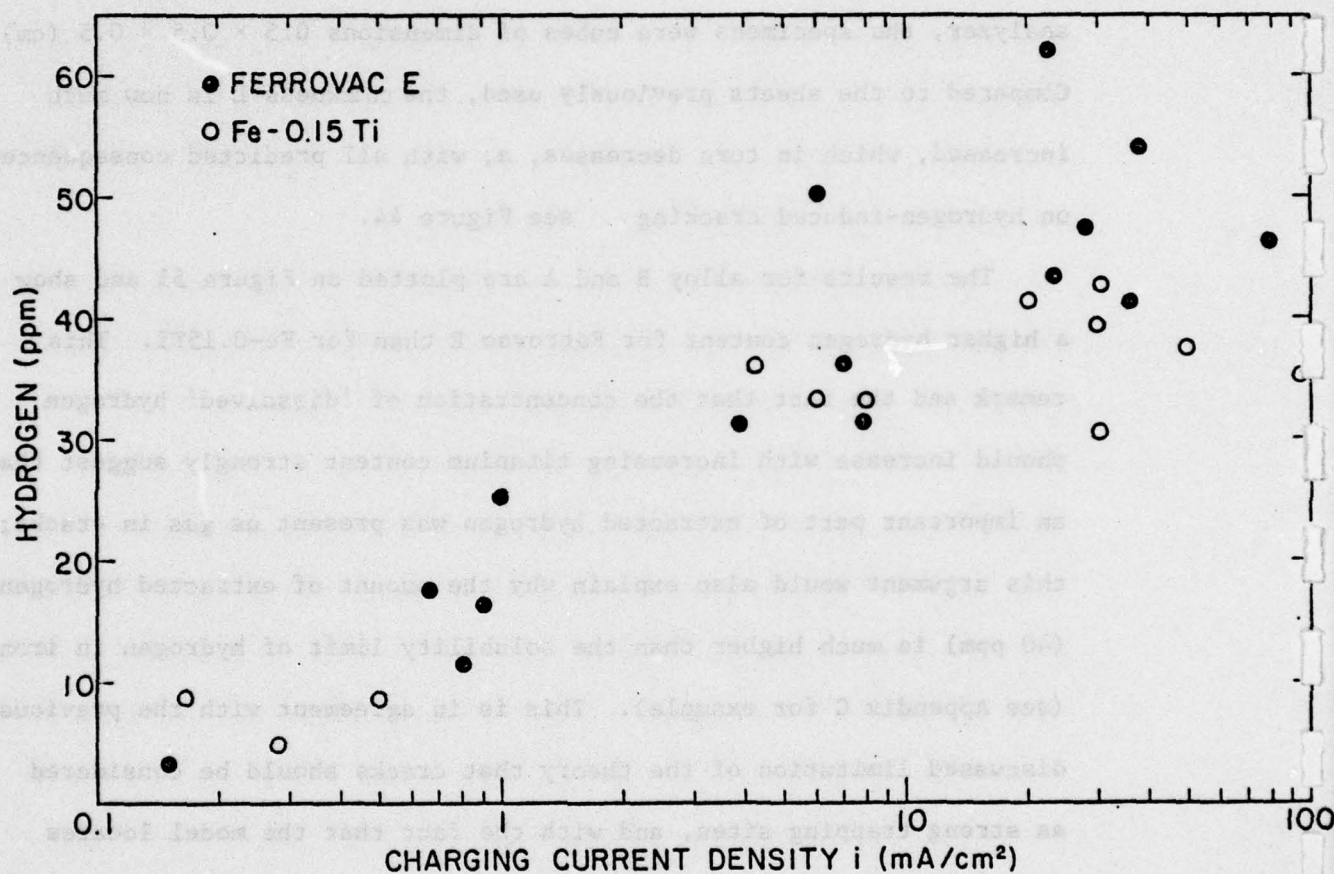


FIGURE 51.

Solubility of Hydrogen in Ferrovac E and Fe-0.15Ti Versus Charging Current Density,  $i$ , as determined using a Leco Hydrogen Analyzer.

Assume that cracks are lenticular voids of dimensions  $2a$  and  $2b$ , which from optical microscopy were on the average  $1.8 \times 10^{-2}$  cm and  $2 \times 10^{-3}$  cm, respectively; the average volume of a crack is then  $V = 2 a^2 b \pi$  ( $V = 5 \times 10^{-7}$  cm<sup>3</sup>), and its average base area  $A = \pi a^2$  ( $A = 2.5 \times 10^{-4}$  cm<sup>2</sup>). Now, the area of a spherical grain of diameter  $d = 80 \mu$  ( $8 \times 10^{-3}$  cm) is  $A' = \pi d^2$  ( $A' = 2 \times 10^{-4}$  cm<sup>2</sup>), and its volume  $V' = \pi d^3/6$  ( $V' = 2.7 \times 10^{-7}$  cm<sup>3</sup>). The number of grains per cm<sup>3</sup> is thus  $N' = 1/V'$  ( $N' = 3.7 \times 10^6$  grains/cm<sup>3</sup>). The total grain boundary area/cm<sup>3</sup>,  $A'_t$ , may be approximated by:  $A'_t = N' A'/14$ , where 14 is the number of faces on a tetrakaidecahedron (the ideal volume of a grain). The number of cracks per cm<sup>3</sup>,  $N$ , corresponding to a certain percent, (%), of grain boundary area cracked/cm<sup>3</sup> is thus:

$$N = (\%) A'_t / A \quad (177)$$

and the total volume of cracks/cm<sup>3</sup>,  $V_t$ , corresponding to this (%) is:

$$V_t = NV. \quad (178)$$

With the values given above, a typical value of  $N$  at 10% damage is  $N = 2.1 \times 10^4$  cracks/cm<sup>3</sup>, and  $V_t$ , also at 10% is  $V_t = 1.2 \times 10^{-2}$  cm<sup>3</sup> of cracks/cm<sup>3</sup>. The pressure in a crack,  $P$  is then given by, assuming an ideal gas:

$$P = n RT/V_t \quad (179)$$

where  $n$  = number of moles of  $H_2$ /cm<sup>3</sup>, as converted from the value in ppm of the hydrogen solubility corresponding to a certain % of damage (%)



(1 ppm  $H_2 = 3.9 \times 10^{-6}$  moles  $H_2/cm^3$ );  $R$  = gas constant ( $R = 0.082$  atm. liter/mole. $^{\circ}K$ );  $T = 300^{\circ}K$ . Using  $(\%) = 10$ ,  $P$  is found to be:

$$\begin{aligned} P(\text{Ferrovac E}) &= 1.3 \times 10^5 \text{ atm.} \\ P(\text{Fe-0.15Ti}) &= 2.1 \times 10^5 \text{ atm.} \end{aligned} \quad (180)$$

Since these pressures are of the order of the theoretical cohesive strength,<sup>(112)</sup> the formation of cracks and blisters (i.e., of the separation of grain boundaries, or particle-matrix interface, at whatever is a nucleus) is easily justified. The assumption of an "ideal" gas pressure here is probably debatable, although it has been widely used in the literature<sup>(112)</sup> with similar results. The values of the pressures should then be taken only as order of magnitude.

#### B.4.b Surface effect as a possible explanation for the observed extent and kinetics of hydrogen-induced cracking in Fe-Ti alloys:

As discussed in the Experimental Procedure (page 187), the crack study specimens were not plated with palladium. The major reason for this was that in poisoned acid and at the fugacities of hydrogen involved in the cracking experiment, the palladium layer would be destroyed. Therefore, as discussed in Chapter II, surface trapping by titanium atoms is to be expected. A direct consequence of this is that less hydrogen will enter the lattice than if palladium was present. However, in the experimental conditions of the cracking test (i.e., high input fugacity), the importance of this effect is

minimized and cannot be used to explain the observed kinetics of cracking, as will now be demonstrated.

#### Surface effect versus amount of damage

Because a surface effect would reduce the amount of hydrogen entering the lattice, it could be held responsible for the observed decrease in the amount of damage with increasing titanium content (i.e., with increasing titanium surface trapping). Indeed, it was shown in Figure 30 that  $J_{\infty}$  (and thus  $C_0$ ) did not increase in proportion to the current density, particularly at high current densities (such as  $30 \text{ mA/cm}^2$ , used in this study). However, as illustrated in the same figure and as evidenced by the solubility results, the amount of hydrogen entering Fe-Ti alloys is higher than that entering pure iron: thus, although the surface effect is present, it never reduces the concentration of hydrogen in Fe-Ti alloys to a level below that of hydrogen in pure iron. Because the concentration of hydrogen is higher in iron when it contains titanium, even though a surface effect is present, another reason has to be invoked to explain a lesser amount of damage in Fe-Ti. The most probable reason is of course trapping of hydrogen by substitutional titanium atoms.

#### Surface effect versus the kinetics of hydrogen-induced cracking

The most noticeable feature of the kinetics of hydrogen-induced cracking in Fe-Ti alloys is the existence of an intermediate plateau (see Figures 47 to 49). It is difficult to justify the presence of this feature in terms of a surface effect. For example, one could propose that, when the plateau is reached a layer or film impermeable to



hydrogen has been formed on the surface, and then when the plateau is terminated and further damage occurs, this film suddenly "breaks down" allowing more hydrogen to enter. This hypothetical layer would in some way have to be related to titanium, since no plateau exists when charging pure iron. The formation of a titanium hydride or oxide that would form and then decompose, is hard to imagine since these compounds are highly stable at room temperature. On the other hand, if this film was simply physically detaching itself from the surface and falling in the solution, the newly exposed titanium atoms would reform another film and create another plateau, and so on. This was not experimentally observed. Furthermore, a hypothetical layer of this type would not explain why, for example, the plateau length increases with increasing density of TiC particles, at a constant titanium content (see Figure 48) as was experimentally observed. Thus, the proposed theory of internal trapping remains the best explanation. Let us now examine if some more direct evidence for the validity of this theory can be found.

#### B.4.c. Other experimental evidence of the validity of the theory:

##### high fugacity permeation experiment.

Because  $N_N^{GB}(t)$  exhibits a maximum and a minimum (see Figure 41),  $N_H^{Ti}(t)$  and  $N_H^d(t)$  should also vary in a similar manner, since these populations are considered to be in equilibrium with one another. Consequently, the first polarization curve for Fe-Ti alloys, which is related to the diffusing hydrogen  $N_H^d(t)$  should exhibit a similar behavior (since irreversible trapping, which is responsible for the minimum, only plays a role during the first polarization). If one

examines the first polarization transients of Figure 15,16, it may be seen that no such maximum or minimum is observed, although the curves for higher titanium contents are somewhat distorted (compared to a normal diffusion curve); in particular, these distorted curves (for alloys C and D<sub>2</sub>) regain a more "diffusion-like" appearance during the second polarization, when the irreversible traps responsible for the maximum are saturated.

The reasons why no discernable maxima or minima are visible have been previously discussed. The most probable one is that for the input fugacity and solution (.IN NaOH, no poison) used in the permeation experiments of Chapter II, "a" and  $N_{HS}^T$  are very low. To test this hypothesis, the following experiment was performed, using the permeation cell of Chapter II, with the only difference that now the input side solution was replaced by the poisoned IN-H<sub>2</sub>SO<sub>4</sub> used in the cracking experiment and the input current density was increased to 30mA/cm<sup>2</sup>. The input side of the membrane was also palladium plated, but, as mentioned earlier, the coating was destroyed as the experiment progressed. The results are plotted in Figure 52, along with the corresponding cracking curves. The diffusion of hydrogen across the Fe and Fe-0.15Ti membranes now exhibits maxima and minima.

Consider first the case of Ferrovac E: at a time of about 1.5 minutes, the hydrogen flux decreases to a minimum at  $t \approx 80$  minutes, then rises again until steady state is reached. According to the theory the density of irreversible traps (e.g., Fe<sub>4</sub>N) is not large enough in iron to justify a plateau. We are thus faced again with the main limitation of the theory, i.e., cracks were ignored as potential traps.



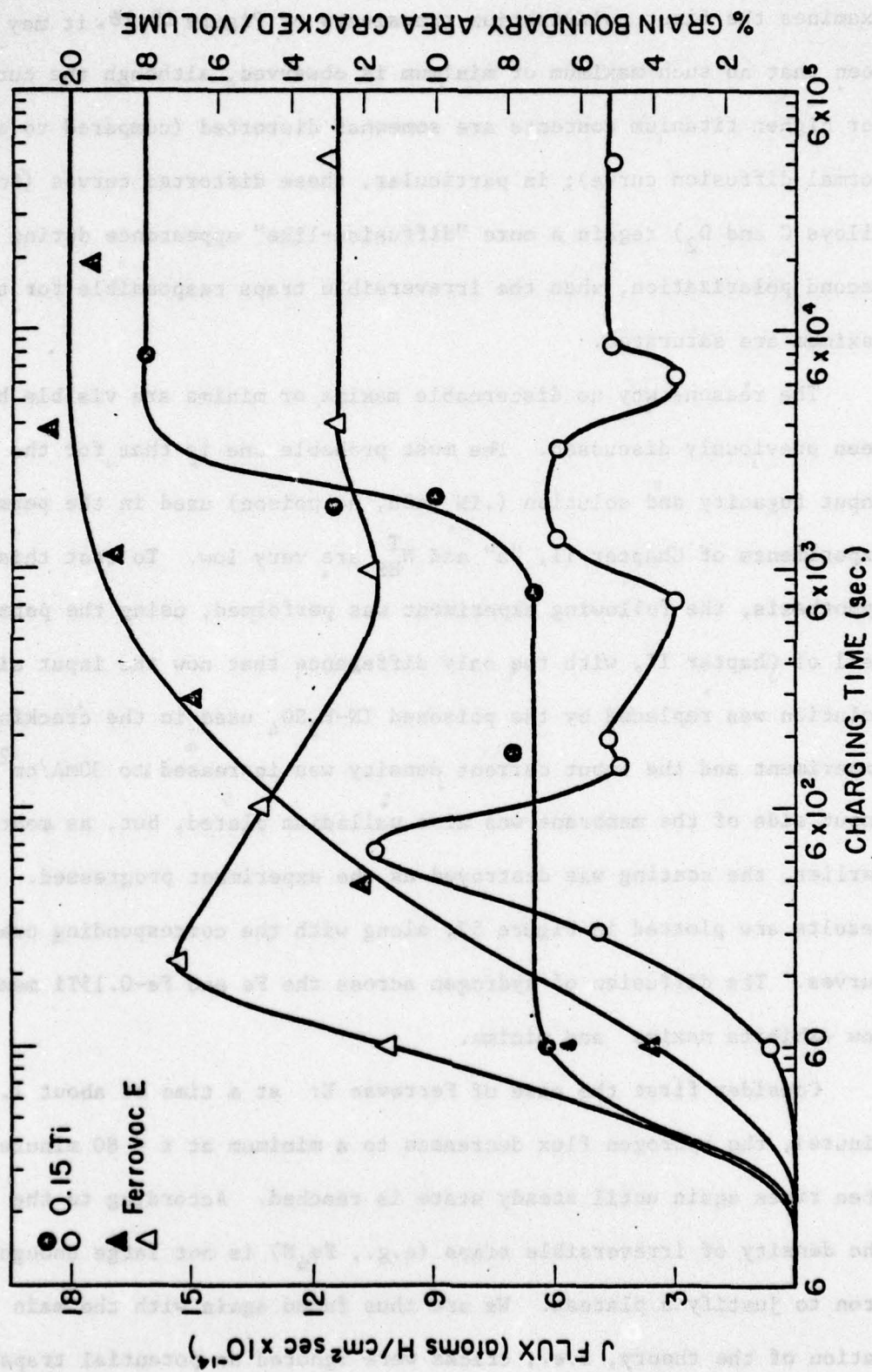


FIGURE 52. First Polarization Permeation Transients (light symbols) Superimposed on the Corresponding Grain Boundary Cracking Curves (dark symbols) for Ferrovac E (triangles) and Fe-0.15Ti (circles).

This is probably what is happening in this case; when the maximum in  $J(t)$  is reached, cracks must have begun to appear in the iron membrane, and hydrogen collapses into them. Although the theory did not include the induced cracks as irreversible traps, it nevertheless allows us to predict that when an irreversible trap (in this case cracks) is present (no matter when), some of the hydrogen originally on lattice sites and reversible traps will leave to be irreversibly trapped. This rationalizes the existence of a maximum. Furthermore, the theory also predicts that once the irreversible traps (cracks) are filled, the amount of hydrogen on lattice sites and reversible traps should again increase before reaching saturation. This is evidenced by the minimum. The fact that the steady state flux does not regain a value at least as high as that of the maximum may be evidence of some equilibrium between the hydrogen gas pressure in the cracks and diffusing hydrogen (see discussion on page 185).

Consider now the case of Fe-0.15Ti; since cracks are also going to be nucleated, and since other irreversible traps (e.g., TiC) and a surface effect are also going to be present, one would expect a complex behavior of the diffusion of hydrogen. According to Figure 52, this is indeed the case. Three maxima and three minima are observed (not including the steady state). The following tentative explanation for their existence is as follows:

As permeation proceeds, a critical concentration of hydrogen will be reached at the grain boundaries and cracks will be nucleated.

According to the model, and as discussed for Ferrovac E, some of the



diffusing hydrogen will collapse into the cracks, giving rise to a maximum; this is probably the explanation for the first maximum (see Figure 52). The cracking behavior of Fe-0.15Ti is however complex: recall that a plateau behavior is reached, after which cracks again are formed. Consequently, the second increase in cracking after the plateau should also result in another maximum. Comparing the times at which cracking re-initiated and the times of the second and third maxima, Figure 52 shows that the third maxima most likely corresponds to the after-plateau increase in damage. There only remains to explain the origin of the second plateau. While a possibility is that it could be due to a surface effect, this is unlikely because for the high fugacity used, the coverage of the surface and therefore surface trapping will happen very fast, while the time of this second maximum is about 20 minutes. A more likely candidate is irreversible trapping of hydrogen by TiC particles, which should now be more significant. There are, in fact, two reasons why this is the more probable reason for the second maximum:

- (1) after the collapse of some of the diffusing hydrogen in the cracks after the first maximum, the lattice concentration in hydrogen has decreased; according to the theory developed for irreversible trapping, the total capture rate  $\bar{k}$  increases, making irreversible trapping more dominant.
- (2) the decrease in hydrogen flux between the first maximum and the first minimum is about  $8 \times 10^{14}$  at.H/cm<sup>2</sup>s for Fe-0.15Ti versus  $4 \times 10^{14}$  for Ferrovac E. Since there are less cracks in Fe-0.15Ti than in Ferrovac E, the contradiction between

the relative magnitudes of the decrease in flux disappears if one considers that a good part of the  $8 \times 10^{14}$  at.H/cm<sup>2</sup>.s. went to TiC particles instead of cracks.

The most important conclusion of this series of experiments is that, in the presence of irreversible trapping be it due to cracks or TiC particles, the population of hydrogen on lattice and reversible trapping sites will have kinetics governed by the irreversible trapping kinetics; at least until irreversible traps are filled; this will manifest itself by maxima and minima, as predicted by theory.

#### B.5. Conclusion on the hydrogen-induced cracking model:

A theory solely based upon our analysis of hydrogen trapping and permeation has been developed to explain the extent and kinetics of hydrogen-induced cracking in Fe and Fe-Ti alloys. Experimental results are qualitatively in agreement with the theory, whose major predictions are:

- (1) the extent of damage depends on the relative quantities of hydrogen on reversible traps other than grain boundaries (itself a reversible trap). For example, increasing the density of a reversible trap such as Ti atoms will decrease the amount of damage on grain boundaries.
- (2) the occurrence of a plateau in the kinetics of hydrogen-induced cracking is solely due to the presence of significant irreversible trapping. The absence of a plateau does not rule out irreversible trapping, but simply indicates a diminution of its importance relative to diffusion and reversible trapping.



Quantitative use of the theory is difficult because in some cases, only orders of magnitude of the parameters are known. The major limitation of the theory preventing a close matching of theory and experiment, is that created cracks have not been considered as potential irreversible and partially reversible traps. However, since the theory predicts or rationalizes all the effects that the introduction of a trap spectrum would have on the extent and kinetics of hydrogen-induced cracking, most discrepancies between theory and experiment can be explained in terms of the model's limitation. More direct evidence for the model's validity, while accounting for its limitations, has been obtained by a high fugacity permeation experiment, where as predicted, the time dependency flux of diffusing hydrogen exhibits minima and maxima behavior. Finally, it has been demonstrated that a surface effect could not be held responsible for the obtained experimental results.

### C. A TEM Study of Some Effects of Hydrogen Charging

#### C.1. Experimental technique.

Specimen sheets of dimensions similar to those used for the hydrogen-induced cracking experiment (see page 187) were mechanically polished to a thickness of about  $2.5 \times 10^{-2}$  cms (10 mils). The sheets were then charged in hydrogen using exactly the same technique as previously (i.e., poisoned IN- $\text{H}_2\text{SO}_4$ ,  $30 \text{ mA/cm}^2$ ). Charging was performed for various lengths of time, ranging from 5 to 30 minutes. The charged specimens were then prepared as thin foils for observation by transmission electron microscopy.

It was found that in low titanium content alloys (B,BC) due to the sudden nucleation of large densities of cracks, preferential dissolution occurred around the cracks during electropolishing and good foils could not be obtained. On the contrary, medium titanium content alloys were found more suitable for electro-thinning after hydrogen charging. The kinetics of hydrogen-induced cracking are slower in these alloys, making it easier to stop the charging before too much damage occurs, and the extent of damage is less, so that the foil may be sufficiently thinned before preferential dissolution around the cracks becomes a problem. The alloy selected for the study to be described was alloy CC (Fe-0.5Ti-0.064C), which possesses all the interesting trapping features discussed, e.g., titanium atoms and TiC particles. Charging times were limited to less than 20 minutes to avoid problems during thinning.

## C.2 Experimental observations.

After charging with hydrogen alloy CC exhibited both dislocation formation and twin formation. The latter was observed only after the former had already taken place, usually for charging times longer than 10 minutes.

### C.2.a. Event I: dislocation formation

Figures 53(a) through 53(e) illustrate the formation of dislocations due to hydrogen charging in alloy CC, without the imposition of an external stress; a close examination of these micrographs revealed that the dislocations were arranged in tangles. The formation of dislocations tangles in iron during or after cathodic charging



with hydrogen is a well established fact (e.g., Ref. 113, 114). In alloy CC some particularly interesting features are observed. As the charging time increases, the density of dislocations increases; for example, after 5 minutes of charging (Figure 53a), the dislocation density is quite low; interestingly, no surface blisters were observed at this charging time). At a charging time of about 7-10 minutes (Figures 53b to 3), tangles begin to form, mainly between TiC particles (Figures 53c, e) or between particles and grain boundaries (Figures 53b, d); the rest of the matrix is still relatively free of dislocations. At a longer charging time (20 min), (when the number of surface blisters and cracks in the pre-thinned specimens is now quite large), the density of tangles has increased considerably (Figures 53f, h). While most are still between particles or particles and grain boundaries, cell walls of dense tangles of dislocations are also observed. The number of dislocations tangles meeting a grain boundary has also considerably increased.

#### C.2.b. Event II: twin formation

The formation of twins at room temperature in bcc metals such as Fe-Ti alloys is an event of considerable interest since their observation in these alloys is quite rare. Indeed, because of the high stacking fault energy of most bcc metals, twin nucleation and growth can occur only in particular circumstances, such as deformation at low temperatures, or impact loading at room temperature (mechanical twins), or during the recrystallization process (annealing twins) or the  $\alpha/\gamma$  transformation (transformation twins).

In this particular experiment, the main question is: are the observed twins a result of the presence of hydrogen, or were they present in the material before charging? (Such would be the case if

they were annealing or transformation twins). Statistically, it was observed that in about 50 foils made from uncharged specimens, only once was a twin-like feature observed. It was not identified as a twin, and in fact could have been a TiN particle (see Chapter I).

On the contrary, of the 20 foils that were prepared from charged sheets, twins and twin-like features were observed in all cases.

Since the charged and uncharged foils invariably came from adjacent regions of the same specimens, the probability is considered very low that the observed differences are a result of chance.

Consider now Figures 54a through 54i. Figure 54a has been included among the twin pictures because it appeared that for short charging times (10 minutes), the feature shown in this Figure 54a (straight dense tangles of dislocations) was a precursor of the twins that appeared later on. This observation was not documented however. Figure 54(b) to (i) illustrates the various twin configurations encountered in this experiment. That these are indeed twins has been proven by analysis of selected area diffraction pattern, as described in detail in Appendix F; they were found to have the usual crystallographic orientations for twins in a bcc metal, i.e.,  $\{211\} \langle 111 \rangle$ .

The shape of the twins varied from lenticular (Figures 54b to f) to prismatic (Figures 54g to i) when the charging time was increased. The location of the twins was invariably in a region close to a grain boundary; in fact, a good number of the twins were either nucleated from or were obstructed by grain boundaries (Figures 54g,h). Also of



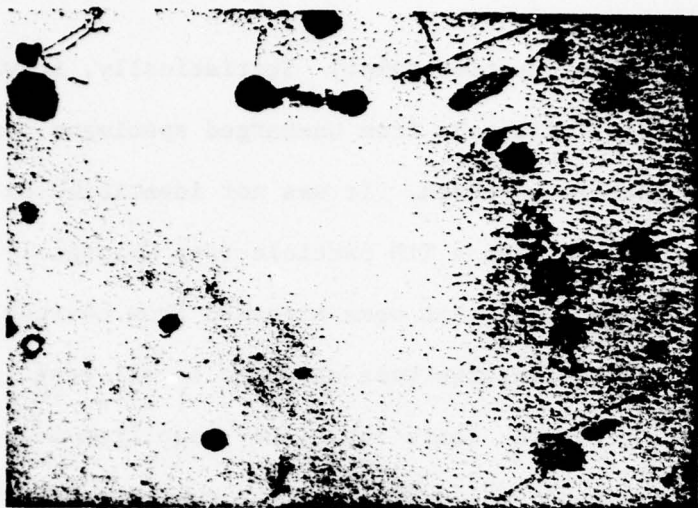


Figure 53  
Event I: Dislocation Formation  
Transmission electron micrograph  
of hydrogen charged Alloy CC

(a) Charged at  $30 \text{ mA/cm}^2$  for 5 min.

$0.7 \mu$



(b) Charged at  $30 \text{ mA/cm}^2$  for 7 min.

$0.7 \mu$



(c) Charged at  $30 \text{ mA/cm}^2$  for 7 min

$1 \mu$



Figure 53 ( continued )

(d) Charged at  $30 \text{ mA/cm}^2$  for 7 min.

1  $\mu$



(e) Charged at  $30 \text{ mA/cm}^2$  for 7 min.

0.7  $\mu$



(f) Charged at  $30 \text{ mA/cm}^2$  for 20 min.

1.5  $\mu$



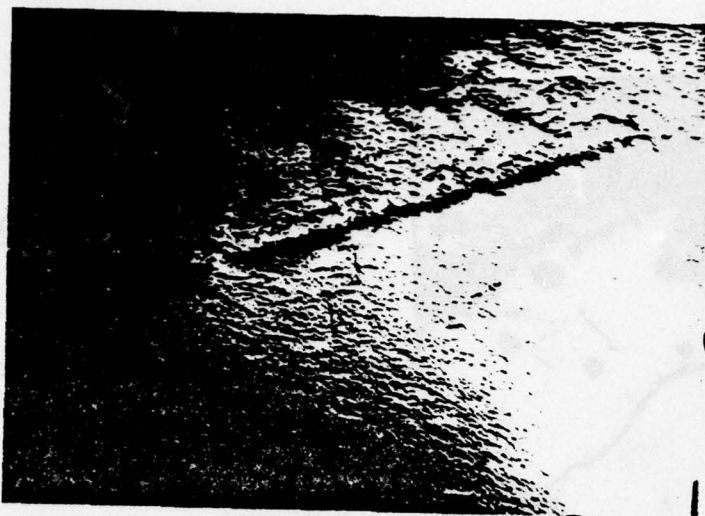


Figure 54  
Event II : Twin Formation  
Transmission electron micrographs  
of hydrogen charged Alloy CC

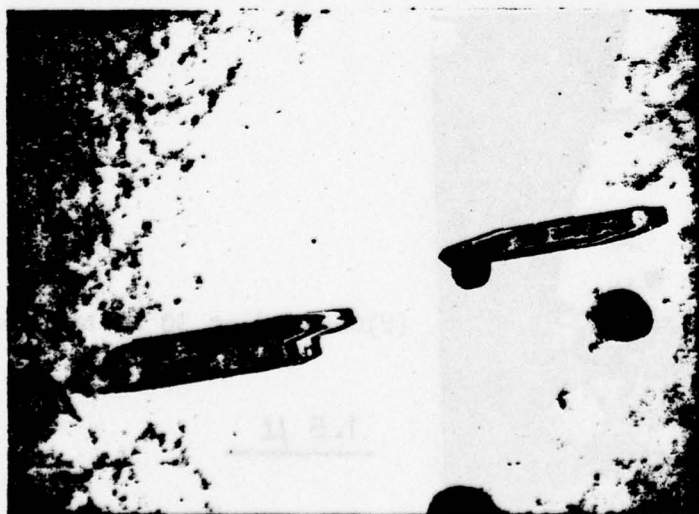
(a) Charged at  $30 \text{ mA/cm}^2$  for 10 min.

$1 \mu$



(b) Charged at  $30 \text{ mA/cm}^2$  for 20 min.

$0.4 \mu$



(c) Charged at  $30 \text{ mA/cm}^2$  for 20 min.

$0.3 \mu$



Figure 54 ( continued )

(d) Charged at  $30 \text{ mA/cm}^2$  for 20 min.

$0.3 \mu$



(e) Charged at  $30 \text{ mA/cm}^2$  for 20 min.

$0.1 \mu$



(f) Charged at  $30 \text{ mA/cm}^2$  for 20 min.

$0.4 \mu$



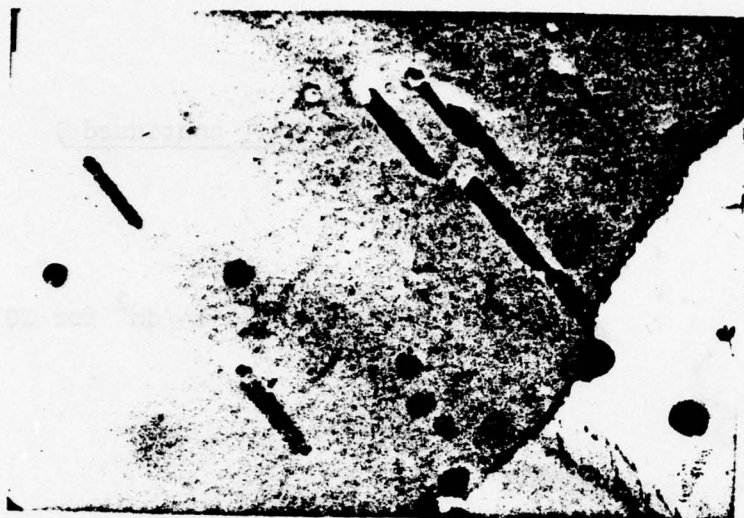


Figure 54 ( continued )

(g) Charged at  $30 \text{ mA/cm}^2$  for 20 min.

1  $\mu$



(h) Charged at  $30 \text{ mA/cm}^2$  for 30 min.

2.4  $\mu$



(i) Charged at  $30 \text{ mA/cm}^2$  for 30 min.

1.2  $\mu$

importance is the observation that a large number of twins seemed to be associated with TiC particles (Figure 54b).

The density of twins increased with charging time, as may be seen, for example by comparing Figures 54g and 54h; although at "low" charging times (20 minutes), twins seem to nucleate in dislocation free regions (Figures 54b through g), increasing the charging time increased the number of dislocations associated with the twins.

### C.3. Discussion

#### C.3.a. Interpretation and significance of dislocation formation

The fact that dislocations form during cathodic charging in hydrogen is clearly an indication of lattice deformation occurring during the process. Since the appearance of dislocations was closely associated with the formation of surface blisters and internal cracks, these phenomena must be somehow related. Furthermore, dislocation nucleation appears to have occurred at particles and, for the case of dislocation tangles, at grain boundaries.

What is the reason for the nucleation of dislocations at particles and grain boundaries? According to Chapter II and to the model describing the kinetics of hydrogen-induced cracking, the largest population of hydrogen is distributed at particles and grain boundaries. We thus propose that the excess of hydrogen atoms, accumulating at these sites leads to the formation of dislocations either directly or due to molecular hydrogen formation at high pressures. These dislocations can act



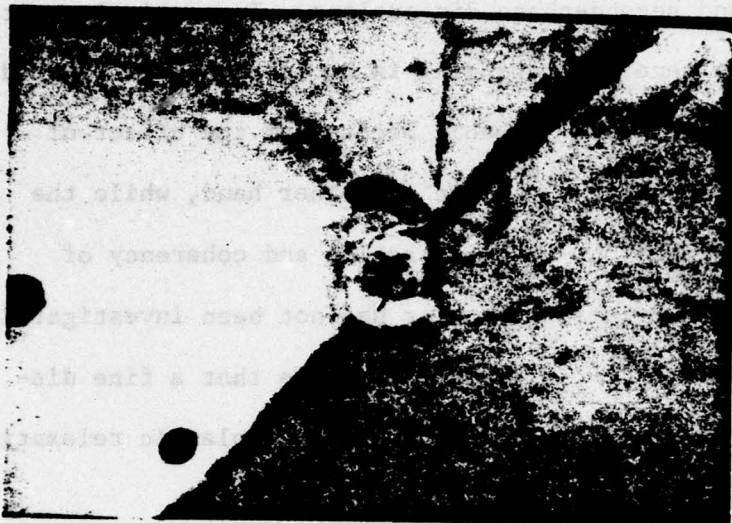
as traps for hydrogen from the lattice, and since particles are saturated before grain boundaries, (see Chapter III, page 162) some of this hydrogen trapped on dislocations tangles could be channelled to the grain boundaries enhancing still further the formation of grain boundary cracks. This last observation and the fact that dislocation nucleation adds reversible hydrogen traps have not been considered in the previous model (Section B) The consequences of this added limitation may be discussed in the same way as was done for crack nucleation (see page 185).

Possible grain boundary nucleation sites were observed. For example, Figure 55 shows the presence of several grain boundary holes which originated at a particle, or between two particles. Certainly, since a TiC particle on a grain boundary is such a strong trap, it is probably the site where a critical hydrogen concentration for cracking will be reached first.

#### C.3.b. Interpretation and significance of twin formation

As stated before, twins in bcc iron alloys can be classified as either deformation twins, annealing twins, or transformation twins. Because it was observed that twins were present only in charged specimens, the possibility that these features are annealing or transformation twins seems unlikely. It is much more likely that they are deformation twins induced by the hydrogen produced by cathodic charging. Usually, because of their high stacking fault energy, <sup>(115,116)</sup> deformation twins are only observed in bcc iron after low temperature deformation or shock-loading. However, there

**Figure 55**  
**Possible crack nucleation sites**  
**Transmission electron micrographs**  
**of hydrogen charged Alloy CC**



(a) Charged at  $30 \text{ mA/cm}^2$  for 7 min.

$0.6 \mu$



(b) Charged at  $30 \text{ mA/cm}^2$  for 13 min.

$0.4 \mu$



are other variables, besides temperature and high strain rates, which influence twin formation. Of greatest interest here is the influence of alloying elements and second-phase dispersions. In particular, it has been observed that generally twinning in bcc lattices is favored by solid solution alloying,<sup>(117)</sup> probably because of the effect of solutes on dislocation behavior.<sup>(118)</sup> On the other hand, while the influence of size, distribution, volume fraction and coherency of second-phase particles on twinning behavior has not been investigated in as systematic a manner;<sup>(116)</sup> it seems reasonable that a fine dispersion of particles could inhibit twinning, so that plastic relaxation occurs solely by slip.<sup>(116)</sup>

Let us now consider the particular case of alloy CC, which contains both substitutional solute and second-phase particles. Room temperature twinning has never been observed in this alloy either during the extensive studies performed by Honeycombe and co-workers (see Chapter I, Ref. 31 to 35 ), or by us in the absence of cathodic charging. The fine dispersion of TiC particles present, may have inhibited twinning. On the other hand, alloys of Fe-V-C and Fe-Nb-C, with microstructures very similar to Fe-Ti-C exhibited large numbers of transformation twins.<sup>(119,120)</sup> The explanations offered for the existence of twinning in these alloys were that either the solute reduces the stacking fault energy of the alloy, the solute inhibits cross-slip, or twins form to relieve stresses associated with either the  $\alpha/\gamma$  transformation, or the stresses developed at the particle/matrix interface. None of the explanations were found<sup>(119,120)</sup> to be entirely satisfactory.

In our particular case, (alloy CC) we have observed that stresses have been introduced in the lattice during cathodic charging, as evidenced by dislocation formation; further, we have discussed why we believe these are not annealing twins. Thus, the most logical hypothesis would appear to be that twins have been created in alloy CC to relieve stresses introduced by hydrogen charging (for example, at a particle/matrix interface, close to a grain boundary); the nucleation of such twins is made easier by the possibility that titanium lowers the stacking fault energy of the lattice. However, if only titanium produced a lowering of the stacking fault energy, annealing twins should be more commonly observed in Fe-Ti alloys. This is not the case.<sup>(119)</sup> The possibility then arises that since titanium solute atoms trap hydrogen, it is the presence of such clusters of TiH that sufficiently lowers the stacking fault energy while the effect of titanium alone was not sufficient. If this explanation is correct, then it would be consistent with the hydrogen embrittlement theory (see Introduction) that hydrogen lowers in some way the cohesive energy between atoms of the iron matrix.

#### C.4. Conclusion

The present TEM study has shown that, upon cathodic charging of alloy CC in hydrogen both dislocation formation and twin formation occurred. The former always preceded the latter, and exhibited dislocation tangles linking TiC particles or particles and grain boundaries, increasing with increasing charging time, i.e., with increasing hydrogen



content. Dislocation tangles have tentatively been attributed to hydrogen-induced stress concentrations at particles and grain boundaries.

Deformation twins appeared to nucleate either in the matrix or at particles; in either case, the twin population was always located near a grain boundary, and it increased with increasing charging time. The energetically favorable conditions for the nucleation of the twins are suggested to arise from the presence of titanium solute atoms and titanium-hydrogen clusters, which lower the stacking fault energy.

Some speculation as to the origin of crack nucleating sites is also possible since dislocations tangles are mainly associated with TiC particles and grain boundaries, and since these inhomogeneities were previously shown to be sites of strong trapping; particles and grain boundaries, and particularly particles on grain boundaries will accumulate large populations of hydrogen. Depending on which interface is weaker (TiC/ $\alpha$ Fe, or grain boundary interface, or TiC/grain boundary) and depending on the capacity of hydrogen trapping at the interface, a crack may nucleate at the weakest of these heterogeneities.

#### D. General Conclusions on Static Hydrogen Embrittlement and Proposed Criteria for Its Control

A model has been proposed to explain the kinetics and extent of hydrogen-induced cracking in Fe-Ti alloys. The two major conclusions

of the theory, confirmed by experimental results are:

- 1) Increasing the density of reversible traps such as titanium substitutional atoms decreases the maximum extent of grain boundary cracking for a given hydrogen fugacity. On the contrary, changing the density of irreversible traps such as  $TiC$  particles does not have a significant effect on the maximum extent. The kinetics are also affected in that reversible traps reduce the effective hydrogen diffusivity.
- 2) However, irreversible trapping is important in controlling the kinetics. It leads to a constant, low cracking plateau in the time dependence for hydrogen-induced cracking in Fe-Ti alloys, whose duration varies with the restrictions of the model, such as the trapping behavior of hydrogen-induced cracks and dislocations while neglected in the model has been discussed. The effects of such introduced traps (i.e., cracks, dislocations) on grain boundary cracking have been discussed to successfully rationalize the few discrepancies between theory and experiment.

A TEM study of hydrogen charged Fe-Ti alloys has shown that dislocations tangles and more significantly, deformation twins are produced during cathodic charging. The nucleation of deformation twins has been rationalized in terms of Ti-H clusters lowering the intrinsic stacking fault energy of the alloys.

Based on the above findings, a proposed set of criteria for the design of an alloy resistant to static hydrogen embrittlement has been developed:



Specifically, in order to reduce the extent of static hydrogen embrittlement, the microstructure of an iron alloy should consist of a homogeneous and fine distribution of reversible hydrogen traps. In addition, the addition of fine and homogeneously distributed irreversible traps (such as  $\text{TiC}$  particles), should help in delaying the onset of cracking.

The following Table proposes more general guidelines as to how specific traps operate.

TABLE XVIII

	Nature of trap	Example of such a trap	Effect on extent of damage.	Effect on kinetics of damage.
Good Trap	Finely and homogeneously distributed reversible trap $E(\text{trap-H}) < 0.6\text{eV}$	Solute atoms (e.g., Ti) low angle grain boundaries <sup>(24)</sup> microvoids. <sup>(57)</sup>	Decrease	Delay
Neutral Trap	Finely and homogeneously distributed irreversible trap $E(\text{trap-H}) > 0.6\text{eV}$	Small $\text{TiC}$ particles (size $< 1\mu$ ; density $> 10^{18}/\text{m}^3$ ).	None	Delay (plateau)
Bad Trap	Heterogeneously distributed strong trap	Microcrack large particle (e.g. $\text{TiC}$ with size $> 1\mu$ , density $< 10^{15}/\text{m}^3$ ). High angle grain boundary.	Increase	-

Table XVIII: Set of criterias for a static hydrogen embrittlement resisting alloy.

Small TiC particles have been considered on balance on neutral towards static embrittlement because due to their irreversible character, they do not influence the maximum extent of damage, and, due to their small size, they do not accumulate enough hydrogen to allow crack nucleation. However, their ability as traps to delay hydrogen diffusivity is still important, and they should be considered as a valuable addition.



## CHAPTER IV

### EFFECT OF HYDROGEN ON MECHANICAL PROPERTIES

#### OF FE-TI ALLOYS (DYNAMIC HYDROGEN EMBRITTLEMENT)

##### A. Summary of Past Studies on the Effect of Hydrogen on Mechanical Properties of Iron Alloys:

The effect of hydrogen on the mechanical properties of Fe-Ti alloys, particularly the degree of embrittlement, have been monitored by the loss of ductility during a tensile test, and is evidenced by a decreased reduction in area. The following review of the literature will be concerned with previous work relative to this manifestation of this form of embrittlement.

As pointed out by Bernstein,<sup>(106)</sup> a major difficulty in ascertaining whether hydrogen has a direct effect on mechanical behavior is the fact that hydrogen charging can be accompanied by extensive dislocation generation, as was illustrated in Figure 53. Since hydrogen will interact with dislocations (whether the dislocations are hydrogen induced or generated during the tensile test), and since dislocations structures also influence mechanical behavior, any claims of hydrogen modifying the yield stress, hardness, work hardening, or yield point removal must be viewed with caution.<sup>(106)</sup> Nevertheless, as with hydrogen-induced cracking and as discussed in the introduction, all deleterious effects of hydrogen probably result from its accumulation at particular sites in the lattice. In the particular case of dynamic hydrogen embrittlement, the question arises as to not only what are the dangerous

sites, but also as to how hydrogen was transported to those sites, during the time of the experiment.

#### A.1. Transport of hydrogen during a tensile test:

It is now a well established fact that hydrogen is trapped at dislocations during charging (see Chapter II, Figure 10, for example); however, the less obvious fact that trapping can persist during dislocation motion <sup>by</sup> dislocation sweeping during plastic deformation has now also been directly confirmed experimentally.<sup>(21)</sup> Indeed, by measuring tritium release during tensile testing of tritium charged 304 stainless steel, Donovan<sup>(21)</sup> has shown that: (see Figure 56).

- 1) A constant tritium release occurred during the elastic region of the stress-strain curve,
- 2) The release rate rapidly rises as plastic deformation begins, then decreases monotonically until necking and fracture occur. This was reasonably interpreted by Tien<sup>(22,121)</sup> as direct evidence for dislocation sweep-out of hydrogen atoms. According to Tien,<sup>(22,121)</sup> saturation of the dislocations is reached early during the plastic deformation (when the dislocation density is about  $10^9/\text{cm}^2$ ), giving rise to the observed sharp maximum in tritium release (see Figure 56). However, as the dislocation density continues to increase with plastic deformation, the average hydrogen concentration on dislocations will consequently decrease (for a fixed initial quantity of tritium), and so will the number of



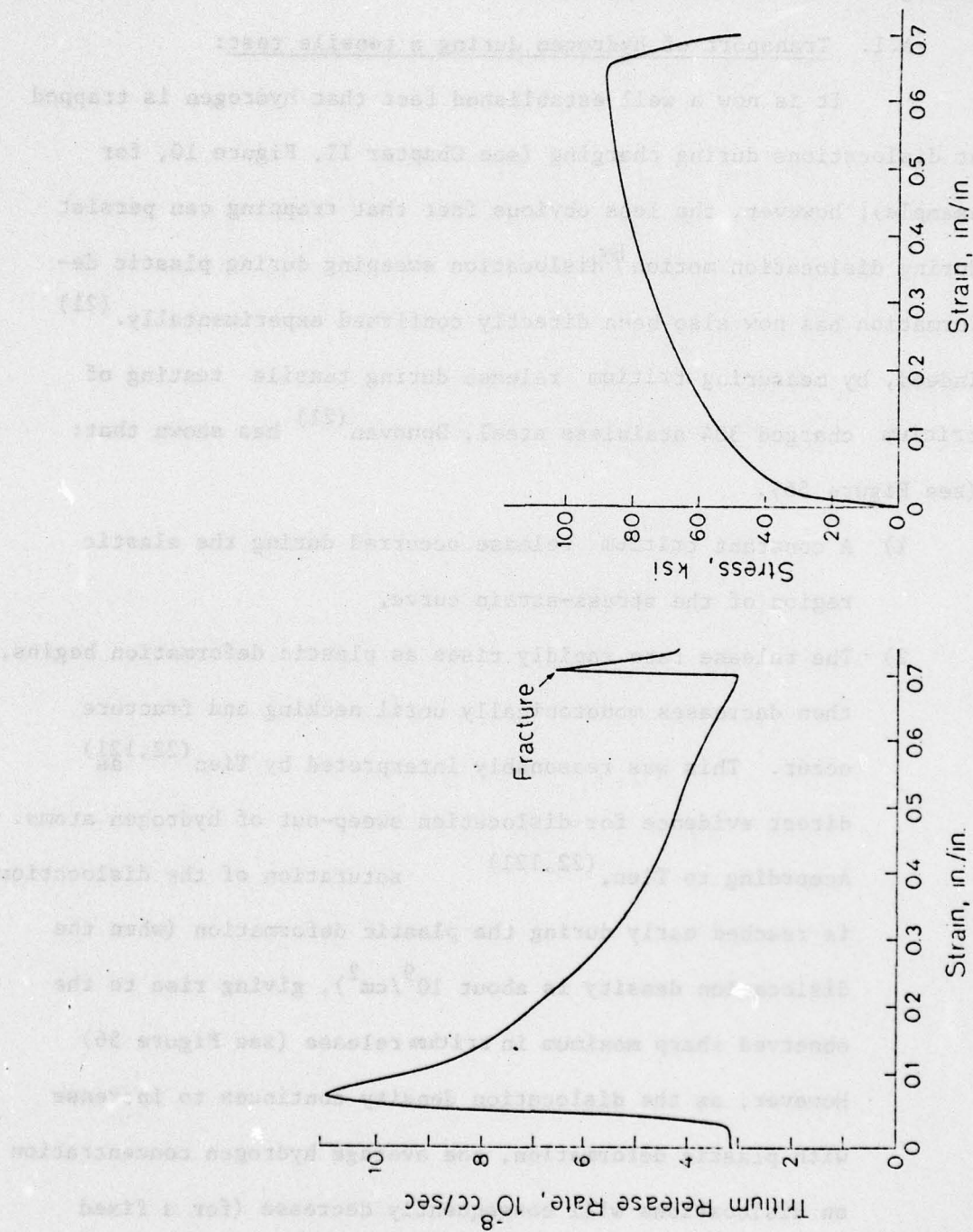


**Figure 56 :** The empirical release rate of tritium (a) as a function of strain in 304L stainless steel specimen, whose stress-strain behavior is shown in (b). Work of Donovan. (Ref. 21,22)

hydrogen atoms swept out. This rationale is in agreement with the ideas discussed in Chapter III, namely that increasing the number of reversible traps (here dislocations), for a fixed hydrogen concentration, will at the same time decrease their occupancy.

- 3) The release rate exhibits a second sharp maximum during necking and fracture. Donovan<sup>(21)</sup> attributed this to the rupture of voids which had been pressurized with hydrogen swept in by the dislocations. The idea that dislocation sweeping can result in accumulations of hydrogen at such microstructural traps as inclusion has recently been discussed on a theoretical basis by Tien.<sup>(22,121)</sup>

In this model the penetration depth ratio for lattice diffusion ( $Dt$ ) versus dislocation transport of hydrogen in iron alloys is calculated,<sup>(22,121)</sup> and it was seen that hydrogen will diffuse during the same length of time to a much greater depth by dislocation transport than by lattice diffusion, for the usual range of laboratory strain rates. Finally, there is also proof that grain boundaries and dislocation pipes are not short circuit paths<sup>(22,121)</sup> for diffusion of hydrogen at room temperature. There thus seems to be reasonable evidence, both experimental and theoretical, that hydrogen can and most probably will be transported by dislocation during a tensile test.

#### A.2. Hydrogen embrittlement of iron alloys during a tensile test:

Hydrogen embrittlement of iron alloys during a tensile test may take various forms, depending mainly on the microstructure (i.e.,



trapping characteristics) of the alloy under consideration; this variety is at the core of the different mechanisms of hydrogen embrittlement proposed in the literature, and discussed in the Introduction. Accordingly, the hydrogen-induced fracture surface may range from microvoid coalescence, to intergranular, or to cleavage, with the distinct possibility that all these features will be present at the same time.

Microvoid coalescence has been observed in fractured tensile specimens of charged plain carbon steels or austenitic stainless steels.<sup>(e.g.124)</sup> Although the fractography was the same when the specimens were not charged in hydrogen, the loss in reduction in area associated with the presence of hydrogen could be in excess of 50%.

Intergranular fracture is also seen in hydrogen-charged steels, and may involve other fracture features such as tear ridges and slip line markings.<sup>(23)</sup>

Finally, cleavage or quasi-cleavage has been found in such steels as tempered high-chromium steels,<sup>(125)</sup> with an RA loss over 60%. Here again, the fracture can be preceded and accompanied by highly localized plastic deformation.

Most steels however, will exhibit a fracture surface having a mixed character and where features associated with plastic deformation are commonly seen. From these general observations the following remarks can be made:

- 1) the variety in fracture morphology reinforces the idea presented in the Introduction, that there are as many aspects of hydrogen embrittlement as there are forms of existence of hydrogen in the lattice. For example, microvoid coalescence could originate

from hydrogen pressure build-up in voids produced by decohesion of the particles/matrix interface during tension;<sup>(124)</sup> on the other hand, intergranular cracking can occur if grain boundaries are potential sources of weaknesses in the material studied (e.g. Ref.41) and/or because particles on grain boundaries act as nucleation sites,<sup>(104,126)</sup> for hydrogen to be initially adsorbed.

2) the fact that plastic fracture processes seem to be associated with most "brittle" fractures<sup>(127)</sup> is indicative of the heterogeneity of the fracture, and therefore, of the heterogeneity of the crack nucleation sites. Indeed, if hydrogen embrittlement was, for example, solely due to a reduction in the binding energy between atoms of the host lattice, and if hydrogen was homogeneously distributed throughout the lattice, then the fracture surface would most probably exhibit a uniform aspect, i.e., cleavage or intergranular; such is not the case however, and several features are usually present at the same time. In fact, some regions of the surface appear not to be embrittled at all. This is probably explained in terms of our introductory premise, i.e., hydrogen will dangerously accumulate at specific sites in the lattice. Depending on the nature of the accumulation site (e.g., particle, grain boundary, internal flaw), the fracture morphology will vary accordingly (e.g., void coalescence, intergranular, cleavage); when such sites are absent or weaker, plastic deformation (as in the absence of hydrogen) will occur. We are assuming for now that hydrogen does not directly modify the deformation processes.



### A.3. Distinction between static and dynamic hydrogen embrittlement:

A distinction was made in the Introduction between a static form (i.e., hydrogen-induced cracking) and a dynamic form of hydrogen embrittlement. This distinction arises from the fact that in the absence of an external stress, hydrogen will diffuse mainly by lattice jumps (normal diffusion), and most trap densities will remain constant (except for dislocations and cracks, as seen in Chapter III). On the other hand, during a tensile test, for example, hydrogen will diffuse mainly as dislocation atmospheres, while the density of traps considerably increases (e.g., dislocations generated during plastic deformation, decohesion of particles/matrix interfaces, crack nucleation etc...). The distinction between the two forms of hydrogen embrittlement is thus merely a question of relative mobility of hydrogen and constancy of trap densities. As we shall see, the distinction will result in a criterion for a hydrogen-resistant alloys which will be somewhat different for dynamic hydrogen embrittlement than for hydrogen-induced cracking (see Chapter III). However, the findings of the previous chapters concerning trapping parameters and kinetics will again be demonstrated to be applicable.

### B. Experimental Procedure

Cylindrical specimens with standard ASTM dimensions were used for all tensile tests (the dimensions were: gage diameter: 0.625 cm; diameter at thread: 1cm; gage length: 2.5cm; overall length: 7.5cm; thread length: 2cm). All specimens were machined from recrystallized

alloys with an average grain size of about  $80\mu$  (see heat treatment section in Chapter I).

Prior to charging, all tensile specimens were mechanically and chemically polished to a mirror-like finish, and the thread region was painted with a hydrogen-impermeable lacquer (micro-stop). Cathodic charging was done using the same poisoned  $\text{IN-H}_2\text{SO}_4$  solution described in Chapter III, at various current densities. All specimens were charged for a length of time that guaranteed complete saturation in hydrogen at the current density involved; the time for saturation was calculated using the diffusion data of Chapter II and the  $x\propto\sqrt{Dt}$  relation. Since the diffusion coefficients of Chapter II were obtained at low hydrogen input fugacities, they were an underestimate of the diffusion coefficients valid at higher input fugacities (due to the concentration effect); consequently, the saturation times obtained from the Chapter II data were overestimates (i.e., saturation was safely achieved).

Following charging, all specimens were electrolytically plated with a cadmium layer of thickness about  $25\mu$ , using a bath consisting of 32g/l  $\text{CdO}$ , 112 g/l  $\text{NaCN}$ , 12g/l  $\text{NaOH}$  and 4.5 g/l of brightening agent dissolved in water; the plating cell was similar to that used for hydrogen charging (see Chapter III), but the anode was now made of cadmium wire; the plating conditions to obtain the desired thickness were: charging time 30 minutes, plating current density  $2.15 \times 10^{-2} \text{ amp/cm}^2$ . Plating the specimen with cadmium ensured that hydrogen would not escape



during tensile testing, as previously demonstrated by Troiano and co-workers<sup>(128)</sup> (this is due to the very low diffusivity of hydrogen in cadmium).

Finally, tensile tests were performed on an Instron machine at room temperature and at crosshead speed. 0.127 cm/min. (0.05 in/min.) unless otherwise specified; such strain rate has been widely used before, and its choice is governed by reasons that will be developed in a later section. After fracture, all specimens surfaces were observed by scanning electron microscopy (SEM JEOL 35U), and the percent reduction in area (%RA) measured by optical microscopy.

### C. Experimental Results:

#### C.1. Preliminary remarks:

Since all tensile specimens were charged in a poisoned  $\text{IN-H}_2\text{SO}_4$  solution, at relatively high charging current densities, hydrogen-induced cracking had taken place in every specimen before testing. The extent of hydrogen-induced cracking with current density has already been measured in Chapter III, Figure 50, and it was shown that the maximum amount of damage increased with current density to reach a plateau when  $i > 30\text{--}50 \text{ mA/cm}^2$ ; the height of the plateau was found to decrease with increasing titanium content. Since hydrogen-induced cracks will be present during tensile testing, their presence will have to be taken into account when interpreting subsequent mechanical results. In any case, cracks per se did not affect much mechanical properties of the uncharged alloys; this was verified by charging a tensile specimen of each alloy at high current density (i.e., numerous hydrogen cracks were generated), then heat-treating it

without cadmium plating for a few hours in a furnace at 300°C (to remove the hydrogen by degassing), and pulling to fracture.

All alloys regained their original ductility. On the contrary, there should be an influence of hydrogen-induced cracks on the tensile behavior of charged specimens that will reflect either an indirect effect of hydrogen (where hydrogen is present either as a high pressure gas in the crack, or absorbed or adsorbed at the crack tip), or the fact that cracks may act as induced notches if the fracture is brittle.

Finally, increasing the current density increased the solubility of hydrogen in all tensile samples. This was shown in Figure 51, where the solubility was measured on a Leco hydrogen analyzer (as described in Chapter III). As was also demonstrated in this Figure, Chapter III, most of the extracted hydrogen was probably present as high pressure gas in the cracks, or trapped at titanium carbide particles.

#### C.2. The stress-strain curves:

Although no detailed analyses of the stress-strain curves were carried out, the following observations were made:

- 1) As was previously noticed in steels (e.g., Ref.129)), charging with hydrogen influenced the properties associated with ductility, while the yield strength remained relatively unaffected. The only apparent effect of charging was to reduce the strain at fracture on the stress-strain curve.
- 2) Ferrovac E is the only alloy in which hydrogen had a marked effect on the yield point; as the charging current



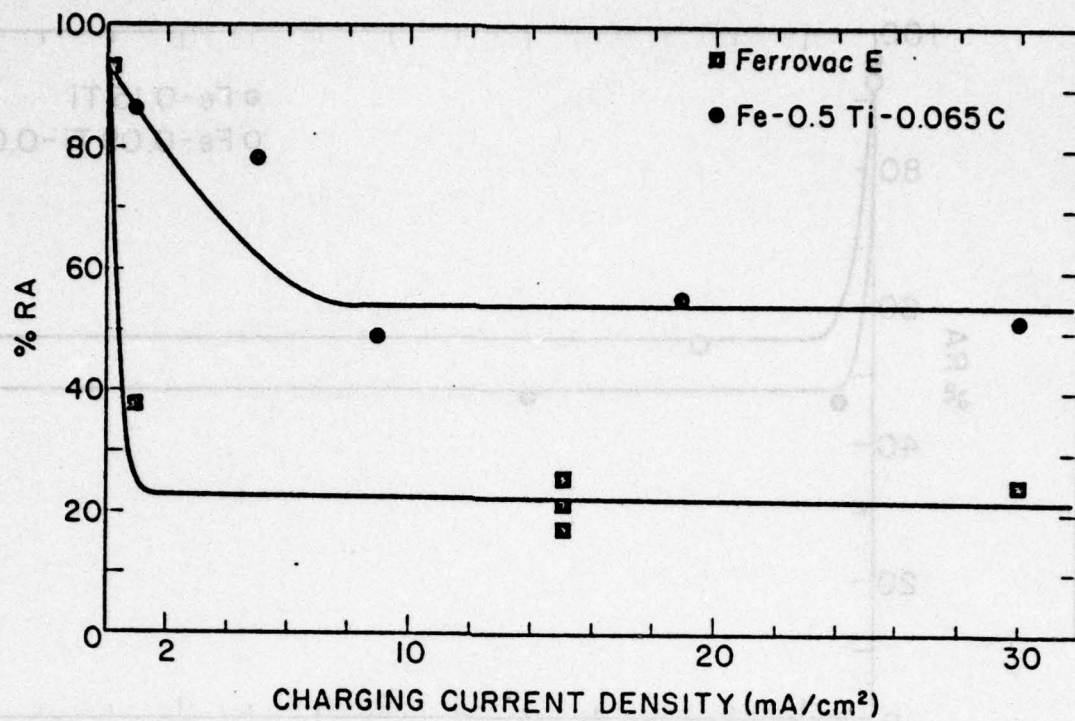
density increased, the yield point progressively disappeared (it completely disappeared after  $10\text{mA}/\text{cm}^2$ ). All Fe-Ti alloys did not exhibit a yield point in the uncharged state, and never exhibited one when charged with hydrogen.

These points will be further developed in the Discussion Section.

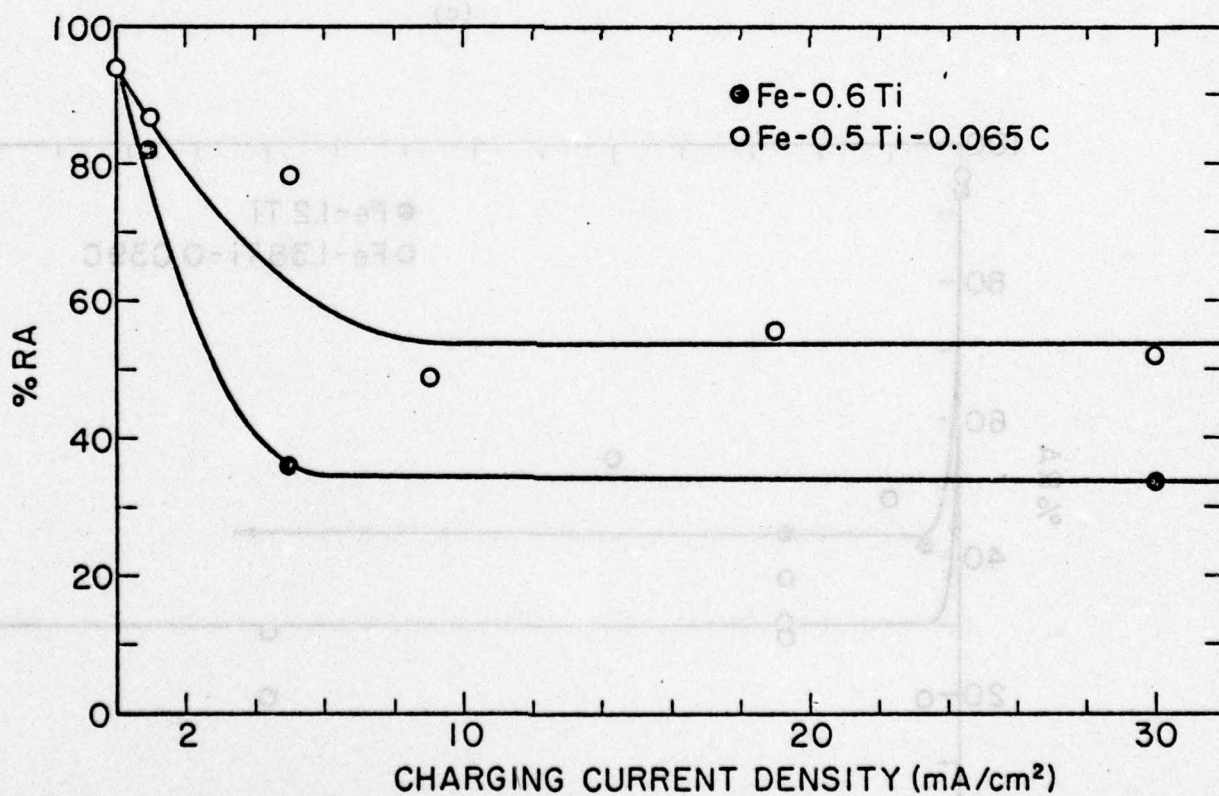
C.3. Hydrogen embrittlement of Fe-Ti alloys as measured by the loss in reduction in area

The percent reduction in area (%RA) was measured for all alloys and the results plotted in Figures 57, versus charging current density. Several important facts emerge comparing those Figures.

- 1) Alloy A (Ferrovac E) is the most embrittled material of all, followed closely by alloy DC (which has a high titanium content and large particles of titanium carbide).
- 2) Adding carbon to an uncarbured Fe-Ti alloy may improve the ductility (e.g., alloys B-BC and C-CC) or increase hydrogen embrittlement (alloys D-DC). It is quite interesting in view of the introductory statement (see Introduction), that improvement in ductility occurs in alloys containing large populations of small-sized particles, while the reverse is true for alloys containing large particles.
- 3) The best alloys in terms of ductility are alloys BC and CC (containing small particles); indeed, these two alloys exhibit a %RA of 55%, versus 23% for Ferrovac E (see Figure 57), when tested containing hydrogen.



(a)



(b)

FIGURE 57.

RA Loss Versus Charging Current Density.

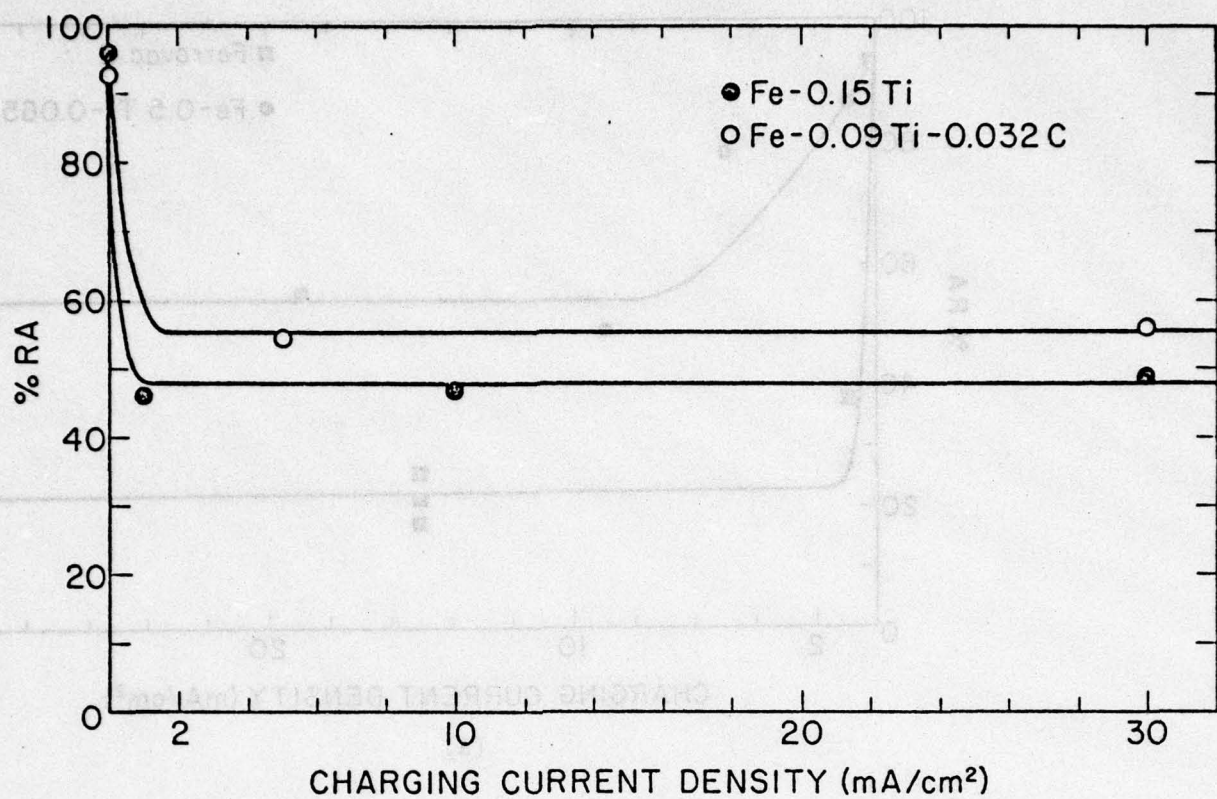
(a) Comparison between Ferrovac E and the Best Alloy, Alloy CC.

(b) Comparison between Alloy C and CC.

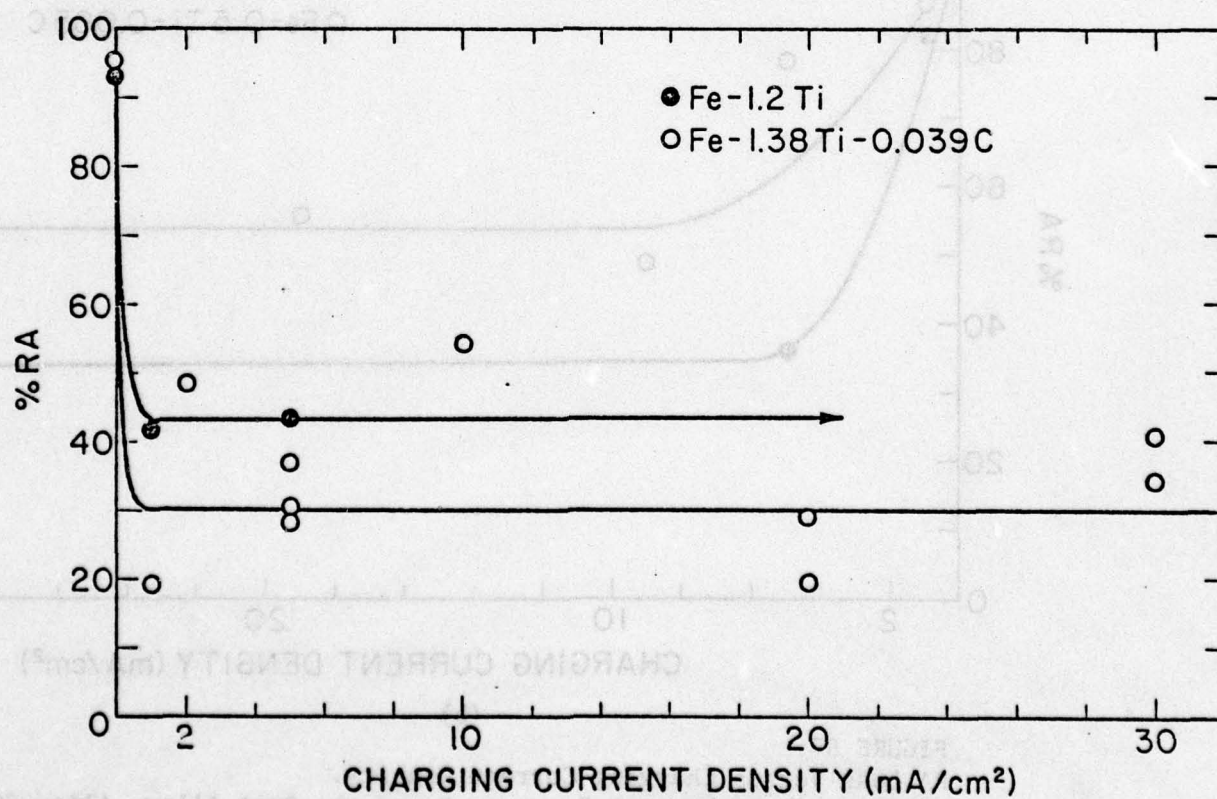
(c) Comparison between Alloy B and BC.

(d) Comparison between Alloy D and DC.





(c)



(d)

- 4) Adding more titanium to the uncarbured alloys does not seem to bring about much improvement; indeed, the %RA for alloy D is 44%, for alloy C: 35%, and for alloy B: 47%. This result is contrary to the results on hydrogen-induced cracking, as will be discussed.

C.4. Effect of strain rate and temperature on the RA loss of Fe-Ti alloys due to hydrogen embrittlement.

a) Effect of strain rate:

The effect of strain rate has been observed on alloy B, comparing the %RA of uncharged and charged specimens as a function of strain rate, Figure 58. The effect of increasing strain rate is to bring the ductility of the charged specimen back to its normal value, in agreement with previous studies (e.g., Ref. 130). As will be discussed, this is indirect proof of dynamic hydrogen embrittlement being transport-controlled.

b) Effect of temperature:

The effect of test temperature is illustrated in Figure 59 for alloys B and C, where the difference in %RA ( $\Delta(\%RA)$ ) between charged and uncharged specimens is plotted versus temperature. Since a large  $\Delta(\%RA)$  is significant of a large loss in ductility, hydrogen embrittlement exhibits a maximum in the room temperature region, while the deleterious effect of hydrogen disappears at lower temperature ( $T < -100^{\circ}\text{C}$ ) and high temperatures ( $T > 100^{\circ}\text{C}$ ). This result is in agreement with similar studies performed on steels<sup>(131)</sup> and is also in agreement, as we shall see, of dynamic hydrogen embrittlement being transport controlled.



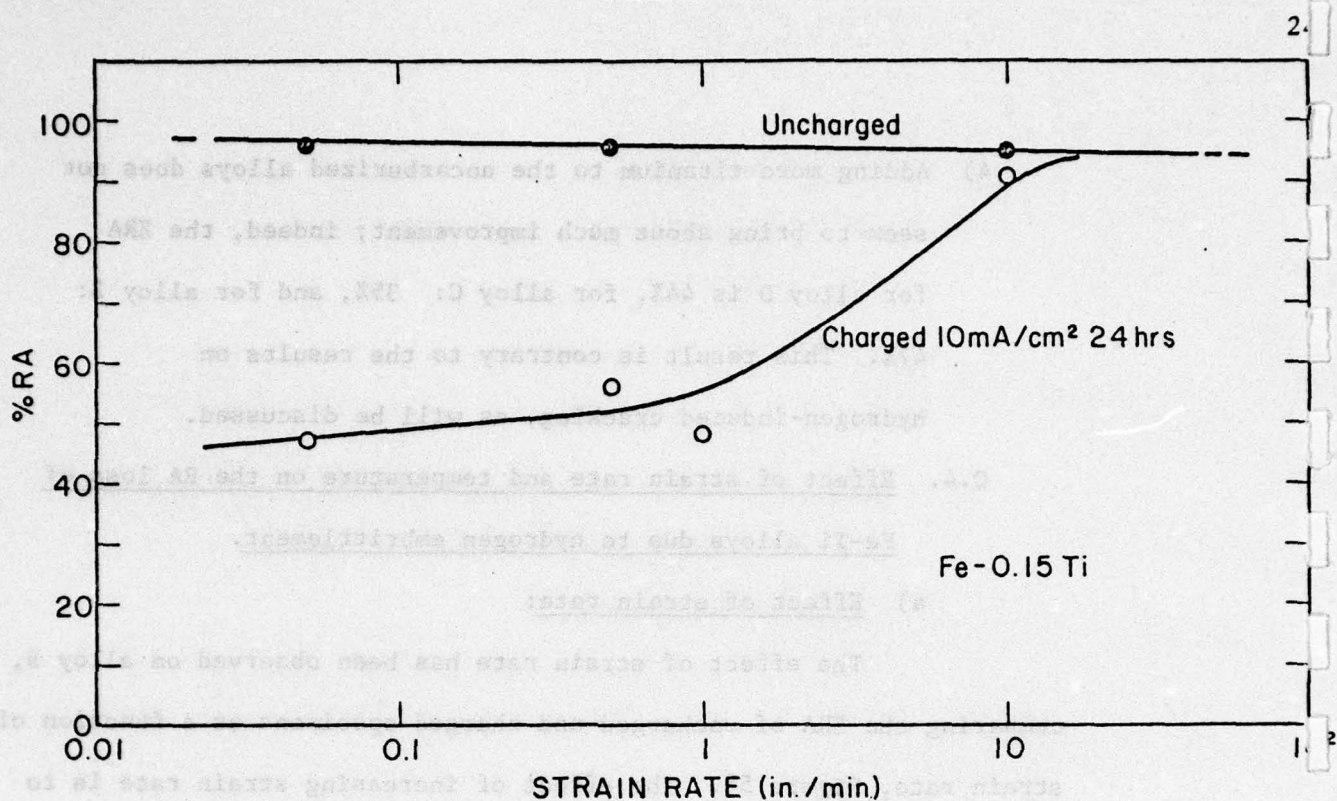


FIGURE 58.

RA Loss Versus Strain Rate for Alloy B.

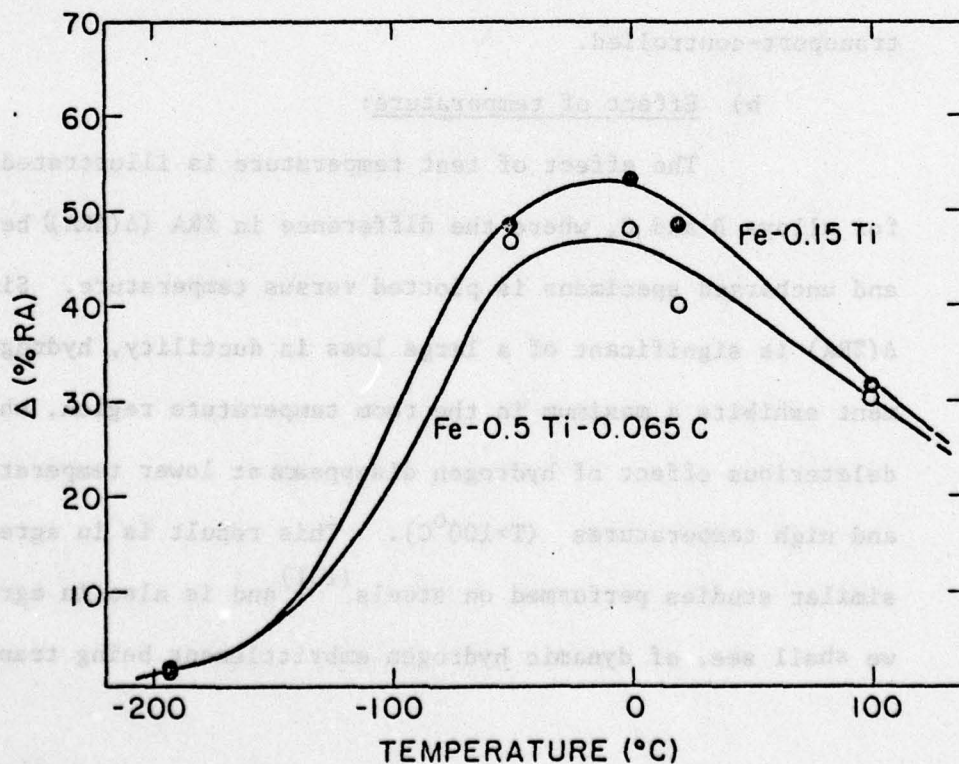


FIGURE 59.

Difference in RA Loss ( $\Delta$ (%RA)) between Uncharged and Charged Specimens of Alloys B and CC, Versus Test Temperature.

### C.5. Fractography of hydrogen-charged Fe-Ti alloys

#### fractured in tension:

All fractured tensile specimens were examined by scanning electron microscopy, so as to determine the fractographic characteristics of each material. Mixed modes of ductile and brittle monotonic loading fractures were most often observed, i.e., stretching, dimpled rupture and tearing when the fracture was ductile, cleavage and intergranular fracture when the fracture was brittle. Stretching was often present as slip markings or serpentine glide<sup>(132)</sup> It was also often observed that brittle regions appeared flat and featureless, without obvious cleavage crystallographic facets: these regions will be termed as quasi-cleavage. The following is a detailed review of the major fracture features of each alloy. For the sake of comparison, fractography of uncharged specimens was performed in Chapter I, and always consisted of dimpled rupture (see Figure 6, Chapter I).

#### a) Ferrovac E:

Hydrogen-charged Ferrovac E tensile specimens exhibited a mixed fracture mode, consisting mainly of cleavage facets separated by regions of dimpled rupture and tear ridges, as shown in Figure 60a1. The origin of the cleavage crack was most often traced back to a small intergranular crack (denoted, for example, by A in Figure 60a2), that ran perpendicular to the fracture plane; because hydrogen-induced cracking in Ferrovac E used in this study is intergranular, it is thus highly possible that cleavage nucleation sites were hydrogen-induced cracks. The arrow on Figure 60a1 indicates a direction of crack



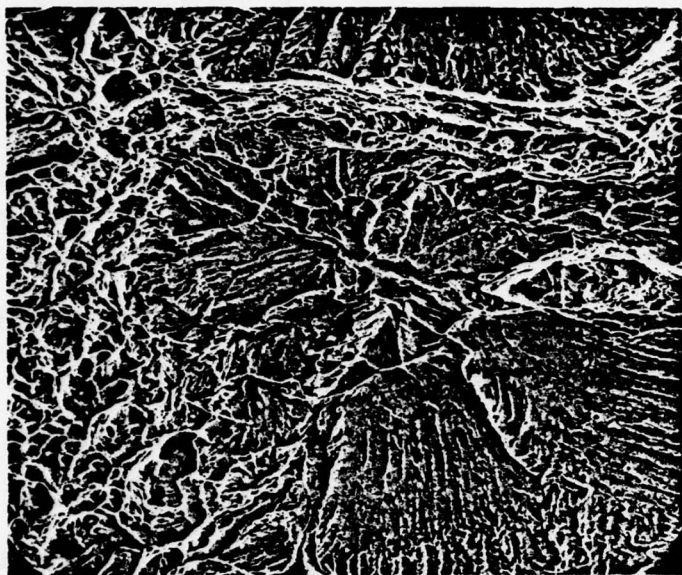
Figure 60

Scanning electron fractographs  
of all hydrogen charged alloys  
after tensile test.

(a) Ferrovac E, 10 mA/cm<sup>2</sup>

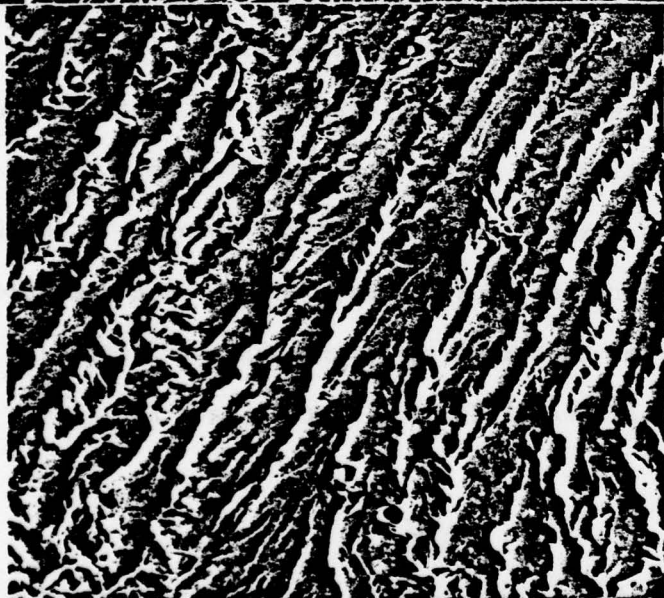
(a.1)

0.1 mm



(a.2)

0.02mm



(a.3)

0.03mm



propagation, as indicated by the local tear dimples (see Figure 60a1) and by the river-like patterns (i.e., the crack propagates radially from the central intergranular crack). In fact, the river-like patterns which look at low magnification like cleavage steps (Figure 60a1), are more reminiscent of tear ridges at a higher magnification (Figure 60a3). Hence, the term quasi-cleavage is more appropriate here. Also note, that the density of these features increases away from the cleavage nucleation site; this may be a sign of increasing plasticity away from that site.

b) Alloy B:

The fracture of this alloy is typical of most subsequent fractures, in the sense that it originates first intergranularly at the surface of the tensile specimen, probably at the site of the hydrogen-induced cracks. This sequence is illustrated in Figure 60b. Afterwards (this aspect is not typical of all other fractures), the fracture exhibits mixed tearing and intergranular mode, and, as one progresses toward the center of the specimen, tearing and dimpled rupture. No cleavage features were observed; increasing the current density simply increased the intergranular borderline regions (in agreement with the fact that increasing the current density up to  $30\text{mA/cm}^2$  also increases the density of hydrogen-induced cracks, as was shown in Figure 50, Chapter III).

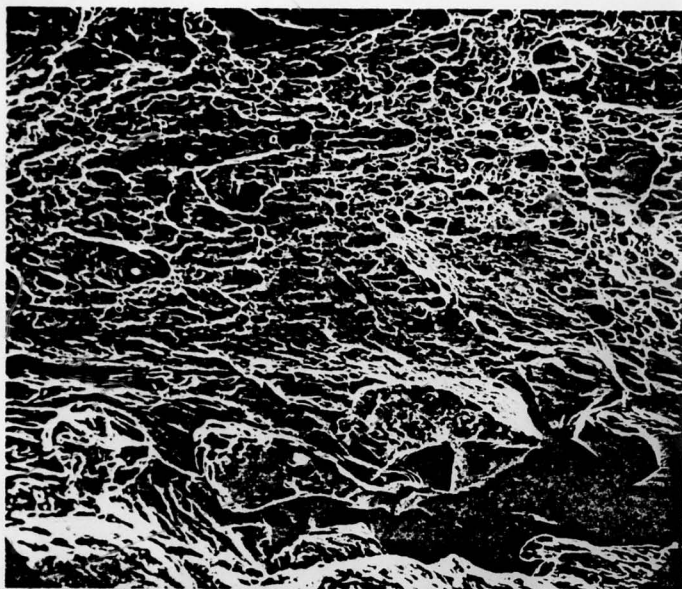
c) Alloy BC:

The fracture mode of this alloy is very complex, but may be characterized as quasi-cleavage mixed with ductile regions of tearing,



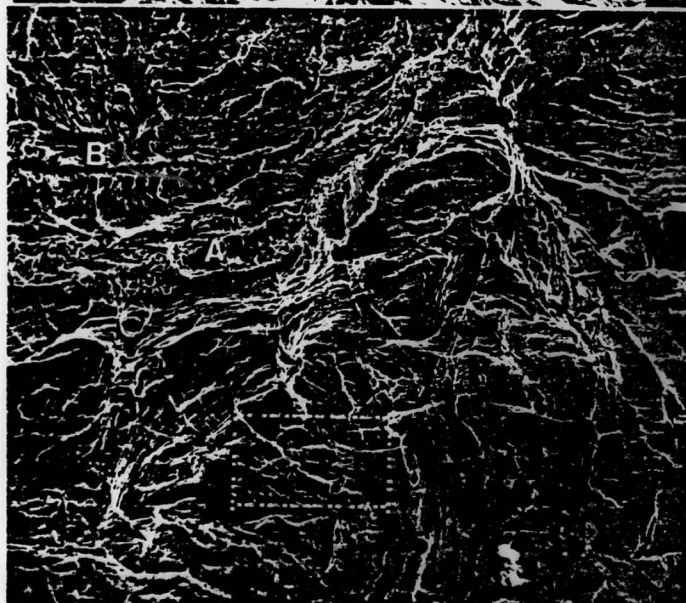
Figure 60 ( continued )

(b) Alloy B,  $30 \text{ mA/cm}^2$



0.13 mm

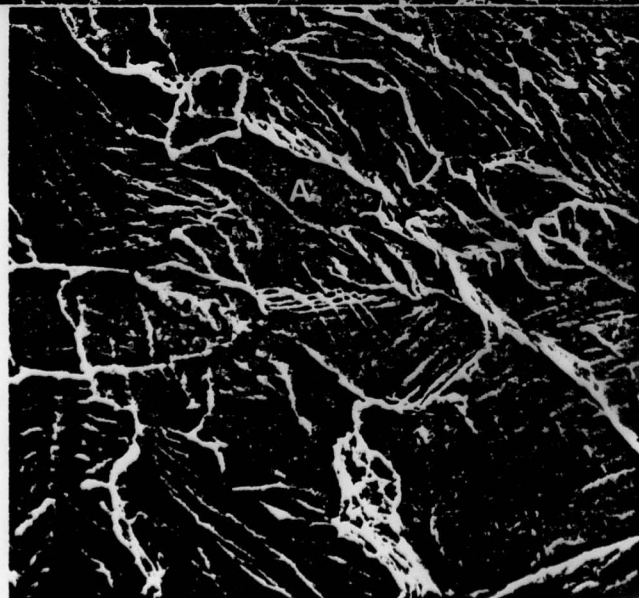
(c) Alloy BC  $15 \text{ mA/cm}^2$



(c.1)

0.1 mm

(c.2) High magnification view of  
boxed region on figure c.1.



0.02 mm

dimpled rupture (as in A on Figure 60c1) and serpentine glide. Secondary cracking is also present (region B in Figure 60c1, but no intergranular cracking was ever found.

d) Alloy C:

The fracture of this alloy is in every respect similar to that of alloy B, as it starts intergranularly (Figure 60d1), and progresses by tearing, dimpled rupture and serpentine glide (Figure 60d1). A secondary intergranular crack perpendicular to the main fracture face is also shown on Figure 60d2, illustrating that crack branching occurred (as was discussed in Chapter III, page 189).

e) Alloy CC:

As was seen before (Section C.3), this alloy retained more ductility than all other alloys. Its fractography exhibited all fracture modes previously encountered on other alloys, i.e., intergranular, cleavage, dimpled rupture, serpentine glide, and tearing. Figure 60e illustrates that, generally, fracture started intergranularly and spread by a cleavage (or quasi-cleavage) mode, until plasticity progressively dominated, producing generally the sequence, tearing, serpentine glide, and dimpled rupture (Figure 60e1). Details of each type of fracture mode are shown in Figure 60e3, to Figure 60e4, showing that regions of intergranular fracture also exhibit plastic deformation (as serpentine glide, for example); this also seems to be the case in the cleavage fracture of Figure 60e1 (lower left). In all cases, the fractures showed evidence of the presence of small titanium carbide particles. Moreover, as shown in Figure 60e5, it is interesting to note



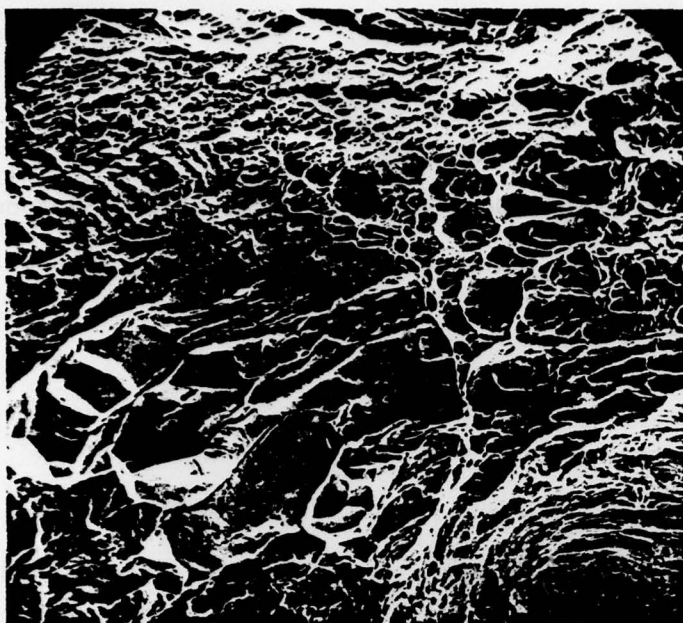
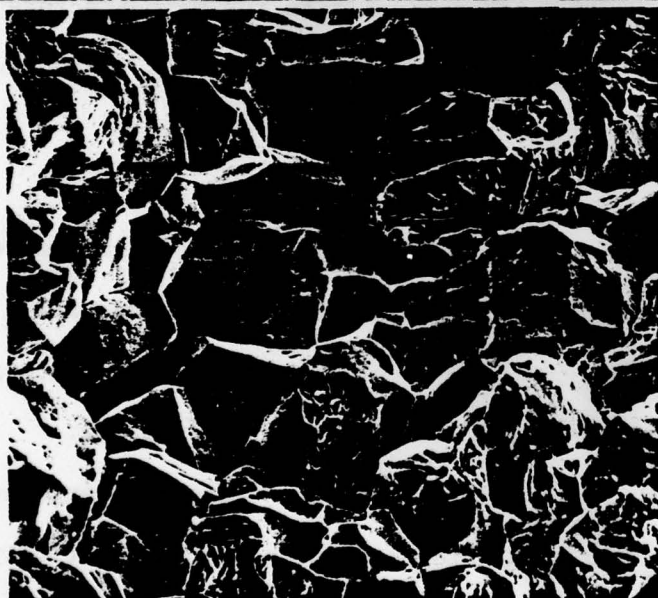


Figure 60 ( continued )

(d) Alloy C, 30 mA/cm<sup>2</sup>

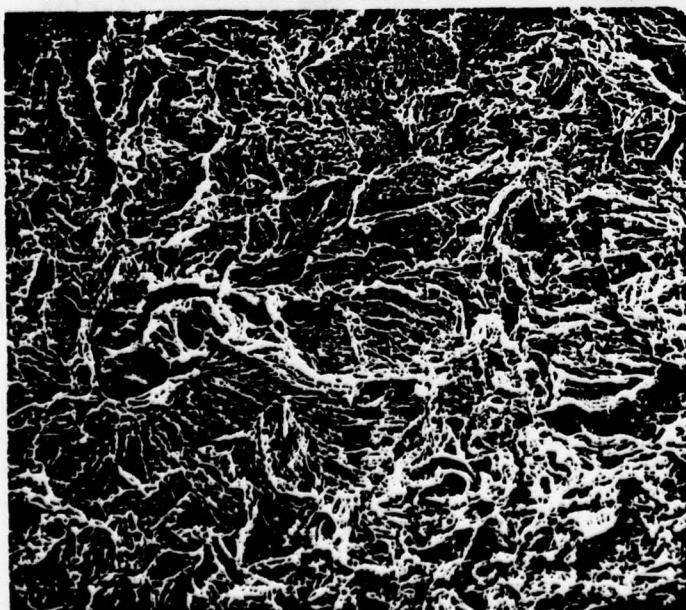
(d.1)

0.08mm



(d.2)

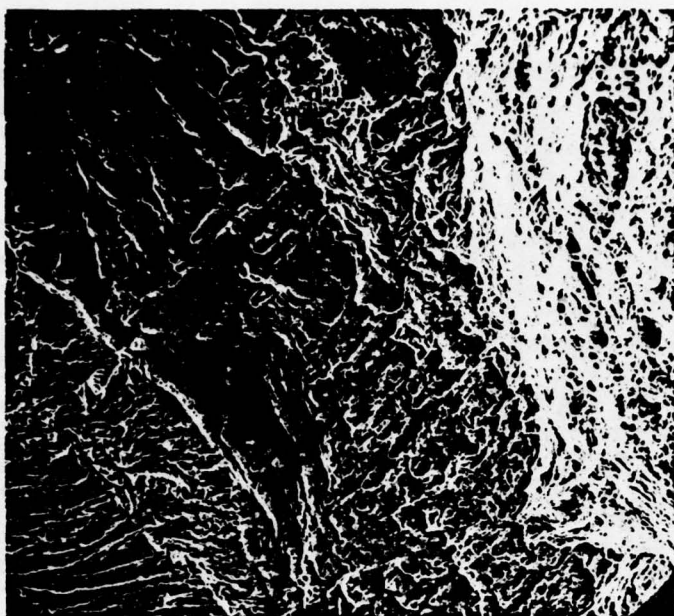
0.06mm



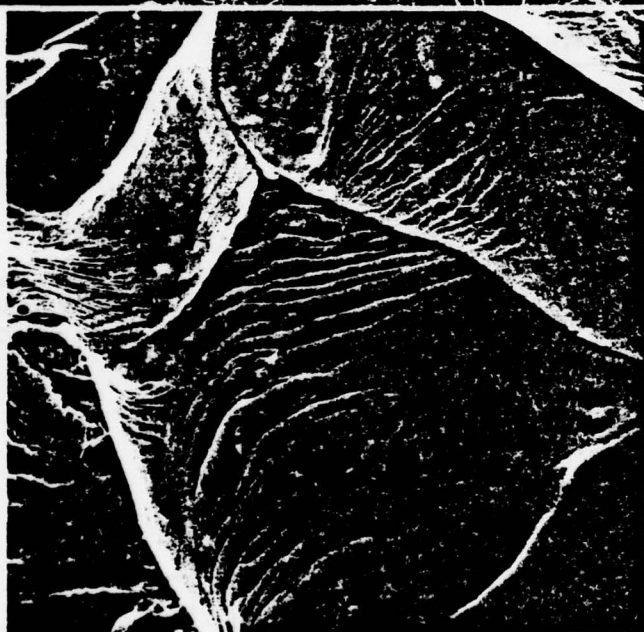
(e) Alloy CC, 30 mA/cm<sup>2</sup>

(e.1)

0.15mm



(e.2)

0.2 mm

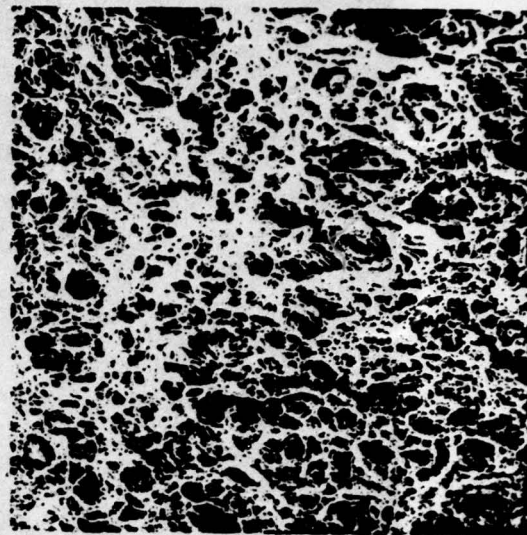
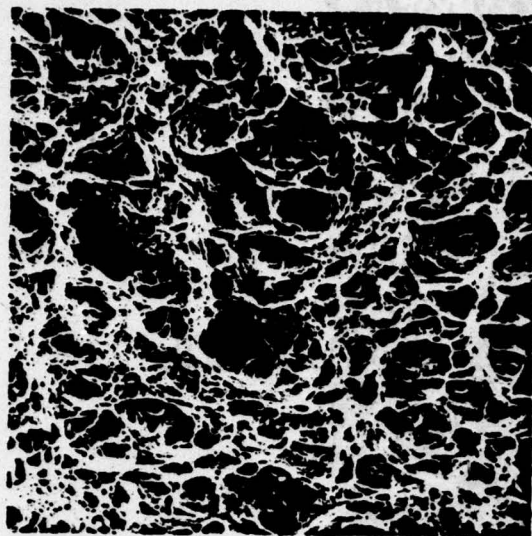
(e.3)

0.02 mm

(e.4)

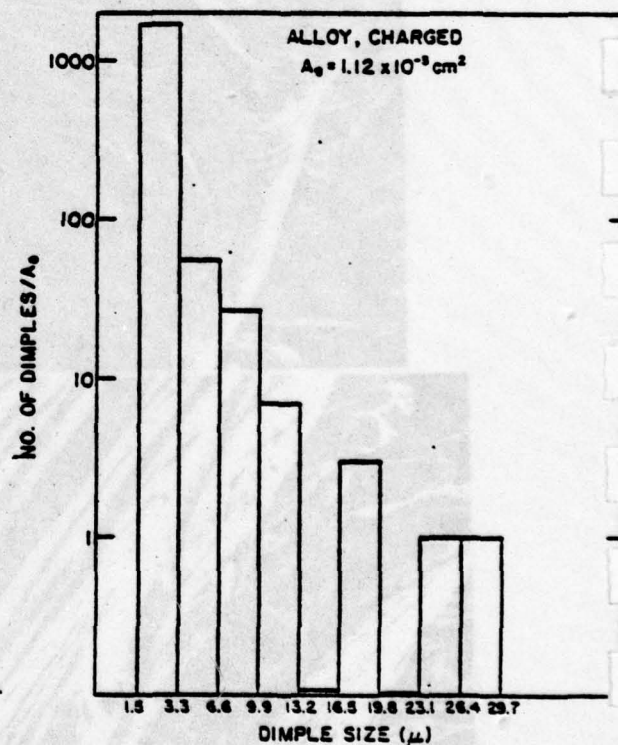
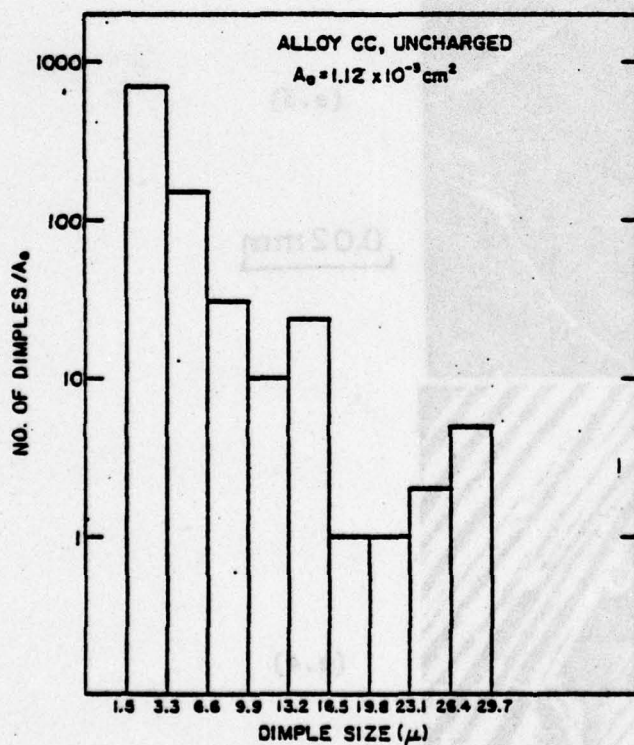
0.02 mm





0.1mm

(e.5) Dimpled rupture of Alloy CC, both in the charged (right) and uncharged (left) state. (  $9 \text{ mA/cm}^2$  ).



(e.6) Density of dimples in the fractographs of Figure (e.5), for uncharged (left) and charged (right) Alloy CC. (Dimples sizes are statistical averages)

that the number of fine dimples on the fracture surface notably increased when the specimen was charged, as compared to an uncharged specimen. This observation will be shown in the discussion to be in agreement with the previous results on the role of trapping. Finally, although intergranular fracture was present, its occurrence was limited, and the main fracture consisted of cleavage and ductile regions.

f) Alloy D:

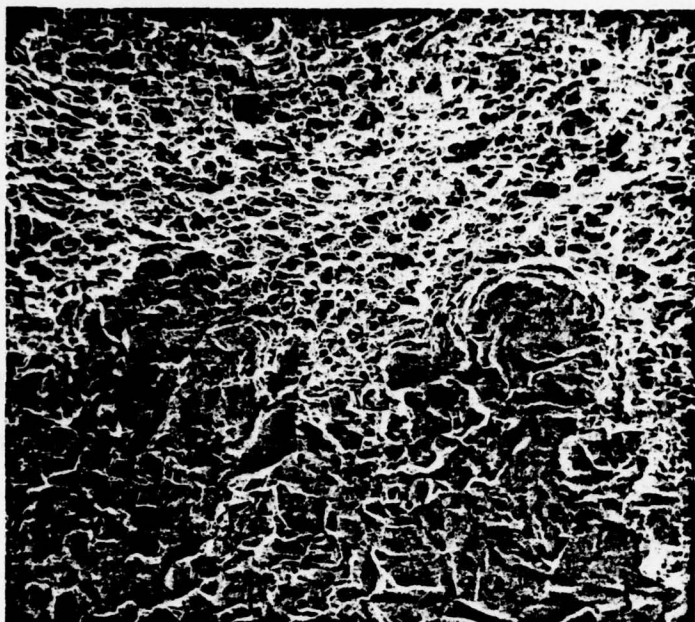
The fracture characteristics of this alloy were similar to those of the other uncarburized alloys B and C, (i.e., intergranular fracture plus ductile regions. However, as illustrated in Figure 60f the relative amounts of intergranular/ductile fracture have now changed to predominantly more intergranular regions.

g) Alloy DC:

The fractography of this alloy is also important, because alloy DC had the greatest sensitivity to hydrogen embrittlement. The fracture mode was complex and exhibited mixed characteristics of intergranular and cleavage regions, separated by ductile regions of dimpled rupture plus tearing and serpentine glide. Where this fracture differs from the fracture of alloy CC (which also features all the above mentioned modes) is the presence of a considerable amount of brittle fracture (particularly intergranular fracture) compared to the ductile regions. Figure 60g, illustrate this point by showing regions of intergranular fracture (with secondary intergranular and transgranular cracks) and cleavage. Note in particular how each cleavage step is associated with a large titanium carbide particle (Figure 60g2), as contrasted with the

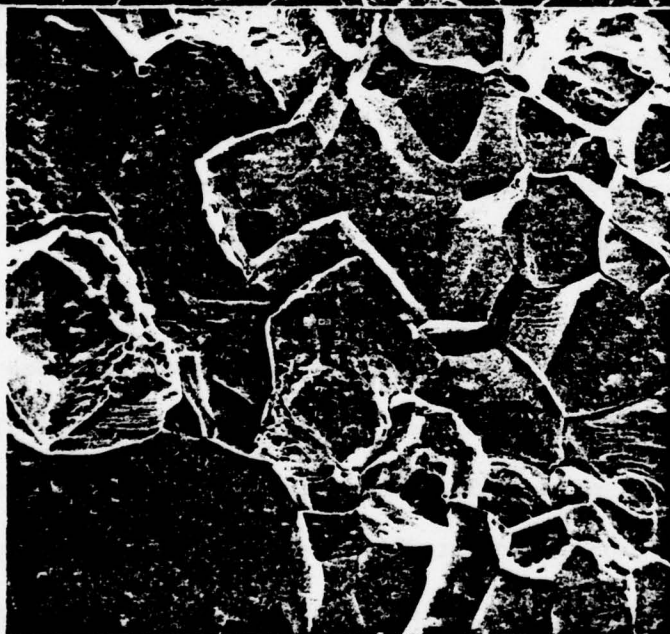


Figure 60 ( continued )



(f) Alloy D,  $1 \text{ mA/cm}^2$

0.2 mm



(g) Alloy DC,  $20 \text{ mA/cm}^2$

(g.1)

0.1 mm



(g.2)

0.02 mm

cleavage fracture of alloy CC, for example, (Figure 60e . Finally, it is important to note that cleavage is now often associated with a large particle (Figure 60g , as opposed to the other alloys where cleavage initiated most often as an intergranular crack.

#### D. A Qualitative Model of Hydrogen Embrittlement

##### D.1. Development of the model.

It is significant that the most hydrogen embrittlement-resistant alloys (BC and CC) are those with large densities of finely distributed small particles, i.e., strong irreversible hydrogen traps. Remembering the introductory statement (see Introduction) that hydrogen embrittlement may be prevented by finely distributing hydrogen in the lattice, this is in fact what is probably happening for alloys BC and CC, where hydrogen trapping by titanium carbide particles is occurring. In the same way, the most embrittled alloys are alloys DC and D, which exhibit few large particles at which, from previous considerations, large deleterious accumulations of hydrogen can occur. These most important results will constitute the basis of a subsequent criteria for a hydrogen embrittlement resisting alloy.

It was also found that increasing the titanium content does not appear to decrease the susceptibility of an alloy to dynamic hydrogen embrittlement, contrary to the case for hydrogen-induced cracking (static hydrogen embrittlement). We believe that this disparity arises from the basic differences, discussed previously in Section A.3, existing between the dynamic and static forms of hydrogen embrittlement.



In the dynamic form of hydrogen embrittlement, hydrogen is mainly transported by dislocations, with an interaction energy of about 0.25 eV. Therefore, accumulation of hydrogen at a particular site is possible only if the moving dislocations can "dump" their hydrogen at this site and if this site has a higher interaction energy with hydrogen than does dislocations. Referring to Table XVII, Chapter II, it can be seen that trapping sites with an interaction energy significantly higher than dislocations are titanium carbide particles (0.8-0.98 eV<sup>(25)</sup>) and grain boundaries (0.27 eV<sup>(62)</sup> and 0.55-0.61 eV<sup>(25)</sup>). As was mentioned before, the higher value of 0.55-0.61 eV<sup>(25)</sup> for grain boundaries was probably obtained for high angle grain boundaries (since they were shown to trap more than low angle boundaries<sup>(24,25)</sup>); moving dislocations will then have more chances to dump their hydrogen on high angle boundaries than on low angle ones. Other possibilities include voids<sup>(56)</sup> and microcracks.<sup>(13,14)</sup> Titanium has a similar interaction energy (0.27 eV) and lattice sites are much weaker than dislocations (0.08 eV). Therefore dislocations will release some of their hydrogen at titanium carbide particles, at some boundaries (probably high angle ones), or at voids and microcracks. On the contrary, traps with a lower interaction energy with hydrogen, e.g., lattice sites and possibly titanium atoms will, in fact, enrich the moving dislocations with hydrogen, leading to dislocations dumping additional hydrogen on particles and grain boundaries.

The process of hydrogen distribution throughout the lattice of a specimen being tensile tested can thus be visualized as being a

result of dislocation transport whereby strong hydrogen traps (TiC), grain boundaries, voids, microcracks, are preferentially enriched at the expense of weaker traps like titanium atoms, and lattice sites, which, in turn, lose their hydrogen. The fact that strong irreversible traps such as titanium carbide particles could already be saturated at the start of the tensile test (see Chapter III) is not an obstacle for further trapping during dynamic hydrogen embrittlement, because as discussed in Section A.3 of this chapter, deformation of the iron matrix around the hard TiC inclusions during tensile testing, and subsequent void formation will introduce new equally effective trapping sites.

If one accepts the above picture of hydrogen distribution in a specimen being dynamically tested, then the original premise that the origins of hydrogen embrittlement are directly related to the presence of traps which receive most of the hydrogen, namely titanium carbide particles, voids, microcracks and some grain boundaries is strengthened. This model predicts a reduction in hydrogen embrittlement whenever a trap with an interaction energy with hydrogen much above  $0.25\bar{eV}(E(-H))$  is present in the matrix as a fine homogeneous distribution. The only difference that this approach has with that previously developed (Chapter III) for hydrogen-induced cracking rests in the critical interaction energy value of  $0.25\bar{eV}$ ; in fact, the prediction for hydrogen-induced cracking is similar in every respect to the above, except that in this case, the critical interaction energy is  $0.08\bar{eV}$ . This is due to the fact that in static hydrogen embrittlement, hydrogen diffuses by lattice



jumps (normal diffusion) and only weakly interacts with lattice sites.

The validity of the model will now be checked against the experimental results.

#### D.2. Application of the model to experimental results

Experimental results are in good agreement with the ideas developed in the above model. Consider first the results of the RA loss with charging current density. As was shown in Figures 60a through g the alloys that best retained their ductility are those with a fine distribution of numerous TiC particles, such as alloys BC and CC. On the contrary, an increased particle size and a decreased density of particles, such as alloys BC and CC,

increased the susceptibility of an alloy to embrittlement, even though the titanium content was higher, such as in alloy DC.

The effects of strain rate and temperature on the RA loss, as shown in Figures 58,59 can also be rationalized with the model's predictions. Indeed, increasing the strain rate or the test temperature will result in less hydrogen being transported by dislocations, since at a high strain rate dislocations will be freed from their hydrogen atmospheres, while at high temperature, hydrogen will be too mobile to be retained at medium-strength traps, such as dislocations. On the other hand, lowering the test temperature lowers the mobility of hydrogen and dislocations, so that less hydrogen is transported to the strongest traps.

The fractography results are less obvious to interpret, but some remarks may be made concerning their relationship with the model:

1) The "best" alloys, BC and CC, display very little intergranular fracture, with their brittle regions mostly consisting of cleavage or quasi-cleavage (see Figure 60c and 60e). A particularly interesting result is that, when dimpled rupture occurs, the dimple size is much smaller than when the specimen is uncharged (Figure 60e). This could be explained by the possibility that in the charged specimens, moving dislocations have "dumped" much of their hydrogen at the numerous small particles. Therefore, these particles could act as nucleation sites for dimples either because hydrogen has reduced the cohesive energy of the interface between the particle and matrix, or because high gas pressures formed at the interface, or both.

2) The "worst" alloy DC displays large areas of intergranular fracture, and where cleavage is present, large TiC particles seem to play an important role in crack propagation (see Figure 60g). This last observation may be explained as above by evoking trapping of hydrogen at large TiC particles and subsequent large deleterious accumulations at these sites.

Such an accumulation on a grain boundary at some specific sites (large TiC particles) will certainly weaken the boundary and facilitate intergranular fracture, as is the case in this alloy. The fact that the TiC particles are not closely spaced on the grain boundaries of alloy DC may further lead to an intrinsic weakness of these boundaries since, as proposed in the literature, (25, e.g.) the presence of small and closely spaced TiC particles act as grain boundaries strengtheners.



### E. Criterion for the Design of an Alloy Resisting Dynamic Hydrogen Embrittlement

Since the previously proposed model seems to be in general agreement, not only with the experimental data collected on dynamic hydrogen embrittlement, but also with the results and theories developed in preceeding chapters, it is then possible to propose a set of criterion for the design of an alloy resisting dynamic hydrogen embrittlement, as follows:

In order to resist 'dynamic hydrogen embrittlement,' a suggested microstructure for an iron alloy is that it should consist of a homogeneous and fine distribution of strong hydrogen traps having an interaction energy with hydrogen of considerably more than  $0.25\text{eV}$ .

The following table provides guidelines as to what kind of traps should be used, as suggested by the present work.

Table XIX : Criteria for a dynamic hydrogen embrittlement resisting alloy

Nature of trap		Example of such a trap	Effect on susceptibility to hydrogen embrittlement
Good Trap	Finely distributed, strong, irreversible, trap. $E(\text{Trap-H}) \gg 0.25\text{eV}$	microvoids <sup>(56)</sup> Particles such as $\text{TiC}$ , of size $\ll 1\mu$ , density $> 10^{18}/\text{m}^3$	Decrease
Neutral	Trap strength $E(\text{Trap-H}) = 0.25\text{eV}$	Solute atom such as $\text{Ti}$ , low angle boundary <sup>(62)</sup>	None
Bad Trap	Heterogeneously distributed strong trap $E(\text{Trap-H}) \gg 0.25\text{eV}$	microcrack large particle such as $\text{TiC}$ size $> 1\mu$ , density $< 10^{15}/\text{m}^3$	Increase
	weak trap $E(\text{Trap-H}) \ll 0.25\text{eV}$	solute atom such as $\text{C}, \text{N}$ <sup>(63,64)</sup> lattice sites	Increase

Bad traps, on the other hand, are those where a heterogeneously distributed strong trap will dangerously concentrate hydrogen at a specific site, or where a weak trap will enrich the moving dislocations in hydrogen which, in turn, will dump their hydrogen on other bad traps.

#### F. Conclusions

Tensile tests have been performed on hydrogen charged Fe-Ti alloys, with the result that the alloys most resistant to dynamic hydrogen embrittlement are those having a microstructure consisting of finely and homogeneously distributed particles (alloys BC and CC). On the contrary, alloys with a few large particles were very susceptible to dynamic hydrogen embrittlement. Increasing the titanium content did not have the beneficial effect encountered with static hydrogen embrittlement.

Based on these results, and on the previous findings of Chapter II and III, a model for dynamic hydrogen embrittlement and criterion for the design of an alloy resisting dynamic hydrogen embrittlement have been proposed.



### CONCLUSIONS - SUMMARY

Detailed conclusions have been offered at the end of each Chapter. The following is thus intended as a general summary to underline the major findings of the thesis.

The results of this study of the influence of trapping on hydrogen transport and embrittlement have demonstrated that by varying the microstructure and therefore the trapping characteristics of Fe-Ti alloys, one could either control or delay hydrogen embrittlement. The entire thesis could, in fact, be viewed in summary as a pyramid (see Figure 61 ) whose base is developed from the results of the first chapters on microstructure and trapping characterization. This information concerning the density, distribution, nature, strength and capacity of the traps is then to be applied to static and dynamic hydrogen embrittlement, finally leading to criteria for their control. From this logical attack on this problem, the major results of this research can be summarized as follows:

#### Microstructural characterization:

From chemical analysis of the samples, and from detailed optical and electron microscopy work, all alloys have been shown to consist of a matrix of ferrite in which titanium substitutional atoms and titanium carbide particles are present in various quantities. Also present, but in negligible quantity, are iron and titanium nitrides, and titanium oxide particles.

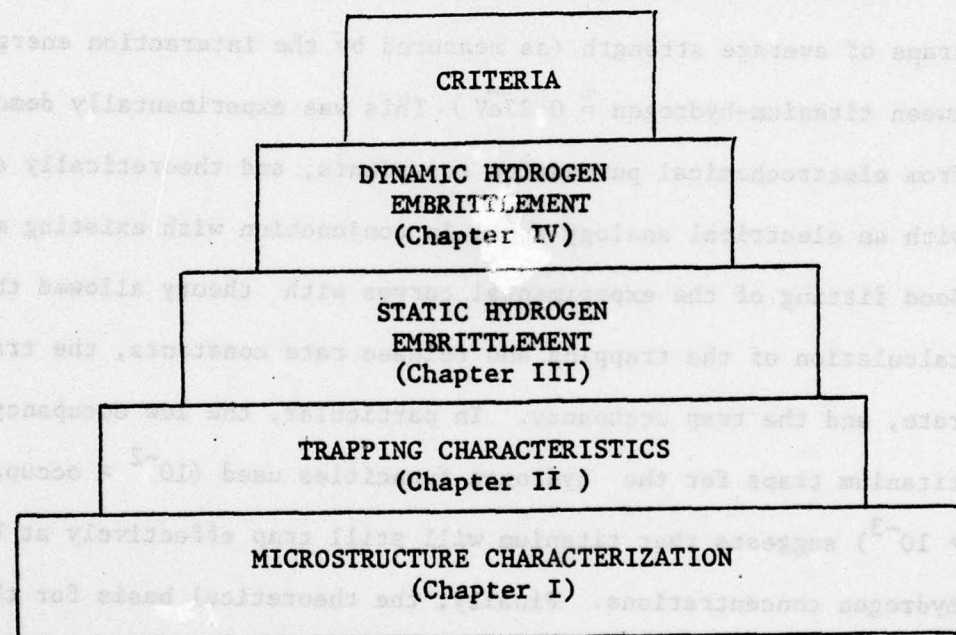


Figure 61

Summary of the organization of the present research.



All alloys, in the absence of hydrogen, exhibited a large ductility (RA = 95%), and similar tensile strengths when tested at room temperature in tension.

Trapping characterization:

Two major types of traps in Fe-Ti alloys have been identified in this study: titanium substitutional atoms and titanium carbide particles.

Titanium substitutional atoms have been shown to be reversible traps of average strength (as measured by the interaction energy between titanium-hydrogen  $\approx 0.27\text{eV}$ ). This was experimentally demonstrated from electrochemical permeation transients, and theoretically analyzed with an electrical analogy model in conjunction with existing models. Good fitting of the experimental curves with theory allowed the calculation of the trapping and release rate constants, the trapping rate, and the trap occupancy. In particular, the low occupancy of titanium traps for the hydrogen fugacities used ( $10^{-2} > \text{occupancy} > 10^{-3}$ ) suggests that titanium will still trap effectively at higher hydrogen concentrations. Finally, the theoretical basis for the existence of an attraction between titanium and hydrogen has been discussed in terms of the existence of thermodynamical and electronic forces.

Titanium carbide particles have been shown to act as strong irreversible traps (interaction energy between titanium carbide and hydrogen close to  $1\text{eV}$ ). This was demonstrated theoretically by modifying the trapping reactions so as to include irreversible

trapping, and by considering global trapping parameters. Experimentally, the ranking of diffusivities of the alloys, generally agreed with predictions of the model. Discrepancies between theory and experiment have been rationalized in terms of reversible trapping by small coherent TiC particles, whose behavior was not significantly accounted for. Since titanium atoms present on the surface of the permeation specimens could have influenced the rate of entry of hydrogen (i.e., by surface trapping), all permeation specimens had been plated on the input side with palladium. It was shown that by doing so, bulk diffusion was rate controlling; in other words, palladium plated Fe-Ti alloys behaved as Ferrovac E when tested for surface effects. An alternative explanation for the decreased diffusivity in Fe-Ti alloys in terms of a dominant surface effect is thus not valid. On the contrary, if the trapping characterization had been performed on uncoated Fe-Ti alloys, it was demonstrated both theoretically and experimentally that titanium surface trapping would have been significant. A concentration effect was quickly eliminated since an increasing titanium content also increased the concentration of dissolved hydrogen, and hence should increase the diffusivity; the opposite behavior was found.

Finally, a classification of all hydrogen traps present in the alloys was proposed, thereby serving as a basis for subsequent development for resistant alloys.

#### Static hydrogen embrittlement

Static hydrogen embrittlement, i.e., hydrogen-induced cracking in the absence of an external stress, has been studied both theoretic-



cally and experimentally.

A model has been developed to explain the extent and kinetics of hydrogen-induced cracking in Fe-Ti alloys. The model is derived completely from the results of the previous chapters, and starts with the fundamental assumption that irreversibly trapped hydrogen cannot be considered in equilibrium with the diffusing hydrogen, while reversibly trapped hydrogen can. With this assumption, the model then predicts that both kinds of traps (irreversible and reversible) influence the kinetics of embrittlement. Irreversible trapping possesses the unique feature that it can create a plateau in the kinetics of embrittlement (due to different saturation kinetics); reversible trapping will more directly influence the extent of damage i.e., increasing the concentration of reversible traps decreases the amount of hydrogen-induced damage.

By experimentally measuring the amount of damage due to hydrogen charging (as manifested in Fe-Ti alloys by the percentage of grain boundary cracks), most predictions of the theory were found to be verified. Discrepancies between theory and experiment were rationalized in terms of the main limitations of the model, i.e., hydrogen-induced cracks were not considered as potential traps. This limitation is only a quantitative one since the model can predict the effect of such newly introduced traps on grain boundary cracking. Confirmation of the validity of the model was also demonstrated from high input fugacity permeation experiments, where cracks were generated during

permeation. Finally, an alternative explanation for the observed results as being controlled by surface effects has been ruled out.

A TEM study of hydrogen charged Fe-Ti alloys has shown that, in addition to dislocation tangles, deformation twins were generated during cathodic charging with hydrogen. This effect was rationalized by suggesting that Ti-H clusters could reduce the stacking fault energy of the lattice.

Finally, by an extension of the criteria developed for traps an additional set of criteria was proposed to aid in the design of alloys resistant to static hydrogen embrittlement; specifically a list of good, neutral, and bad traps was presented.

#### Dynamic hydrogen embrittlement

Specimens of all alloys were fractured in tension after being charged in hydrogen. From a fractographic SEM study, and the RA loss produced after hydrogen charging, it was established that the most resisting alloys were those containing a fine, homogeneous distribution of irreversible traps (i.e. TiC particles). Alloys containing few large particles, particularly on grain boundaries, or only numerous weak traps (e.g. Ti atoms) exhibited high embrittlement.

These results were rationalized by a qualitative model where hydrogen is viewed as being transported during the test by dislocations, and 'dumped' at all sites stronger than dislocations.

A set of criteria is also proposed, which enumerates good, neutral and bad traps for alloys resistant to dynamic hydrogen embrittlement.



### General Conclusions

The introductory premise that a fine distribution of traps should decrease the susceptibility of an alloy to hydrogen embrittlement by taking part of the hydrogen away from potential crack sites has been verified.

Since the sets of criteria are slightly different for static and dynamic hydrogen embrittlement, a combined criterion for an alloy resisting both static and dynamic hydrogen embrittlement has been developed:

An alloy designed to resist both static and dynamic hydrogen embrittlement should have a microstructure consisting of fine homogeneously distributed reversible and/or irreversible traps; in the case of reversible traps, their interaction energy for hydrogen should be higher than dislocations.

The fact that the traps are reversible should help in lowering the extent of static hydrogen embrittlement, while the condition on the interaction energy and on irreversibility should reduce the damage due to dynamic hydrogen embrittlement.

### SUGGESTIONS FOR FUTURE WORK

The following developed from the results of this study are areas of study that should be investigated to improve our understanding of how traps affect the susceptibility of ferrous alloys to hydrogen:

1) In order to verify the general criteria proposed in the Conclusions section, similar experiments should be performed with alloys containing solute additions such as La, Nd, or Ta which also possess strongly negative interaction coefficients with hydrogen ( $e_{\text{H}}^{\text{La}} = 4.3^{(72)}$ ,  $e_{\text{H}}^{\text{Ta}} = -4.4^{(72)}$  and  $e_{\text{H}}^{\text{Nd}} = -6.0^{(72)}$  versus  $e_{\text{H}}^{\text{Ti}} = -1.1^{(72)}$  at 1600°C.)

2) The observation that deformation twins are produced during hydrogen charging deserves considerably more attention. In particular, an estimation of the reduction in stacking fault energy of ferrite by Ti, and Ti-H clusters could shed important light on the amount by which hydrogen reduces the cohesive energy of the lattice, if indeed this hypothesis is shown to be correct.

3) Crack nucleation sites have not been clearly identified in this study. A useful experiment would be to charge thin foils in hydrogen, and subsequently examine them in a high voltage electron microscope, to monitor where cracks actually originate. The use of thicker specimens with high voltage electron microscopy should allow one to distinguish between hydrogen-induced cracks and any artifacts, e.g., holes due to electropolishing, or particles being detached from the foil.



4) The assumption that no equilibrium exists between diffusing and irreversibly trapped hydrogen could be checked by various experiments. In particular, precise solubility measurements would establish whether or not increasing the density of TiC particles also influences the solubility of diffusing hydrogen.

5) The qualitative dynamic hydrogen embrittlement model could be further developed in a more quantitative fashion, thereby allowing more accurate predictions.

6) Both criteria (for static and dynamic embrittlement control) could be confirmed on other alloy systems, once their microstructure and trapping parameters have been well characterized.

## APPENDIX A

## IDENTIFICATION OF TITANIUM CARBIDE PARTICLES

Identification of titanium carbide particles was done by selected area diffraction analysis in the transmission electron microscope. Figure A.1.c and A.1.e illustrate the obtained diffraction pattern on which the identification was performed. As seen from those figures and the reconstructed pattern on Figure A.1.f, the matrix (e.g. spot M) has a  $[100]$  zone axis. Furthermore, as discussed in Chapter I, TiC particles have FCC lattice, of variable parameter  $a_{\text{TiC}_x} = 4.313\text{--}4.329\text{\AA}^{(45-47)}$  or  $a_{\text{TiC}} = 4.360\text{\AA}^{(45)}$ , depending on the carbon composition of the particles. The small coherent particles obey the Baker-Nutting relationship<sup>(31-35)</sup>, i.e., for planes in the matrix and in the particles:

$$(001)_{\alpha\text{Fe}} // (001)_{\text{TiC}} \quad (\text{A.1.1})$$

$$[100]_{\alpha\text{Fe}} // [\bar{1}\bar{1}0]_{\text{TiC}} \quad (\text{A.1.1})$$

Since the matrix is in a  $[100]$  orientation, the  $[\bar{1}\bar{1}0]$  diffraction pattern, for a FCC crystal with a lattice parameter of  $a_{\text{TiC}} = 4.34\text{\AA}$  (i.e. the lattice parameter that best fits the patterns), has been constructed in Figure A.1.f. The TiC pattern has also been oriented so that condition (A.1.1) is also satisfied.

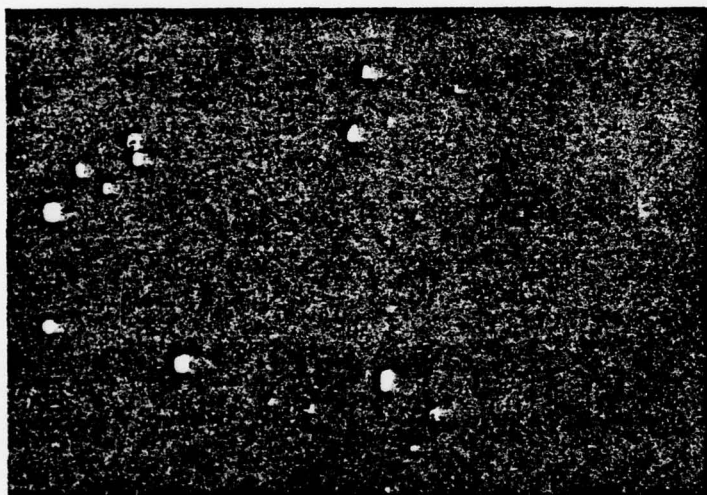
Superimposing the  $[\bar{1}\bar{1}0]$  TiC pattern on the  $[100]$  ferrite pattern is shown in Figure A.1.f, and then superimposing another  $[\bar{1}\bar{1}0]$  TiC pattern at  $90^\circ$  to the TiC pattern of Figure A.1.f (to satisfy condition (A.1.1) for the other planes), will satisfy all diffraction spots such as P (from which the dark field of Figure A.1.b was obtained),





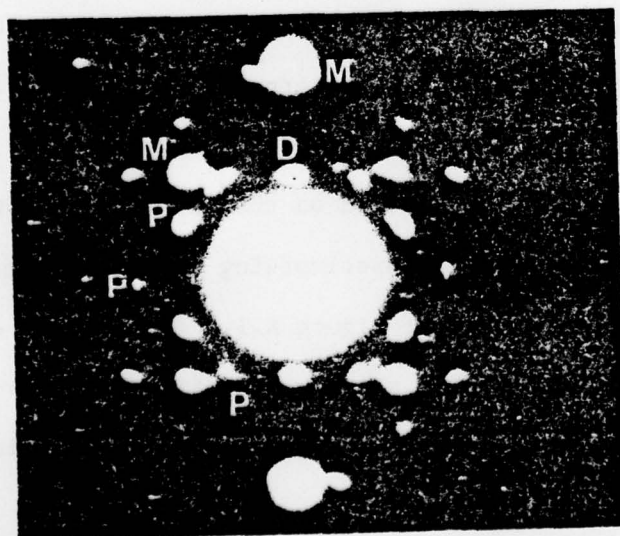
Figure A.1

- (a) Bright field transmission electron micrograph of TiC particles in Alloy BC.



0.75 μ

- (b) Dark field of particles of Fig.A.1.a, obtained with spot P on Fig.A.1.c.



- (c) Diffraction pattern obtained from the region of Fig.A.1.a, with a zone axis.

Examples of spots:

M : matrix

P : particle ( TiC )

D : double diffraction

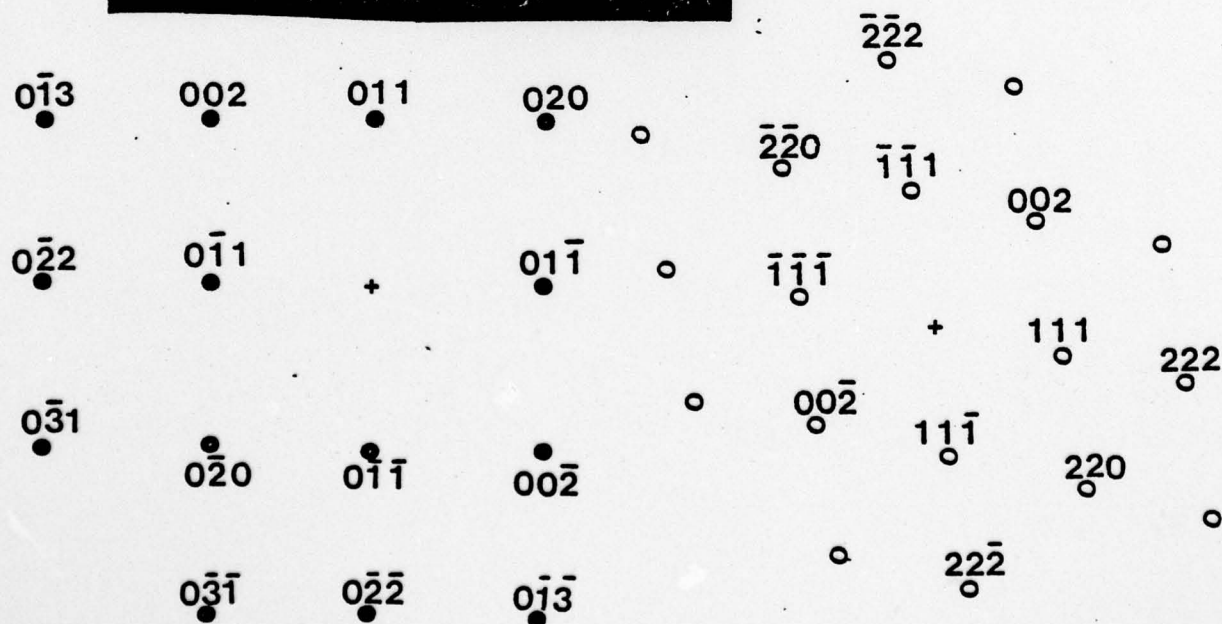
See text for other spots.

Figure A.1. ( continued )

- (d) Dark field of TiC particles in Alloy CC, obtained on spot D, Fig.A.1.e. ( double diffraction )

0.6  $\mu$

- (e) Diffraction pattern obtained from the region of Fig.A.1.d.



- (f) Reconstructed diffraction patterns for matrix (left) and a TiC particle (right) having the Baker Nutting orientation relationship with the matrix.



as well as the diffuse scatter associated with lattice spots. Diffraction spots such as D may be obtained by double diffraction on matrix spots such as M (which are strongly excited). This has been demonstrated, although not shown by translating the superimposed TiC pattern and centering it on these matrix spots. The resulting dark field (Figure A.1.d) is characteristic of double diffraction<sup>(114)</sup>, probably resulting from interaction with the particles embedded in the matrix.

Sharp spots such as S correspond to diffraction by TiC particles which do not obey the Baker-Nutting relationship (e.g. on Figure A.1.b, not all particles were imaged in dark field from spot P).

D-A045 331

CARNEGIE-MELLON UNIV PITTSBURGH PA DEPT OF METALLURG--ETC F/G 7/4  
THE ROLE OF TRAPPING ON HYDROGEN TRANSPORT AND EMBRITTLEMENT.(U)  
JUL 77 G M PRESSOUYRE, I M BERNSTEIN N00014-75-C-0265

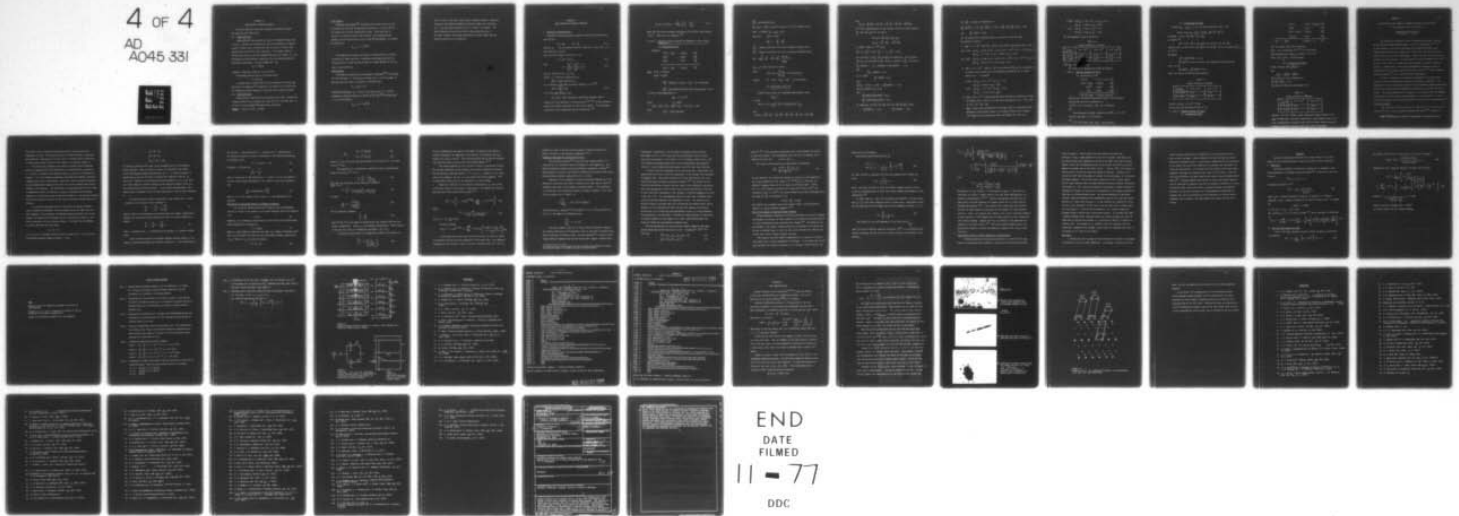
INCLASSIFIED

TR-7

NL

4 OF 4

AD  
A045 331



END  
DATE  
FILMED

11 - 77

DDC



## APPENDIX B

## COMPUTATION OF PARTICLE DENSITY

Particles densities have been evaluated by different methods for large and small particles:

B.1. Large Particles

Large particles were defined as those of a diameter larger than 1 micron. Counting was performed on optical micrographs at a magnification of X1000; thus, all particles less than 1mm in diameter were rejected and classified as small particles. The average numbers of TiC per unit area,  $N_A$ , and the average number per unit length,  $N_L$ , were calculated, and the density of particles,  $N_V$ , was obtained using the following relationship: (see for example Ref. 28)

$$N_V = \pi N_A^2 / 2N_L$$

(assuming a spherical shape for all particles).

The average particle size  $X$  is obtained from:

$$X = N_L / \pi N_A$$

It should also be noted that since the densities of TiN and  $Fe_4N$  particles are negligible<sup>(25)</sup> compared to the density of TiC particles, all counting was done assuming all particles were titanium carbides.

B.2. Small Particles

Small particles densities were evaluated in two ways: using known volume fractions of the carbides for known wt% of Ti and wt%C (Ref. 31 to 35), or using standard TEM quantitative techniques.

Example: Alloy CC (0.5Ti - 0.064C).

First method:

Honeycombe and Freeman<sup>(35)</sup> calculated the volume fraction of TiC in 0.5Ti-0.11C as 0.45%; decreasing both contents to 0.25Ti-0.05C did not change this fraction appreciably (0.43%). Since our alloy is similar, we assume the same volume fraction, and by measuring the average size of the particles as  $0.2\mu$  (from TEM micrographs), we compute the density as:

$$N_{V_1} = 1.1 \times 10^{18}/m^3$$

This number also includes the density of large particles; however, the density of small particles is generally much higher than that of large particles, so that  $N_{V_1}$  may be taken as a good estimate of the density of small particles.

Second method:

According to quantitative metallographic techniques<sup>(133)</sup>, by knowing the foil thickness,  $t$ , the particle average size,  $d$ , and the number of particles per unit area, the density is obtained from:

$$N_V = N_A/(t + d)$$

Using TEM micrographs,  $N_A$  in alloy CC was found to be  $1.5 \times 10^{12}/m^2$ .

Assuming an average thickness of  $1500 \text{ \AA}$  for the foil<sup>(133)</sup> and measuring  $d = 0.2\mu$ , one obtains:

$$N_{V_2} = 4.3 \times 10^{18}/m^3$$



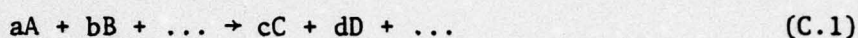
This is close to the above value using a different method. Obviously, because of the implied assumptions (particle shape, foil thickness, etc.), all particles densities have to be taken as estimates. The huge differences between densities of small particles (see p are real, however, since these differences are much larger than any possible errors due to estimations.

## APPENDIX C

## FREE ENERGIES FOR HYDRIDE FORMATION

1. Theoretical Considerations

Consider the following general chemical reaction for the specific case of iron:



where  $\underline{A}$ ,  $\underline{B}$ , ... are the species involved, dissolved in iron, and  $a$ ,  $b$ , ... the quantities involved.

Then, the free energy of reaction C.1 is:

$$\Delta G = \Delta G^0 + RT \ln Q. \quad (\text{C.2})$$

with

$$Q = \frac{(a_{\underline{C}})^c (a_{\underline{D}})^d (\dots)}{(a_{\underline{A}})^a (a_{\underline{B}})^b (\dots)} \quad (\text{C.3})$$

and  $a_{\underline{i}}$  = activity of  $\underline{i} = f_{\underline{i}} (\% \underline{i})$

where:  $f_{\underline{i}}$  = activity coefficient of  $\underline{i}$

$(\% \underline{i})$  = weight percent of  $\underline{i}$ .

$f_{\underline{i}}$  is related to the other dissolved elements,  $j$ , by: <sup>(69)</sup>

$$\log f_{\underline{i}} = \sum_j e_{\underline{i}}^j (\% j) \quad (\text{C.4})$$

as a first approximation, and

$e_{\underline{i}}^j$  = first order interaction coefficient between  $j$  and  $i$ .

Values of  $e_{\underline{i}}^j$  are tabulated in various places <sup>(71,72,73)</sup> in the literature, mainly for elements dissolved in liquid iron (1600°C). The corresponding value at room temperature may be estimated by: <sup>(74)</sup>



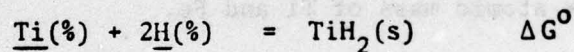
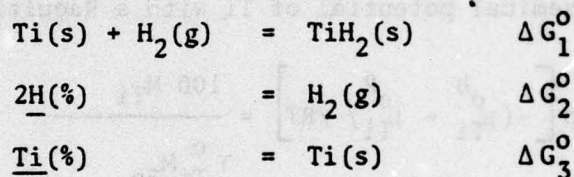
$$e_i^j(T_1) = e_i^j(T_2) + \frac{h_i^j}{2.3R} \left[ \frac{1}{T_1} - \frac{1}{T_2} \right] \quad (C.5)$$

where  $h_i^j$  is the excess enthalpy coefficient of the first order between  $i$  and  $j$ . These are also tabulated. (72)

## 2. Case 1: Reaction between Titanium and Hydrogen in Iron at Room Temperature

### (i) Calculation of $\Delta G^\circ$

Consider:



Note:  $\text{Ti(s)} = \text{Ti(solid)}$

$\text{H}_2(\text{g}) = \text{H}_2(\text{gas})$

$\Delta G_1^\circ$ : Reference 75 gives:  $\Delta G_1^\circ = -25.13 \text{ kcal/mole}$

$\Delta G_2^\circ$ : From Reference 139, the equilibrium weight % of H

in iron at room temperature is:

$$(\%H) = 5.4 \times 10^{-8}$$

Since

$$\text{H}_2 = 2\text{H}(\%)$$

Then  $\Delta G_2^\circ = -RT \ln (\%H)^2 / p\text{H}_2$  with  $p\text{H}_2 = 1 \text{ atm.}$

Then:

$$\Delta G_2^\circ = -19.82 \text{ kcal/mole}$$

$\Delta G_3^0$ : From Reference 135

$RT \ln \gamma_{Ti}^0 = -11000$ , in bcc Fe with bcc Ti as the standard state.

Then: at 298°K,  $\gamma_{Ti}^0 = 9.65 \times 10^{-9}$ .

And since:  $Ti(\%) = Ti(s)$

$$\Delta G_3^0 = \mu_{Ti}^{OR} - \mu_{Ti}^{Oh}$$

$\mu_{Ti}^{Oh}$  = chemical potential of Ti with a Henrian standard state,

$\mu_{Ti}^{OR}$  = chemical potential of Ti with a Raoultian standard state,

$$\text{and } \exp \left[ -(\mu_{Ti}^{Oh} - \mu_{Ti}^{OR}) / RT \right] = \frac{100 M_{Ti}}{\gamma_{Ti}^0 M_{Fe}}$$

$M_{Ti, Fe}$  = atomic mass of Ti and Fe.

Then:

$$\Delta G_3^0 = RT \ln \frac{100 M_{Ti}}{\gamma_{Ti}^0 M_{Fe}} = 13.65 \text{ kcal/mole}$$

$$\text{Finally: } \Delta G^0 = \Delta G_1^0 + \Delta G_2^0 + \Delta G_3^0 = -31.3 \text{ kcal/mole}$$

#### (ii) Calculation of $RT \ln Q$

Consider that  $TiH_2(s)$  has completely precipitated; then,

$$a_{TiH_2} = 1$$

so that:

$$RT \ln Q = RT \ln a_{Ti} a_H^2 = RT \ln \left[ (\%Ti) f_{Ti} (\%H)^2 f_H \right]$$

but:

$$\log f_{Ti} = e_{Ti}^{Ti} (\%Ti) + e_{Ti}^C (\%C) + e_{Ti}^N (\%N) + e_{Ti}^O (\%O) + e_{Ti}^H (\%H)$$



and:

$$\log f_H = e_H^H (\%H) + e_H^C (\%C) + e_H^N (\%N) + e_H^O (\%O) + e_H^{Ti} (\%Ti)$$

As a first approximation, we may consider (since all other products  $e_{Ti}^i (\%Ti)$  and  $e_H^i (\%Ti)$  are small).

$$\log f_{Ti} \approx e_{Ti}^{Ti} (\%Ti) + e_{Ti}^H (\%H)$$

$$\log f_H \approx e_H^H (\%H) + e_H^{Ti} (\%Ti)$$

at 1600°C, Table III (72) gives:

$$e_H^H = 0.0, e_{Ti}^{Ti} = 0.013, e_{Ti}^H = -1.1, e_H^{Ti} = -0.019$$

The variations of  $e_{Ti}^H$ ,  $e_{Ti}^{Ti}$  and  $e_H^{Ti}$  with temperature, are not known.

However, the variation of  $e_{Ti}^N$ , which is similar to  $e_{Ti}^H$ , is given as:

$$e_{Ti}^N (1600^\circ C) = -1.8 \quad (\text{compared to } e_{Ti}^H (1600^\circ C) = -1.1)$$

and:

$$e_{Ti}^N = -13900/T + 5.61$$

at  $T = 298^\circ K$ :

$$e_{Ti}^N (298^\circ K) = -41.0$$

Also:

$$e_N^{Ti} (T) = -4070/T + 1.643 = > e_N^{Ti} (298^\circ K) = -12.0$$

$$\text{and } e_N^{Ti} (1600^\circ C) \text{ was } = -0.53$$

Thus:

$$e_N^{Ti} (298^\circ K) / e_N^{Ti} (1600^\circ C) = 22.6$$

$$e_{Ti}^N (298^\circ K) / e_{Ti}^N (1600^\circ C) = 22.8$$

By comparison, we take the same ratio for  $e_{Ti}^H$  and  $e_H^{Ti}$ , so that:

$$e_{Ti}^{Ti} (298^\circ K) = -0.43$$

$$e_{Ti}^H (298^\circ K) = -25.1$$

For  $e_{Ti}^{Ti}$ , we make the comparison to

$$e_{Al}^{Al} (1873^{\circ}K) = 0.45, e_{Al}^{Al} (298^{\circ}K) = 0.222 \Rightarrow e_{Al}^{Al} (298)/e_{Al}^{Al} (1873) = 4.96$$

and  $e_{Ti}^{Ti} (298^{\circ}K) = 0.064$

All one needs now to calculate  $RT \ln Q$  is to select a value for  $(\%H)$ .

We consider 3 values:

- 1)  $(\%H) = 5.4 \times 10^{-8}$  (Ref.134), which is the lowest equilibrium value. Then:

For 0.15Ti  $\log f_{Ti} = 0.064 (0.15) + (-25.1) (5.4 \times 10^{-8}) = 9.6 \times 10^{-3}$  or  $f_{Ti} = 1.0$

$$\log f_H = 0 - 0.43 \times 0.15 = -0.064, \text{ or } f_H = 0.86$$

For 1.5Ti  $\log f_{Ti} = 0.064 (1.5) - (25.1) (5.4 \times 10^{-8}) = 9.6 \times 10^{-2}$  or  $f_{Ti} = 1.2$

$$\log f_H = 0.43 (1.5) = 0.64, \text{ or } f_H = 0.23$$

- 2)  $(\%H) = 1.18 \times 10^{-5}$ , which is the value obtained from  $C_0$ , the concentration at steady state obtained for our permeation experiments for a current density of  $i = 0.8 \text{ mA/cm}^2$

0.15Ti  $\log f_{Ti} = 9.3 \times 10^{-3}$ , or  $f_{Ti} = 1.02$

$$\log f_H = 0.064, \text{ or } f_H = 0.86$$

1.5Ti  $\log f_{Ti} = 9.6 \times 10^{-2}$ , or  $f_{Ti} = 1.25$

$$\log f_H = -0.64, \text{ or } f_H = 0.23$$

- 3)  $(\%H) = 0.62 \times 10^{-2}$ , supersaturation value obtained by considering 2 atoms of hydrogen for 1 atom of Ti in the alloy containing 0.15Ti. This value is  $0.62 \times 10^{-1}$  for 1.5Ti.

Note: Such a high concentration of hydrogen in Fe-Ti is obtainable when charging at high current density, in  $\text{H}_2\text{SO}_4$  solution with a poison (see Chapter II on concentration effect and Chapter III, Fig. 51).



$$0.15\text{Ti} \quad \log f_{\text{Ti}} = 1.46 \times 10^{-1}, \text{ or } f_{\text{Ti}} = 0.71$$

$$\log f_{\text{H}} = 0.064, \text{ or } f_{\text{H}} = 0.86$$

$$1.5\text{Ti} \quad \log f_{\text{Ti}} = 1.46, \text{ or } f_{\text{Ti}} = 0.03$$

$$\log f_{\text{H}} = 0.64, \text{ or } f_{\text{H}} = 0.23$$

The corresponding values of  $RT\ln Q$  are:

Table C.1.

Values of  $RT\ln Q$  in kcal/mole

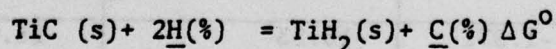
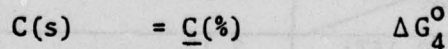
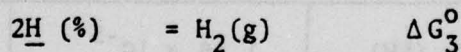
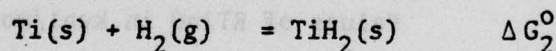
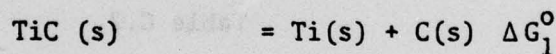
Alloy $\downarrow$ (%) $\rightarrow$	$5.4 \times 10^{-8}$	$1.18 \times 10^{-5}$	$0.62 \times 10^{-2}$
Fe -0.15Ti	21.16	14.73	7.48
Fe -1.50Ti	20.45	14.02	6.04

Then,  $\Delta G = \Delta G^\circ + RT\ln Q$ .

The values of  $\Delta G$  obtained are listed in Table VI.

### 3. Case 2: Reaction between TiC and H

(i) Calculation of  $\Delta G^\circ$ :



$\Delta G_3^\circ$  has been previously calculated as  $\Delta G_3^\circ = -19.82$  kcal/mole

$\Delta G_1^\circ$  and  $\Delta G_2^\circ$  are given in Reference 75

and  $\Delta G_1^\circ = 43.13$  kcal/mole,  $\Delta G_2^\circ = -25.13$  kcal/mole,

$\Delta G_4^\circ$ :

From Reference 136,  $(\%C)$  in ferrite at  $298^\circ\text{K} = 2.3 \times 10^{-7}$ .

and  $\Delta G_4^\circ = RT\ln(\%C) = 9.11$  kcal/mole.

$\Delta G^\circ$ :

$$\Delta G^\circ = \Delta G_1^\circ + \Delta G_2^\circ + \Delta G_3^\circ + \Delta G_4^\circ = 7.29 \text{ kcal/mole.}$$

(ii) Calculation of RTlnQ:

Taking  $a_{\text{TiC}} = a_{\text{TiH}_2} = 1$ , i.e. in the precipitated state, then:

$$RT\ln Q = RT\ln (a_{\text{C}} \times a_{\text{H}}^{-2}) = RT\ln (f_{\text{C}} (\% \text{C}) f_{\text{H}}^{-2} (\% \text{H})^{-2})$$

as before:  $\log f_{\text{C}} \approx e_{\text{C}}^{\text{H}} (\% \text{H}) + e_{\text{C}}^{\text{Ti}} (\% \text{Ti})$

at 1600°C: (72)

$e_{\text{C}}^{\text{H}} = 0.67$ ;  $e_{\text{C}}^{\text{Ti}}$  is not known, but since Ti has the same affinity for C as for O or N, and,  $e_{\text{O}}^{\text{Ti}} = -0.6$ , and  $e_{\text{N}}^{\text{Ti}} = -0.53$ , we estimate  $e_{\text{C}}^{\text{Ti}} \approx -0.5$  at 1600°C.

Therefore:

$$e_{\text{C}}^{\text{Ti}} \approx e_{\text{N}}^{\text{Ti}} (298^\circ \text{K}) = -12.0.$$

$e_{\text{C}}^{\text{H}} (298^\circ \text{K})$  is also not given, but assuming the same variation for it as for

$$e_{\text{C}}^{\text{H}} (298^\circ \text{K}) = e_{\text{C}}^{\text{Ti}} (298^\circ \text{K}) \approx -15.2$$

Then, the values of RTlnQ are calculated as

Table C.2.

Values of RTlnQ in kcal/mole

Alloy (%H)	$1.18 \times 10^{-5}$	$0.62 \times 10^{-2}$
Fe -0.15Ti	2.12	-5.21
Fe -1.5Ti	-18.53	-25.87

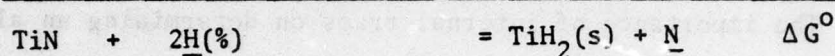
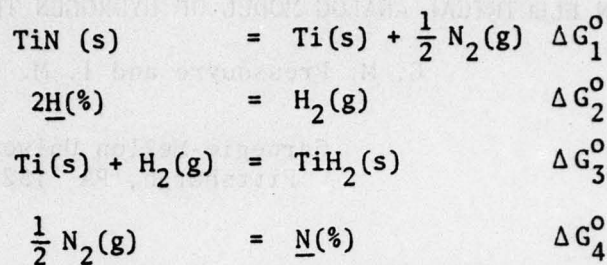
Finally, for  $\Delta G$ :  $\Delta G = \Delta G^\circ + RT\ln Q$ .

Values of  $\Delta G$  are tabulated in Table VI (p.

4. Case 3: Reaction between TiN and H

(i) Calculation of  $\Delta G^\circ$





$\Delta G^0$ : As before,  $\Delta G_2^0 = -19.82$  kcal/mole;

$\Delta G_3^0 = -25.13$  kcal/mole;  $\Delta G_1^0 (75) = 73.6$  kcal/mole;

From Reference 139:  $(\%N)_{\alpha\text{Fe}}$  at  $298^\circ\text{K} = 4.91 \times 10^{-7}$

Then;  $\Delta G_4^0 = \sum_{i=1}^4 \Delta G_i^0 = 36.78$  kcal/mole

(iii) Calculation of RTlnQ:

$$\text{RTlnQ} = \text{RTln}(f_N (\%N) f_H^{-2} (\%H)^{-2})$$

and:

$$\log f_N = e_N^H (\%H) + e_N^{\text{Ti}} (\%Ti)$$

$e_N^H$  is given as 0.39 in Reference 73

and  $e_N^{\text{Ti}} (298^\circ\text{K}) = 12.0$ .

The values of RTlnQ are calculated to be:

Table C.3.

Values of RTlnQ in kcal/mole

Alloy \ (%H)	$1.18 \times 10^{-5}$	$0.62 \times 10^{-2}$
Fe -0.15Ti	2.57	-4.89
Fe -1.50Ti	-18.1	-25.5

Finally:  $\Delta G = \Delta G^0 + \text{RTlnQ}$ . These values are listed in Table VI (p.

Note: Because many interaction coefficients were estimated (due to the lack of experimental value, for these coefficients) for results should be viewed as estimates having an error of at least 5 kcal/mole.

## AN ELECTRICAL ANALOG MODEL OF HYDROGEN TRAPPING IN IRON ALLOYS \*

G. M. Pressouyre and I. M. Bernstein

Carnegie-Mellon University  
Pittsburgh, PA 15213

The importance of internal traps on determining an alloy's susceptibility towards hydrogen embrittlement is now well established.<sup>(1-3)</sup> It is thus important to be able to determine from permeation studies such trapping characteristics as trapping and release rates and the interaction energy between a given trap and hydrogen. Several theories exist where this situation has been analyzed. The most general is that of McNabb and Foster<sup>(4)</sup> in which Fick's first and second laws were modified to include a trapping reaction. Unfortunately, the resulting differential equations cannot be solved explicitly, although numerical solutions do exist.<sup>(5)</sup> Other proposed analytical models<sup>(6,7)</sup> also suffer from this shortcoming.

We wish to describe an alternative development for which explicit solutions for the permeation rise and decay transients is possible. This approach utilizes an electrical simulation of the important trapping parameters and as will be shown has the advantages of simplicity of solution and flexibility. The analog approach will be applied to the specific case of trapping of hydrogen by titanium solute atoms dissolved in an iron matrix. In this system, the number, nature, and distribution of traps is well characterized.<sup>(8)</sup>

The Analog Network

The electrical network chosen has already been used to simulate heat transfer<sup>(9)</sup> and, in fact, hydrogen evolution from steel,<sup>(10)</sup> although in

\*Note : This paper will shortly be published in Corrosion Science



this latter case no physical representation of the various electrical components was made. The analog consists of a ladder network of resistors and capacitors, equivalent in the real case to a single crystal consisting of atomic plane layers, each one atom diameter in thickness (Figure 1).

The resistors  $R$ , represent the barrier to normal lattice diffusion, while the trapping ability per atomic plane is represented by a capacitor,  $C$ . In turn,  $C$  consists of two additive terms,  $C_0$  and  $C_T$ , as illustrated in Figure 2.  $C_0$  is the trapping capacitance resulting from normally occurring trapping sites such as dislocations, impurities, voids, and grain boundaries;  $C_T$  are extraordinary trapping sites which will be the variable under consideration in this analysis. The reversible or irreversible nature of the traps is modelled by the use of switches,  $K_0$  and  $K_T$ , controlling the discharge capability of a particular type of capacitor (Figure 2). The physical counterpart of this system is a series of iron alloys containing varying amounts of titanium.

To illustrate the application of the electrical analog, consider a typical permeation experiment in which hydrogen enters the input side of a metal membrane, and the quantity of hydrogen leaving the output side is monitored. The analog of the hydrogen flux is the electrical current, or the flux of electrons, in the electrical network. The input flux of hydrogen,  $\phi_0$ , may be separated into two terms:

$$\phi_0 = \phi_1 + \phi_1'$$

$\phi_1$  is the flux of hydrogen passing directly through plane 1,  $\phi_1'$  is the flux of hydrogen remaining trapped on plane 1. Thus

$$\phi_1 = \phi_2 + \phi'_2$$

$$\phi_2 = \phi_3 + \phi'_3$$

$$\phi_{N-2} = \phi_{N-1} + \phi'_{N-1}$$

All fluxes  $\phi_i$  diminish with time, as the trapping sites on corresponding planes saturate. When all traps on a plane  $i$  are saturated with respect to the surrounding hydrogen concentration,  $\phi'_i = 0$ . It seems reasonable to assume that  $\phi'_1$  will be the first to satisfy this condition, then  $\phi'_2$ ,  $\phi'_3$ , and so on. Similarly, in the analog electrical network,  $i_0 = i_1 + i'_1$ , where  $i'_1$  is the current of electrons flowing in the capacitive branch, while  $i_1$  is the current going to the next branch. In this simple representation, each atomic plane is assumed to have the same capacitance  $C$ , and the same resistance  $R$ .

For the electrical circuit the potential  $v$  and current flow  $i$ , across a length  $dx$  of the network can be expressed as:

$$\frac{di}{dx} = -C' \frac{dv}{dt} = -\frac{1}{R'} \frac{d^2v}{dx^2} \quad (1)$$

where  $C'$  and  $R'$  are capacitance and resistance per unit length, respectively.

Equation (1) can now be directly related to Fick's 1st law for diffusion of matter:

$$\frac{dj}{dx} = -\frac{dc}{dt} = -D \frac{d^2c}{dx^2}, \quad (2)$$

where  $J$  = hydrogen flux,  $c$  = concentration of hydrogen,  $D$  = diffusion coefficient.

These relations express the analogies between electric charge,  $q$ , and number of dissolved hydrogen ions (protons); potential,  $v$ , and concentration,  $c$ ;



and current,  $i$ , and hydrogen flux,  $J$ . Moreover, if  $\ell$  = length between two successive capacitors, which is analogous to the atomic plane spacing in diffusion, then:

$$R' = R/\ell \text{ and } C' = C/\ell \quad (3)$$

Therefore, it follows that

$$\frac{1}{R'C'} = \frac{\ell^2}{RC}, \quad (4)$$

which is equivalent to the diffusivity,  $D$ . Finally, if  $N$  is the number of discrete atomic planes (equivalent to the number of electrical branches), then

$$\frac{1}{RC} \text{ is equivalent to } \frac{N^2 D}{L^2} \quad (5)$$

where  $L = N\ell$  = total length of the circuit, i.e. the thickness of the specimen.

#### Application of the Analog Network to Hydrogen Permeation

The electrical capacitance per unit length of the two-dimensional network is related to the quantity  $Q$  of stored electrons, and to the potential  $V$  by:

$$C = Q/V \quad (6)$$

Similarly, the "diffusional capacitance" per unit area  $\bar{C}$  of the three-dimensional crystal may be defined as:

$$\bar{C} = n n_H / X_H \quad (7)$$

Where  $n$  = total number of traps per unit area,  $n_H$  = number of hydrogen atoms that can be stored by one trap when the surrounding hydrogen concentration is  $X_H$ . Since  $C = C_O + C_T$ , then by analogy:

$$\bar{C} = \bar{C}_O + \bar{C}_T \quad (8)$$

$$\bar{C}_O = n^O n_H^O / X_H^O \quad (9)$$

and

$$\bar{C}_T = n^T n_H^T / X_H^T \quad (10)$$

where  $n^i$ ,  $n_H^i$ , and  $X_H^i$  have the same meaning as in equation (7), for traps of the  $i^{\text{th}}$  kind.

From equation (5), the diffusion coefficient when no extraordinary traps are present ( $n^T = 0$ ) is:

$$D_O = \frac{L^2}{N^2} \times \frac{X_H^O}{\bar{R} n^O n_H^O} \quad (11)$$

where  $\bar{R}$  is the resistance of the lattice to diffusion.

When  $n^T \neq 0$ :

$$D = \frac{L^2}{N^2} \times \frac{1}{\bar{R} (n^O n_H^O / X_H^O + n^T n_H^T / X_H^T)} \quad (12)$$

so that:

$$\frac{D_O}{D} = 1 + \frac{n^T n_H^T X_H^O}{n^O n_H^O X_H^T} \quad (13)$$

For all practical purposes,

$$\frac{n^T}{n^O} = \frac{N^T}{N^O} \quad (14)$$

where  $N^T$  and  $N^O$  are the number of extraordinary and ordinary traps per unit volume, respectively. Finally, at low hydrogen concentration: (which usually is the case for  $\alpha$ -iron in a permeation experiment),  $X_H^O \approx X_H^T$ :

From these considerations and assumptions, equation (13) reduces to:

$$\frac{D_O}{D} = 1 + N^T \left( \frac{n_H^T}{N^O n_H^O} \right) \quad (15)$$



If it is assumed that the capacity and number of ordinary traps remains constant throughout the experiment, then equation (15) predicts that  $D_0/D$  should vary linearly with  $N^T$ . Both this prediction and the form of equation (15) have been found to agree with other proposed models. (6,7)

The analog approach can also be used to obtain a closed form solution for the time dependence of the hydrogen flux during a permeation transient, for the boundary conditions where at  $t \geq 0$ ,  $C_H = C_0 = \text{constant}$ , at the input side of the membrane, and  $C_H = 0$  at the output side of the membrane. This is equivalent electrically to the imposition of a step voltage.

Under the conditions in the electrical analog case,  $i_N$ , the current in the final branch of the network, (equivalent to the output flux of hydrogen) has been solved analytically by Weber: (11)

$$i_N(t) = i_\infty \left[ 1 + (-1)^N e^{-t/T_N} + 2 \sum_{n=1}^{N-1} (-1)^n e^{-t/T_n} \right] \quad (16)$$

where:

$$T_n = \frac{RC}{2 [1 - \cos(n\pi/N)]} \quad (17)$$

and  $i_\infty$  is:  $i_\infty = \lim_{t \rightarrow \infty} (i_N(t))$

By direct analogy:

$$J/J_\infty = 1 + (-1)^N e^{-t/T_N} + 2 \sum_{n=1}^{N-1} (-1)^n \exp \left( - \frac{2DN^2 (1 - \cos \frac{n\pi}{N}) t}{L^2} \right) \quad (18)$$

It was found that twenty terms of the series were all that was needed to accurately describe the time dependence of the output flux. One immediate advantage of this solution is that  $J/J_\infty$  varies uniformly from 0 to 1 for all

values of  $n$ ; this is not the case for Laplace or Fourier solutions of Fick's law used in other modelistic approaches.<sup>(12)</sup>

#### Trapping of Hydrogen by Titanium Solute Atoms

We have shown elsewhere<sup>(13)</sup> that dissolved titanium atoms\* in  $\alpha$ -iron can act as a reversible trap for hydrogen at room temperature. Permeation transients obtained from electrochemical through-put studies<sup>(13)</sup> were analyzed to calculate the effective diffusivity for several iron alloys having titanium contents ranging from 0.15 to 1.5wt%.

Equation (15) has predicted a linear relationship between  $D_0/D$  (the diffusivity ratio with and without titanium in the iron) and the number of titanium traps (equal to the number of titanium atoms\*). This prediction is verified for iron containing titanium, as shown in Figure 3. The slope of the straight line of Figure 3 is:

$$\frac{n_H^T}{N^O n_H^O} = 6.26 \times 10^{-21} \text{ cm}^3/\text{site}$$

Following Oriani's approach,<sup>(6)</sup> and taking  $N^O = 2.6 \times 10^{23}$  sites/cm<sup>3</sup> in  $\alpha$ -iron (i.e. the number of octahedral sites):

$$\frac{n_H^T}{n_H^O} = 1.6 \times 10^3$$

Thus the occupancy, and, for at least similar interaction energies, the trapping efficiency of extraordinary sites is more than a thousand times greater than that of ordinary sites. We have obtained<sup>(13)</sup> a similar result using different arguments and the more analytically complex McNabb-Foster

---

\*In these alloys we shall ignore in the analytical developments the small and constant amount of titanium combined in carbonitrides.



formulation. Specifically, the occupancy of ordinary sites in  $\alpha$ -iron was found to be  $1.1 \times 10^{-6}$ , while for the extraordinary sites (Ti atom) this value was between  $1 \times 10^{-3}$  and  $5 \times 10^{-3}$ , yielding a ratio of  $0.9 \times 10^3$ . The electrical analogue approach thus yields complementary and supportive results in a more simple and direct manner than other open form solutions.

To further test the usefulness of the analog approach, experimental permeation data was fitted to the time dependence of the hydrogen flux described by equation (18). The second instead of the first polarization rise transients were used for reasons discussed elsewhere.<sup>(13)</sup> The results for the Fe-0.15Ti were fitted to obtain the best value of the diffusional capacitance due to the presence of 0.15wt% Ti. This value was then multiplied by four and by ten, since this corresponds to the increase in titanium trapping sites with 0.63Ti and 1.5Ti. The corresponding values of D were used in equation (18), which was plotted along with the experimental curves. The results are depicted in Figure 4 and show that while the precise fit between theory and experiment is only reasonable for the 0.63 and 1.5Ti samples, the relative positioning of the theoretical and experimental curves is in good agreement. More importantly, the agreement is obtained by simply varying the capacitance in direct proportion to the number of Ti atoms, demonstrating again that these are indeed the extraordinary trapping sites.

The analog technique can also be used to obtain bounds for the interaction energy  $E_{Ti}^H$  between dissolved Ti and H. Assuming  $R^{Fe} = R^{Fe-1.5Ti}$  and since,

$$D^{Fe-1.5Ti} / D^{Fe} = \bar{C}^{Fe} / \bar{C}^{Fe-1.5Ti} \quad (19)$$

$$\bar{C}^{Fe-1.5Ti} = \bar{C}^{Fe} + \bar{C}^{1.5Ti} \quad (20)$$

where  $\bar{C}^{1.5\text{Ti}}$  is the additional capacitance due to the presence of 1.5wt%Ti in the iron lattice. from experimental data the ratio of equation (19) is found to be 0.10; thus  $\bar{C}^{1.5\text{Ti}} / \bar{C}^{\text{Fe}} = 9$

This value is substituted in the equivalency relationship:

$$E_{\text{Ti}}^{\text{H}} = \frac{\bar{C}^{1.5\text{Ti}} \times n_{\text{H}}^{\text{O}} \times N^{\text{O}} \times E^{\text{O}}}{\bar{C}^{\text{Fe}} \times n_{\text{H}}^{\text{T}} \times N^{\text{T}}} \quad (21)$$

In this relation, the interaction energies are related to the capacitance of a single trapping Ti atom, equal to  $\bar{C}^{1.5\text{Ti}} / N^{\text{T}} n_{\text{H}}^{\text{T}}$ ;  $n_{\text{H}}^{\text{T}}$  describes the effective trapping since not all Ti atoms are efficient traps. Taking  $N^{\text{O}} = 2.6 \times 10^{23}$  ordinary sites/cm<sup>3</sup> and a range for  $E^{\text{O}}$  from 0.08<sup>(6)</sup> (for octahedral sites) to 0.25<sup>(14)</sup> (for grain boundaries and other heterogeneities), the range for  $E_{\text{Ti}}^{\text{H}}$  is determined to be:

$$0.14\bar{\text{e}}\text{v} < E_{\text{Ti}}^{\text{H}} < 0.44\bar{\text{e}}\text{v}$$

This agrees with a maximum interaction energy of  $E_{\text{Ti}}^{\text{H}} = 0.27\bar{\text{e}}\text{v}$  previously found by us, using different arguments.<sup>(13)</sup>

#### Use of the Analogy to Describe Surface Trapping

During permeation experiments which were performed to test bulk trapping of hydrogen by titanium, the input surface of the alloys was palladium plated to insure reproducible entry conditions for hydrogen.<sup>(8)</sup> If instead the input surface is not plated, titanium atoms will be present on the surface and can act as surface traps, so that the total area available for diffusion decreases with time as surface trapping increases.

This behavior has been modelled experimentally, by partially covering the surface with a lacquer impermeable to hydrogen. It was found that as the area available for diffusion decreases, for a constant current density, the



output flux also decreased.

Electrically we can describe this as:

$$\begin{aligned} t < 0 \quad i_i &= 0 \\ t \geq 0 \quad i_i &= i_o \times \frac{1}{k_1 + k_2} \left[ k_1 + k_2 e^{-kt} \right] \end{aligned} \quad (22)$$

The input current  $i_i$  decreases with time and asymptotically reaches the value,

$$i(\infty) = \frac{i_o k_1}{k_1 + k_2}, \quad (23)$$

where  $k$  describes the rate at which the surface trapping reaction occurs,  $k_1$  and  $k_2$  are proportional to those areas where trapping and diffusion occurs respectively. (8)

In other words,  $k_1 = A_d^\infty$  = area available for diffusion, at steady state, and  $k_2 = A_t^\infty$  = area where trapping occurs at steady state. Equivalently then, the corresponding flux of hydrogen when surface trapping is present,  $J'_\infty$ , is:

$$J'_\infty = \frac{A_d^\infty}{A_d^\infty + A_t^\infty} J_\infty \quad (24)$$

The solution to the time dependence of this flux ratio,  $\frac{J'}{J_\infty}$ ,

under the initial boundary condition equivalent to (22), can be obtained using Laplace transforms and the sum of the residues theorem, as described in the Appendix:

$$J'/J_{\infty} = \frac{A_d^{\infty}}{A_d^{\infty} + A_t^{\infty}} \left[ 1 + \frac{(A_t^{\infty}/A_d^{\infty}) e^{-kt}}{2^{N-1} \prod_{i=1}^N \left[ 1 - \cos\left(\frac{2i-1}{N} \times \frac{\pi}{2}\right) - \frac{kL^2}{2DN^2} \right]} \right] \quad (25)$$

$$+ \frac{1}{N} \sum_{i=1}^N (-1)^i \left[ \frac{1 - (A_t^{\infty}/A_d^{\infty})}{\left[ \frac{kL^2}{2DN^2} \left( 1 - \cos\left(\frac{2i-1}{N} \times \frac{\pi}{2}\right) \right) - 1 \right]} \right] \cot\left(\frac{2i-1}{2N} \times \frac{\pi}{2}\right) e^{-c_i/T}$$

with:

$$Ti = \frac{L^2}{2DN^2 \left[ 1 - \cos\left(\frac{2i-1}{N} \times \frac{\pi}{2}\right) \right]}$$

The behavior of this function is illustrated in Figure 5. Note that the transients can exhibit a humped shape as has been found experimentally by a variety of investigators.<sup>(16,17)</sup> Previous explanations have been that the hump results from the formation of internal cracks due to a high internal hydrogen gas pressure.<sup>(16)</sup> In the present case, cracks were not observed, and the low input fugacities used makes the development of a high pressure unlikely. Since a low fugacity was a general rule in most literature examples of such behavior, it would appear that the hump results not from cracking but from surface trapping. Support for this is evidenced by the appearance of deposits on the input surface.<sup>(17)</sup> Thus when surface trapping occurs, the polarization behavior is better describable by equation (25), than by equation (18).

#### Experimental Study of Surface Trapping by Titanium Atoms

Hydrogen permeation through uncoated Ferrovac -E iron and Fe-Ti membranes at increasing current densities, resulted in the build-up transients



shown in Figure 6. While steady state was normally achieved with Ferrovac -E iron, a hump appeared with the Fe-Ti specimen. Such humps were not observed when this membrane was coated on the input side with palladium. Figure 7 shows the corresponding values of the steady state flux  $J_{\infty}$  plotted against the square root of the input current density  $\sqrt{i_c}$ , for Ferrovac E and Fe-0.15Ti, in both the coated and uncoated condition. Ferrovac E and coated Fe-0.15Ti obey the predicted straight line relationship, in the absence of surface effects. On the other hand, uncoated Fe-0.15Ti results depart from a linear behavior when the humped permeation behavior becomes significant (see Figure 6). This could be attributed as discussed to surface trapping of hydrogen by titanium, or possibly to the formation of an hydrogen impermeable layer due to titanium surface atoms. The latter hypothesis is considered unlikely, since the presence of an impermeable layer at the entry side should decrease  $J_{\infty}$ , rather than increase it, as was observed for uncoated Fe-0.15Ti. In fact  $J_{\infty}$  for uncoated Fe-0.15Ti can be twice as high as for a coated specimen (see Figure 7.) Thus the first hypothesis, i.e. surface trapping of hydrogen around titanium atoms, seems more plausible. We estimate that about a hundred hydrogen atoms clustered around one surface titanium atom would be sufficient to justify the decrease in  $J_{\infty}$  occurring at  $8\text{mA/cm}^2$ , according to equation (24). The increase in  $J_{\infty}$  indicates that this trapping should be reversible, although on the average, large clusters of hydrogen would have to be present at all times on the surface.

### Conclusion

A simple electrical analogy has been developed to simulate the trapping of hydrogen in  $\alpha$ -iron at room temperature. The analogy is based on the sim-

ilarity between the ability of a capacitor to store electrons and of a trap to retain hydrogen. Simple formulae have been developed to analyze experimental permeation data. In particular, expressions for the variation of the output flux and of the diffusivity of hydrogen with the density of traps have been derived. All results have been applied to bulk and surface trapping of hydrogen by titanium solute atoms in Fe-Ti alloys. These results are consistent with those found by the authors using the McNabb-Foster model.<sup>(13)</sup> Although somewhat more limited in scope, the present approach has the advantage of simplicity and ease of analytical solutions, so long as the imposed input conditions possess a Laplace transform (see Appendix). Moreover, the electrical analogy can be experimentally manipulated; by changing the value or distribution of the capacitors, or even by using a different type of network, most experimental data should be able to be fitted.



## Appendix

Solutions are presented below for the current density in the last branch of the electrical network, using various input initial conditions.

### A. Step Flux:

This input condition, illustrated in Figure 8a, is thought to exist during permeation of hydrogen through palladium.<sup>(18)</sup> Electrically, the condition is:

$$t \geq 0 \quad i_i = i_o \quad \text{at } x = 0$$

the general solution is:<sup>(11)</sup>

$$I_q(p) = I_i(p) \frac{\cosh(N-q)\Gamma}{\cosh N\Gamma} \quad (26)$$

where  $I_q(p)$  = Laplace transform of current  $i$  in branch  $q$ ,  $p$  = Laplace parameter,  $I_i(p)$  = Laplace transform of the initial current, and  $\Gamma$  is defined by:

$$\cosh \Gamma = 1 + pRC/2$$

In this case,  $L(i_o) = I_o p = I_i(p)$

The solution  $i_N = f(t)$  is given by Weber,<sup>(11)</sup> which translates in diffusion as:

$$J/J_\infty = 1 + \frac{1}{N} \sum_{n=1}^N (-1)^n \cot\left(\frac{2n-1}{2N} \times \frac{\pi}{2}\right) \exp\left[-\frac{2DN^2 \left[1 - \cos\left(\frac{2n-1}{N} \times \frac{\pi}{2}\right)\right] t}{L^2}\right] \quad (27)$$

### B. Step Flux Decreasing with time

This is the input condition used for surface trapping, as described in Figure 8b:

$$t \geq 0 \quad i_i = \frac{i_o}{k_1 + k_2} \left[ k_1 + k_2 e^{-kt} \right] \quad \text{at } x = 0 \quad (28)$$

The general solution (26) is still valid, but  $I_i(p)$  has changed:

$$I_i(p) = L(i_i) = \frac{p(k_1+k_2) \cdot I_0 + k_1 k I_0}{(k_1+k_2) p (p+k)} \quad (29)$$

Replacing in (26), using the theorem of residues and  $q=N$  gives:

$$i_N(t) = \frac{i_0}{k_1+k_2} \left[ k_1 + \frac{k_2 e^{-kt}}{2^{N-1} \prod_{i=1}^N \left[ \frac{T(1-kT_i)}{T_i} \right]} \right] + \frac{1}{N} \sum_{i=1}^N (-1)^i k_1 \left[ 1 - \frac{k_2}{k_1(kT_i-1)} \right] \cot \left( \frac{2i-1}{2N} \times \frac{\pi}{2} \right) e^{-t/T_i} \quad (30)$$

$$\text{where } T_i = \frac{T}{1 - \cos \left( \frac{2i-1}{N} \times \frac{\pi}{2} \right)}, \quad T = RC/2$$

Finally, using the analogy  $1/RC \leftrightarrow N^2 D/L^2$

one finds Formula (25) for surface trapping.



# LIST OF FIGURE CAPTIONS

Fig. 1. Analogy between hydrogen trapped ( $H_T$ ) and diffusing ( $H_D$ ) fluxes

in a crystal, and current flowing through capacitive ( $C_T$ ) and

resistance ( $R_T$ ) branches in the analog network.

Fig. 2. Illustration of the existence of two kinds of traps in the lattice;

the choice of ordinary traps ( $C_1$ ) as irreversible and exit-

Figures 1 and 2 are labelled as Figures D.1 and D.2 in this Appendix.

Figures 3, 4, 5, 6 and 7 correspond to Figures 24, 28, 33, 31 and 30 in the thesis, respectively.

Figure 8 is labelled as Figure D.3 in the Appendix.

catalytic atoms in the iron.

Fig. 4. Fitting of experimental data using equation (13). The transient for

Fe-0.15Ti was best fitted; the obtained diffusional capacitance was

then scaled by the number of Ti atoms to fit the transients cor-  
responding to Fe-0.65Ti and Fe-1.5Ti.

Fig. 5. Theoretical modelling of surface trapping.

Curve 1:  $A_1/A_2 = 1$ ;  $k = 10^{-2}$  s $^{-1}$ ;  $D = 2 \times 10^{-6}$  cm $^2$ /s.

Curve 2:  $A_1/A_2 = 1$ ;  $k = 10^{-4}$  s $^{-1}$ ;  $D = 10^{-6}$  cm $^2$ /s.

Curve 3:  $A_1/A_2 = 1$ ;  $k = 10^{-4}$  s $^{-1}$ ;  $D = 2 \times 10^{-6}$  cm $^2$ /s.

Curve 4:  $A_1/A_2 = 0.1$ ;  $k = 10^{-4}$  s $^{-1}$ ;  $D = 10^{-6}$  cm $^2$ /s.

Fig. 6. Difference in steady state behavior between uncoated Fe-0.15Ti and un-

coated Fe-0.65Ti, when the input current density is increased.

$A = 2.4$  mA/cm $^2$ ;  $B = 2.3$  mA/cm $^2$ ;  
 $C = 8$  mA/cm $^2$ ;  $D = 16$  mA/cm $^2$ ;  
 $E = 24$  mA/cm $^2$

### LIST OF FIGURE CAPTIONS

- Fig. 1. Analogy between hydrogen trapped ( $\phi_i'$ ) and diffusing ( $\phi_i$ ) fluxes in a crystal, and currents flowing through capacitive ( $i_i'$ ) and resistance ( $i_i$ ) branches in the analog network.
- Fig. 2. Illustration of the existence of two kinds of traps in the lattice; the choice of ordinary traps ( $C_o$ ) as irreversible ( $K_o$  open) and extraordinary traps ( $C_T$ ) as reversible ( $K_T$  closed) is for illustrative purposes only.
- Fig. 3. Experimental verification of a straight line relationship between the diffusivity ratio  $D_o/D$  without and with titanium, and the density of titanium atoms in the iron.
- Fig. 4. Fitting of experimental data using equation (18). The transient for Fe-0.15Ti; was best fitted; the obtained diffusional capacitance was then scaled by the number of Ti atoms to fit the transients corresponding to Fe-0.63Ti and Fe-1.5Ti.
- Fig. 5. Theoretical modelling of surface trapping.
- Curve 1:  $A_t^\infty / A_d^\infty = 1$ ;  $k = 10^{-2} \text{ s}^{-1}$ ;  $D = 2 \times 10^{-6} \text{ cm}^2/\text{s}$ .
- Curve 2:  $A_t^\infty / A_d^\infty = 1$ ;  $k = 10^{-4} \text{ s}^{-1}$ ;  $D = 10^{-6} \text{ cm}^2/\text{s}$ .
- Curve 3:  $A_t^\infty / A_d^\infty = 1$ ;  $k = 10^{-4} \text{ s}^{-1}$ ;  $D = 2 \times 10^{-6} \text{ cm}^2/\text{s}$ .
- Curve 4:  $A_t^\infty / A_d^\infty = 0.1$ ;  $k = 10^{-4} \text{ s}^{-1}$ ;  $D = 10^{-6} \text{ cm}^2/\text{s}$ .
- Fig. 6. Difference in steady state behavior between uncoated Fe-0.15Ti and uncoated Ferrovac E, when the input current density is increased.
- $A = 2.4 \text{ mA/cm}^2$ ;  $B = 3.2 \text{ mA/cm}^2$ ;  
 $C = 8 \text{ mA/cm}^2$ ;  $D = 16 \text{ mA/cm}^2$ ;  
 $E = 24 \text{ mA/cm}^2$ .



Fig. 7. Illustration of the fact that a straight line relationship  $J_{\infty}$  vs  $\sqrt{i_c}$  is not obeyed for uncoated Fe-0.15Ti. (Uncoated specimens dark symbols; palladium coated specimens light symbols).

Fig. 8. Different entry conditions typically found in permeation experiments:

a). step flux, or  $t \geq 0$ :  $i_i = i_o$  at  $x = 0$

b). step flux decreasing with time, or

$$t \geq 0 : i_i = \frac{i_o}{k_1 + k_2} \left[ k_1 + k_2 e^{-kt} \right] \text{ at } x = 0$$

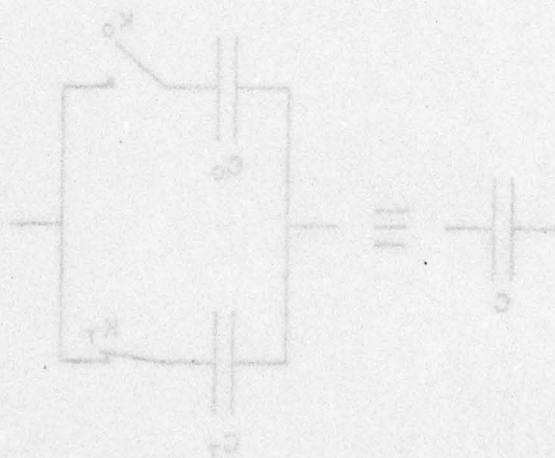


FIGURE D.2. Illustration of  $C = E \cdot C_0$  for linear-  
trative purposes only.  $E$  is represented as  
irreversible ( $K$  switch open) and  $C_0$  as  
reversible ( $K$  switch closed).

FIGURE D.1.  
Input Side Condition  
Chosen to Illustrate  
Surface Effect.

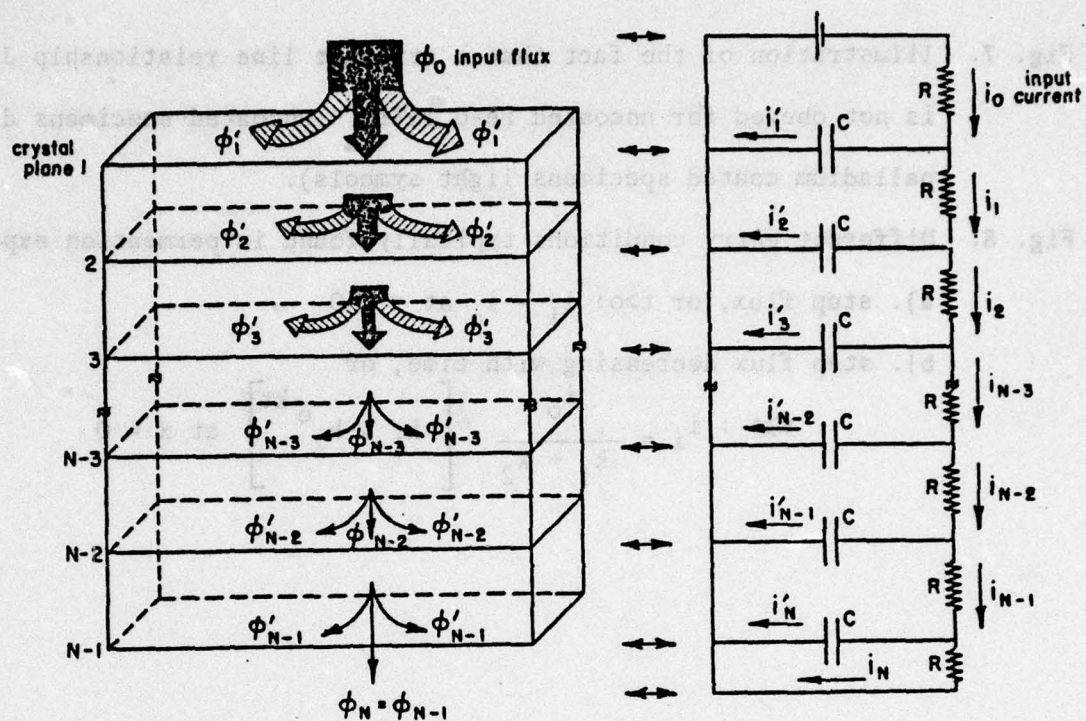


FIGURE D.1.  
Analogy Existing between Trapping in a Crystal (left diagram) and a Capacitive Ladder Network (right).

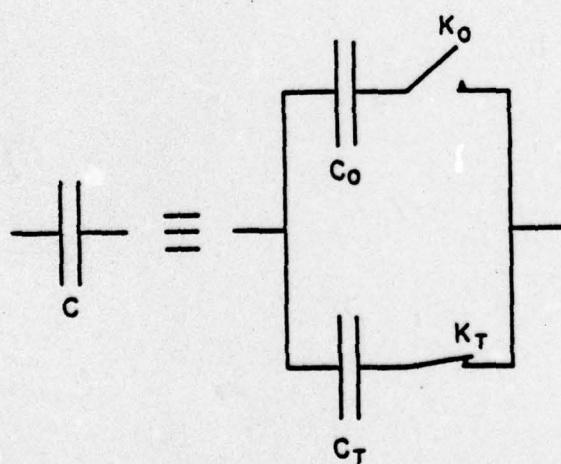


FIGURE D.2.  
Illustration of  $C = C_0 + C_T$ . For Illustrative Purposes Only,  $C$  is represented as Irreversible ( $K_0$  switch open) and  $C_T$  as Reversible ( $K_T$  switch closed).

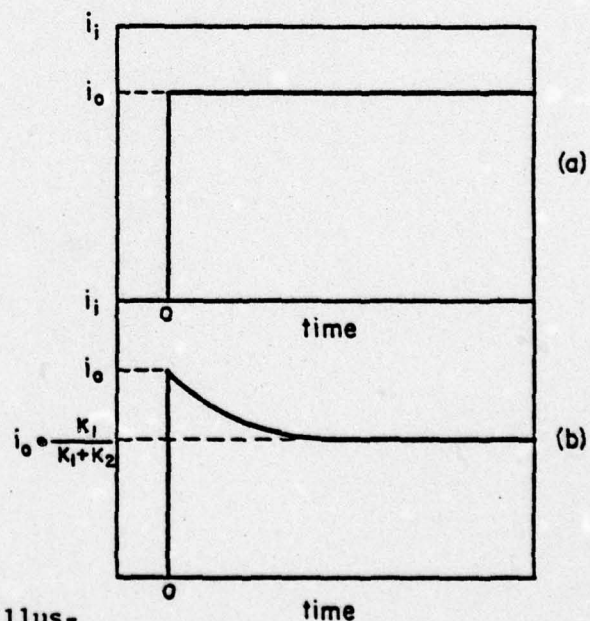


FIGURE D.3.  
Input Side Conditions Chosen to Illustrate Surface Effect.



# REFERENCES

1. A. W. Thompson and B. A. Wilcox, Scripta Met. 6, 689, (1972).
2. A. W. Thompson and I. M. Bernstein, "Advances in Corrosion Science and Technology," Plenum Press, (in press).
3. I. M. Bernstein, R. Garber, and G. M. Pressouyre, "Effect of Hydrogen on Behavior of Materials," TMS-AIME, p. 37, (1976).
4. A. McNabb and P. K. Foster, TMS-AIME, 227, 618, (1963).
5. G. R. Caskey and W. L. Pillinger, Met. Trans. 6A, p467, (1975).
6. R. A. Oriani, Acta Met., 18, 147, (1970).
7. M. Koiwa, Acta Met., 22, 1259, (1974).
8. G. M. Pressouyre, Ph.D. Thesis, Carnegie-Mellon University (1977).
9. J. Crank, "The Mathematics of Diffusion," (2nd Ed.), Clarendon Press, Oxford, (1975).
10. J. D. Hobson, "Hydrogen in Steel," Harrogate Conference, British Iron and Steel Institute, 62 (1971).
11. E. Weber, "Linear Transient Analysis," J. Wiley and Sons, London, (1956).
12. J. McBreen, L. Nanis and W. Beck, J. Electrochem Soc., 113, No. 11, 1218, (1966).
13. G. M. Pressouyre and I. M. Bernstein, submitted to Acta Met.
14. O. D. Gonzalez, TMS-AIME, 245, 607, (1969).
15. R. Gibala, TMS-AIME, 239, 1574, (1967).
16. W. Beck, J. O'M. Bockris, J. McBreen and L. Nanis, Proc. Royal Soc., A290, 220, (1966).
17. R. D. McCright, Techn. Report AFML-72-102, Part I, 375, (1972).
18. M. A. Fullenwider, J. Electrochem. Soc., 122, No. 5, 648, (1975).

ALGOL M164GP15, ,C=10 T=10 P=12 M=80

STANFORD ALGOL W (16JAN72)

```

0000 1-      BEGIN
0001 --      COMMENT *****
0001 --
0001 --      G      M      P
0001 --      MODEL FOR HYDROGEN TRAPPING IN A CRYSTAL, ASSUMING :
0001 --      TRAPPING REACTION :  $DN/DT = KNT(1-N) - PN$ 
0001 --       $NT = NTI + ND + NGB + NTIC$ 
0001 --      NT : EXPONENTIAL RISE
0001 --      NTIC : IRREVERSIBLE , P=0
0001 --      NTI: EQUILIBRIUM WITH ND, CONSTANT K1
0001 --      ND: EQUILIBRIUM WITH NGB, CONSTANT K2
0001 --      SOLVE FOR NGB
0001 --      SMALL OCCUPANCY CASE
0001 --      *****
0001 --      REAL NHS,NTI,NTIH,NGBH,NTICH,NDH,NT,NGB,ND,NTHETA,K2 ;
0002 --      REAL ARRAY A(0::2);
0003 --      REAL ARRAY KPRIME(0::2);
0004 --      REAL ARRAY K1(0::2);
0005 --      REAL ARRAY T(0::9);
0006 --      NHS:=1.88*10**20 ;
0007 --      NTHETA:=3*10**19;
0008 --      NTI:=1.48*10**20;
0009 --      NGR:=10**22;
0010 --      ND:=2.6*10**23;
0011 --      KPRIME(0):=8*10**(-23);KPRIME(1):=10**(-22);KPRIME(2):=2*10**(-22);
0014 --      A(0):=9*10**(-5);A(1):=8*10**(-5);A(2):=7*10**(-5);
0017 --      K1(0):=12000;K1(1):=15000;K1(2):=18000;
0020 --      T(0):=100;T(1):=500;T(2):=1000;T(3):=3000;T(4):=5000;T(5):=7500 ;
0026 --      T(6):=10000;T(7):=15000;T(8):=20000;T(9):=10**5;
0030 --      FOR IA:=0 UNTIL 2 DO
0030 --      FOR IKPRIME:=0 UNTIL 2 DO
0030 --      FOR IK1:=0 UNTIL 2 DO
0030 --      FOR IT:=0 UNTIL 9 DO
0030 2-      BEGIN
0031 --      NT:=NHS*(1-EXP(-A(IA)*T(IT)));
0032 --      NTICH:=NTHETA*(1-EXP(-KPRIME(IKPRIME)*NHS*(T(IT)-(1/A(IA))
0032 --      +(EXP(-A(IA)*T(IT))/A(IA)))));
0033 --      K2:=(-5.6*10**18)*NGB/((5.6*10**18)*NTI*K1(IK1)+(5.6*10**18)*ND
0033 --      -ND*(NHS-NTHETA));
0034 --      NGBH:=(NT-NTICH)/((K1(IK1)*K2*NTI/NGB)+(K2*NC/NGB)+1);
0035 --      NDH:=K2*ND*NGBH/NGB;
0036 --      NTIH:=K1(IK1)*NTI*NDH/ND;
0037 --      WRITE(T(IT),A(IA),K1(IK1),KPRIME(IKPRIME));
0038 --      WRITEON(NTHETA,NGB,K2,NT,NTICH,NDH,NTIH,NGBH);
0039 -2      END;
0040 -1      END

```

EXECUTION OPTIONS: DEBUG,1 TIME=10 SECONDS PAGES=12

000.99 SECONDS IN COMPILATION, (03096, 01432) BYTES OF CODE GENERATED

BEST AVAILABLE COPY



FALGOL M164GP15,

,C=10 T=10 P=12 M=80

S ANFORD ALGOL W (16JAN72)

BEST AVAILABLE COPY

```

C000 1-      BEGIN
C 01 --      COMMENT *****
C 01 --
C001 --
C 01 --      G      M      P
C 01 --      MODEL FOR HYDROGEN TRAPPING IN A CRYSTAL, ASSUMING :
C 01 --      TRAPPING REACTION :  $DN/DT = KNT(1-N) - PN$ 
C001 --       $NT = NTI + ND + NGB + NTIC$ 
C 01 --      NT : EXPONENTIAL RISE
C 01 --      NTIC : IRREVERSIBLE , P=0
C001 --      NTI: EQUILIBRIUM WITH ND, CONSTANT K1
C001 --      ND: EQUILIBRIUM WITH NGB, CONSTANT K2
C 01 --      SOLVE FOR NGB
C 01 --      LARGE OCCUPANCY CASE
C001 --      *****;
C 01 --      REAL NHS,NTI,NTIH,NGBH,NTICH,NDH,NT,NGB,ND,NTHETA,K2 ;
C 02 --      REAL ARRAY A(0::2);
C003 --      REAL ARRAY KPRIME(0::2);
C 04 --      REAL ARRAY K1(0::2);
C 05 --      REAL ARRAY T(0::9);
C006 --      NHS:=1.88*10**20 ;
C007 --      NTHETA:=3.5*10**19;
C 08 --      NTI:=1.48*10**20;
C 09 --      NGB:=10**22;
C010 --      ND:=2.6*10**23;
C 11 --      KPRIME(0):=8*10**(-23);KPRIME(1):=10**(-22);KPRIME(2):=2*10**(-22);
C 14 --      A(0):=10**(-4);A(1):=5*10**(-5);A(2):=10**(-5);
C017 --      K1(0):=1;K1(1):=10;K1(2):=50;
C 20 --      T(0):=100;T(1):=500;T(2):=1000;T(3):=3000;T(4):=5000;T(5):=7500 ;
C 26 --      T(6):=10000;T(7):=15000;T(8):=20000;T(9):=10**6;
C030 --      FOR IA:=0 UNTIL 2 DO
C030 --      FOR IKPRIME:=0 UNTIL 2 DO
C 30 --      FOR IK1:=0 UNTIL 2 DO
C030 --      FOR IT:=0 UNTIL 9 DO
C030 2-      BEGIN
C 31 --      NT:=NHS*(1-EXP(-A(IA)*T(IT)));
C 32 --      NTICH:=NTHETA*(1-EXP(-KPRIME(IKPRIME)*NHS*(T(IT)-(1/A(IA))
C032 --      +(EXP(-A(IA)*T(IT))/A(IA)))));
C 33 --      K2:=(10**(-5))*(8.4*NGB-8.6*(NHS-NTHETA)+1.76*(10**(-4))*(1+
C 33 --      (K1(IK1)*NTI/ND))*ND)/(4*(NHS-NTHETA)-8.4*(10**(-5))*(1+(K1(IK1)
C033 --      *NTI/ND))*ND);
C034 --      NGBH:=0.5*(NGB+NT-NTICH+((1+(K1(IK1)*NTI/ND))*K2*ND)
C 34 --      -SQRT((NGB+NT-NTICH+((1+(K1(IK1)*NTI/ND))*K2*ND))**2
C034 --      -4*NGB*(NT-NTICH)));
C035 --      NDH:=K2*NGBH*ND/(NGB-NGBH);
C 36 --      NTIH:=K1(IK1)*NTI*NDH/ND;
C 37 --      WRITE(T(IT),A(IA),K1(IK1),KPRIME(IKPRIME));
C038 --      WRITEON(NTHETA,NGB,K2,NT,NTICH,NDH,NTIH,NGBH);
C 39 -2      END;
C 40 -1      END

```

EXECUTION OPTIONS: DEBUG,1 TIME=10 SECONDS PAGES=12

C01.12 SECONDS IN COMPILATION, (03344, 01432) BYTES OF CODE GENERATED

## APPENDIX F

## TWIN IDENTIFICATION

Several articles in the literature<sup>(137-139)</sup> treat the problem of twin spot identification in a diffraction pattern. Use will be made here of the latest reference<sup>(139)</sup> by J. M. Haudin.

Consider a diffraction pattern, P, of zone axis  $\langle u \ v \ w \rangle$ ; the twin spots contained in this pattern are transformed from the matrix spots contained in a diffraction pattern P' of zone axis  $\langle u'v'w' \rangle$ , where:

$$\langle u'v'w' \rangle = \lambda \langle u \ v \ w \rangle S(pqr)$$

and S(pqr) is the matrix:

$$S(pqr) = \frac{1}{p^2 + q^2 + r^2} \begin{vmatrix} -p^2 + q^2 + r^2 & -2pq & -2pr \\ -2pq & p^2 - q^2 + r^2 & -2qr \\ -2pr & -2qr & p^2 + q^2 - r^2 \end{vmatrix}$$

where (pqr) is the twin plane, and  $\lambda$  is a coefficient chosen such that  $u'$ ,  $v'$ ,  $w'$  are prime integers.

In the case of a BCC lattice (for example,  $\alpha$ -iron), the twin plane is of the  $\{112\}$  type. From the symmetry of the cubic lattice, twinning on a  $\{112\}$  type plane is crystallographically equivalent to twinning on a  $\{111\}$  plane, since every  $\{111\}$  plane is perpendicular to three  $\{112\}$  planes.

Figure F.1 shows a bright field micrograph of a twin, with its corresponding diffraction pattern. The dark field image was obtained using one of the extra non lattice spots marked T. As seen from the pattern, the matrix zone axis is  $\langle u \ v \ w \rangle = [111]$ . The transformed plane by twinning is thus, using the previous equations:

$$\langle u'v'w' \rangle = \lambda [111] S(\bar{1}11)$$



The twinning plane was taken as (211), ( $\bar{1}\bar{2}1$ ) or ( $1\bar{1}2$ ), since the ( $\bar{1}11$ ) is perpendicular to any of those three planes. Performing the matrix product will give:

$$S_{(\bar{1}11)} = \frac{1}{3} \begin{vmatrix} 1 & 2 & 2 \\ 2 & 1 & -2 \\ 2 & -2 & 1 \end{vmatrix}, \text{ and therefore } \langle u'v'w' \rangle = [511] \text{ with } \lambda=3.$$

The  $[111]$  diffraction pattern has been drawn on Figure F.2 as well as the transformed  $[511]$  pattern. Superimposing the two makes all twin spots coincide with lattice spots. This arises from the fact that, for example,  $d(1\bar{1}\bar{4})_T = d(30\bar{3})_{\text{matrix}} = 0.676 \text{ \AA}$ ; similar coincidence exists for other spots. Therefore, no extra spots due to twinning should be present. However, extra spots have been found which are capable of dark field imaging of the twin. The reason for this is as follows:

When the predicted twin spots are far away from the direct beam (for example, three rows away), a system of spots from a plane close to ( $u'v'w'$ ) will be seen<sup>(139)</sup>. Here, ( $u'v'w'$ ) = (511); according to the possible values of angles between (511) and planes, the planes (411) and (311) are quite close, making angles with (511) of  $3.68^\circ$  and  $9.45^\circ$ , respectively.

Using first a  $[411]$  diffraction pattern, it will be seen that this pattern consists of {110} and {442} type spots. Since  $d(422) = 0.465 \text{ \AA}$ , the corresponding spots explain the origin of the extra row of spots (see diffraction pattern with reduced camera length). We did not however try dark field imaging on their spots, but only on the T spots.

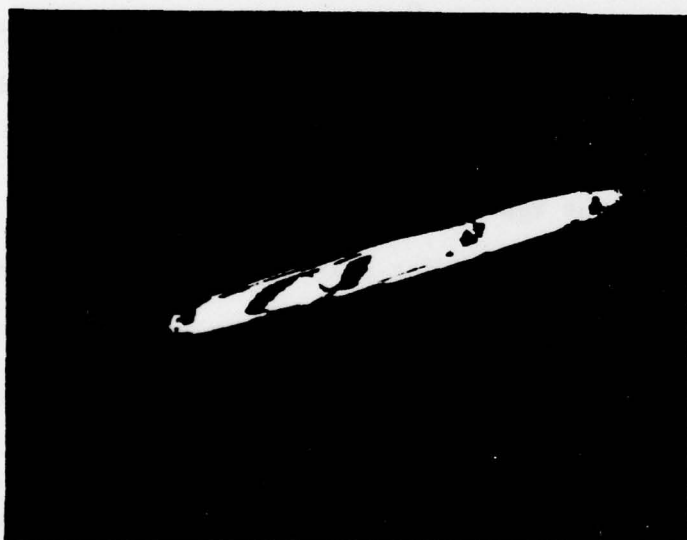
Consider now the  $[311]$  pattern, whose indexing is given in Figure F.2, where also is superimposed the matrix diffraction pattern. As seen on this figure, the superimposition of the  $[311]$  pattern matches the



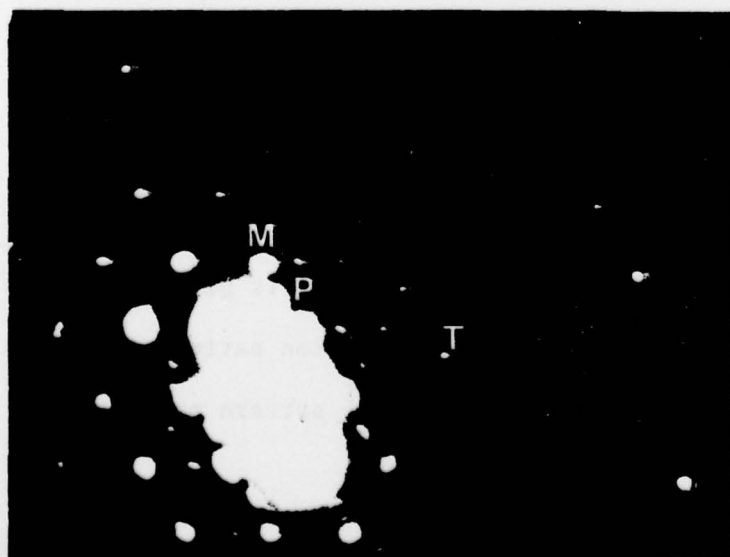
Figure F.1.

- (a) Bright field transmission electron micrograph of twin in hydrogen charged Alloy CC

0.2  $\mu$



- (b) Dark field of twin of Fig.F.1.a obtained with spot T on Fig.F.1.c.



- (c) Diffraction pattern obtained from the region of Fig.F.1.a, with a  $111$  zone axis.  
Twin spot is marked as T  
Particle spot is marked as P  
Matrix spot is marked as M.



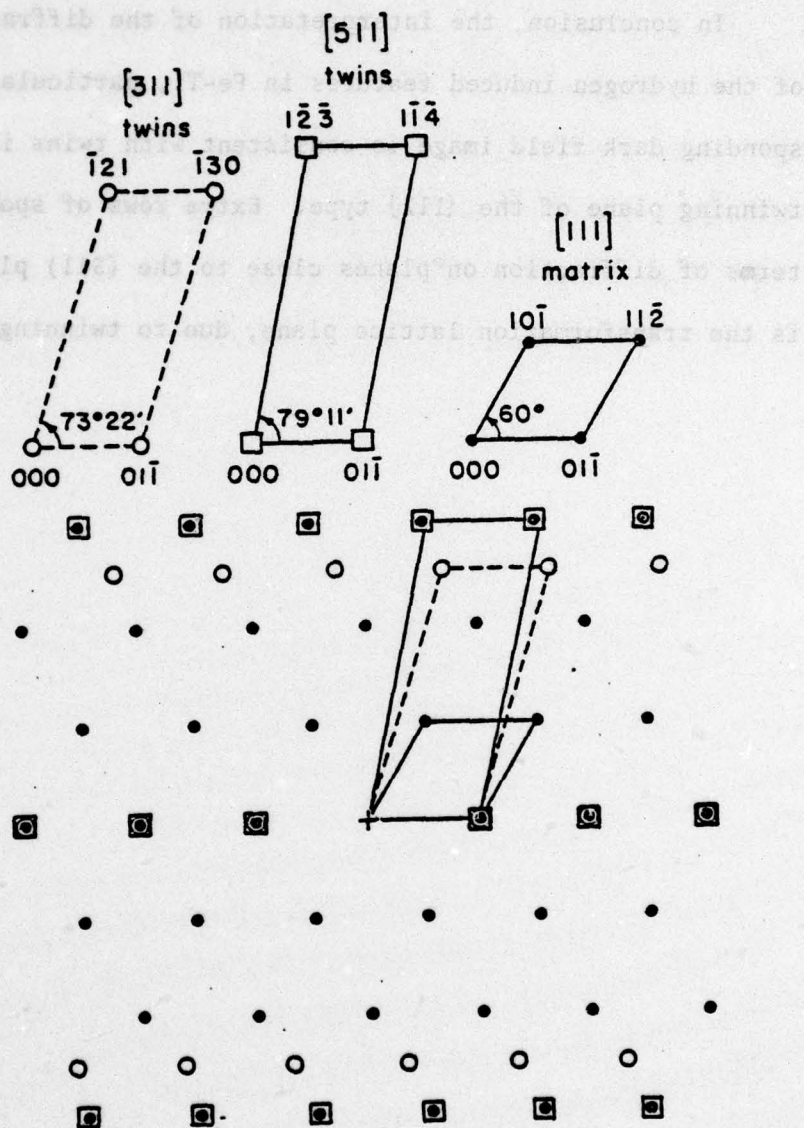


FIGURE F.2.  
Schematic of the 111 Diffraction Pattern, with Superimposed  
511 and 311 Twin Reflections.

spots T of the intermediate extra row where the dark field image was obtained.

In conclusion, the interpretation of the diffraction pattern of the hydrogen induced features in Fe-Ti, particularly its corresponding dark field image is consistent with twins in BCC  $\alpha$ Fe, with twinning plane of the  $\{112\}$  type. Extra rows of spot are explained in terms of diffraction on planes close to the (511) plane, which in turn is the transformation lattice plane, due to twinning of the (111) plane.

FIGURE 1  
Schematic of the 111 diffraction pattern with superimposed  
111 and 112 twin reflections



# REFERENCES

1. W. H. Johnson, Proc. Roy. Soc., London, 23, 168, (1875).
2. A.W.Thompson and I.M.Bernstein , in Advances in Corrosion Science and Technology, ed. by R. W. Staehle and M. G. Fontana, vol. 7, Plenum, N.Y., in press.
3. R. A. Oriani, in Proceedings of Conference on Fundamental Aspects of Stress Corrosion Cracking, Ohio State University, p.32 (1967).
4. J. Friedel, Adv. in Physics, 3, 446, (1954).
5. W. R. Heller, Acta Met., 9, 600, (1961).
6. D. N. Beshers, J. Appl. Phys., 36, 290, (1965).
7. L. S. Darken and R. P. Smith, Corrosion, 5, 1, (1949).
8. C. A. Zapffe and C. E. Sims, Metals and Alloys, 11, 145, (1940).
9. B. A. Bilby and J. Hewitt, Acta Met., 10, 587, (1962).
10. F. Garofalo et al., Acta Met., 8, 504, (1960).
11. A. S. Tetelman in Fracture of Solids, InterScience, N.Y., 671, (1963).
12. G. G. Hancock and H. H. Johnson, Trans AIME, 236, 513, (1966).
13. A. R. Troiano, Trans. Am. Soc. Met., 52, 54, (1960).
14. R. A. Oriani, Ber. der. Bunsen-Gesellschaft ., 76, 848, (1972).
15. M. Brachet, L'Hydrogene dans les Metaux, Coll. Intern. Valduc, France, 25, (1967).
16. J. C. M. Li, R. A. Oriani and L. S. Darken, Z. Physik. Chem., 49, 271, (1966).
17. N. J. Petch and P. Stables, Nature, 169, 842, (1952).
18. N. J. Petch, Phil. Mag., 1, 331, (1956).
19. J. R. Rice in Effect of Hydrogen on Behavior of Materials, ed. by A. W. Thompson and . . M. Bernstein, AIME, p.455, (1976).
20. R. A. Oriani, Private Communication, cited in: I. M. Bernstein, Mat. Sci. Eng., 6, 1, (1970).

21. J. A. Donovan, Met. Trans. 7A, 1677, (1976).
22. J. K. Tien, id. as Ref. 19, p. 309.
23. C. D. Beachem, Met. Trans., 3, 437, (1972).
24. I. M. Bernstein and B. B. Rath, Met. Trans., 4, 1545, (1973).
25. T. Asaoka, Thèse Docteur - Ingénieur, Univ. Paris - Sud., (1976).
26. Honeycombe and co-workers, see Ref. 31 to 35.
27. G. F. Comstock, Titanium in Iron and Steel, J. Wiley and Sons, N.Y. (1957).
28. A.S.M. Metals Handbook, Vol. 8, 8th Ed., (1973).
29. W. Tofaute and A. Büttinghaus, Arch. Eisenhüttenw., 12, 33, (1938).
30. G. K. Wertheim and J. H. Wernick, Acta Met., 15, 297, (1967).
31. R. W. K. Honeycombe, in Conference on Effect of Second Phase Particles on the Mechanical Properties of Steel, BSC/isi, p.136, (1971).
32. S. Freeman, ibid., p. 152.
33. R. W. K. Honeycombe, Met. Trans. 7A, 915, (1976).
34. A. Youle, B. Ralph, S. Freeman and R. W. K. Honeycombe, Metallography, 7, 333, (1974).
35. S. Freeman and R. W. K. Honeycombe, Met. Sci., 5g, (1977).
36. E. Nes and G. Thomas, Met. Trans., 7A, 967, (1976).
37. P. Grieveson, Proc. Brit. Ceram. Soc., 8, 137, (1967).
38. W. C. Leslie, Met. Trans., 3, 5, (1972).
39. H. J. Rack, Met. Trans., 3, 1667, (1972).
40. I. Gupta and F. Garofalo, Mat. Sci. Eng., 5, 271, (1969/70).
41. J. R. Rellick and C. J. McMahon, Jr., Met. Trans., 1, 929, (1970).
42. W. C. Leslie and R. J. Sober, Trans. ASM, 60, 99, (1967).
43. A. Kelly and R. B. Nicholson, Progr. Mat. Sci., 10, 289, (1963).
44. T. Marrison, id. as Ref. 31.



45. K. W. Andrews et al. , Interpretation of Electron Diffraction Patterns, Plenum Press, 2nd ed., (1971).
46. P. Ehrlich, Z. Anorg. Chem., 259, 1, (1949).
47. P. Duwez and F. Odell, J. Electrochem. Soc., 97, 299, (1950).
48. G. Thomas, in Modern Diffraction and Imaging Techniques in Materials Science, ed. by S. Amelinckx, R. Gevers, G. Renaut, and J. Wan Landuyt, North-Holland Pub. Co., p. 131, (1970).
49. H. K. Birnbaum and C. A. Wert, Ber. der. Bunsen-Gesellschaft, 76, 806, (1972).
50. J. Volkl and G. Alefeld <sup>in</sup> Diffusion in Solids, Recent Developments, ed. by R. S. Nowich and J. J. Burton, Academic Press, (1975).
51. A. McNabb and P. K. Foster, Trans. AIME, 227, 618, (1963).
52. R. A. Oriani, Acta Met., 18, 147, (1970).
53. K. Ono and L. A. Rosales, Tran. AIME, 242, 244, (1968).
54. T. Boniszewski, Report P/10/66 of the British Welding Research Association, (1966).
55. D. M. Allen-Booth and J. Hewitt, Acta Met., 22, 171, (1974).
56. G. M. Evans and E. C. Rollason, JISI, 207, 1591, (1969).
57. M. Yamada, C. Ouchi, and I.M. Bernstein, Unpublished Research.
58. A. J. Kumnick and H. H. Johnson, Met. Trans., 5, 1200, (1974).
59. JP. Laurent et al, in Hydrogen in Metals, ASM 2, ed. by I. M. Bernstein and A. W. Thompson, p. 559, (1974).
60. R. Gibala, Trans. AIME, 239, 1574, (1967).
61. B. B. Rath and I. M. Bernstein, Met. Trans., 2, 2845, (1971).
62. I. M. Bernstein, Scripta Met., 8, 343, (1974).
63. C. Baker and H. K. Birnbaum, Acta Met., 21, 865, (1973).
64. R. Gibala, cited in Reference 63.
65. J. O'M. Bockris et al, Electrochimica Acta, 15, 47, (1970).

66. W. Dresler and M. G. Froberg, JISI, 211, 298, (1973).
67. W. Beck et al, Met. Trans., 2, 883, (1971).
68. M. A. V. Devanathan and Z. O. J. Stachursky, Proc. Roy. Soc., A270, 90, (1962).
69. C. Wagner, Thermodynamics of Alloys, Addison-Wesley, Reading, Mass., 47, (1952).
70. C. H. P. Lupis and J. F. Elliott, Acta Met., 15, 265, (1967).
71. J. F. Elliott, M. Gleiser and V. Ramakrishna, Thermochemistry for Steelmaking, Addison-Wesley, Reading, Mass., (1963).
72. G. K. Sigworth and J. F. Elliott, Metal Science, 8, 298, (1974).
73. M. Weinstein and J. F. Elliott, Trans. AIME, 227, 382, (1963).
74. C. H. P. Lupis and J. F. Elliott, Acta Met., 14, 529, (1966).
75. Janaf Thermochemical Tables, NSRDS-NBS37, U.S. Department of Commerce, National Bureau of Standards, (1971).
76. J. Friedel, Ber. der. Bunsen-Gesellschaft, Bd. 76, No. 8, 828, (1972).
77. J. C. Smithells, Metals Reference Book, London (1949).
78. M. A. Fullenwider, J. Electrochem. Soc., 122, 648, (1975).
79. J. McBreen et al. , , J. Electrochem. Soc., 113, 1218, (1966).
80. T. K. Namboodhiri and L. Nanis, Acta Met., 21, 663, (1973).
81. O. D. Gonzalez, Trans. AIME, 245, 607, (1969).
82. G. R. Caskey, Jr. and W. L. Pillinger, Met. Trans. 6A, 467, (1975).
83. M. Koiwa, Acta Met., 22, 1259, (1974).
84. G. M. Pressouyre and I. M. Bernstein, Corrosion Science, in press.
85. J. Crank, The Mathematics of Diffusion, Oxford, Clarendon Press, (1956).
86. J. L. Dillard, Thèse Université Paris VI, (1973).
87. L. Nanis and T. K. Namboodhiri, J. Electrochem. Soc., 119, 691, (1972).



88. G. R. Caskey and W. L. Pillinger, Proc. of International Conf. on Hydrogen in Metals, ASM 2, ed. by I.M. Bernstein and A.W. Thompson, p.683, (1974).
89. J. McBreen and M. A. Genshaw, see Ref. 3, p. 51, (1967).
90. J. O'M. Bockris, J. McBreen and L. Nanis, J. Electrochem. Soc., 112, 1025, (1965).
91. S. Schuldiner, J. Electrochem. Soc., 108, 384, (1961).
92. C. D. Kim and B. E. Wilde, J. Electrochem. Soc., 118, 202, (1971).
93. R. Ash and R. M. Barrer, Phil. Mag., 4, 1197, (1959).
94. G. C. Bond, Surface Sci., 18, 11, (1969).
95. D. E. Beck and E. Miyazaki, Surface Sci., 48, 473, (1975).
96. C. O. Steinbrüchel, Surface Sci., 51, 539, (1975).
97. S. Wach and A. P. Miodownik, Corr. Sci., 8, 271, (1968).
98. D. R. Paul, J. of Polymer Sci., A27, 181, (1969).
99. W. Beck et al, Proc. Roy. Soc., A290, 220, (1966).
100. A. S. Tetelman and W. D. Robertson, Trans. AIME, 224, 775, (1962).
101. M. Gell, Ph.D. Thesis, Yale University, (1965).
102. M. Gell, J. P. Briant, and W. D. Robertson, Trans. AIME, 239, 813, (1967).
103. D. J. Van Ooijen and J. D. Fast, Acta Met., 11, 211, (1963).
104. H. P. Van Leeuwen, Corrosion, 29, 197, (1973).
105. I. M. Bernstein, Met. Trans., 1, 3143, (1970).
106. I. M. Bernstein, Mat. Sci. Eng., 6, 1, (1970).
107. C. J. McMahon, Jr., Acta Met., 14, 839, (1966).
108. H. Uhlig, K. E. Perumal and M. Talerman, Corrosion, 30, 229, (1974).
109. L. S. Darken, in Proceedings of the Darken Conference, ed. by R. M. Fisher, R. A. Oriani and E. T. Turkdogan, USS, August (1976).
110. J. O'M. Bockris and P. K. Subramanyan, J. Electrochem. Soc., 118, 1114, (1971).

111. C. S. Smith and L. Guttman, Trans. AIME, 197, 81, (1953).
112. A. S. Tetelman, id. as Ref. 3.
113. M. Dadian and S. Talbot-Besnard, Mém. Sci. Rev. Mét., LXIII, 4, 375, (1966).
114. J. C. Williams, Private Communication.
115. R. E. Reed-Hill, in Physical Metallurgy Principles, 2nd Ed., Van Nostrand Co., (1973).
116. S. Mahajan and D. F. Williams, International Metallurgical Reviews, 18, 43, (1973).
117. J. O. Stiegler and C. J. McHargue, quoted in Reference 116.
118. G. F. Bolling and R. H. Richman, Can. J. Phys., 45, 541, (1967).
119. T. N. Baker, Acta Met., 21, 261, (1973).
120. V. K. Heikkinen, Scand. J. Metallurgy, 3, 41, (1974).
121. J. K. Tien, A. W. Thompson, I. M. Bernstein and R. J. Richards, Met.Trans., 7A, 821, (1976).
122. L. M. Foster, T. H. Jack and W. W. Hill, Met. Trans., 1, 3117, (1970).
123. D. N. Beshers Diffusion, ASM, Metals Park, Ohio, 209. (1973).
124. R. Garber, I. M. Bernstein and A. W. Thompson, Scripta Met., 10, 341, (1976).
125. C. D. Beachem, J. Basic. Eng., 87, 299, (1965).
126. H. P. Van Leeuwen, Mém. Sci. Rev. Mét., LXXI, 9, 509, (1974).
127. A. W. Thompson and I. M. Bernstein, Fracture 1977, 2, Waterloo, p.249, (1977), in press.
128. H. H. Johnson, J. G. Morlet and A. R. Troiano, Trans. AIME, 212, 528, (1958).
129. R. P. Frohberg, W. J. Barnett and A. R. Troiano, Trans. ASM, 47, 892, (1955).
130. M. B. Whiteman and A. R. Troiano, Corrosion, 21, 53, (1965).
131. M. R. Louthan, Jr., id as Reference 59, p. 56, (1973).
132. J. C. Williams and N. E. Paton, in Systematic Materials Analysis, ed. by J. Richardson and R. Peterson, in press.



133. P. B. Hirsch et al. , . Electron Microscopy of Thin Crystals, Washington, Butterworths, (1965).
134. J. D. Fast, Interaction of Metals and Gases, Vol. 1, Acad. Press, N. Y., (1965).
135. C. H. P. Lupis, Private Communication.
136. R. E. Reed-Hill, Physical Metallurgy Principles, 2nd Ed., D. Van Nostrand, (1973).
137. E. S. Meiran and M. H. Richman, Trans. AIME, 227, 1044, (1963).
138. O. Johari and G. Thomas, 230, 597, (1964).
139. J. M. Haudin, Metallography, 9, 209, (1976).

SECURITY CLASSIFICATION OF THIS PAGE (When Data Entered)

REPORT DOCUMENTATION PAGE		READ INSTRUCTIONS BEFORE COMPLETING FORM
1. REPORT NUMBER N00014-75-C-0265 NR 036-099-7 (C-MU)	2. GOVT ACCESSION NO.	3. RECIPIENT'S CATALOG NUMBER
4. TITLE (and Subtitle) The Role of Trapping on Hydrogen Transport and Embrittlement	5. TYPE OF REPORT & PERIOD COVERED Technical Report	6. PERFORMING ORG. REPORT NUMBER 14 TR-75 CMU-036-099-7
7. AUTHOR(s) Gerard M. Pressouyre I. M. Bernstein	8. CONTRACT OR GRANT NUMBER(s) N00014-75-C-0265	9. PROGRAM ELEMENT, PROJECT, TASK AREA & WORK UNIT NUMBERS
10. PERFORMING ORGANIZATION NAME AND ADDRESS Department of Metallurgy & Materials Science Carnegie-Mellon University Pittsburgh, PA 15213	11. CONTROLLING OFFICE NAME AND ADDRESS ONR Code 471 Arlington, VA 22217	12. REPORT DATE 9 Jul 77
13. MONITORING AGENCY NAME & ADDRESS (if different from Controlling Office)	14. NUMBER OF PAGES 336 p. 167	15. SECURITY CLASS. (of this report) Unclassified
16. DISTRIBUTION STATEMENT (of this Report) Qualified requesters may obtain copies from DDC Reproduction in part or in whole is permitted for any purpose of the U. S. Government	17. DISTRIBUTION STATEMENT (of the abstract entered in Block 20, if different from Distribution Unlimited) Unlimited	
18. SUPPLEMENTARY NOTES		
19. KEY WORDS (Continue on reverse side if necessary and identify by block number) Hydrogen, permeation, trapping, fracture, diffusion, particles.		
20. ABSTRACT (Continue on reverse side if necessary and identify by block number) The achieved goal of the present research was to propose sets of criteria that would help in the design of alloys more resistant to hydrogen embrittlement. The research is based upon the original idea that a fine and homogeneous distribution of particular kinds of traps could achieve the above goal. This starting idea was developed from an investigation of existing hydrogen embrittlement theories, which showed that a common factor of all theories was the presence in the matrix of large deleterious accumulations of hydrogen at specific		

DD FORM 1 JAN 73 1473

EDITION OF 1 NOV 66 IS OBSOLETE  
S/N 0102-LP-014-6601

Unclassified

SECURITY CLASSIFICATION OF THIS PAGE (When Data Entered)

next  
page  
bpg



20. Abstract (continued)

sites. Fe-Ti alloys in both the carburized and uncarburized condition were chosen as the model material to simulate internal trapping of hydrogen. Microstructure characterization revealed that all alloys consisted of a ferrite matrix in which free substitutional titanium atoms and titanium carbide particles were present. Techniques were developed to distinguish between reversible traps (titanium atoms, dislocations, grain boundaries, coherent particles) and irreversible traps (such as titanium carbide particles). This characterization separation was achieved both experimentally (using an electrochemical permeation cell) and theoretically (by proposing two new models of reversible and irreversible trapping, and by comparison with existing theories).